



University
of Glasgow

Ziegler, Spencer Wilson (2003) *The rigid-body dynamics of tethers in space*. PhD thesis.

<http://theses.gla.ac.uk/5338/>

Copyright and moral rights for this thesis are retained by the author

A copy can be downloaded for personal non-commercial research or study, without prior permission or charge

This thesis cannot be reproduced or quoted extensively from without first obtaining permission in writing from the Author

The content must not be changed in any way or sold commercially in any format or medium without the formal permission of the Author

When referring to this work, full bibliographic details including the author, title, awarding institution and date of the thesis must be given

The Rigid-body Dynamics of Tethers in Space

by

Spencer Wilson Ziegler

September 2003

A dissertation submitted to the Faculty of Engineering, University of Glasgow,
in fulfilment of the requirements for the degree of Doctor of Philosophy.



UNIVERSITY
of
GLASGOW

Abstract

Space tethers are high strength, low-density cables that connect satellites, probes or space stations to each other in space. The cables are typically very long structures ranging from a few hundred metres to several kilometres and have a relatively small diameter, being only a few millimetres thick. Many applications have been proposed for tethers and much experience and knowledge has been gained through in-orbit flight-testing of conductive and non-conductive tethers. Tethers are also being supported by the major space agencies and companies can already foresee the possibility of commercially exploiting tethers to make a profit. The aim of this thesis was to address some of the issues relating to the performance and dynamics of momentum exchange tethers.

The multiple scales perturbation method successfully generated an approximate closed-form solution to the three dimensional motion of a tethered dumbbell on an elliptical orbit, which is valid for small initial angular displacements close to the gravity vector and orbit eccentricities less than 0.1. However, numerical integration has to be employed if the dynamics of the tether are to be comprehensively studied for values greater than the given initial conditions and those likely to be encountered in space. The planar and three-dimensional attitude dynamics of a tethered dumbbell on an elliptical orbit were, therefore, explored numerically. The largest stable region exists for a tether with no initial angular velocity and initially positioned close to the local vertical. For certain initial conditions the tether libration occurs as a transient and a remarkable structure was uncovered within the region that governs the duration of the transient. The generation of velocity increments upon completion of a single orbit through the spin-orbit coupling on an elliptical orbit was not found to be of particular use. Few initial conditions exist that allow the payload to be reliably released above the facility when the spinning tether is aligned exactly along the gravity vector at perigee. The dumbbell deviated from the planar tether's qualitative behaviour only when the initial out-of-plane angular displacement became sufficiently large. A strong link was observed between libration and regular tether motion and between chaos and a tumbling dumbbell, which suggests a dumbbell librating either within or out of the orbital plane is associated with regular motion and a chaotic regime gives rise to tumbling.

Three fundamental tether motions were considered for payload orbital transfer with tethers: hanging, prograde libration and prograde motorised spin. The symmetrical double-ended motorised spinning tether performed best and was most efficient, improving by two orders of magnitude on the librating tether which in turn improved on the hanging tether by roughly a factor of two. An upper payload using long tethers with a motorised tether on a circular orbit

can be transferred from a low to a geostationary Earth orbit by employing relatively high motor torque and a safety factor on the tether strength close to unity. Two common literature results, the constant efficiency index of seven for a hanging tether upper payload release and the maximum efficiency index of fourteen for an upper payload released from a prograde librating tether, were found to be a lower bound and quite readily breached, respectively. Orbit circularisation through tether release was found to be feasible with retrograde librating tethers. When the point of release does not occur along the local vertical then a non-optimum release of the payload was found to severely reduce the performance of payload transfer with tethers. Consequently, a very precise and accurately timed release is important for the success of payload orbital transfer with tethers since missing the point of release by a single degree with a spinning tether, say, can cause the payload to miss its required target. The best design for the outrigger system to provide the necessary resistive torque is to utilise the gravity gradient and trap the outrigger system within the gravitational potential well. In this manner the outrigger tether length can be significantly reduced and the outrigger end masses can be minimised, thus saving valuable launch mass and cost, as well as exposing less tether surface area to the space environment. With current materials the maximum ΔV to be expected with a motorised tether is between 600-1400 m/s depending on the tether length and payload mass. The duration of the spin-up lasts approximately between half and a full Earth day but may vary by an hour, say, depending on the initial conditions and orbit eccentricity. Ensuring the motor torque axis remains perpendicular to the orbital plane was found to be vital otherwise the spin-up time is greatly increased. The motorised tether has the ability to shift the datum of a hanging tether, which may have useful applications in Earth monitoring or tethered interferometry. Out-of-plane initial angular displacements or the motor torque axis not remaining perpendicular to the orbital plane caused the motorised tether to precess. Furthermore, the motion of the motorised tether with a constant motor torque was found to be regular, but quasi-periodic, which implies that the payload cannot be reliably delivered at perigee along the local vertical.

Table of Contents

Abstract	ii
Table of Contents	iv
Acknowledgements	vii
Publications	ix
Nomenclature	x
1. An Introduction to Tethers in Space	1
1.0 Introduction	1
1.1 Definition of a Space Tether	2
1.2 Electrodynamic Tethers	3
1.3 Gravity Gradient Stabilisation	8
1.4 Mechanics of Payload Orbital Transfer with Momentum Exchange Tethers	9
1.5 Further Suggested Applications of Tethers	14
1.6 Historical Background	15
1.7 Past Tether Missions	15
1.8 Tether Missions Planned for the Near Term	21
1.9 Tether Survivability and Design	23
1.10 Nonlinear Dynamics of a Tethered Dumbbell	24
1.11 Aims and Objectives	28
2. Derivation of the Governing Equations of Motion	29
2.0 Modelling the Motion of a Tether in Space	29
2.1 Co-ordinate System	31
2.2 Derivation of the Equations of Motion Governing a Tethered Dumbbell	34
2.3 Concept of Symmetrical Motorised Tether	40
2.4 Derivation of the Equations of Motion Governing a Symmetrical Motorised Tether	41
2.5 Conclusions	50
3. Derivation and Evaluation of Closed-Form Solutions for the Tethered Dumbbell	51
3.0 Introduction	51
3.1 2 nd Order Method of Multiple Scales Analysis of the Tethered Dumbbell on an Elliptical Orbit	51
3.2 Alternative Closed-Form Solutions for the Planar Tethered Dumbbell on	56

Elliptical Orbits	
3.3 3 rd Order Method of Multiple Scales Analysis of the Tethered Dumbbell on a Circular Orbit	57
3.4 Evaluation and Comparison of the Derived Closed-Form Solutions	64
3.5 Conclusions	74
4. Planar Dynamics of a Tethered Dumbbell on Elliptical Orbits	75
4.0 Introduction	75
4.1 Numerical Methods	75
4.2 Data and Tether Models	78
4.3 Transition from Libration to Spin	79
4.4 Transition from Regular to Chaotic Motion	89
4.5 Comparison between the Onset of Spin and Chaos	99
4.6 Velocity Increment Generation Through Tether Spin-Orbit Coupling	106
4.7 Conclusions	111
5. Three-Dimensional Dynamics of a Tethered Dumbbell on Circular and Elliptical Orbits	112
5.0 Introduction	112
5.1 Steady-state Boundary between Libration and Spin	112
5.2 Tether Tumbling during First Completed Orbit	115
5.3 Duration of Transient Librations	117
5.4 Comparison between the Onset of Tumbling and Chaos	120
5.5 Conclusions	134
6. Payload Orbital Transfer with Motorised Tethers	135
6.0 Introduction	135
6.1 Orbital Elements of the Payload after Tether Release	135
6.2 Altitude Gain or Drop of a Payload Released from a Tether Aligned Along the Gravity Gradient	139
6.3 Tether Angular Velocity, Tether Strength and Spin-up Criterion	140
6.4 Definition of Performance and Efficiency Indices	141
6.5 Results and Discussion for Optimum Release of Payload	142
6.6 Orbit Circularisation with Tethers	156
6.7 Effect of Non-optimum Release on Payload Orbital Transfer with Tethers	157
6.8 Conclusions	164

7. Design Considerations and Dynamics of a Symmetrical Motorised Tether	166
7.0 Introduction	166
7.1 Design of Outrigger System	166
7.2 Design Data for the Motorised Tether	171
7.3 Spin-Up Dynamics of a Motorised Tether	173
7.4 Duration of Spin-up	184
7.5 Conclusions	187
8. Conclusions and Further Work	188
8.0 Conclusions	188
8.1 Further Work	191
References	194

Acknowledgements

Acknowledgements in theses tend to be rather short with an all too quick sentence thanking the supervisor. I feel with the supervision, or better, the support and advice Matthew Cartmell has given me that a swift sentence would not only fail to capture the gratitude I owe him but also be downright inappropriate. My limited experience with academia has quickly taught me that a person like Matthew is definitely a rare breed. The project he invited me to work on in the summer of 1998 was an idea he had independently generated and subsequently put a lot of effort into. His concept attracted funding from the European Space Agency and was still very much in its infancy when I enquired about possibilities of doing a PhD under his tutelage. I imagine most academics would have pursued a concept in its state of development alone in order to receive the possible accolades and single author publications. Matthew, on the other hand, is a humble and selfless person who had the courage and generosity to suggest this topic for my thesis. I am very grateful for this as a lot of the experiences, opportunities and events I have experienced throughout the PhD are probably solely attributable to the research topic itself. A quality I admire in Matthew is his fairness in his approach to all his colleagues and students. He took tremendous care and effort over my personal development and his support throughout has been fantastic. His patience with my research methodology and personality is exceptional. Any work I have given him to read has always been promptly returned with valuable comments appended. His technical support is good and whenever he was unable to provide an immediate answer he would devote time to find possible solutions. I enjoy his enthusiasm for research and his willingness to debate ideas and concepts. Matthew cannot be faulted for the amount of access he gives his students, especially for such an exceptionally busy professor. He has always been there if I needed him, offered regular meetings, and quickly responded to any emails. In short, he possesses all the attributes a student would hope for in their PhD supervisor. I thank him for all he has done for and offered me. I also want to thank him for an exciting and productive period at the University of Glasgow.

I wish to thank Colin McInnes for his tremendous support, friendship and numerous discussions. It is clear to me that without Colin my education and development in astronautics would have been more limited. His ambitiousness and enthusiasm for research is infectious and I am very grateful his time. I also want to thank him for his support and effort he has given me in my personal development.

During my three years at the University of Glasgow I made three very good friends: Arek Żak, David Forehand and Lorna Smith. Their friendship means a lot to me and definitely

enriched the PhD experience. I also want to thank Arek and David for their help and advice on technical matters.

My thesis relies heavily on computational resources and in conjunction with this I want to thank Kenny Stephenson, Walter Robinson and Craig Veitch for all their help. In particular I really wish to thank Kenny for his tremendous advice, help and technical support without whom I would not have been able to take full advantage of the available computers and software in the department.

I have had conversations with many people during the PhD who have given me good advice, useful suggestions and new ideas. In relation to this, I wish to thank in alphabetical order: Dennis Bernstein, Raya Khanin, Andre Mazzoleni, Arun Misra, Phil Palmer, Martin Schagerl, Dan Scheeres, Steven Tragesser, Hans Troger, and Georg Wiedermann.

At UMIST I thank Keith Davey, Graham Thompson and Dave Bond for their fabulous encouragement, patience and understanding.

I wish to thank my parents, my maternal grandmother and the Faculty of Engineering at the University of Glasgow for their immense financial support throughout my PhD. I am very grateful for this, as without the support I would not have been able to devote all my efforts to research. I also wish to acknowledge the financial assistance from the following bodies, which allowed me to attend numerous conferences during the PhD: Department of Mechanical Engineering at the University of Glasgow, Outreach Office at the European Space Agency, Scottish International Education Trust, Institution of Mechanical Engineers, and the Royal Aeronautical Society.

Finally, but certainly not least, I wish to thank Mhairi Brunton for all her love and support. She has been through all the highs and lows with me and without her the last years would not have been as bright, interesting, and fun.

Publications

The work presented in this thesis has so far either contributed or led to the following publications:

- CARTMELL, M. P., ZIEGLER, S. W., KHANIN, R., and FOREHAND, D. I. M., “Multiple Scales Analyses of the Dynamics of Weakly Nonlinear Mechanical Systems”, *ASME Applied Mechanics Reviews*, Vol. 56, No. 5, pp. 455-492.
- CARTMELL, M. P., ZIEGLER, S. W., and NEILL, D. S. (2003). “On the Performance and Scale Modelling of a Motorised Momentum Exchange Propulsion Tether”, *Proceedings of the Space Technology and Applications International Forum*, American Institute of Physics, Vol. 654, pp. 571-579.
- ZIEGLER, S. W., and CARTMELL, M. P. (2001). “Using Motorized Tethers for Payload Orbital Transfer”, *Journal of Spacecraft and Rockets*, Vol. 38, No. 6, pp. 904-913.
- ZIEGLER, S. W., and CARTMELL, M. P. (2001). “On the Validity of Recent Predictions for Tethers on Elliptical Orbits”, *Advances in the Astronautical Sciences*, Spaceflight Mechanics 2001, Vol. 108, Part 2, pp. 1831-1838.
- CARTMELL, M. P., and ZIEGLER, S. W. (2001). “Experimental Scale Model Testing of a Motorised Momentum Exchange Propulsion Tether”, *37th AIAA/ASME/SAE/ASEE Joint Propulsion Conference & Exhibit*, AIAA Paper 2001-3914, 8-11 July, Salt Lake City, Utah, USA.
- CARTMELL, M. P., and ZIEGLER, S. W. (2001). “Ground Testing of a Spinning Tether Transfer System”, *Final Report for European Space Agency*, ESTEC Contract No 13845/99/NL/MV, 3 May 2001.
- ZIEGLER, S. W., and CARTMELL, M. P. (2001). “On the Validity of Recent Predictions for Tethers on Elliptical Orbits”, *11th AAS/AIAA Space Flight Mechanics Meeting*, AAS Paper 01-233, 11-15 February, Santa Barbara, California, USA.
- ZIEGLER, S. W., and CARTMELL, M. P. (2000). “Investigating the Use of Motorised Tethers for Payload Orbital Transfer”, *AIAA/AAS Astrodynamics Specialist Conference and Exhibit*, AIAA Paper 2000-4529, 14-17 August 2000, Denver, Colorado, USA.
- CARTMELL, M. P. and ZIEGLER, S. W. (2000). “Terrestrial Scale Model Testing of a Motorised Propulsion Tether”, *36th AIAA/ASME/SAE/ASEE Joint Propulsion Conference & Exhibit*, AIAA Paper 2000-3612, 16-19 July, Huntsville, Alabama, USA.
- CARTMELL, M. P. and ZIEGLER, S. W. (1999). “Symmetrically Laden Motorised Tethers for Continuous Two-way Interplanetary Payload Exchange”, *35th AIAA/ASME/SAE/ASEE Joint Propulsion Conference & Exhibit*, AIAA Paper 99-2840, 20-24 June, Los Angeles, California, USA.

Nomenclature

α	out-of-orbital-plane angular displacement of tether
β	planar angular displacement of outrigger tether
γ	angular displacement of motor torque axis about the tether's longitudinal axis
δ	L/r_C
δ_1	L_1/R
δ_2	L_2/R
ε	a small parameter in multiple scales perturbation method, which serves as a book-keeping device
η	discrete quantity measuring last perigee passing prior to the onset of tether tumbling
η_{\max}	maximum number of completed orbits used to inspect the onset of tumbling
Θ, θ	true anomaly
θ'	tether's angular orbital velocity
Θ_0	transfer orbit's true anomaly at the point of release
θ_{\max}	maximum libration angle between tether and the gravity vector
$\Theta_{\Delta\pi,apo}$	true anomaly at the location of the ideal or required apoapsis
$\Theta_{\Delta\pi,per}$	true anomaly at the location of the ideal or required periapsis
λ	Lyapunov exponent
μ	product of the universal gravitational constant and the planet's mass
ρ	density of tether material
ρ_{disc}	density of reaction momentum wheel
σ	tensile strength of tether material
σ_{\max}	ultimate tensile strength of tether material
τ	motor torque
ν	Poisson's ratio
Φ	shift in the orbit's apoapsis or periapsis in relation to the ideal periapsis or apoapsis
ψ	angular displacement of tether within the orbital plane
ψ_0	initial in-plane angular displacement
ψ_{50000}	in-plane angular displacement after the passing of 50,000 seconds
ψ'	$\frac{d\psi}{dt}$
ψ'_v	angular pitch velocity when tether is aligned along the local vertical

$\dot{\psi}$	$\frac{d\psi}{d\theta}$
Ω	right ascension
ω	argument of perigee
ω_a	natural frequency of out-of-plane libration
ω_ψ	natural frequency of in-plane libration
A	cross-sectional area of tether
a	semi-major axis
d_0	measure of initial perturbation between two trajectories in state space
D_i^j	partial differential operator
E	modulus of elasticity
e, \bar{e}	orbit eccentricity
F	τ/L
$F_{tension}$	resulting tensile force within the tether
F_x, F_y, F_z	Cartesian components of the force = τ/L
G	universal gravitational constant
H	angular momentum
i	inclination of the orbit
I_M	motor's mass moment of inertia
I_{out}	outrigger's mass moment of inertia
I_P	payload's mass moment of inertia
I_T	tether's mass moment of inertia
L	tether length
l	distance from motor hub to the infinitesimally small tether element
L_1	length from tether's centre of mass to end mass M_1
L_2	length from tether's centre of mass to end mass M_2
M_1	mass of upper end mass
M_2	mass of lower end mass
M_E	Earth's mass
M_M	mass of motor
M_P	mass of payload
N	number of discretised tether masses
p	semilatus rectum
P	power of motorised tether
Q_i	non-conservative forces acting on tether
R	orbital radius from Earth's centre to tether's centre of mass

r_0	orbital radius of payload at release from tether
R_1	distance from Earth's centre to the upper end mass
R_2	distance from Earth's centre to the lower end mass
$r_{\text{apogee}}, r_{AP}$	orbital radius at the orbit's apogee
r_C	circular orbit radius
r_{disc}	radius of reaction momentum wheel
r_E	orbital radius from Earth's centre to the released payload
R_M	distance from Earth's centre to the motor of a motorised tether
r_M	motor radius
R_{P1}	distance from Earth's centre to the upper payload of a motorised tether
R_{P2}	distance from Earth's centre to the lower payload of a motorised tether
r_{Payload}	payload radius
$r_{\text{perigee}}, r_P, r_{PE}$	orbital radius at the orbit's perigee
r_T	tether radius
r_{Ti}	inner tether radius of a hollow braided tether
r_{To}	outer tether radius of a hollow braided tether
r_π	orbital radius of released payload after completing half of the elliptical orbit
$S.F.$	factor of safety
T	tether's kinetic energy
t	time
T_0	fast time scale
T_1	medium time scale
T_2	slow time scale
U	tether's potential energy
U_{out}	outrigger's potential energy
V	velocity of released payload on an elliptical orbit
V_{COM}	tether tip velocity about tether's centre of mass
V_E	payload's orbital velocity
V_N	normal velocity component
V_R	radial velocity component
X, Y, Z	Cartesian coordinate system with origin at the Earth's centre and the X - Y plane coplanar with the orbital plane
x_0, y_0, z_0	Cartesian coordinate system placed at tether's centre of mass with the x_0 - y_0 plane coplanar with the orbital plane
x_1, y_1, z_1	Cartesian components of the upper end mass taken about the Earth's centre
x_2, y_2, z_2	Cartesian components of the lower end mass taken about the Earth's centre

X_E, Y_E, Z_E	Cartesian coordinate system with origin at the Earth's centre and X_E pointing towards the First Point in Aries
x_M, y_M, z_M	Cartesian components of the motor mass of a motorised tether taken about the Earth's centre
x_{P1}, y_{P1}, z_{P1}	Cartesian components of the upper end mass of a motorised tether taken about the Earth's centre
x_{P2}, y_{P2}, z_{P2}	Cartesian components of the lower end mass of a motorised tether taken about the Earth's centre
x_{T1}, y_{T1}, z_{T1}	Cartesian components of the upper tether's centre of mass of a motorised tether taken about the Earth's centre
x_{T2}, y_{T2}, z_{T2}	Cartesian components of the lower tether's centre of mass of a motorised tether taken about the Earth's centre
ΔR	difference in orbital radius between expected circular and actual orbit of a tethered dumbbell
Δr_π	radial separation between the payload half an orbit after release and the tether centre of mass' circular orbital radius at release
$\Delta r_\pi/L$	efficiency index
ΔV	velocity increment imparted by tether tip
δW	virtual work
$\delta x, \delta y, \delta z$	Cartesian components of virtual displacement

Abbreviations:

COM	centre of mass
ISS	International Space Station
SSTO	single stage to orbit

Chapter 1

An Introduction to Tethers in Space

1.0 Introduction

Telecommunication is now largely done through satellites in space and this trend is set to continue with the ever-growing use of wireless application products, global positioning handsets and mobile phones. Furthermore, a better understanding has not only been achieved of the Earth but also of the solar system and the universe with the use of satellites and probes. The importance and value of space technology to industry, science, culture and society is significant and yet the cost and risk involved with putting an object into and travelling through space is immense. Depending mainly on the type of launcher used the current launch costs per kilogram of payload range, according to Beardsley (1999), between \$15,000-\$20,000. Clearly, the cost of the launch alone is prohibiting the continued exploration of space and thus slowing the breakthroughs that could be made in science, the untapped resources that industry could exploit and tourism in space, which has always captured the public's imagination.

The current use of expendable multi-stage to orbit rockets generates a lot of debris in orbit and is posing a greater threat not only for satellites and the International Space Station (ISS) already in orbit but also for vehicles reaching space and then re-entering the Earth's atmosphere. In addition the construction and operation of expendable rockets is costly since new parts have to continuously be manufactured and proceed through rigorous testing to ensure their function is reliable. A possible solution to this problem is to employ reusable single-stage-to-orbit (SSTO) rockets such as the proposed Roton Rotary Rocket or fully reusable multi-stage-to-orbit rockets as proposed by the US company Scaled Composites. Although hopes were initially high that NASA would quickly develop a reusable SSTO rocket to replace the Space Shuttle, it is now evident that significant developments in technology are still required to achieve an SSTO rocket that can realistically replace the Shuttle. Furthermore, budget constraints and cuts suggest that many years will pass until SSTO rockets are a realistic replacement for expendable multi-stage rockets.

On Earth humanity has developed many forms of propulsion and employs these in their most economical and appropriate manner. For example, heavy cargo is transported over several thousand kilometres by airplanes or boats whereas bicycles or automobiles are employed to transport humans over tens to hundreds of kilometres. Moreover, different forms of

propulsion are combined to generate very effective transportation networks. A person travelling from their house to a meeting in another city might well use the combination of a bicycle, train, conveyor belt, airplane, car and an elevator to reach their destination. To reach a low Earth orbit in space, however, only one form of propulsion system is currently used: chemically fuelled rocket engines. Once in orbit, the same primary method of propulsion is employed and enhanced by gravity assists. The great challenge facing astronomical engineers is therefore to develop new propulsion methods that are safe, reliable and effective, as well as being financially viable. Only by having an array of propulsion systems will it be possible to optimally employ these methods to propel a given payload and evolve a space transportation network, similar in principle to that on Earth, that will ultimately drive costs down and make space more accessible.

Many concepts for advanced space propulsion exist and span a large range of ideas from antimatter propelled spacecraft to the recent successful implementation of ion propulsion as the primary propulsion system on NASA's Deep Space 1 mission, launched in 1998. Of the many proposed forms of advanced space propulsion, space tethers have the potential in the near term to reduce the operational costs of the ISS, decrease costs of launching payloads into orbit, deorbit space junk, transfer payloads from low to high orbits and vice versa, and ultimately offer the possibility of a low cost and reusable transportation system for cargo destined from Earth to space stations, asteroids, moons or planets.

1.1 Definition of a Space Tether

Space tethers are high strength, low-density cables that connect satellites, probes or space stations to each other in space. The cables are typically very long structures ranging from a few hundred metres to several kilometres and have a relatively small diameter, being only a few millimetres thick. Consequently, the material used to manufacture the tether has to endure high stresses and be lightweight to ensure the mass penalty at launch is kept to a minimum. A common material that has been employed in the past is DuPont's high strength polymer, Spectra 1000, which, according to Lorenzini and Carroll (1991), has an ultimate tensile strength of approximately 3 GPa and a density of 970 kg/m^3 . Note, that this polymer has a similar density to water but has an ultimate tensile strength approximately 3.5 times greater than a titanium alloy. Space tethers can be broadly categorised into two classes: conductive and non-conductive tethers. A tether that possesses a conductive core permits the tether to interact with the Earth's magnetic field and is termed an *electrodynamic* tether. Many potential applications exist for tethers that are completely non-conductive but when employed to generate propulsive effects, such a tether is termed a *momentum-exchange* tether.

1.2 Electrodynamic Tethers

The Earth possesses a magnetic field with its north and south magnetic poles currently aligned roughly along the Earth's geometric north and south poles. Whilst orbiting the Earth on a low inclination orbit with respect to the Earth's equator, the conductive core of the electrodynamic tether will move through the Earth's magnetic field. This is in principle how a dynamo is employed to generate electricity and, similarly, a current will be generated in the conductive core of the tether, which can be utilised to power the tether's end masses instead of using heavy on-board batteries. Since electrical energy is derived from the tether's kinetic energy, this method of power generation will cause a decrease in the tether's orbital altitude. Bekey (1983) estimates that the energy conversion occurs with an efficiency of approximately 70% and proposes continuous or periodic reboosts to make up the altitude loss, thus converting chemical energy into electrical energy at relatively high efficiencies. The power output from an electrodynamic tether is a function of tether length and Bekey (1983) suggests that 10-100 kW of power could be readily produced with a tether length ranging between 20-100 km. Cosmo and Lorenzini (1997) present calculations for a 200 kW system and indicate that electrodynamic tethers may possibly generate power in the megawatt range. Bekey (1983) goes on to claim that this method of power generation would be a simpler and cheaper way than achieving the same power output with solar arrays.

As the conducting tether moves through the Earth's magnetic field the electro-motive force generates a potential difference across the tether. The tether ends must make electrical contact with the plasma in the Earth's ionosphere to enable a current to flow from the potential difference, thereby generating a closed circuit or current loop. Cosmo and Lorenzini (1997) describe three concepts for plasma contactors: (a) a passive large area conductor at both tether ends, e.g. a metallic balloon, (b) a passive large area conductor at one end and an electron gun at the other, and (c) a plasma generating hollow cathode at both ends. Of the three configurations Cosmo and Lorenzini (1997) recommend the third option as being the most promising since it does not rely, as do the first two concepts, on a large conducting surface to passively collect electrons. Instead, the hollow cathodes generate an expanding cloud of conductive plasma, which has a sufficient thermal electron density to carry the full tether current in either direction at any distance from the tether end. Hollow cathodes, however, do require an on-board power and gas supply to operate but Cosmo and Lorenzini (1997) comment that a hollow cathode requires less power than an electron gun and that a gas supply would not represent a severe weight penalty. Beletsky and Levin (1993) remark that the predicted performance of hollow cathodes is somewhat optimistic and that a large development in technology is still required to ensure the plasma contactors only

cause a low voltage drop. Indeed the design of plasma contactors is a very active field of research with new concepts being developed, such as the field emitter array cathodes. A field emitter array cathode, as Morris *et al.* (2000) explain, consists of many hundreds or thousands of small micron level cathode/gate pairs printed on a semiconductor wafer that effect a cold field emission at relatively low voltages. Morris *et al.* (2000) express the hope that this inexpensive technology will provide the required high level of current emissions for an electrodynamic tether mission, whilst being simple to integrate and demanding little power.

Electrodynamic tethers are usually thought of as long conductive cables covered by an insulating sheath, which allows the exchange of electrical charge with the ionosphere to occur at either end of the tether. A recent development in the design of electrodynamic tethers is the concept of a bare tether, where a portion of the conducting cable is itself exposed to the ionosphere to permit electron collection. Estes *et al.* (2000b) argue that relatively simple bare electrodynamic tethers situated in low Earth orbit should attain currents in the 10 A range and be unaffected by plasma density variations encountered on orbit, which is a problem for large passive area collectors. This would permit bare tethers to operate both at night and day because of the system's inherent self-adjusting electron collection area. Rather than being fixed, the bare portion of the tether collecting the electrons can be varied, thus allowing a greater area to be exposed to the ionosphere if the electron density drops during the orbit revolution. Consequently, a bare electrodynamic tether should, according to Estes *et al.* (2000b), maintain a steady output.

The ability to reverse the current with hollow cathodes, say, permits the electrodynamic tether not only to be operated as a generator but also as a thruster. If an on-board solar power generated current is driven along the conductive cable then the tether will generate its own magnetic field and consequently interact with that of the Earth's. Depending on the direction of the current flow along the tether, the resulting electro-motive force will either point in the same direction as the tether's orbital velocity vector, thereby causing a positive thrust and increasing the tether's orbital radius, or it will oppose the orbital velocity and generate a negative thrust, leading to a reduction in the orbital radius. The significant achievement of this concept is the ability to alter the tether's orbital altitude without the ejection of chemical fuel, thereby saving valuable launch mass. Cosmo and Lorenzini (1997) point out that it is necessary to distinguish between electrodynamic tethers orbiting at sub-synchronous altitudes and those on orbits greater than the synchronous altitude, where the sense of relative velocity between the tether and the magnetic field's rotating reference frame is reversed. Hence, a power generating electrodynamic tether orbiting at an altitude greater

than the synchronous orbit will, according to Cosmo and Lorenzini (1997), generate a thrust on the tether instead of a drag.

Propulsive electrodynamic tethers offer the attractive possibility of deorbiting satellites, defunct or other spent bodies, after they have reached the end of their operational life in orbit. The US company, Tethers Unlimited, are developing several products that hope to commercially exploit electrodynamic tethers. The first is the Terminator Tether, which is a device attached prior to launch to a satellite. During the operational period of the satellite the Terminator Tether remains dormant but upon activation the tether is deployed, causing the satellite to deorbit. Tethers Unlimited's device is designed to be 2-3% of the host's mass and Forward *et al.* (2000) claim that depending on the initial orbit configuration the Terminator Tether can deorbit a typical communication satellite within several weeks or months. Forward *et al.* (2000) also present the concept of the Remora Remover, a device that after attaching itself to an enemy satellite deploys an electrodynamic tether to deorbit the hostile craft. Another company, Delta-Utec, based in the Netherlands, has explored the use of electrodynamic tethers to deorbit space debris. Heide and Kruijff (2000) conclude that tethers 5-10 km long and operating within the maximum plasma density can achieve deorbit rates between 2 and 50 km per day, thereby helping mitigate the in-orbit debris risk. Ahedo and Sanmartín (2002) analyse the performance, design criteria and system mass of bare electrodynamic tethers for deorbiting satellites and deduce from a trade off comparison with electric thrusters that bare tethers are by far the cheapest deorbiting option for low and mid inclination orbits. For electrodynamic tethers to be commercially exploited, however, Vas (2000) comments that additional investigation is required into the design of the conducting tether, method of tether deployment, tether lifetime, safety aspects regarding power demand, and safe tether release methodologies.

Since a few months are required to deorbit spent satellites with electrodynamic tethers, the risk of a several kilometre long tether striking another object in orbit is greatly increased. Chobotov and Mains (1999), Matney *et al.* (2000) and Patera (2002) developed analytical and numerical techniques to quantify the probability of the tether colliding with satellites and debris. Chobotov and Mains (1999) focussed their study on the Tethered Satellite System flown in 1996 (see Section 1.7.3) and concluded that the tether experienced several impacts by particles of 0.1 mm in diameter. However, the probability of collision with larger in-orbit bodies was estimated to be in the order of 10^{-3} per month. The numerical results of Patera (2002) reveal the collision probability of a tether is several hundred times greater than that of a space body with a 6m radius.

A study carried out by Vas *et al.* (2000) into the possibility of utilising a propulsive electrodynamic tether to reboost the International Space Station's decaying orbit due to atmospheric drag, estimates a 7 km long partially bare tether operating at a power level of 5 kW could provide savings over a ten year period of more than a \$1 billion. The savings arise due to the reduction in flights delivering propellant to the station for reboost and with greater use of the tether could possibly be increased. Furthermore, should the delivery of propellant be for any reason delayed then an on-board electrodynamic tether would provide a backup system for the space station. Vas *et al.* (2000) also suggest the tether may improve the microgravity environment on the International Space Station since during quiescent periods atmospheric drag could be neutralised, as well as optimising the positioning of laboratories with respect to acceleration contours.

Jupiter possesses a particularly strong magnetic field and with the high orbital velocities required to orbit Jupiter's great mass, very large relative velocities between the magnetic field and the spacecraft should be expected. The feasibility study carried out by Gallagher *et al.* (1998) found the use of electrodynamic tethers in the Jovian system presents entirely new engineering challenges but on the basis of Jupiter's plasma physics is theoretically possible. Their study estimates that induced tether voltages could reach as high as 50 kV, current levels may exceed 20 A, power levels can top 1 MW, and propulsive forces of 50N could be attained. Tethers one kilometre long could be employed for power generation or facilitating orbital manoeuvres but would have to be relative heavy to manage the large power levels. Moreover, the large predicted currents imply a special thermal control will be necessary to stop the spacecraft from overheating. Gallagher *et al.* (1998) conclude that utilising electrodynamic tethers about Jupiter is beyond the currently available technology and that further investigation is required to assess whether the tether dynamics will permit stability either naturally or by means of control.

Cosmo and Lorenzini (1997) explain that in addition to the in-plane component, the electromagnetic force on the tether current generally has an out-of-plane component, pointing perpendicular to the tether velocity. This effect allows electrodynamic tethers to achieve orbital plane changes since the out-of-plane force component acts to change the orbital inclination whilst, according to Cosmo and Lorenzini (1997), inducing no electromotive force to oppose the current flow in the conductive cable. Hoyt (2000b) reports Tethers Unlimited hope to exploit this through their μ PET propulsion system, in which orbital transfer and inclination changes for micro-satellites are achieved through electrodynamic tethers.

The electrodynamic forces acting on conductive tethers have been found in numerical simulations to exhibit complex dynamics. Beletsky and Levin (1993) demonstrated that the electrodynamic forces drive the in- and out-of-plane motions of a flexible tether on a circular, equatorial orbit, such that the tether's equilibrium positions become unstable and result in the tether spinning end over end. According to Ruiz *et al.* (2001), Lorenzini *et al.* (1999) and Peláez *et al.* (1999) extended Beletsky and Levin's model to take account of the tether moving on inclined orbits and found many more factors affecting the instabilities observed in their numerical investigations. In an attempt to understand the observed instabilities better, Peláez *et al.* (2000) adopted the approach of studying a simplified one-bar tether model, which would allow the basic mechanism causing the instability to be investigated. This simplified model was extended by Peláez *et al.* (2002) to take account of a two-bar tether on an inclined orbit. The simplified models discovered the electrodynamic forces in the long-term continually pump energy into the system, which over long periods of time leads the in-plane motion to shift from libration to rotation. Moreover, the simplified models suggested that the destabilising mechanism is independent of tether flexibility or rigidity, unlike the one identified by Beletsky and Levin (1993), which was dependent on the tether's longitudinal flexibility. By studying the lateral oscillations of an electrodynamic tether, Dobrowolny (2002) concluded that only the mechanism proposed by Peláez *et al.* (2002) could account for the inherently unstable motions of the lateral tether oscillations.

Peláez and Lara (2003) developed a numerical algorithm to search the parameter space for possible periodic solutions, which successfully uncovered a class of periodic solutions not found with analytical asymptotic techniques. Peláez and Lara (2003) conclude, though, that these periodic solutions are rather unstable and not practically suited for the operation of electrodynamic tethers. Consequently, a control methodology is required to ensure the long-term operation of propulsive electrodynamic tethers is feasible. Corsi and Iess (2000) investigated an on-off modulation of the tether current, which is phased with the sign of the mechanical power, to ensure the libration amplitude of the tether remains bounded. Corsi and Iess (2000) demonstrated that the attitude dynamics can be effectively controlled in this manner but the deorbiting times will consequently be reduced by a factor of 0.8-0.95. Peláez *et al.* (2001) attempt to control the attitude motion of the electrodynamic tether by adding damping in form of a dashpot to the system. From their preliminary findings, Peláez *et al.* (2001) conclude that nonlinear coupling between the in- and out-of-plane motion is weak and therefore lateral oscillations of the tether cannot be damped out with control laws based on a single state variable. A further conclusion drawn is that due to the weak nonlinear coupling the out-of-plane oscillations will be the more difficult to control.

1.3 Gravity Gradient Stabilisation

Consider the case of two masses connected by a tether, which is aligned along the gravity vector, and its common centre of mass (COM) prescribing, say, a circular orbit about the Earth. Without the tether, the mass closest to the planet would have a greater angular velocity to ensure the orbit is maintained, since the reaction to centripetal acceleration must balance with the greater gravitational pull. Similarly, the gravitational attraction is reduced for the mass on the larger orbit because it is further from the planet and so a smaller reaction to centripetal acceleration is necessary to preserve the orbit. However, the tether connection ensures both masses orbit the Earth with the same angular velocity and that a gravity gradient acts along the tether. Since the lower end mass is orbiting the Earth with the now lower than required angular velocity, the mass must experience a net force pointing towards the Earth. At the same time the mass furthest from the Earth is orbiting at a greater than required angular velocity and hence a net force experienced by the upper mass must be directed away from the Earth. Consequently, the end masses are not in force equilibrium and the tether must therefore go into tension, establishing a force equilibrium across the tethered system. Assuming the tether is on a circular orbit and no other forces perturb the tether, then the tether will remain aligned along the gravity vector, which is a stable equilibrium. The configuration is stabilised by the gravity gradient and is termed a hanging tether.

When a hanging tether is perturbed away from its equilibrium position, either within or out of the orbital plane, then due to the gravity gradient a torque is created about the tether's COM. There are no additional forces that can balance the system once the tether has moved away from its stable equilibrium position and consequently the tether proceeds to oscillate, or librate, about the COM. The librations would continue indefinitely without the presence of damping but a real tether system in orbit experiences material damping within the tether and some atmospheric drag that ultimately returns the tether to its stable equilibrium. Assuming the perturbation is small and the tether length is short in comparison to the orbital radius, then Arnold (1987) demonstrates by means of a simple but elegant analysis that the in- and out-of-plane librations are decoupled and oscillate at a frequency equal to $\sqrt{3}$ and 2 times the orbital angular rate, respectively.

Beletsky and Levin (1993) obtain two further equilibrium states for a rigid massless tether on a circular orbit. The first is when the tether is aligned tangentially to the orbit and within the orbital plane, and the second when the tether is tangential to the orbit and perpendicular to the orbital plane. Both of these configurations are found by Beletsky and Levin (1993) to be unstable, since small perturbations cause the tether to diverge from these two stationary points. The physical explanation for this is that the reaction to centripetal acceleration and

the gravitational attraction are no longer in line with each other and thus cannot maintain tether tension. In practice the two unstable configurations are best avoided since the tether may go slack and endanger the end masses and the mission. Adams (1970) finds a closed form solution by means of elliptic integrals of the first kind for the idealised massless and planar tether on a circular orbit in order to predict regimes when the tether may go slack. When Adams (1970) included damping he observed that the motion of the tether aligns itself along the gravity vector and that the tether slackness subsides.

1.4 Mechanics of Payload Orbital Transfer with Momentum Exchange Tethers

Tethered masses, orbiting a source of gravity in space, possess the same orbital angular velocity as its common centre of mass (COM). If the upper payload is released from a hanging tether, i.e. always aligned along the gravity vector, the upper payload carries more angular velocity than it requires to stay on that circular orbit, but since the upper payload does not have enough energy to escape the Earth's gravity, the upper payload goes into an elliptical orbit with the release point being the perigee of the orbit, as shown in Figure 1.1. Similarly, the lower payload does not have enough velocity to stay on its circular orbit when it is released and so the lower payload goes into an elliptical orbit, too, but this time with the release point being the apogee of the orbit. Half an orbit later the upper payload reaches its apogee and is hence further from the Earth than it was at the point of release. Upon reaching the perigee of the orbit, the lower payload is closer to the Earth than it was at release. Thus, the upper and lower masses released from a hanging tether are respectively raised and lowered. A prograde swing or spin will add velocity to the upper payload and decrease the velocity of the lower. A retrograde swing or spin will decrease the upper payload's velocity which means the payload at release will either have more, just the correct amount of, or not enough velocity to stay on its original orbit. The release point, therefore, will either be the perigee or the apogee of the elliptical orbit or it could stay on the original circular orbit. The reverse holds for the lower payload experiencing a retrograde spin or swing, which will have either not enough, just the right amount of, or too much velocity to stay on orbit. The release point will, consequently, be the apogee or perigee of an elliptical orbit or the released mass could stay on its circular orbit. For maximum apogee altitude gain and perigee altitude loss the most desirable tether motion has to be either a prograde swing or spin as more tangential velocity is added to the upper and subtracted from the lower payload. The optimum release point for a swinging or spinning tether is when the tether is aligned along its gravity vector and when the motion itself is coplanar with the orbital plane. The radial separation, Δr_* , between the payload half an orbit after release and the tether COM's circular orbital radius at release is greater than the tether's length, L , for orbit raising and less than L for orbit lowering.

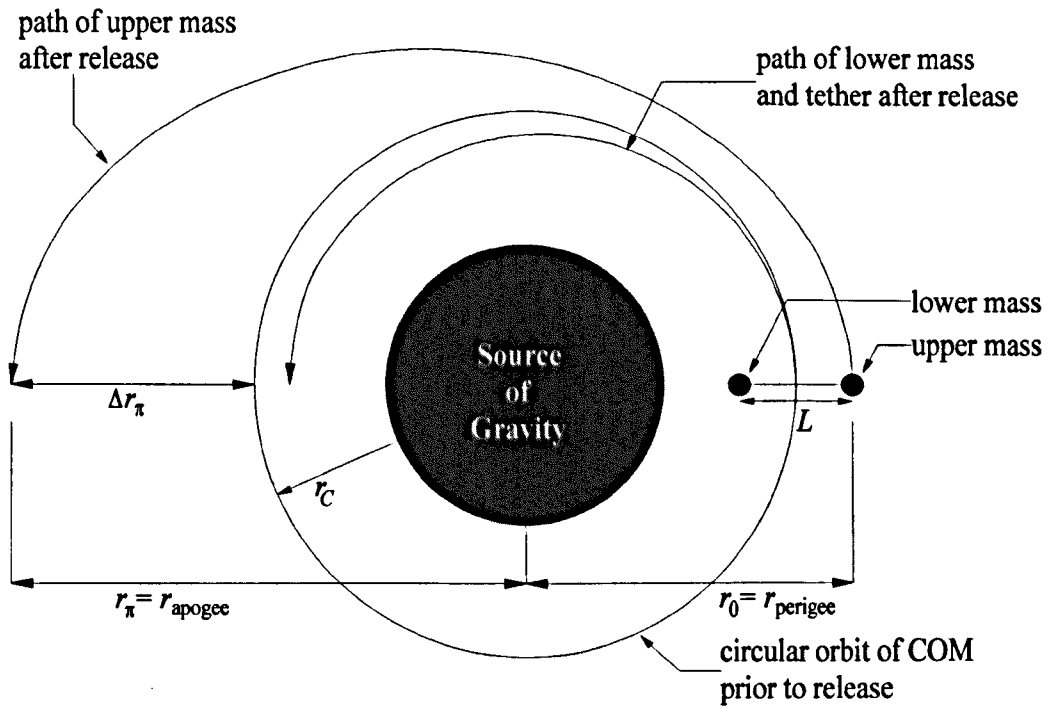


Figure 1.1 Orbital path of a payload released above the tether's COM on a circular orbit

Colombo *et al.* (1982) were one of the first to propose raising or lowering a payload's orbit with momentum exchange tethers. A hanging tether in a circular orbit was considered by Bekey and Penzo (1986) for transferring a payload from low Earth orbit (LEO) to geostationary Earth orbit (GEO). However, a potentially dangerous drop in the shuttle's perigee after release and resulting tether tension exceeding the strength of any known material were cited as problems against this proposal. Kelly (1984) suggested tethering the space shuttle to its external fuel tank at separation in order to raise the shuttle's orbit and to simultaneously deorbit the tank, concluding that the proposal was attractive but control stability and guidance dispersion issues of the external tank had to be addressed. Lorenzini *et al.* (2000) investigated propelling a payload from LEO to GEO using a two-stage tether system, where the transfer time was found to be comparable to that of a chemical upper stage. Their study claims that a two-stage tether system is more competitive on a mass basis than a chemical-propellant upper stage after two orbital transfers.

The results for Δr_π , treating the case of upper payload release, are given by Bekey and Penzo (1986), Carroll (1986), Arnold (1987), Cosmo and Lorenzini (1997), and Lorenzini *et al.* (2000), to be

$$\Delta r_\pi \approx 7L \quad \text{hanging tether} \quad (1.1)$$

$$\Delta r_\pi < 14L \quad \text{swinging tether} \quad (1.2)$$

$$\Delta r_{\pi} > 14L \quad \text{spinning tether} \quad (1.3)$$

Bekey (1983) claimed the spinning tether release generates $\Delta r_{\pi} > 25L$. Cosmo and Lorenzini (1997) give a formula to calculate Δr_{π} for a swinging release, provided the tether and its end mass remain on the original circular orbit

$$\Delta r_{\pi} \approx (7 + \sqrt{48} \sin \theta_{MAX})L \quad (1.4)$$

where θ_{MAX} , the maximum libration angle between the tether and the gravity vector, is positive for prograde and negative for retrograde rotation. Moreover, Cosmo and Lorenzini (1997) state that (1.1)-(1.4) only hold as long as $\Delta r_{\pi} \ll r_C$.

Kyroudis and Conway (1988) tried to improve the orbital transfer achieved with tethers by examining the use of a librating tethered dumbbell system on an elliptical orbit for satellite transfer to GEO. They reported that the ΔV savings and payload gain compared to a Hohmann transfer improve with higher eccentricity orbits, longer tether lengths and faster deployment speeds for similar initial periapse altitudes. Kumar *et al.* (1992) studied the effects of various tether deployment schemes as well as the out-of-plane libration on payload orbit raising of a tethered dumbbell on an elliptical orbit. For the swinging in-plane dumbbell on a circular orbit they derived the following expression

$$\Delta r_{\pi} \approx (7 + 4\psi'_v/\theta')L \quad (1.5)$$

where ψ'_v is the angular pitch velocity when the tether is aligned along gravity vector and θ' is the angular orbital velocity. Equation (1.5) holds for both swinging and spinning systems assuming $L \ll r_C$. Contrary to the analysis of Kyroudis and Conway (1988), who observed an increase in apogee altitude of the payload with deployment rate, Kumar *et al.* (1992) found from their 3D analysis that the apogee altitude gain versus deployment rate relationship is characterised by non-trivial peaks and valleys. Furthermore, Kumar *et al.* (1992) claim that non-zero initial roll angles have little effect on the orientation of the payload orbit after its release.

Equations (1.4) and (1.5) support the results in (1.1)-(1.3) that a payload released above a hanging tether rises approximately seven times the tether's length half an orbit later. This result is independent of the COM's orbital radius, despite the tangential orbital velocity being a function of the orbital radius. Equation (1.4), moreover, is independent of both the facility's orbital radius and payload mass, where both should affect the payload's momentum. Equation (1.5) takes the angular orbital and pitch velocities into account but is not directly dependent on the orbital radius. The results in the literature, therefore, do not appear to fully capture the physics of payload orbital transfer with tethers. With some papers in the literature discussing the use of longer tethers and mission designers needing to know

where to optimally place momentum exchange tethers in orbit, revisiting the validity of the above expressions would appear to be warranted. Moreover, if the performance of different momentum exchange tethers is to be compared, then accurate expressions instead of approximations are desirable.

Moravec (1977) considered a planar prograde rotating momentum exchange tether orbiting a planet on a circular orbit, where the orbit altitude and tether length are designed in such a way that the tether's tip touches the planet's surface if no atmosphere is present, e.g. the Moon, or the upper echelons of an atmosphere-bearing planet. The tether's rotation is selected to ensure the tip velocity cancels the orbital velocity during a contact, when both the velocity vector directions are parallel to each other. Having a relative zero velocity between the tether and the planet offers the opportunity in relative terms to easily transfer a payload from the planet to the tether, or vice versa. Moravec christened his idea a skyhook but the skyhook in orbit about the Moon has colloquially become known as the Lunavator. Rather than employing a tether of constant cross-sectional area, Moravec (1977) proposed a tapered tether, where the tether has the approximate shape of a narrow onion in order to have a greater cross-sectional area at the point of greatest stress. Following on from this, Moravec (1977) discusses various difficulties with the skyhook, such as modal vibrations of the long tether cables, varying orbital velocity and the change in altitude of the skyhook when releasing or catching payloads. An issue that Moravec (1977) does not discuss is the fact that a payload attached to the skyhook is not only translating but also rotating about the skyhook's centre of mass. Upon release, the payload's linear velocity relative to the planet's surface would be zero but the payload will continue to spin with an angular rate equal to that of the tether's angular velocity. This velocity would have to be cancelled if the payload's orientation is critical to the handover.

Hoyt and Forward (1997) exploit the skyhook concept of Moravec (1977) to propose a continuous payload exchange between the Earth and Moon that solely employs momentum exchange tethers. Two momentum exchange tethers orbiting the Earth ensure the lunar bound payload first transfers into a higher orbit and subsequently reaches the required escape velocity in order to transfer to the Moon. A Lunavator at the Moon catches the incoming payload and delivers it to the lunar surface. The outward journey causes all three tethers to alter their orbital altitude since the total momentum must be preserved, hence, Hoyt and Forward (1997) ingeniously propose to establish all of the tethers' orbital height by returning a payload from the Moon to Earth. Hereby, momentum exchange tethers are utilised to transfer payloads between two celestial bodies without the use of rocket engines or chemical fuel as the primary in-space propulsion technique. The Moon-Earth payload exchange

concept is developed further by Hoyt and Uphoff (2000), whereas Nordley and Forward (2001) model a continuous payload exchange with momentum exchange tethers between Earth and Mars. These studies represent initial feasibility studies but there is clearly scope for further work here, as the treatment of the orbital mechanics appears to be relatively simplified.

Crellin and Jansses (1996) investigate the velocity increments a planar momentum exchange tether could generate on an elliptical orbit. The maximum value they report for a 100 km long tether was 102.8 m/s after completing its first orbit, which is a magnitude not particularly useful for payload orbital transfer with tethers. Although Crellin and Janssens (1996) comment that the velocity increment generation requires further investigation, the low velocity suggests a drive may be required to intentionally spin the momentum exchange tether. The first to propose an intentionally torque driven tether were Puig-Suari *et al.* (1995b), who discuss the power requirements and design configurations of the tether sling. An electric motor located at the tether's centre is driven by solar panels and generates the necessary torque to spin the tether, thereby allowing both ends to carry a payload. To provide the necessary resistive torque for the motor to rotate the tether, the motor's stator will have to be unacceptably large and the spin rates will probably be very high. Consequently, Puig-Suari *et al.* (1995b) propose adding an additional counter rotating tether to the momentum exchange tether to supply the required torque resistance. Cartmell (1998) also proposes a design for a motorised momentum exchange tether but instead of locating the motor at the tether's centre, as done by Puig-Suari *et al.* (1995b), the motor is situated at one of the tether's ends with another pair of tethers providing the necessary resistance. The advantage of the symmetrical concept from Puig-Suari *et al.* (1995b) is that the tether's orbit should remain largely unperturbed if a simultaneous release of the payloads can be ensured, whereas the design of Cartmell (1998) will lose orbital altitude upon payload release. Moreover, the symmetrical motorised tether concept lends itself beautifully to a continuous interplanetary payload exchange with tethers as the facility naturally accommodates an in and out coming mass. Cartmell and Ziegler (1999), who independently of Puig-Suari *et al.* (1995b) invented the symmetrical motorised tether concept, carry out a preliminary analysis of a continuous payload exchange between the Earth and Moon with motorised tethers. However, the numerical results obtained by Cartmell (1998) demonstrate that the three dimensional dynamics of the motorised tether can affect the system's performance and definitely warrants further analysis to assess the viability of motorised momentum exchange tethers.

1.5 Further Suggested Applications of Tethers

A plethora of concepts exist for the use and exploitations of space tethers, which Cosmo and Lorenzini (1997) present in a fairly comprehensive overview. Tethers have been proposed to aid in the detection of gravity waves, measurement of the Earth's atmospheric properties, construction of tethered platforms, interplanetary travel of spacecraft by utilising the interaction between electrodynamic tethers and the solar wind, generation of low frequency waves by an orbiting electrodynamic tether for worldwide communications, return of samples from comets and asteroids, collection of micrometeoroids from the upper atmosphere, generation of variable or low gravity in-orbit laboratories, docking of the Space Shuttle with the International Space Station, and passive attitude stabilisation of spacecraft. Tethers have also been proposed to aid in the provision of artificial gravity for long space missions involving humans. A tether connecting the astronauts' living and working quarters with another mass, say, could be spun around the system's common centre of mass to provide a 1 g environment for an appropriate rate of rotation and tether length.

Clarke (1981) reinvigorated the ideas of Tsiolkovsky (1961) of constructing a tower at the Earth's equator to a point just beyond geostationary Earth orbit, which promises to revolutionise travel into space. Clarke (1981) also considered the possibility of tethering the Martian moon Deimos to Mars, and Lemke (1985) studied the possibility of constructing a space elevator from the Moon's surface. Pearson (1975) was one of the first to investigate the design issues of building a tethered space elevator, proposing various ideas on the tower's construction and use. Recently, Edwards (2000) conducted an excellent conceptual design study of a space elevator, which demonstrated that the concept's viability is not only limited by required advances in material science but also by relatively trivial matters, in technology terms, such as geographic location and political unrest.

Cosmo and Lorenzini (1997) describe a method, termed orbital pumping, which involves the reeling in and out of a tether in phase with the natural libration of the tether. In this manner electrical energy is employed, assuming proper timing is established, to affect the spacecraft's orbit eccentricity. Gratus and Tucker (2003) derive a control methodology for orbital pumping and find a suitably varied tether of 50 km can achieve an increase in the spacecraft's orbital altitude of 300 m an hour.

In an attempt to eliminate the need for a retro-propulsive manoeuvre to circularise a spacecraft's orbit, tethers have been considered for aerobraking at an atmosphere-bearing planet. A spacecraft deploying a tether could dip a body into the planet's atmosphere, thus slowing the craft. Puig-Suari *et al.* (1995a) develop a model of the flexible tether interacting

with the atmosphere and suggest the aerobraking tether can achieve aerocapture at any atmosphere-bearing planet in the solar system for less mass than a corresponding propellant of a typical retro firing rocket system. Biswell and Puig-Suari (2001) find the use of a lifting probe improves the performance of the aerobraking tether and propose several methods for cutting the tether to ensure the spacecraft is not deorbited once the desired orbit is reached.

A formation of spacecraft could be utilised to form interferometers in space but the formation flying of spacecraft could be costly if each craft has its own propulsion system and fuel source. Furthermore, the control and stability of formation free flying spacecraft possess its own technological challenges. Tethers have been proposed as a lower cost means of maintaining the formation. DeCou (1989) investigates the use of a spinning, multi-tether Michelson interferometer, Moccia *et al.* (1996) describe the possibility of employing a tethered synthetic aperture radar for natural disaster monitoring, and Maccone (1999) proposes a design of a tethered radio telescope to observe the black hole at the galactic centre.

1.6 Historical Background

K. E. Tsiolkovsky is credited by Clarke (1981), Bekey (1983), and Beletsky and Levin (1993) to be the first person in 1895 to propose tethering large masses in space by a long thin cable to the Earth's surface to allow gravity gradient forces to be exploited. Beletsky and Levin (1993) claim Tsiolkovsky also devised at the time a 500 m long rotating tethered structure to create artificial gravity in space. In 1910, according to Beletsky and Levin (1993), F. Tsander calculated the necessary cable taper to connect the Earth to the Moon with a steel cable. Beletsky and Levin (1993) state that Artsutanov, Isaaks, and Pearson respectively reinvented the idea for a space elevator or Earth-Moon tether in the 1960s. However, the modern era of space tethers began, as Cosmo and Lorenzini (1997) explain, in the early 1970s by Mario Grossi of the Smithsonian Astrophysical Observatory and Giuseppe Colombo of Padua University proposing the concept of the tethered satellite system to NASA and the Italian Space Agency. Between 1979 and 1984 various committees and bodies considered the concept and finally announced in April 1984 their approval for flight-testing of the tethered satellite system aboard the Space Shuttle.

1.7 Past Tether Missions

1.7.1 Gemini Missions

The very first time a tether was employed in space was, according to Bekey (1983) and Beletsky and Levin (1993), on the Gemini 11 flight launched on 12 September 1966. A 15 m

long tether deployed a counter balance mass from the Gemini spacecraft and after 20 minutes the motion of the tether settled sufficiently to allow the tethered system to be spun. The aim of the experiment was to explore the feasibility of generating artificial gravity with tethers. Although the mission successfully generated artificial gravity, Lang and Nolting (1967) report that the measured acceleration was only one thousandth of that on Earth. The experiment lasted for three hours and the tether plus its end mass were ejected from the Gemini module. Gemini 12 was launched on 11 November 1966 and carried out the same experiment as on Gemini 11 but with a 30 m long tether. Rotation of the tethered system generated again a miniscule amount of artificial gravity. The tether was observed to remain a little slack yet very stable throughout the test.

1.7.2 Tethered Satellite System 1 (TSS-1)

TSS-1 was launched 31 July 1992 on the Space Shuttle, STS-46, and deployed a conductive tether with an insulating sheath to a length of 268 m directly above the Orbiter where it remained for most of the mission. A positively biased subsatellite, shaped as a metallic sphere of 1.6 m diameter and a mass of 500 kg, served as the electron collector. Twenty hours of stable deployment were recorded in the vicinity of the Orbiter at an orbital altitude of 300 km, which Cosmo and Lorenzini (1997) explain was one of the greatest concerns during mission planning. According to Cosmo and Lorenzini (1997) the TSS-1 mission conclusively proved the feasibility of gravity gradient stabilised tethers, overcame issues on tether deployment, and reduced concerns about safety, thus paving the way clear for the TSS-1R mission to focus on scientific objectives.

1.7.3 Tethered Satellite System 1 Reflight (TSS-1R)

The TSS-1R mission was launched aboard the Space Shuttle, STS-75, on 22 February 1996 with the aim of generating power for 20 hours through a 20.7 km long electrodynamic tether. This was to be followed by a second test at a length of 2.5 km to carry out additional science experiments for 7-9 hours. However, the total length of 20.7 km was not achieved on the 300 km high circular orbit and instead the tether deployed to 19.7 km before it was severed. The true cause of the tether severing has to this day not been found but according to Estes *et al.* (2000b) the commonly accepted explanation is air contained within the tether fibres escaped from a worn part of the tether and sufficiently ionised to act as a plasma contactor, which ultimately formed a spark severing the cable. Nonetheless, TSS-1R represents the longest electrodynamic tether to be deployed in orbit. Cosmo and Lorenzini (1997) highlight several other successes of the mission. Five hours had passed from the moment the tether had begun deploying to the point when the tether was lost and during this period a quality data set was gathered, such as the measurement of the electro-motive force, satellite and Orbiter potential,

tether current, charged particle distributions, and electric and magnetic field strengths. From the collected data the following three conclusions are listed by Cosmo and Lorenzini (1997):

- The tether collected current of 0.3 A exceeded the numerically predicted level by a factor of three. Estes *et al.* (2000b) report a current of 1 A was collected immediately before and after the tether failure.
- Electrons, not of natural ionospheric origin and whose energy ranged as high as 10keV, were probably energised by wave-particle interactions since they were observed to flow coincident with the tether current.
- The plasma density was enhanced by the ionisation of the neutral gas emitted by the tether's end mass thrusters.

Cosmo and Lorenzini (1997) feel that these results have improved the understanding of current collection with electrodynamic tethers and will aid in the future development and design of tether missions.

1.7.4 Small Expendable Deployer System (SEDS)

NASA Marshall Spaceflight Center awarded Joe Carroll a Small Business Innovative Research contract to provide hardware that could deploy a 20 km long tether in space. The design of SEDS is in comparison to the TSS missions, as Lorenzini and Carroll (1991) explain, drastically simplified because the tether is not retrieved at the end of its mission, therefore, avoiding complex control systems for retrieval. The developed technology was tested twice as a secondary payload on Delta II launches of global positioning satellites. The SEDS-1 mission was launched on 29 March 1993 and demonstrated the capability of deorbiting through aerodynamic drag a 25 kg payload from a perigee altitude of 190 km and allowed the re-entry of a cut tether into the atmosphere to be studied. SEDS-1 successfully re-entered the Earth and landed off the coast of Mexico. The SEDS-2 mission flew on 9 March 1994 and verified the use of a closed loop control law to deploy a tethered payload along the gravity vector. The mission's aim was to achieve a final libration angle of 10° along the local vertical. Cosmo and Lorenzini (1997) report the deployment law exceeded expectations as the final libration angle was estimated to be within 4°. SEDS-2 was placed in a 350 km high circular orbit but after five days the tether was, according to Cosmo and Lorenzini (1997), severed by micrometeoroids or space debris.

1.7.5 Plasma Motor Generator (PMG)

The PMG was launched on 26 June 1993 and used hollow cathodes for charge exchange at both ends of the tether, allowing it to operate both in a generator and motor mode. According to Estes *et al.* (2000a), the PMG mission has so far been the only tether experiment to use an active node, which measured a current of 0.3 A and an anodic bias of 100 V. Cosmo and

Lorenzini (1997) explain that a 500 m long tether was employed to ensure a complete separation between the tether ends, thereby forcing current closure to occur through the ionosphere rather than with a local overlap between each end masses' plasma cloud. Contact with the plasma was maintained for seven hours until the onboard batteries expired. Estes *et al.* (2000a) comment that a disappointing fact observed with the PMG mission was the sharp decrease of collected current with the ambient electron density.

1.7.6 Tether Physics and Survivability Spacecraft (TiPS)

The two mission objectives for TiPS were to investigate the long-term orbit and attitude dynamics of a non-conducting tether, and the survivability of a tether. TiPS was designed and built within a year by the US Naval Research Laboratory and launched on 20 June 1996. Tether deployment from two free flying satellites began immediately after being jettisoned from its host spacecraft and deployed to a length of 4 km. Cosmo and Lorenzini (1997) report that ground based visual observations through a laser ranging network permitted the attitude and orbital motion of the tethered system to be tracked, which observed the libration amplitude decrease from a maximum 47° to 12° with respect to the local vertical over a period of 3 months. According to the US Naval Research Laboratory's website the TiPS tether survived for at least 15 months, which is a tremendous achievement considering all previous tether missions did not survived for longer than five days.

1.7.7 OEDIPUS A

OEDIPUS is short for Observations of Electric-field Distribution in the Ionospheric Plasma – a Unique Strategy. The OEDIPUS program was jointly run between the National Research Council of Canada, Communication Research Center in Ottawa, NASA, various Canadian universities, the US Air Force Phillips Laboratory, and Bristol Aerospace Ltd. The OEDIPUS A was a large double probe and designed to make sensitive measurements of the weak electric fields in the aurora's plasma. On 30 January 1989 a three stage sounding rocket, Black Brant X, launched OEDIPUS A, consisting of two tethered spinning payloads with a mass of 84 kg and 131 kg, respectively, from Andøya in Norway. The mission objectives were, according to Cosmo and Lorenzini (1997), to make passive observations of the auroral ionosphere, measure the large probe's response in the ionospheric plasma, and to observe the plane- and sheath-wave radio frequency propagation in plasma. The conducting tether was deployed during the suborbital flight of 11 minutes to a length of 958 m. The mission objectives were successfully met but Cosmo and Lorenzini (1997) report that a post-flight analysis found the motion of the tether had rather unexpectedly interacted with the dynamics of the end masses causing a rapid increase in the coning angle, despite the short

flight time and the tether's mass being negligible in comparison to the end bodies' mass. The tethered masses re-entered the atmosphere after 13.5 minutes and were not recovered.

1.7.8 OEDIPUS C

The second flight of the OEDIPUS program was launched on 6 November 1995 from the Poker Flat Research Range, near Fairbanks, Alaska. Cosmo and Lorenzini (1997) say the mission objectives for OEDIPUS C were identical as those for OEDIPUS A apart from launching the tethered bodies into a higher orbit where the plasma density was expected to be greater. Furthermore, the conductive tether was deployed to a greater length of 1174 m and for the second half of the suborbital flight the tether was cut at both ends to enable the radio frequency wave propagation between the payloads to be studied. During the suborbital flight data was returned for 15 minutes until the payloads re-entered and landed in the Arctic Ocean.

1.7.9 Advanced Tether Experiment (ATEX)

On 3 October 1998 the Space Technology Experiment (STEX) spacecraft was launched from the Vandenberg Air Force Base reaching a 751 km circular orbit at 85 degrees inclination. The orbit transfer and spacecraft checkout were completed by January 1999 and from this point the Advanced Tether Experiment (ATEX) was to start with a planned duration of 61 days. STEX contained ATEX, which was built by the US Naval Research Laboratory as a subsidiary experiment to the active spacecraft. The aims of the ATEX mission, as stated by Zedd (1997), were to demonstrate tether system stability and control, demonstrate end-body attitude determination and control, and fly a tether designed for survivability.

The ATEX system consisted of a passive, unpowered upper end body and a lower end body, attached to the top of the STEX spacecraft, which housed the 6.05 km long tether, electronics and deployer mechanism. During the tether deployment and libration control experiments, the lower end body was to remain fixed to the STEX craft and subsequently separate for the tether survivability phase of the mission. Attempting to increase the tether's chances of survivability in Space, a thin, flat, tape tether was adopted with a thickness and width of 0.127 mm and 25 mm, respectively. The tether was manufactured from a 6.5 km continuous extrusion of low-density polyethylene with three reinforcing wires made from Spectra running lengthways down the tether.

The tether deployment commenced by raising the upper end body 2.5 cm off its contact points and in so doing avoided any possibility of recontact and ejection perturbations. To allow any excited oscillations to dampen down, the raised state of the upper end mass was

held for 10 min, after which the stepper motor was instructed to produce a steady 2 cm/s deployment rate. This rate was to be maintained for the entire deployment, expected to last approximately 3.5 days. However, roughly 18 min after starting the stepper motor and only 22 m of tether deployed, the tether departure angle sensor detected the tether in an anomalous location and shortly afterwards the tether passed an out-of-bounds limit causing an unacceptable risk to the STEX spacecraft. The lower end body was subsequently jettisoned from the STEX craft, thereby, ending the ATE_x mission.

Excessive tether slackness most probably caused the mission to be aborted, and Gates *et al.* (2001) propose four possible failure mechanisms. Despite the polyethylene material being capable of amassing electrostatic charge, ground experiments did not show any static charge build-up during testing. However, the charged particles in the Space environment may have led to a charged tether possibly sticking to the deployer mechanism and thus manifesting itself as an apparent slack tether condition.

A second failure mechanism could have been excessive tipoff rates, required to be less than 0.2 deg/s, during the initial separation of the upper end body from the STEX craft. This requirement was stipulated to avoid contact between the upper end mass and the tether as the occurrence of such could disrupt the deployment and possibly lead to excessive tether slackness. Furthermore, the pitching motion of the spacecraft in response to the initial reel acceleration could also have contributed to increased tipoff rates.

Shape memory and strain relief properties of the tether are the third possible failure mechanism. On exiting the pinch rollers of the deployer during ground tests in air and thermal vacuum, the tether was found to assume a sinusoidal shape with a wavelength of 38 mm and an amplitude of 3 mm. Analysis carried out by Gates *et al.* (2001) found that the net effect of this shape memory effect was to reduce the deployment stream to less than 2 cm/s and, thereby, possibly generate tether slack. Additional shape memory curvature may have occurred from the tether being stored on its reel for nearly 24 months. The tether strain relaxation during deployment may also have caused a drop in the effective deployment rate. The tether on the reel experiences a tension of 4.5 N and as the tether transitions off the reel the tension drops to 1.8 N. After exiting the deployer's pinch rollers in the early part of deployment the tension drops to nearly zero. If a complete relaxation of the tether occurred outboard rather than over the contact point within the pinch rollers then the tether would experience an effective contraction in length.

The telemetry was not designed to record early deployment dynamics nor anomaly resolution and thus the returned data was rather coarse and limited. Consequently, a definitive cause for the excessive tether slackness cannot be determined but Gates *et al.* (2001) believe that the thermal expansion of the tether was most likely the principal cause of the tether passing the out-of-bounds limit. The tether exited the deployer at a temperature of 10 °C and because deployment began in full eclipse the tether would rapidly cool to -100 °C upon entering the cold of space. The drop in temperature would cause the tether to contract, thus slowing the deployment rate of the upper end body below the required 2 cm/s. Despite the tether contraction the telemetry did not register any anomalies that occurred during the deployment conducted in eclipse. 17.5 min after commencing deployment the ATE_x entered sunlight inducing a rapid heating from -100 °C to -30 °C. The 70 °C temperature increase is estimated to have expanded the 22 m tether by 15.5 cm. The first anomaly was registered 36 seconds after leaving the eclipse and 10 seconds later the onboard instrumentation registered the tether having a 10 cm horizontal displacement and therefore jettisoning ATE_x, as the out-of-bounds limit had been passed. The thermal expansion rate of the tether was not considered in the tether deployment simulations carried out during the design phase of the deployer and the importance of thermal expansion was only realised in the post-jettison failure analysis.

1.8 Tether Missions Planned for the Near Term

1.8.1 Propulsive Small Expendable Deployer System (ProSEDS)

The ProSEDS experiment, according to Ahedo and Sanmartín (2000), will be a secondary payload on a Delta II rocket and aims to demonstrate the on-orbit propulsive capability of electrodynamic tethers by deorbiting the rocket's second stage in two to three weeks from a 400 km high circular orbit by means of a 0.4 N electrodynamic drag, which is generated by a 1-2 A current. The mission objective is to demonstrate that the tether can decrease the orbit by at least 5 km per day, although Balance and Johnson (2001) report that the ProSEDS tether should in theory be capable of decreasing the orbit on average by 14 km per day. Vaughn *et al.* (2000) state the total tether length is 15 km of which 5 km is a bare aluminium cable. The flight was initially scheduled for the end of 2000 and then for 2001 but as yet has still not been flown.

1.8.2 STEP-Airseds

Gilchrist *et al.* (2000) state that designs are being carried out for a tether mission to follow ProSEDS, called STEP-Airseds, which aims to demonstrate multiple boost/deboost and inclination change operations over a period of a year, covering an orbital altitude range between 400-700 km.

1.8.3 Advanced Safety Tether Operation and Reliability (ASTOR) Satellite

Originally scheduled for 2003, the 65 kg ASTOR satellite is to be ejected from the Space Shuttle and subsequently separate into two equal masses connected by a 2 km long tether. The project, according to Mazzoleni (2000), is managed by the Texas Space Grant Consortium, NASA Marshall Space Flight Center and the Michigan Technic Corporation. The University of Texas at Dallas, Texas Christian University and the Smithsonian Astrophysical Observatory are also involved in the project. The four mission objectives are to: (a) investigate the performance of the Emergency Tether Deployment system which is designed to overcome tether snags during deployment, (b) demonstrate the feasibility of generating artificial gravity by spinning a tethered system about its centre of mass, (c) transfer one end mass via momentum transfer to a higher orbit, and (d) provide a platform for school children to design and fly space-based experiments.

Once on orbit gas jets will initiate the satellite to separate and commence deployment of the tether. After the initial 500 m of tether are freely deployed, a passive brake will deploy the remaining 1500 m of tether. As the tether reaches its fully deployed length, thin wires intentionally connecting the tether to the spacecraft will be broken by the tether's own momentum, thereby causing a jerk in the tether and simulating a snag condition. The main concern about a snag occurring is the possible rebound and contact of the tether and end mass with the deployer. Hoffman *et al.* (2001) propose to deploy from the other end mass, the so-called Emergency Tether Deployer, 10 m of solder embedded tether to mitigate the snapback possibility.

The ASTOR spacecraft will accommodate 4-6 science and student supplied experiments, studying primarily the properties of the Earth's atmosphere and Space environment. Upon completion of the snag simulation, tether deployment and onboard experiments, a motorised take-up reel will reel-in up to one half of the tether. As the tether is retrieved, Mazzoleni and Hoffman (2001) claim that a rapid increase in the rotational motion will occur due to conservation of angular momentum and thus cause the system to spin about its centre of mass. This spin-up manoeuvre is to demonstrate a method of developing artificial gravity in a spacecraft that could be employed by humans travelling to other planets in the solar system. The mission will conclude by releasing one of the end masses from the tether, thereby, causing the released end mass' orbit to be raised due to the exchange of momentum between the two end bodies. Both end masses and the tether will eventually burn up in the atmosphere upon re-entry. The initial deployment demonstration will take approximately 60 minutes and the total mission duration is expected to last up to 30 days.

1.8.4 Tether System Experiment (TSE)

The TSE mission is being sponsored by the European Space Agency with the ultimate aim of providing a frequent Earth sample return capability from the International Space Station. After supplying the ISS with cargo, the Russian Progress vehicle will separate from the station and subsequently eject a subsatellite connected to a 35 km long tether. The mission's aims are, according to Gavira-Izquierdo (2000), to demonstrate the operation of a tether deployment mechanism suitable for sample return from the ISS, to demonstrate the necessary technology associated with a re-entry capsule from the ISS, and finally to collect experimental data on the tether oscillations, librations and deployment dynamics. Gavira-Izquierdo (2000) state that the target launch date was 2002 but to date this has not yet taken place.

1.9 Tether Survivability and Design

Tethers that have been deployed in space have been single strand high strength synthetic fibres, such as DuPont's Spectra 1000, Spectra 2000 or Kevlar. Apart from the TiPS mission, all previous tethers have not survived the harsh space environment for longer than five days. McBride and Taylor (1997) present numerical models based on particle flux models and impact damage equations to predict the survivability of tether designs. In addition, McBride and Taylor (1997) carried out hypervelocity impact experiments on tether strands in the region of 5 km/s to verify the applicability of their model. The conclusions of McBride and Taylor (1997) are that tethers with a diameter less than 1 mm are not viable for long duration missions. The model predicts the SEDS-2 tether would fail in less than two weeks and that thicker tethers have a greater life expectancy. For the 4 km long, 2 mm thick TiPS tether McBride and Taylor (1997) predict the tether will have a lifetime of a year and based on the past missions in space, their predictions are found to be correct. The poor capability of single strand tethers to survive micrometeoroid impacts is confirmed by numerical modelling carried out by Anselmo and Pardini (2000). Moreover, Matney *et al.* (2000) point out that further experimental and numerical work is required to investigate the tether's survivability not only of a direct but also of a grazing micrometeoroid impact. Forward and Hoyt (1995) developed the concept of the Hoytether, a tether where the fibres are woven in such a manner to generate a multitude of diamond shapes within the cable, thereby creating a highly redundant structure. The hope is that the redundant fibres will take the strain as soon as other load bearing fibres are severed by debris. Forward and Hoyt (1995) present results that claim their design will ensure the tether survives for tens of years, although these claims still remain unsubstantiated. The future of tether design and materials looks likely to benefit from recent advancements in chemistry. Edwards (2000) reports that in future tethers may be

manufactured out of carbon nanotubes, which have a reported tensile strength of 130 GPa, or synthetically produced spider's silk.

1.10 Nonlinear Dynamics of a Tethered Dumbbell

A system comprising two satellites, treated as point masses, connected by a massless rigid tether is usually referred to as a tethered dumbbell. The model of a tethered dumbbell is very much an idealised version of a real tether in orbit and yet the study of a dumbbell's attitude motion yields very complex and interesting behaviour. When the dumbbell is constrained to orbit within the orbital plane on a circular orbit, the governing equation of motion is very similar to that of a simple pendulum. Moran (1961), Modi and Breerton (1969), and Adams (1970) derive an exact closed form solution for the planar dumbbell on a circular orbit in terms of elliptic integrals of the first kind, which describe the tether's libration about its gravity vector and also its tumbling motion. Consequently, the dumbbell's phase plane is identical to that of a simple pendulum apart from the location of its stable and unstable equilibria, which are shifted by π along the axis depicting angular displacement. Karasopoulos and Richardson (1992) give a succinct and effective summary of the dumbbell's planar dynamics, as well as derive the conditions that determine when the tether will tumble or librate on a circular orbit. Moran (1961) investigates whether the coupling between the tether's librations and the orbital motion is strong and reports that in most cases the disturbances in the orbital motion caused by the tether libration are small. However, in his analysis Moran (1961) discovered certain libration frequencies causing resonance with the orbital motion but advises the reader not to jump to the conclusion that the dumbbell will violently oscillate about the unperturbed orbit until atmospheric drag deorbits the tether. Instead, Moran (1961) speculates that for these identified frequencies the linearised analysis is no longer valid and that the inclusion of nonlinearities would ensure the tether's orbital motion remains bounded.

For a tethered dumbbell restricted to move on a circular orbit but free to oscillate out of the orbital plane, Melvin (1988) discovered a set of initial conditions giving rise to a periodic solution describing the dumbbell oscillating on a figure of eight path through three dimensions. Moreover, Melvin (1988) also discovered another set of initial conditions that yielded very irregular librations, which he claims are chaotic. However, since no Lyapunov exponents are presented this claim remained unsubstantiated. A system that undergoes chaotic motion is in the long-term highly sensitive to perturbations and Lyapunov exponents are a numerical tool from dynamical systems theory that can unequivocally identify chaos. Misra *et al.* (2001) revisited the three dimensional dumbbell on a circular orbit, although the material presented in their paper was originally published by Nixon and Misra (1993).

Through numerical integration Misra *et al.* (2001) obtain time histories, phase plane plots, power spectra, Poincaré maps and Lyapunov exponents for an initial angular displacement equal in the in- and out-of-plane angles, as well as the initial tether angular velocities set to zero, which clearly indicate that the dumbbell exhibits regular, quasi-periodic and chaotic motion. The value for the necessary initial conditions in both the angular displacements to facilitate the change from regular to chaotic motion was found to be 43° . Due to the limited choice of initial conditions investigated by Misra *et al.* (2001), there remains scope for further investigation into the nonlinear dynamics of a dumbbell on a circular orbit.

The dynamics of a dumbbell are rather different when the tether is allowed to prescribe an elliptic orbit. Modi and Brereton (1966) were one of the first to derive an approximate closed form solution to the equation of motion governing a planar tethered dumbbell on an elliptical orbit by employing the Wentzel-Kramers-Brillouin-Jeffreys (WKBJ) perturbation method, which was a considerable improvement on the first-order perturbation technique attempted by Schechter (1964) involving numerical integration to obtain a simulation. Approximate closed-form solutions were also derived by Modi and Brereton (1969) using the method of harmonic balance and by Anand *et al.* (1971), who employed a somewhat unconventional asymptotic perturbation technique. The closed form solution derived by Modi and Brereton (1966) visibly points out a fundamental difference between dumbbells moving on circular and elliptical orbits. A tether on an elliptical orbit continuously executes libration and, unlike the hanging tether on a circular orbit, does not remain aligned along the gravity vector. The physical reason for this lies in the tether's varying orbital radius whilst on the elliptical orbit. As the tether moves from the orbit's perigee to its apogee, say, then the influence of gravity on the tether's end masses decreases. Similarly, the end masses experience a greater gravitational pull as they approach the orbit's perigee. Hence, the varying gravitational attraction manifests itself as a sinusoidal forcing term in the planar dumbbell's attitude motion, resulting in the tether to constantly oscillate.

The analytical approaches yielding closed form solutions only permit the dumbbell to be considered on nearly circular orbits. Consequently, Brereton and Modi (1966) resort to numerical integration to investigate the boundary between libration and tumbling motion for a range of initial conditions. The results are quite remarkable as the boundary between libration and spin is quite complex and found to be highly dependent on the orbit eccentricity and initial values for angular displacement and velocity. When the initial angular velocity and displacement is zero an orbit eccentricity of 0.355 is observed by Brereton and Modi (1966) to be the largest eccentricity that can sustain librational motion. The identical analysis is carried out by Modi and Brereton (1968) for a tether with an additional degree of freedom

in the longitudinal direction and the libration-tumbling boundary is deemed to be qualitatively very similar. Modi and Brereton (1968) conclude though that the introduction of the flexibility in the longitudinal direction encourages the onset of tumbling to occur sooner than for the case of the completely rigid dumbbell.

Beletsky and Levin (1993) expand the equations of motion governing the planar dumbbell on an elliptical orbit in terms of a series and after numerically evaluating the series determine that periodic solutions exist when the eccentricity is less than 0.442. Moreover, their numerical results suggest the tether does not tumble when the orbit eccentricity is less than 0.353 or between 0.427 and 0.442.

Crellin and Janssens (1996) proceed to investigate the boundary between libration and spin more thoroughly for an initial zero value in angular velocity and displacement. When the orbit eccentricity is less than 0.317, Crellin and Janssens (1996) observe the tether to be stable in the long-term, where stability here is equated to a state where the tether is not tumbling. Moreover, the intriguing discovery made by Crellin and Janssens (1996) is that the notion of stability is highly dependent on the number of completed orbits. After three completed orbits the tether is not found to tumble up to an orbit eccentricity of 0.387. After five orbits the tether is librating for eccentricities up to 0.33 and between 0.374 and 0.383. However, if the simulation runs for 20 orbits then the tether is considered only to be stable for eccentricities less than 0.317.

There is a large discrepancy in the literature between the numerically obtained libration-spin boundary. However, the results of Crellin and Janssens (1996) are probably the more credible because the boundary determined by Modi and Brereton (1968) of 0.355 may possibly be affected by a relatively large round-off error, considering the limited computing power in the late 1960s to carry out accurate floating point calculations. Furthermore, the results derived by Beletsky and Levin (1993) are subjected to the number of terms taken into the series expansion, and will consequently at best represent an approximation.

Karasopoulos and Richardson (1992) numerically generate Poincaré maps, bifurcation diagrams, Lyapunov exponents and a chaos plot for a planar gravity gradient satellite, which has the same equation of motion as a tethered dumbbell. Their results unmistakably show that the dumbbell exhibits regular, quasi-periodic and chaotic motion, with the onset of chaos estimated to occur at an orbit eccentricity of approximately 0.3 for both a zero initial displacement and velocity. When Karasopoulos and Richardson (1992), however, focus on the region around the eccentricity of 0.3, they find the boundary between regular motion and

chaos is not trivial. When the orbit eccentricity is 0.312 the dumbbell's motion is found to be chaotic, however, for eccentricity values slightly less than 0.312 the Poincaré map suggests the motion is quasi-periodic. For values slightly greater than 0.312 Karasopoulos and Richardson (1992) detect a period 7 attractor. Similar observations occur for orbit eccentricities between 0.314 and 0.3145, although for values above 0.3145 the global onset of chaos appears to have set in. Fujii and Ichiki (1997) extend this work to consider the effect of the tether's longitudinal extension on the onset of chaos. The obtained Lyapunov exponents show that the onset of chaos drops from roughly 0.31 to 0.28 for an initial value of zero in the angular displacement and velocity, and $EA = 10^4$ N, where E = modulus of elasticity and A = cross-sectional area of the tether. Note, that the results from Fujii and Ichiki (1997) resonate with the results obtained by Modi and Brereton (1968) since the presence of longitudinal flexibility appears to encourage the onset of tumbling and chaos. The literature appears though not to have investigated whether there is a link between the tether tumbling and the tether undergoing chaotic motion, despite the fact that the boundaries of 0.317 and 0.3145 are relatively close to each other.

The Melnikov function from dynamical systems theory is, as Tong and Rimrott (1991) explain, a measure of the behaviour of the trajectories in phase space near the separatrix for small orbit eccentricities. The function, according to Thomsen (1997), determines if transverse intersections of stable and unstable manifolds occur and so may be an analytical prediction for the onset of chaos. Koch and Bruhn (1989) and Teofilatto and Graziani (1996) each independently derive the Melnikov function for the tethered dumbbell. Seisl and Steindl (1989) take into account the atmospheric drag when deriving the Melnikov function for the tethered dumbbell and Tong and Rimrott (1991) derive the Melnikov function for an irregularly shaped satellite, which is applicable to the dumbbell if the appropriate principle inertias are chosen. In summary, the conclusion of all the papers is that the Melnikov function yields a result when the orbit eccentricity is nearly circular but for larger values of eccentricity the function breaks down since the Hamiltonian is non integrable. Thus, an analytical prediction for the onset of chaos could not be obtained via the Melnikov function.

Misra *et al.* (2001) extend the work by Karasopoulos and Richardson (1992) by numerically investigating the in- and out-of-plane motion of a tethered dumbbell on elliptical orbits. Power spectra and Lyapunov exponents are presented for initial conditions where the initial angular velocities are zero and the initial angular displacements equal each other but only for an orbit eccentricity of 0.1. For initial angular displacements less than 26° the motion was found to be regular and above 30° the Lyapunov exponents clearly proved the motion was globally chaotic. In the region between 27° and 28° Misra *et al.* (2001) state the observed

motion is weakly chaotic. In addition to the tether flexibility, the out-of-plane motion also visibly affects the boundary between regular and chaotic motion but a global map describing how the out-of-plane motion influences that boundary is currently lacking in the literature.

1.11 Aims and Objectives

The above literature survey demonstrates that tethers in space have the potential in the near future of becoming a viable and cost-effective propulsion system. Many applications have been proposed for tethers and much experience and knowledge has been gained through in-orbit flight-testing of conductive and non-conductive tethers. Tethers are also being supported by the major space agencies and companies can already foresee the possibility of commercially exploiting tethers to make a profit. The literature survey, however, also identifies many gaps in the understanding of tethers and the aim of this thesis is to address some of the issues relating to the performance and dynamics of momentum exchange tethers. In particular the objectives of the thesis are to:

- Derive an approximate closed-form solution using the perturbation method of multiple scales to the three-dimensional motion governing a tethered dumbbell on elliptical orbits.
- Map the influence of initial conditions on the boundary between regular and chaotic motion of in- and out-of plane motion of tethered dumbbells on circular and elliptical orbits.
- Map the boundary between libration and spin for a tethered dumbbell on elliptical orbits.
- Establish whether a link exists between the dumbbell's chaotic motion and tether tumbling.
- Explore more deeply the number of orbits a tethered dumbbell completes on elliptical orbits before spinning occurs.
- Derive equations governing payload orbital transfer with momentum exchange tethers to permit accurate performance comparisons between tether configurations.
- Compare the performance of hanging and librating tethers, as well as symmetrical motorised momentum exchange tethers, at payload orbit transfer.
- Derive the equations of motion governing a motorised tether so that the planar, spin up and three-dimensional dynamics can be explored.
- Assess whether the required velocities for payload transfer are, based on the simulated dynamics, achievable with motorised tethers.

Chapter 2

Derivation of the Governing Equations of Motion

2.0 Modelling the Motion of a Tether in Space

A tethered satellite system simply consists of two end masses that are connected by a flexible cable. A critical issue when modelling tethers is the decision of how to model the flexible cable. Being a flexible body there are, as Chapel and Flanders (1993) describe, six types of motion that can occur: in- and out-of-plane libration, spring-mass mode, satellite pendulous mode, planar lateral vibration, skip rope mode and finally longitudinal modes. When the tether undergoes in- and out-of-plane libration, the tether, together with the end masses, oscillates about the common centre of mass like a giant pendulum. For the spring-mass mode, also known as the bobbing or plunge mode, the tether acts much like a linear spring causing the end masses to contract and extend relative to each other. The case of the end mass rotating relative to the tether is termed the pendulous mode with the frequency of oscillation dependent on the tether's tension. Chapel and Flanders (1993) note that the end mass' frequency of oscillations are not necessarily identical in the pitch and roll directions because the end body can have different mass moments of inertia in these directions. The tether can also undergo lateral vibrations in a particular mode within the orbital plane, with the maximum amplitude of vibration occurring along the tether whilst the end masses remain almost undisturbed. However, when the tether additionally has a lateral oscillation out of the orbital plane, then these modes are termed skip rope modes. Finally, the longitudinal mode generates motion along the longitudinal axis of the tether with the end masses remaining almost stationary to the system's centre of mass.

In order to capture the possible cable dynamics, Netzer and Kane (1995) state that the tether can be modelled as (a) a rigid, inextensible massless or massive rod, (b) a sequence of rigid or extensible segments, or (c) a continuous, massive, extensible or inextensible cable. The more sophisticated the model the more phenomena the model is likely to capture but at the expense of requiring a lot of complex analysis or computational power.

Modelling the tether as a rigid and massless rod is the simplest of models and is ideal for capturing the system's rigid body motion but does not account for tether bending or extension. The literature on the nonlinear attitude dynamics of tethered dumbbells typically

models the tether as a rigid and massless rod. The rigid massless model is also employed in other areas as the resulting equations permit their treatment with analytical methods. Liaw and Abed (1990) assume the tether is rigid and massless to study the stabilisation of a tether during station keeping by controlling the cable's tension with a nonlinear feedback loop. Netzer and Kane (1993) model the cable as a straight and massless body to optimise proposed control laws for the deployment and retrieval of the tether. An inextensible and straight tether is used by Mazzoleni (2000) to simulate the spin up and retrieval dynamics of the proposed ASTOR satellite.

A tether that is represented by a sequence of elements, such as point masses connected by rigid massless rods or point masses connected by massless springs, will describe the tether's motion more realistically since the model accounts for tether curvature. Banerjee (1990) remarks that the lumped mass model can be considered more general than the continuum models since it deals better with small curvature and large elastic displacement of the tether. Furthermore, geometric nonlinearity is inherent in the bead model, which is a further advantage over continuum models as Kim and Vadali (1995) point out. A large number of point masses or elements are required to obtain a high resolution of the cable dynamics. On the other hand, if too many masses are employed then the complexity of the analysis rises, as well as the necessary computational effort needed to numerically integrate the equations. Consequently, Netzer and Kane (1995) make the comment that this type of model is generally used to simulate the tether's dynamics and rarely made use of in controller design. Banerjee (1990), however, employs a 5 lumped mass model connected by massless springs and in doing so was the first to develop a theory for deployment rate control with a lumped mass model. Puig-Suari *et al.* (1993) analyse the possibility of using an aerobraking tether at Mars and present simulations involving a three-rod model of the tether with no springs. Puig-Suari *et al.* (1995a) extend this to a five hinged model connected by springs to incorporate the tether's extension. Netzer and Kane (1995) represent the tether by eight rigid massive rods that are free to rotate and thereby demonstrate a tethered satellite system can be suitably controlled with a thruster at one of the end masses.

When the tether is modelled as a continuum the cable may be treated as a flexible or inextensible body. The resulting equations of motion are a partial differential equation and usually a numerical method of discretisation must be followed to obtain a solution. Discretisation can be achieved by a finite difference or a finite element approach, as well as transforming the partial differential equations into a set of ordinary differential equations by prescribing a particular mode shape, e.g. by means of Galerkin's method. The Galerkin or assumed-modes methods achieve the discretisation by expanding the solutions in a finite

series of known functions, where in this case the mode shape provides the required information. A decision must be made as to how many modes to include and usually the more modes included the better the approximation is to the real tether. The methods of finite element and finite difference physically discretise the tether into lumped parameters. An important difference between the two approaches, as Min *et al.* (1999) explain, is finite element or finite difference methods can only yield a numerical solution, whereas assumed-modes or Galerkin methods deliver an analytical solution.

Quadrelli (2001) employs a finite difference approximation of the tether's partial differential equation to investigate several tether configurations for use as an interferometer. Krupa *et al.* (1996) utilise a finite difference discretisation to compute the relative equilibria of a flexible tether. Danilin *et al.* (1999) use a finite element model to obtain the spatial motion of the tether's dynamics during deployment and retrieval. Steiner *et al.* (1996) and Wiedermann *et al.* (2000) introduce a spatial discretisation by means of finite elements for the numerical solution of the tether's equations to simulate the deployment of a subsatellite from the Space Shuttle. Keshmiri *et al.* (1996) discretise the continuous tether by an assumed-mode method and proceed to conduct a stability analysis of the tether during its station keeping phase. Liangdong and Bainum (1990) employ the Rayleigh-Ritz solution to obtain a mathematical model of a large tethered antenna. An excellent overview on the attempts to model the flexible tether mechanics is provided by Misra and Modi (1982), who tabularise all the physical effects and discretisation procedures employed in investigations during the 1970s.

The previous literature investigating the nonlinear attitude dynamics of a tethered dumbbell modelled the tether as a massless rigid rod. This simple model allows the dynamics of the tethered satellite system to be efficiently explored without the added complexity of the flexible tether dynamics, which may not significantly affect the motion of the end bodies. Steiner *et al.* (1995) consider two rigid end masses connected by a massive visco-elastic cable and their results suggest that a rigid tether model can satisfactorily approximate a librating or spinning tether provided the tether length is short in comparison to the orbital radius and the mass of the end bodies is much larger than the tether mass. Since this thesis aims to address aspects related to the literature on tethered dumbbells and investigate the dynamics of spinning motorised tethers, the tether will, therefore, be modelled as a rigid body.

2.1 Co-ordinate System

The geocentric co-ordinate system, where the Earth's centre of mass is treated as the origin, is adopted from Chobotov (1996) to provide an inertial system in space in which the

governing equations of motion can be derived for tethered bodies orbiting the Earth. The Z_E axis, as displayed in Figure 2.1, points in the direction of the Earth's north pole and represents the Earth's axis of rotation in a positive direction, noting that the X_E, Y_E, Z_E system is non-rotating with respect to the stars and that the Earth rotates relative to the co-ordinate system. The X_E, Y_E plane is coplanar with the Earth's equator and is inclined by 23.5° to the ecliptic plane, the plane of the Earth's orbit about the Sun, as illustrated in Figure 2.2. On the first day of the northern hemisphere's spring the ecliptic and the X_E, Y_E plane intersect along a line, which is coincidental with the X_E vector, pointing to the first point of the Aries constellation, or the vernal equinox direction.

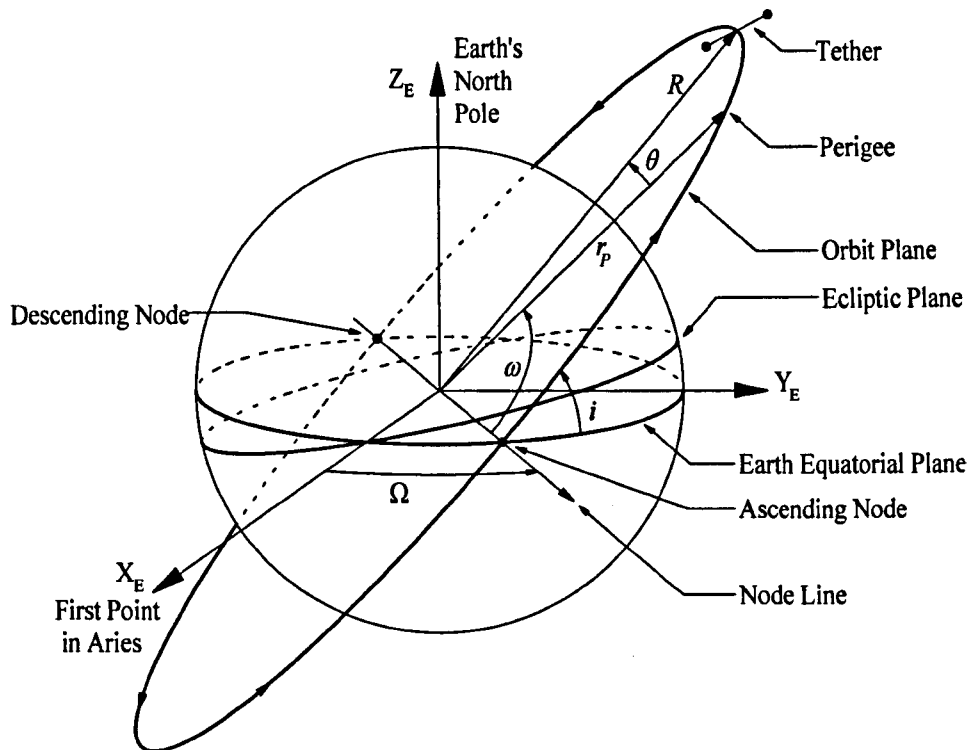


Figure 2.1 Geocentric inertial co-ordinate system

In reality the geocentric system is not a true inertial system. The Earth orbits the Sun on an almost circular orbit and in turn the Sun orbits the centre of the Milky Way on an approximately circular orbit. Thus, the geocentric system is continuously experiencing an acceleration and, therefore, cannot be considered as a proper inertial reference frame. Furthermore, the direction of the Earth's axis of rotation does not remain constant because of the precessional motion due to the Sun with a period, given by Sidi (1997), of 25800 years together with a nutational motion due to the Moon with a period of 18.6 years. Moreover, Sidi (1997) states that both the equatorial and ecliptic plane move with respect to the stars since the planets affect the orientation of the ecliptic plane in the slow rotational motion of planetary precession. Consequently, the geocentric system moves slowly relative to the stars and when extreme precision is required the co-ordinates of an object based on the vernal

equinox direction of a particular year or epoch have to be specified. However, the accelerations are relatively small and for practical purposes the geocentric system can be accepted as being inertial.

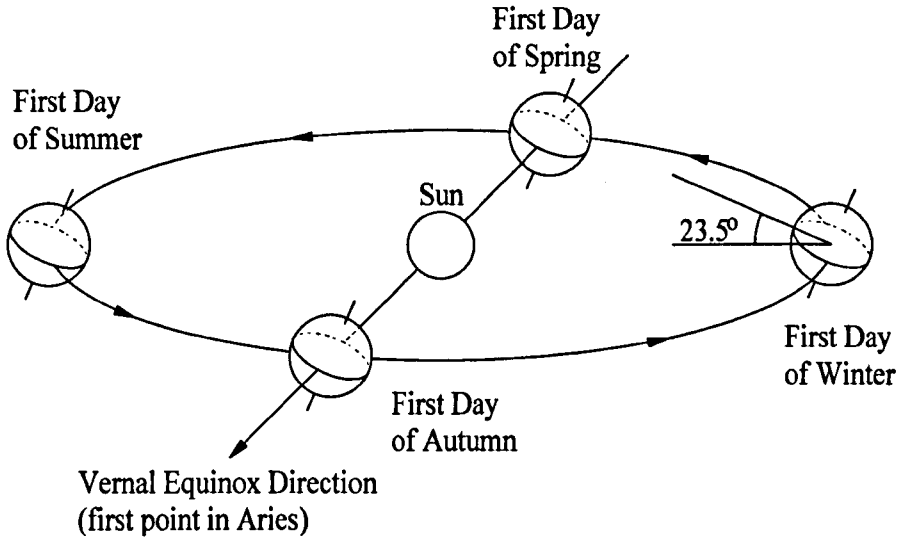


Figure 2.2 Heliocentric ecliptic co-ordinate system defining vernal equinox direction

The plane of the tether's orbit about the Earth is inclined to the Earth's equatorial plane by the angle i , the inclination of the orbit, where the intersection of the two planes occurs at the node line, as depicted in Figure 2.1. The right ascension, Ω , measures the angle in the plane of the equator from the vernal equinox eastward to the ascending node. The angle formed in the orbit plane in the direction of motion from the ascending node to perigee is the argument of perigee, ω . In the orbit plane, R , represents the radius vector to the orbiting tether's centre of mass and r_p , is the radius vector to the perigee of the orbit. The true anomaly, θ , gives the angle in the direction of motion from the perigee to the tether's centre of mass. These parameters together with the orbit eccentricity, e , and mean anomaly are sufficient to completely define the position of the tether's centre of mass in space. The mean anomaly is defined as the orbital mean motion multiplied with the time elapsed since passing perigee.

Figure 2.3 illustrates the two final co-ordinate systems required to describe the tether's rigid body motion in space. The Earth's centre of mass, E , is defined as the origin of the X, Y, Z system and the origin of the relative rotating x_0, y_0, z_0 co-ordinate system is placed at the tether's centre of mass. Both the X, Y plane and the x_0, y_0 plane lie within the orbit plane, where both the Z and z_0 axes are perpendicular to the orbit plane. The X axis is aligned along r_p in the direction of the perigee of the orbit and the x_0 axis rotates aligned with R . The in-plane angle, ψ , measures the angle from the x_0 axis to the projection of the tether onto the orbit plane. The out-of-plane angle, α , spans from the projection of the tether onto the orbit plane to the tether where α is always within a plane normal to the orbit plane.

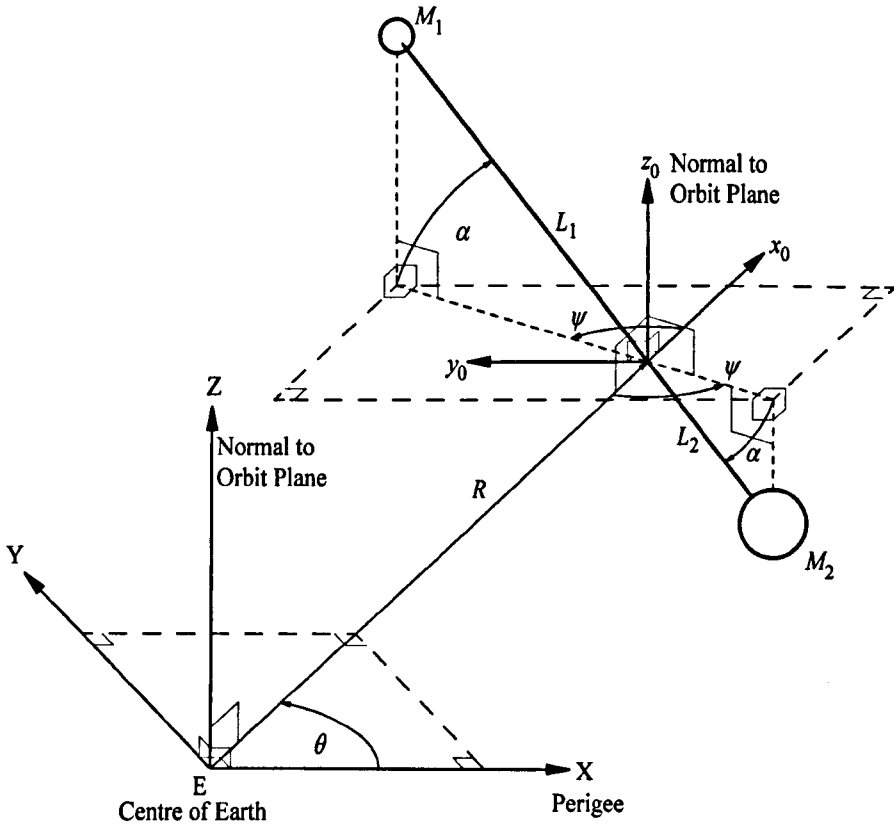


Figure 2.3 Geometry of tethered dumbbell orbiting Earth

2.2 Derivation of the Equations of Motion Governing a Tethered Dumbbell

The equations of motion are obtained through the Lagrangian formulation. The model shown in Figure 2.3 consists of two end masses, M_1 and M_2 , connected by a tether where the distance from the tether's centre of mass to the each end mass is denoted by L_1 and L_2 . Environmental effects such as solar radiation, aerodynamic drag and electrodynamic forces, that can influence the tether, as discussed by Misra and Modi (1989), are assumed to be negligible, as are gravitational perturbations caused by the Earth's oblateness, the Sun and Moon. For this derivation of the tethered dumbbell the tether is assumed to be massless relative to the mass of the two end bodies, which are treated as point masses with no mass moments of inertia. The cartesian components of the end masses taken about E are found from Figure 2.3 to be

$$x_1 = R \cos \theta + L_1 \cos \alpha \cos(\psi + \theta) \quad (2.1)$$

$$y_1 = R \sin \theta + L_1 \cos \alpha \sin(\psi + \theta) \quad (2.2)$$

$$z_1 = L_1 \sin \alpha \quad (2.3)$$

$$x_2 = R \cos \theta - L_2 \cos \alpha \cos(\psi + \theta) \quad (2.4)$$

$$y_2 = R \sin \theta - L_2 \cos \alpha \sin(\psi + \theta) \quad (2.5)$$

$$z_2 = -L_2 \sin \alpha \quad (2.6)$$

where R , θ , α , ψ are the independent generalised co-ordinates and functions of time. The distance from the Earth's centre to the end masses are determined by

$$R_1 = \sqrt{x_1^2 + y_1^2 + z_1^2} = \sqrt{L_1^2 + R^2 + 2L_1R \cos \alpha \cos \psi} \quad (2.7)$$

$$R_2 = \sqrt{x_2^2 + y_2^2 + z_2^2} = \sqrt{L_2^2 + R^2 - 2L_2R \cos \alpha \cos \psi} \quad (2.8)$$

As the end masses are treated as point masses the kinetic energy of the system comprises solely the translation of the end bodies. Hence,

$$T = \frac{1}{2} M_1 (x_1'^2 + y_1'^2 + z_1'^2) + \frac{1}{2} M_2 (x_2'^2 + y_2'^2 + z_2'^2) \quad (2.9)$$

where the prime denotes differentiation with respect to time. Differentiating (2.1)-(2.6) with respect to time and substituting the resulting expressions into (2.9) gives, assuming that moment equilibrium $M_1L_1 = M_2L_2$, holds,

$$T = \frac{1}{2} (M_1 + M_2) (R'^2 + R^2 \theta'^2) + \frac{1}{2} (M_1 L_1^2 + M_2 L_2^2) [\alpha'^2 + (\psi' + \theta')^2 \cos^2 \alpha] \quad (2.10)$$

The gravitational potential energy is obtained by integrating Newton's gravitational law and by convention defining one of the states of the evaluated integral to be zero at infinity. Thus, the tether's potential energy is given by

$$U = -\frac{\mu M_1}{R_1} - \frac{\mu M_2}{R_2} \quad (2.11)$$

where μ is the product of the universal gravitational constant, G , and the Earth's mass, M_E . Substituting (2.7) and (2.8) into (2.11) gives the system's potential energy without resorting to an expansion

$$U = -\frac{\mu M_1}{\sqrt{L_1^2 + R^2 + 2L_1R \cos \alpha \cos \psi}} - \frac{\mu M_2}{\sqrt{L_2^2 + R^2 - 2L_2R \cos \alpha \cos \psi}} \quad (2.12)$$

The kinetic and potential energy, (2.10) and (2.12), are substituted into Lagrange's equation in the form of

$$\frac{d}{dt} \left[\frac{\partial T}{\partial q_i'} \right] - \frac{\partial T}{\partial q_i} + \frac{\partial U}{\partial q_i} = Q_i \quad i = 1, 2, \dots, N \quad (2.13)$$

where Q_i equates to zero since the assumption is made that no non-conservative forces are acting on the system. Evaluating (2.13) generates the following four equations of motion governing the tether's in and out-of-plane angles, true anomaly and radial distance from the focus of the elliptical orbit to the tether's centre of mass:

$$\psi'' + \theta'' - 2 \tan \alpha \alpha' (\psi' + \theta') + \frac{\mu R \sin \psi \sec \alpha}{L_1 + L_2} \left[(R^2 + L_2^2 - 2RL_2 \cos \psi \cos \alpha)^{3/2} - (R^2 + L_1^2 + 2RL_1 \cos \psi \cos \alpha)^{3/2} \right] = 0 \quad (2.14)$$

$$\alpha'' + \frac{1}{2} \sin 2\alpha (\psi' + \theta')^2 + \frac{\mu R \cos \psi \sin \alpha}{L_1 + L_2} \left[(R^2 + L_2^2 - 2RL_2 \cos \psi \cos \alpha)^{-3/2} - (R^2 + L_1^2 + 2RL_1 \cos \psi \cos \alpha)^{-3/2} \right] = 0 \quad (2.15)$$

$$(M_1 + M_2) (R^2 \theta'' + 2RR' \theta') + (M_1 L_1^2 + M_2 L_2^2) [\cos^2 \alpha (\theta'' + \psi'') - \alpha' \sin 2\alpha (\theta' + \psi')] = 0 \quad (2.16)$$

$$R'' - \theta'^2 R + \frac{\mu}{M_1 + M_2} \left[M_1 (R + L_1 \cos \psi \cos \alpha) (R^2 + L_1^2 + 2RL_1 \cos \psi \cos \alpha)^{3/2} + M_2 (R - L_2 \cos \psi \cos \alpha) (R^2 + L_2^2 - 2RL_2 \cos \psi \cos \alpha)^{3/2} \right] = 0 \quad (2.17)$$

The equations of motion in (2.14)-(2.17) are a function of the independent variable of time. Alternatively, the governing equations can also be expressed as a function of the orbit's true anomaly if the tether is assumed to remain on a Keplerian orbit. Transforming from time to the true anomaly results in R , α and ψ becoming functions of θ with the velocities and accelerations given as

$$\psi' = \frac{d\psi}{d\theta} \frac{d\theta}{dt} = \theta' \dot{\psi} \quad (2.18)$$

$$\alpha' = \frac{d\alpha}{d\theta} \frac{d\theta}{dt} = \theta' \dot{\alpha} \quad (2.19)$$

$$\theta' = \sqrt{\frac{\mu(1 + e \cos \theta)}{R(\theta)^3}} \quad (2.20)$$

$$\psi'' = \frac{d}{dt} (\theta' \dot{\psi}) = \theta'^2 \ddot{\psi} + \theta' \dot{\theta}' \dot{\psi} \quad (2.21)$$

$$\alpha'' = \frac{d}{dt} (\theta' \dot{\alpha}) = \theta'^2 \ddot{\alpha} + \theta' \dot{\theta}' \dot{\alpha} \quad (2.22)$$

$$\theta'' = \frac{d}{dt} (\theta') = \theta' \dot{\theta}' \quad (2.23)$$

where the dot denotes differentiation with respect to the true anomaly and

$$R(\theta) = \frac{r_p(1 + e)}{1 + e \cos \theta} \quad (2.24)$$

$$\dot{\theta}' = -2e \sqrt{\frac{\mu}{r_p^3(1 + e)^3}} (1 + e \cos \theta) \sin \theta \quad (2.25)$$

The expression in (2.24) is a consequence of conservation of angular momentum and is a standard result from the two-body problem, which is discussed in detail, for example, by Chobotov (1996). The three dimensional motion of the tether on an elliptical orbit with respect to the true anomaly is obtained by substituting (2.18)-(2.23) and (2.25) into (2.14) and (2.15), giving

$$\ddot{\psi} - \left[\frac{2e \sin \theta}{1 + e \cos \theta} + 2 \tan \alpha \dot{\alpha} \right] (\dot{\psi} + 1) + \frac{R(\theta)^4 \sin \psi \sec \alpha}{(L_1 + L_2)(1 + e \cos \theta)} \left[(R(\theta)^2 + L_2^2 - 2R(\theta)L_2 \cos \psi \cos \alpha)^{-3/2} - (R(\theta)^2 + L_1^2 + 2R(\theta)L_1 \cos \psi \cos \alpha)^{-3/2} \right] = 0 \quad (2.26)$$

$$\ddot{\alpha} - \frac{2e \sin \theta}{1 + e \cos \theta} \dot{\alpha} + \frac{1}{2} \sin 2\alpha (\dot{\psi} + 1)^2 + \frac{R(\theta)^4 \cos \psi \sin \alpha}{(L_1 + L_2)(1 + e \cos \theta)} \left[(R(\theta)^2 + L_2^2 - 2R(\theta)L_2 \cos \psi \cos \alpha)^{-3/2} - (R(\theta)^2 + L_1^2 + 2R(\theta)L_1 \cos \psi \cos \alpha)^{-3/2} \right] = 0 \quad (2.27)$$

The length of the tether is typically two to three orders of magnitude less than the orbital radius. Therefore, the tether's potential energy in (2.12) can be justifiably expanded with $\delta_1 = L_1/R$ and $\delta_2 = L_2/R$, where both $\delta_1 \ll 1$ and $\delta_2 \ll 1$. Up to and including $O(\delta_1^2)$ and $O(\delta_2^2)$, assuming $M_1 L_1 = M_2 L_2$, the potential energy expression becomes

$$U = -\frac{\mu(M_1 + M_2)}{R} + \frac{\mu(M_1 L_1^2 + M_2 L_2^2)(1 - 3 \cos^2 \alpha \cos^2 \psi)}{2R^3} \quad (2.28)$$

Substituting (2.28) and (2.10) into (2.13) gives the equations of motion with respect to time for the in and out-of-plane angles, true anomaly and radial distance, respectively:

$$\psi'' + \theta'' - 2\alpha' \tan \alpha (\psi' + \theta') + \frac{3\mu}{2R^3} \sin 2\psi = 0 \quad (2.29)$$

$$\alpha'' + \frac{1}{2} \sin 2\alpha (\psi' + \theta')^2 + \frac{3\mu}{2R^3} \cos^2 \psi \sin 2\alpha = 0 \quad (2.30)$$

$$R^2 \theta'' + 2RR' \theta' + \frac{M_1 L_1^2 + M_2 L_2^2}{M_1 + M_2} [\cos^2 \alpha (\theta'' + \psi'') - \alpha' \sin 2\alpha (\theta' + \psi')] = 0 \quad (2.31)$$

$$(M_1 + M_2) \left[R'' - R\theta'^2 + \frac{\mu}{R^2} \right] - \frac{3\mu}{2R^4} (M_1 L_1^2 + M_2 L_2^2) (1 - 3 \cos^2 \psi \cos^2 \alpha) = 0 \quad (2.32)$$

Transforming the independent variable from time to the true anomaly gives

$$\ddot{\psi} - \left[2\dot{\alpha} \tan \alpha + \frac{2e \sin \theta}{1 + e \cos \theta} \right] (\dot{\psi} + 1) + \frac{3 \sin 2\psi}{2(1 + e \cos \theta)} = 0 \quad (2.33)$$

$$\ddot{\alpha} - \frac{2e \sin \theta}{1 + e \cos \theta} \dot{\alpha} + \frac{1}{2} \sin 2\alpha \left[(\dot{\psi} + 1)^2 + \frac{3 \cos^2 \psi}{1 + e \cos \theta} \right] = 0 \quad (2.34)$$

Finally, if the expansion is carried up to and including $O(\delta_1^3)$ and $O(\delta_2^3)$, assuming $M_1L_1 = M_2L_2$, then

$$U = -\frac{\mu(M_1 + M_2)}{R} + \frac{\mu(M_1L_1^2 + M_2L_2^2)(1 - 3\cos^2\alpha\cos^2\psi)}{2R^3} - \frac{\mu(M_1L_1^3 - M_2L_2^3)(3\cos\alpha\cos\psi - 5\cos^3\alpha\cos^3\psi)}{2R^4} \quad (2.35)$$

Substituting (2.35) and (2.10) into (2.13) gives the equations of motion with respect to time for the in and out-of-plane angles, true anomaly and radial distance, respectively,

$$\psi'' + \theta'' - 2\alpha' \tan\alpha(\psi' + \theta') + \frac{3\mu \sin 2\psi}{2R^3} + \frac{3\mu(L_1 - L_2)}{2R^4} \sin\psi \sec\alpha(1 - 5\cos^2\psi \cos^2\alpha) = 0 \quad (2.36)$$

$$\alpha'' + \frac{1}{2}\sin 2\alpha(\psi' + \theta')^2 + \frac{3\mu \cos^2\psi \sin 2\alpha}{2R^3} + \frac{3\mu(L_1 - L_2)}{2R^4} \cos\psi \sin\alpha(1 - 5\cos^2\psi \cos^2\alpha) = 0 \quad (2.37)$$

$$R^2\theta'' + 2RR'\theta' + \frac{M_1L_1^2 + M_2L_2^2}{M_1 + M_2} [\cos^2\alpha(\theta'' + \psi'') - \alpha' \sin 2\alpha(\theta' + \psi')] = 0 \quad (2.38)$$

$$(M_1 + M_2) \left[R'' - R\theta'^2 + \frac{\mu}{R^2} \right] - (M_1L_1^2 + M_2L_2^2) \left[\frac{3\mu(1 - 3\cos^2\psi \cos^2\alpha)}{2R^4} - \frac{2\mu(L_1 - L_2)\cos\psi \cos\alpha(3 - 5\cos^2\psi \cos^2\alpha)}{R^5} \right] = 0 \quad (2.39)$$

Transforming the independent variable from time to the true anomaly and setting $e = 0$, gives

$$\ddot{\psi} - 2\dot{\alpha} \tan\alpha(\dot{\psi} + 1) + \frac{3}{2}\sin 2\psi + \frac{3(L_1 - L_2)\sin\psi \sec\alpha}{2r_c} (1 - 5\cos^2\psi \cos^2\alpha) = 0 \quad (2.40)$$

$$\ddot{\alpha} + \frac{1}{2}\sin 2\alpha [(\dot{\psi} + 1)^2 + 3\cos^2\psi] + \frac{3(L_1 - L_2)}{2r_c} \cos\psi \sin\alpha (1 - 5\cos^2\psi \cos^2\alpha) = 0 \quad (2.41)$$

where r_c = orbital radius of a circular orbit.

(2.33) and (2.34) represent the equations of motion governing a tethered dumbbell constrained to move on a Keplerian orbit and are commonly found in the literature. (2.14)-(2.17), however, as well as (2.26)-(2.27), (2.36)-(2.39), and (2.40)-(2.41), are rarely presented, if at all. Note how the acceleration terms in all the sets of equations of motion describing the tether's attitude dynamics are linear and uncoupled, and that the source of the nonlinearity in the remaining terms arises solely due to the potential energy, the kinematic interaction between the in- and out-of-plane motion and the constraint to Keplerian motion.

Expanding the potential energy to $O(\delta_1^2)$ and $O(\delta_2^2)$ and constraining the tether's motion to a Keplerian orbit non-dimensionalises (2.33) and (2.34) and apart from the orbit eccentricity is void of any tethered system or orbital properties. Observe that this is not the case when the potential energy is expanded up to $O(\delta_1^3)$ and $O(\delta_2^3)$.

Figure 2.4 shows the effect on the dumbbell's orbital radius due to the coupling with the tether's libration. As a tether librates or spins its mass moment of inertia about the centre of the Earth will change accordingly, thus causing a change in the tether's angular acceleration about the Earth. Since momentum must be conserved the dumbbell's orbit will change altitude accordingly. The conclusion from Figure 2.4 is that a tether on an initially circular orbit does not prescribe a true circular orbit about a planet. Similarly, a tether initially on an elliptical orbit will also not follow the anticipated elliptical path. Instead the tether orbits close to the expected trajectory but in reality follows a slight non-Keplerian orbit. Consequently, constraining the tether to a Keplerian orbit is therefore an assumption but as the discrepancy depicted in Figure 2.4 is small relative to the orbital radius the assumption can be justified. Although small, a discrepancy of 80 m, say, should not be forgotten when considering payload orbital transfer, as such a distance may be significant for a tether facility about to rendezvous with an incoming payload.

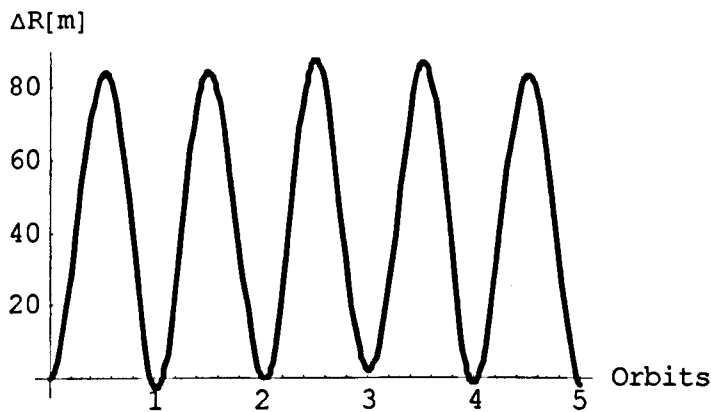


Figure 2.4 Difference in orbital radius between expected circular and actual orbit of a tethered dumbbell with $M_1 = M_2 = 1000$ kg, $L_1 = L_2 = 10$ km and $\psi(0) = 0.1$ rad against the number of orbits completed for an initially circular orbit at $R(0) = 7000$ km.

A small quantitative discrepancy exists, due to both the expansion of the potential energy and the constraint to the Keplerian orbit, in the in- and out-of-plane motion between the output generated from (2.14)-(2.17) and (2.33)-(2.34), as shown in Figure 2.5. However, the response obtained from both forms of equations of motion gives qualitatively very similar

results. Thus, (2.33)-(2.34) represent a valid approximation to the full equations of motion but with the advantage of requiring less computational effort to numerically integrate.

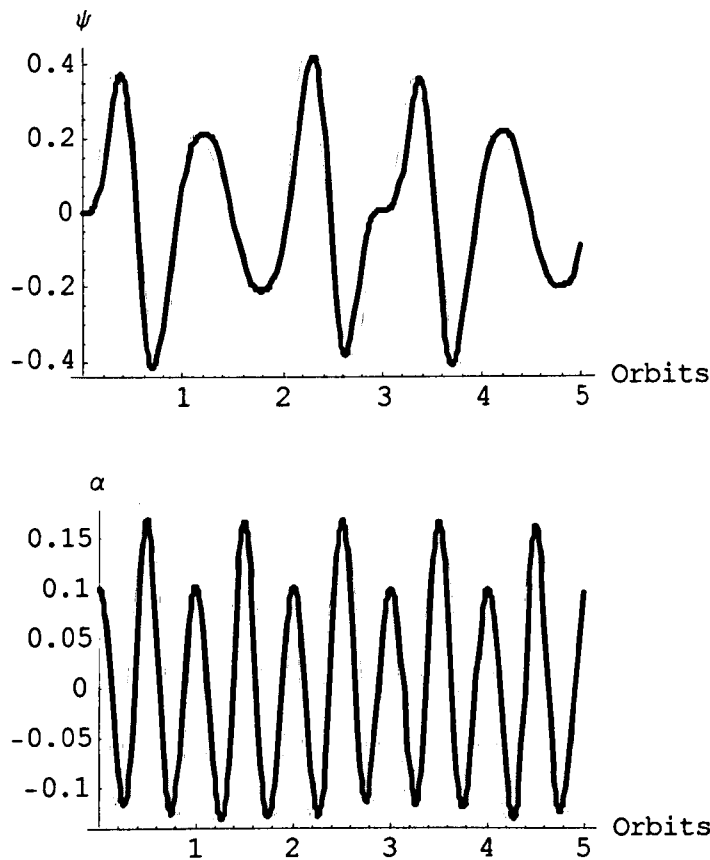


Figure 2.5 Comparison between the time history for the dumbbell's in- and out-of-plane motion from (2.14)-(2.17) (grey) and (2.33)-(2.34) (black). Tether properties are $M_1 = M_2 = 1000$ kg and $L_1 = L_2 = 10$ km with $e = 0.25$, $\dot{\psi}(0) = \dot{\psi}'(0) = 0$ and $\psi(0) = 0.1$ rad.

2.3 Concept of Symmetrical Motorised Tether

Generating velocity increments with a tethered dumbbell is essentially a passive procedure as the amount of ΔV achievable is dependent on the initial conditions, eccentricity of the orbit, the properties and geometry of both the tether and payload. The inclusion of a motor to intentionally spin the tethered system allows an additional ΔV to be generated in addition to that from the initial conditions. Two 'propulsion' tethers are attached in a symmetrical fashion, as suggested by Cartmell and Ziegler (1999) and shown in Figure 2.6, to the casing of an electric motor, which is located at the COM and obtains its electricity from solar panels or a fuel cell. A payload is attached to each remaining free end of the tether. Once the tether is fully deployed the motor is energised, thereby, applying a torque to the tethers. However, the tethers cannot transmit the torque to the payloads at first due to their flexibility and lack of inherent static stiffness. Small tangential boosters are needed in each payload to provide thrust during the initial stages of the tether spin-up to account for the lack of centripetal

acceleration required to keep the tethers taught and hence stop the tethers winding themselves around the motor. The boosters can gradually be switched off as the tethered system's acceleration due to the motor builds up about the COM. Eventually the tangential velocity of the payloads reaches the required level and the payloads are released onto a desired tangential path. If the payloads and tethers are identical and symmetrically attached, then upon simultaneous payload release the tethered facility's COM will not significantly shift. However, with the facility's new mass moment of inertia and perturbational detachment forces some additional boost will probably be required to maintain the facility's altitude. The motor consists of a rotor, which is attached to the propulsion tethers and a stator connected to the rotor by means of a suitable bearing. The power supplies, control systems, and communication equipment are likely to be fitted within the stator assembly in any practical installation. The stator provides the necessary back rotation that is required for the rotor to spin-up in a friction free environment. Deploying a pair of shorter 'outrigger' tethers from the stator housing, which terminate in end masses, controls the stator's angular acceleration by increasing the stator's mass moment of inertia. The motor consists of a rotor, which is attached to the propulsion tethers and a stator connected to the rotor by means of a suitable bearing. The power supplies, control systems, and communication equipment are likely to be fitted within the stator assembly in any practical installation. The stator provides the necessary back rotation that is required for the rotor to spin-up in a friction free environment. Deploying a pair of shorter 'outrigger' tethers from the stator housing, which terminate in end masses, controls the stator's angular acceleration by increasing the stator's mass moment of inertia.

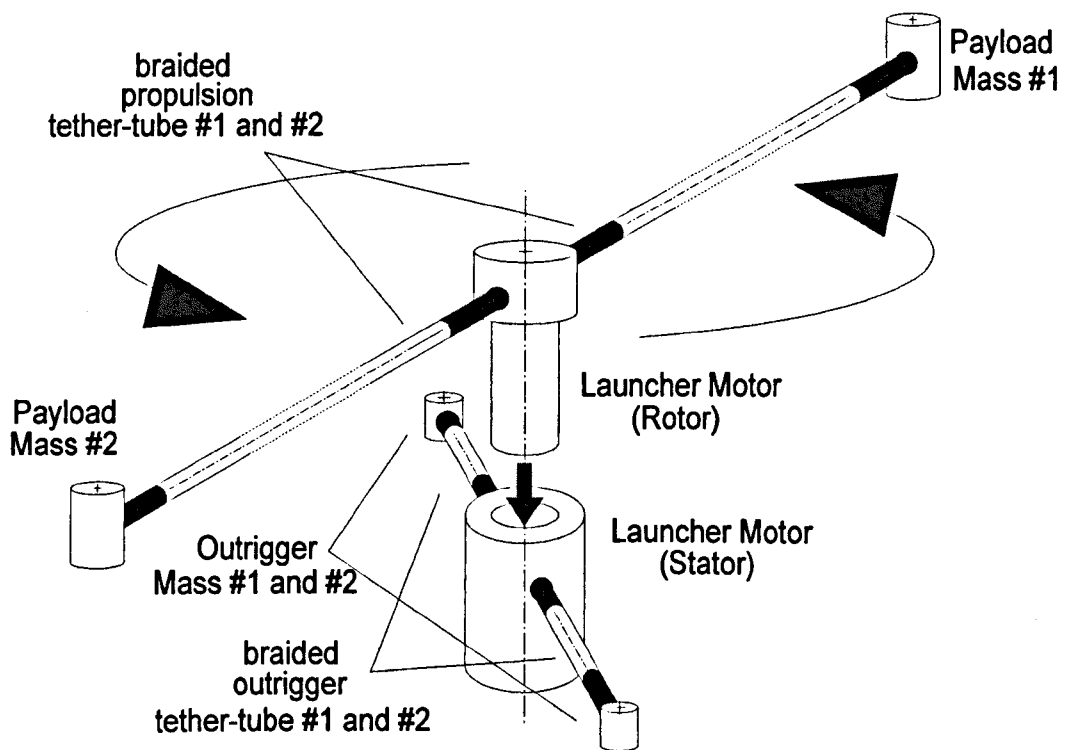


Figure 2.6 Schematic of Symmetrical Motorised Tether Concept, as proposed by Cartmell and Ziegler (1999).

2.4 Derivation of the Equations of Motion Governing a Symmetrical Motorised Tether

In addition to the assumptions made in deriving the equations of motion for the tethered dumbbell, the bearing connecting the motor's rotor and stator will be assumed to be perfect

and cause no significant frictional losses. This assumption implies that the outrigger will behave identically to the propulsion side but rotate in the opposite direction and, thus, requiring only the propulsion side to be modelled. The motor torque will be assumed to remain coplanar with the propulsive tethers and payloads. The connection between the tether and the motor will be modelled as a rigid connection, hence when the tether moves out of the orbital plane the motor will similarly rotate about its centre of mass. If the end masses are substantially more massive than the tethers, then the tether mass may be assumed negligible. Finally, the tether is assumed to be rigid and does not longitudinally extend nor twist in any direction. The kinetic energy of a symmetrical motorised tether is composed of its translational motion in the inertial frame and its rotation about its centre of mass, as shown in Figure 2.7.

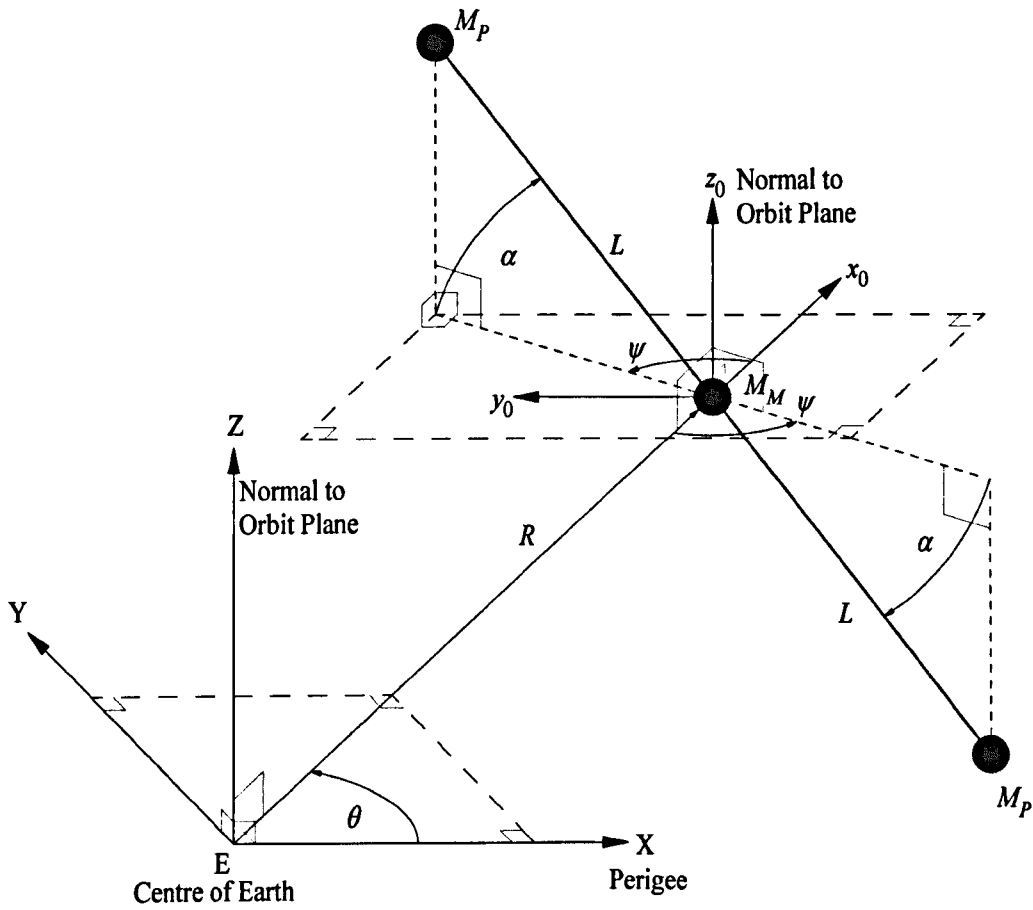


Figure 2.7 Geometry of the motorised tether orbiting Earth

If the motor and the end masses are treated as point masses, then the kinetic energy for the symmetrical tether is given by

$$T = \frac{1}{2} M_P (x_{P1}'^2 + y_{P1}'^2 + z_{P1}'^2) + \frac{1}{2} M_P (x_{P2}'^2 + y_{P2}'^2 + z_{P2}'^2) + \frac{1}{2} M_M (x_M'^2 + y_M'^2 + z_M'^2) \quad (2.42)$$

The Cartesian components of the end bodies plus the motor are given by

$$x_{P1} = R \cos \theta + L \cos \alpha \cos(\psi + \theta) \quad (2.43)$$

$$y_{P1} = R \sin \theta + L \cos \alpha \sin(\psi + \theta) \quad (2.44)$$

$$z_{P1} = L \sin \alpha \quad (2.45)$$

$$x_{P2} = R \cos \theta - L \cos \alpha \cos(\psi + \theta) \quad (2.46)$$

$$y_{P2} = R \sin \theta - L \cos \alpha \sin(\psi + \theta) \quad (2.47)$$

$$z_{P2} = -L \sin \alpha \quad (2.48)$$

$$x_M = R \cos \theta \quad (2.49)$$

$$y_M = R \sin \theta \quad (2.50)$$

$$z_M = 0 \quad (2.51)$$

Differentiating (2.43)-(2.51) with respect to time, squaring and substituting into (2.42) gives

$$T = \left[M_P + \frac{1}{2} M_M \right] (R'^2 + R^2 \theta'^2) + M_P L^2 \left[\alpha'^2 + (\psi' + \theta')^2 \cos^2 \alpha \right] \quad (2.52)$$

The potential energy is given by

$$U = -\frac{\mu M_P}{R_{P1}} - \frac{\mu M_P}{R_{P2}} - \frac{\mu M_M}{R_M} \quad (2.53)$$

where

$$R_{P1} = \sqrt{x_{P1}^2 + y_{P1}^2 + z_{P1}^2} = \sqrt{L^2 + R^2 + 2LR \cos \alpha \cos \psi} \quad (2.54)$$

$$R_{P2} = \sqrt{x_{P2}^2 + y_{P2}^2 + z_{P2}^2} = \sqrt{L^2 + R^2 - 2LR \cos \alpha \cos \psi} \quad (2.55)$$

$$R_M = \sqrt{x_M^2 + y_M^2 + z_M^2} = R \quad (2.56)$$

Substituting (2.54)-(2.56) into (2.53) gives

$$U = -\frac{\mu M_P}{\sqrt{R^2 + L^2 + 2LR \cos \alpha \cos \psi}} - \frac{\mu M_P}{\sqrt{R^2 + L^2 - 2LR \cos \alpha \cos \psi}} - \frac{\mu M_M}{R} \quad (2.57)$$

Before substituting (2.52) and (2.57) into Lagrange's equations in (2.13), the generalised torque exerted by the motor on the system needs to be derived. From first principles virtual work is defined as

$$\delta W = F_x \delta x + F_y \delta y + F_z \delta z \quad (2.58)$$

Considering the virtual work done by all non-conservative forces through a virtual displacement, leads to

$$\delta W_\alpha \equiv Q_\alpha(t) \delta \alpha \quad (2.59)$$

$$\delta W_\psi \equiv Q_\psi(t) \delta \psi \quad (2.60)$$

In other words

$$Q_\alpha(t) = F_x \frac{\partial x}{\partial \alpha} + F_y \frac{\partial y}{\partial \alpha} + F_z \frac{\partial z}{\partial \alpha} \quad (2.61)$$

$$Q_\psi(t) = F_x \frac{\partial x}{\partial \psi} + F_y \frac{\partial y}{\partial \psi} + F_z \frac{\partial z}{\partial \psi} \quad (2.62)$$

Thus, determining the x , y and z -components of the force $F = \tau/L$, shown in Figure 2.8, and partially differentiating these yields the generalised force terms. An additional angle, γ , which does not alter the location of the end masses' centre of mass, needs to be included because the torque axis is free to rotate about the longitudinal axis of the tethers. Note that the orbital angle, θ , does not affect the generalised force as the principle of virtual work only considers the virtual displacements due to the applied non-conservative forces. From above the Cartesian components are

$$x = L \cos \alpha \cos \psi \quad (2.63)$$

$$y = L \cos \alpha \sin \psi \quad (2.64)$$

$$z = L \sin \alpha \quad (2.65)$$

From Figure 2.8 the x , y and z -components of the force $F = \tau/L$ are

$$F_x = -F \cos \gamma \sin \psi - F \sin \gamma \sin \alpha \cos \psi \quad (2.66)$$

$$F_y = F \cos \gamma \cos \psi - F \sin \gamma \sin \alpha \sin \psi \quad (2.67)$$

$$F_z = F \sin \gamma \cos \alpha \quad (2.68)$$

Partially differentiating (2.63)-(2.65) with respect to α and substituting along with (2.66)-(2.68) into (2.61) gives after simplification

$$Q_\alpha = FL \sin \gamma = \tau \sin \gamma \quad (2.69)$$

Similarly, partially differentiating (2.63)-(2.65) with respect to ψ and substituting along with (2.66)-(2.68) into (2.62) yields after simplification

$$Q_\psi = FL \cos \gamma \cos \alpha = \tau \cos \gamma \cos \alpha \quad (2.70)$$

Thus, an initially planar motorised tether with $\gamma = 0$ will exert a torque solely within the orbital plane, as expected.

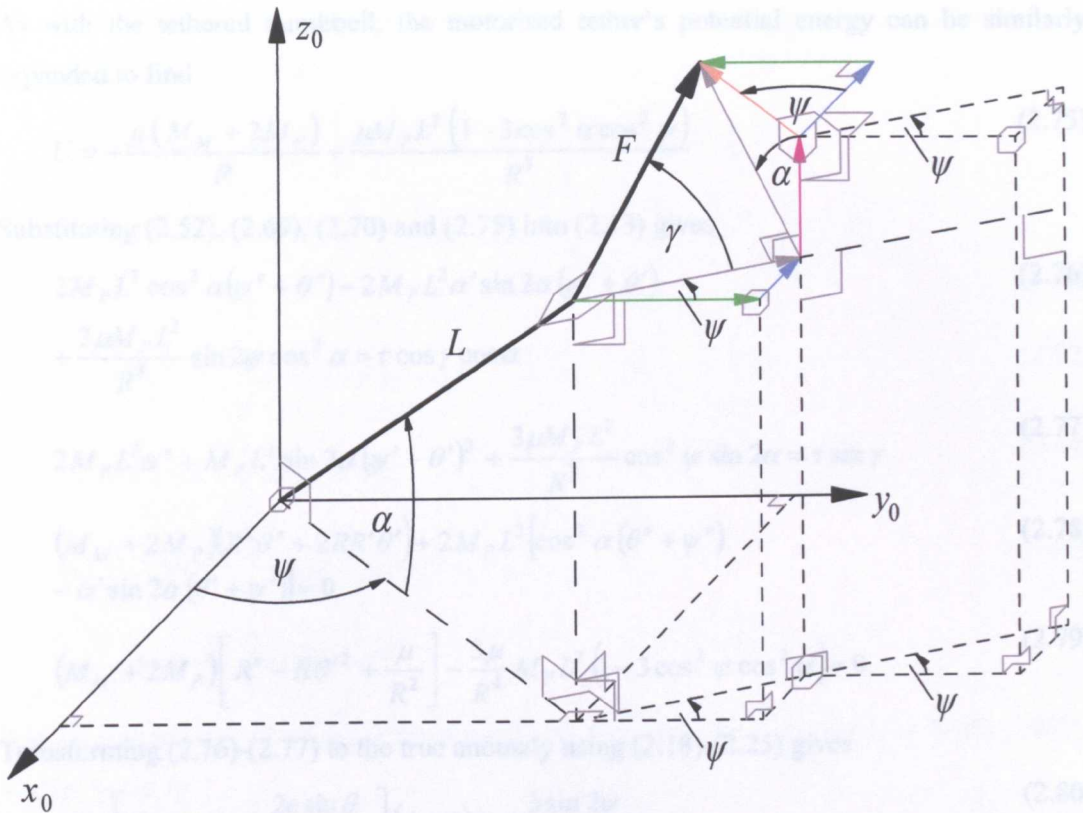


Figure 2.8 Geometrical Depiction of the x_0 - y_0 - z_0 Components of $F = \tau/L$

Substituting (2.52), (2.57), (2.69) and (2.70) into (2.13) gives the governing equations of motion of a motorised tether:

$$2L^2 M_p (\psi'' + \theta'') \cos^2 \alpha - 2L^2 M_p \alpha' (\psi' + \theta') \sin 2\alpha \quad (2.71)$$

$$+ \mu M_p L R \sin \psi \cos \alpha \left[(R^2 + L^2 - 2RL \cos \psi \cos \alpha)^{-3/2} \right. \\ \left. - (R^2 + L^2 + 2RL \cos \psi \cos \alpha)^{-3/2} \right] = \tau \cos \gamma \cos \alpha$$

$$2M_p L^2 \alpha'' + M_p L^2 \sin 2\alpha (\psi' + \theta')^2 \quad (2.72)$$

$$+ \mu M_p L R \cos \psi \sin \alpha \left[(R^2 + L^2 - 2RL \cos \psi \cos \alpha)^{-3/2} \right. \\ \left. - (R^2 + L^2 + 2RL \cos \psi \cos \alpha)^{-3/2} \right] = \tau \sin \gamma$$

$$(M_M + 2M_p)(R^2 \theta'' + 2RR' \theta') \quad (2.73)$$

$$+ 2M_p L^2 [\cos^2 \alpha (\theta'' + \psi'') - \alpha' \sin 2\alpha (\theta' + \psi')] = 0$$

$$(M_M + 2M_p)(R'' - \theta'^2 R) \quad (2.74)$$

$$+ \mu M_p \left[(R + L \cos \psi \cos \alpha)(R^2 + L^2 + 2RL \cos \psi \cos \alpha)^{-3/2} \right. \\ \left. + (R - L \cos \psi \cos \alpha)(R^2 + L^2 - 2RL \cos \psi \cos \alpha)^{-3/2} \right] + \frac{\mu M_M}{R^2} = 0$$

As with the tethered dumbbell, the motorised tether's potential energy can be similarly expanded to find

$$U = -\frac{\mu(M_M + 2M_P)}{R} + \frac{\mu M_P L^2 (1 - 3 \cos^2 \alpha \cos^2 \psi)}{R^3} \quad (2.75)$$

Substituting (2.52), (2.69), (2.70) and (2.75) into (2.13) gives

$$2M_P L^2 \cos^2 \alpha (\psi'' + \theta'') - 2M_P L^2 \alpha' \sin 2\alpha (\psi' + \theta') + \frac{3\mu M_P L^2}{R^3} \sin 2\psi \cos^2 \alpha = \tau \cos \gamma \cos \alpha \quad (2.76)$$

$$2M_P L^2 \alpha'' + M_P L^2 \sin 2\alpha (\psi' + \theta')^2 + \frac{3\mu M_P L^2}{R^3} \cos^2 \psi \sin 2\alpha = \tau \sin \gamma \quad (2.77)$$

$$(M_M + 2M_P)(R^2 \theta'' + 2RR'\theta') + 2M_P L^2 [\cos^2 \alpha (\theta'' + \psi'') - \alpha' \sin 2\alpha (\theta' + \psi')] = 0 \quad (2.78)$$

$$(M_M + 2M_P) \left[R'' - R\theta'^2 + \frac{\mu}{R^2} \right] - \frac{3\mu}{R^4} M_P L^2 (1 - 3 \cos^2 \psi \cos^2 \alpha) = 0 \quad (2.79)$$

Transforming (2.76)-(2.77) to the true anomaly using (2.18)-(2.25) gives

$$\ddot{\psi} - \left[2\dot{\alpha} \tan \alpha + \frac{2e \sin \theta}{1 + e \cos \theta} \right] (\dot{\psi} + 1) + \frac{3 \sin 2\psi}{2(1 + e \cos \theta)} = \frac{\tau r_p^3 (1 + e)^3}{2\mu M_P L^2 (1 + e \cos \theta)^4} \frac{\cos \gamma}{\cos \alpha} \quad (2.80)$$

$$\ddot{\alpha} - \frac{2e \sin \theta}{1 + e \cos \theta} \dot{\alpha} + \frac{1}{2} \sin(2\alpha) \left[(\dot{\psi} + 1)^2 + \frac{3 \cos^2 \psi}{1 + e \cos \theta} \right] = \frac{\tau r_p^3 (1 + e)^3}{2\mu M_P L^2 (1 + e \cos \theta)^4} \sin \gamma \quad (2.81)$$

Note, that unlike the tethered dumbbell these equations of motion are not independent of the tether and orbit properties.

Neglecting the tether mass and mass moment of inertia is justifiable when the qualitative dynamics are of interest. However, some quantitative studies will need to be carried out, such as the time required for the motorised tether to reach the desired release velocity. To obtain accurate quantitative statements a model including the tether's mass and mass moment of inertia is required. Initially a full three-dimensional model of the tether was derived but the nonlinearities due to the mass moment of inertia being dependent on α and γ generated very large equations of motion, which were computationally expensive to evaluate. Hence, an accurate planar model of the motorised tether is derived.

The kinetic energy of a motorised tether taking into account the translation and rotation of each component is given by

$$T = \frac{1}{2} M_P (\dot{x}_{P1}^2 + \dot{y}_{P1}^2) + \frac{1}{2} M_P (\dot{x}_{P2}^2 + \dot{y}_{P2}^2) + \frac{1}{2} M_M (\dot{x}_M^2 + \dot{y}_M^2) + \frac{1}{2} \rho A L (\dot{x}_{T1}^2 + \dot{y}_{T1}^2) + \frac{1}{2} \rho A L (\dot{x}_{T2}^2 + \dot{y}_{T2}^2) + \left[I_P + I_T + \frac{1}{2} I_M \right] (\dot{\psi} + \dot{\theta})^2 \quad (2.82)$$

where

$$x_{T1} = R \cos \theta + \frac{L}{2} \cos(\psi + \theta) \quad (2.83)$$

$$y_{T1} = R \sin \theta + \frac{L}{2} \sin(\psi + \theta) \quad (2.84)$$

$$x_{T2} = R \cos \theta - \frac{L}{2} \cos(\psi + \theta) \quad (2.85)$$

$$y_{T2} = R \sin \theta - \frac{L}{2} \sin(\psi + \theta) \quad (2.86)$$

The mass moments of inertia can be derived from first principles, as shown by Wells (1967), and are given by

$$I_P = \frac{1}{2} M_P r_{Payload}^2 \quad (2.87)$$

$$I_T = \frac{1}{12} \rho A L (3r_T^2 + L^2) \quad (2.88)$$

$$I_M = \frac{1}{2} M_M r_M^2 \quad (2.89)$$

where I_P = mass moment of inertia of the payload, I_T = mass moment of inertia of the tether, I_M = mass moment of inertia of the motor, $r_{Payload}$ = radius of the payload, r_T = radius of the tether, and r_M = radius of the motor. Note, that the parallel axis theorem does not need to be applied since the translation of the body is included separately in (2.82). Differentiating (2.43)-(2.51) and (2.83)-(2.86) with respect to time, squaring and substituting into (2.82) gives

$$T = \left[M_P + \rho A L + \frac{1}{2} M_M \right] (R'^2 + R^2 \theta'^2) + \left[M_P (L^2 + r_{Payload}^2 / 2) + M_M r_M^2 / 4 + \rho A L (4L^2 + 3r_T^2) / 12 \right] (\psi' + \theta')^2 \quad (2.90)$$

The potential energy is given by

$$U = -\frac{\mu M_P}{\sqrt{R^2 + L^2 + 2LR \cos \psi}} - \frac{\mu M_P}{\sqrt{R^2 + L^2 - 2LR \cos \psi}} - \frac{\mu M_M}{R} - \mu \rho A \int_{-L}^L (R^2 + l^2 + 2lR \cos \psi)^{-1/2} dl \quad (2.91)$$

and evaluating the integral gives the total potential energy of the system

$$U = -\frac{\mu M_p}{\sqrt{R^2 + L^2 + 2LR \cos \psi}} - \frac{\mu M_p}{\sqrt{R^2 + L^2 - 2LR \cos \psi}} - \frac{\mu M_M}{R} \quad (2.92)$$

$$+ \mu \rho A \ln \left[\frac{R \cos \psi - L + \sqrt{R^2 + L^2 - 2LR \cos \psi}}{R \cos \psi + L + \sqrt{R^2 + L^2 + 2LR \cos \psi}} \right]$$

Substituting (2.69), (2.70), (2.92) and (2.90) into Lagrange's equations gives

$$(M_M r_M^2 / 2 + M_p (2L^2 + r_{\text{payload}}^2) + \rho AL (4L^2 + 3r_T^2) / 6) (\psi'' + \theta'') \quad (2.93)$$

$$+ \frac{\mu \rho A (L \cos \psi + R)}{\sin \psi \sqrt{R^2 + L^2 + 2RL \cos \psi}} + \frac{\mu \rho A (L \cos \psi - R)}{\sin \psi \sqrt{R^2 + L^2 - 2RL \cos \psi}}$$

$$+ \frac{\mu M_p LR \sin \psi}{\sqrt{R^2 + L^2 - 2RL \cos \psi}} - \frac{\mu M_p LR \sin \psi}{\sqrt{R^2 + L^2 + 2RL \cos \psi}} = \tau$$

$$(M_M + 2M_p + 2\rho AL) (R^2 \theta'' + 2RR' \theta') \quad (2.94)$$

$$+ \frac{1}{6} [4L^2 (3M_p + \rho AL) + 3(M_M r_M^2 + 2M_p r_{\text{payload}}^2 + \rho AL r_T^2)] (\theta'' + \psi'') = 0$$

$$(M_M + 2(M_p + \rho AL)) (R'' - \theta'^2 R) + \frac{\mu M_M}{R^2} + \frac{\mu M_p (R + L \cos \psi)}{\sqrt{R^2 + L^2 + 2RL \cos \psi}} \quad (2.95)$$

$$+ \frac{\mu M_p (R - L \cos \psi)}{\sqrt{R^2 + L^2 - 2RL \cos \psi}} + \frac{\mu \rho AL}{R \sqrt{R^2 + L^2 + 2RL \cos \psi}}$$

$$+ \frac{\mu \rho AL}{R \sqrt{R^2 + L^2 - 2RL \cos \psi}} = 0$$

Note that (2.92) and (2.93) have a singularity at $\psi = \pi$, which means for the case of a spinning motorised tether problems will be encountered when numerically integrating (2.93)-(2.95). To avoid this an alternative description of the potential energy is derived, which discretises the tether mass into point masses, as follows

$$U = -\frac{\mu M_p}{\sqrt{R^2 + L^2 + 2LR \cos \psi}} - \frac{\mu M_p}{\sqrt{R^2 + L^2 - 2LR \cos \psi}} - \frac{\mu M_M}{R} \quad (2.96)$$

$$- \sum_{i=1}^N \frac{\mu \rho AL}{N \sqrt{R^2 + \left[\frac{(2i-1)L}{2N} \right]^2 + \frac{2(2i-1)RL}{2N} \cos \psi}}$$

$$- \sum_{i=1}^N \frac{\mu \rho AL}{N \sqrt{R^2 + \left[\frac{(2i-1)L}{2N} \right]^2 - \frac{2(2i-1)RL}{2N} \cos \psi}}$$

where N is the number of discretised masses considered.

When $N = 1$ the equation of motion governing the full planar motorised tether becomes

$$(M_M r_M^2/2 + M_P(2L^2 + r_{\text{payload}}^2) + \rho AL(4L^2 + 3r_T^2))/6(\psi'' + \theta'') \quad (2.97)$$

$$-\frac{\mu \rho AL^2 R \sin \psi}{2\sqrt{R^2 + L^2/4 + RL \cos \psi}} + \frac{\mu \rho AL^2 R \sin \psi}{2\sqrt{R^2 + L^2/4 - RL \cos \psi}} + \frac{\mu M_P LR \sin \psi}{\sqrt{R^2 + L^2 - 2RL \cos \psi}} - \frac{\mu M_P LR \sin \psi}{\sqrt{R^2 + L^2 + 2RL \cos \psi}} = \tau$$

$$(M_M + 2M_P + 2\rho AL)(R^2 \theta'' + 2RR' \theta') \quad (2.98)$$

$$+ \frac{1}{6} [4L^2(3M_P + \rho AL) + 3(M_M r_M^2 + 2M_P r_{\text{payload}}^2 + \rho AL r_T^2)](\theta'' + \psi'') = 0$$

$$(M_M + 2(M_P + \rho AL))(R'' - \theta'^2 R) + \frac{\mu M_M}{R^2} + \frac{\mu M_P (R + L \cos \psi)}{\sqrt{R^2 + L^2 + 2RL \cos \psi}} \quad (2.99)$$

$$+ \frac{\mu M_P (R - L \cos \psi)}{\sqrt{R^2 + L^2 - 2RL \cos \psi}} + \frac{\mu \rho AL(2R + L \cos \psi)}{2\sqrt{R^2 + L^2/4 + RL \cos \psi}} + \frac{\mu \rho AL(2R - L \cos \psi)}{2\sqrt{R^2 + L^2/4 - RL \cos \psi}} = 0$$

Expanding the number of terms included in the tether's potential energy symbolically is easily implemented in *Mathematica*. Figure 2.9 evaluates how many discrete masses are needed to approximate the tether's potential energy satisfactorily and, as is seen, a minimum of 15 masses is required for a 100 km long tether. Moreover, when the tether's potential energy is differentiated with respect to ψ then the convergence, presented in Figure 2.10, is a little slower, requiring at least 20 masses to adequately approximate the full tether. The number of discrete masses required in Figure 2.9 and Figure 2.10 is observed to be insensitive to the angular displacement and tether length.

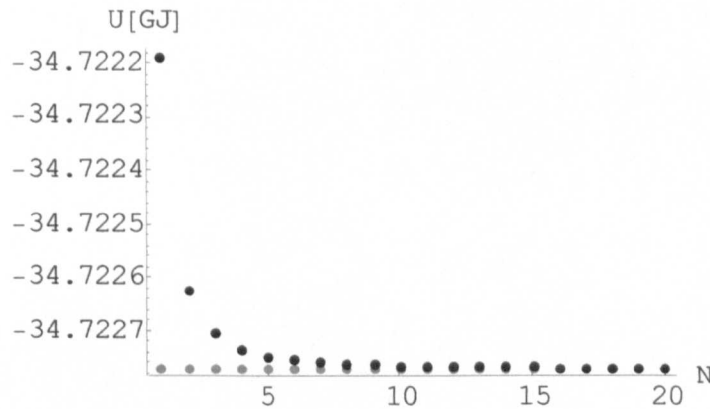


Figure 2.9 Comparison between the discrete (black) and full (grey) tether's potential energy for $\psi = 0.1$ and $L = 100$ km.

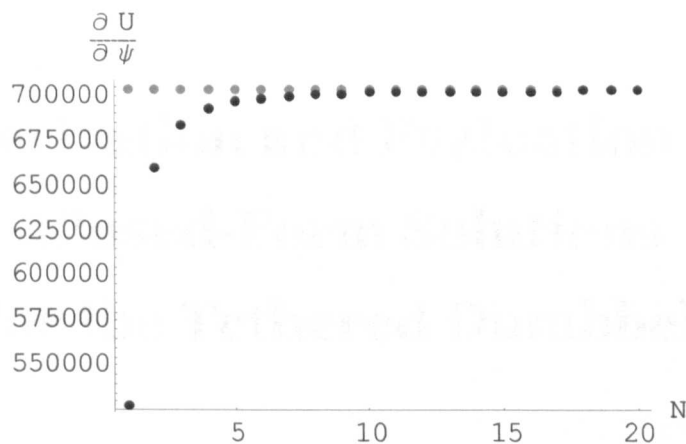


Figure 2.10 Comparison between the discrete (black) and full (grey) tether's potential energy differentiated with respect to ψ for $\psi = 0.1$ and $L = 100$ km.

2.5 Conclusions

The equations of motion governing a rigid massless tethered dumbbell and a rigid symmetrical motorised tether have been derived. Constraining the tether's motion to a Keplerian orbit reduces and considerably simplifies the three dimensional equations of motion from four to two ordinary differential equations, thus making them more expedient to integrate numerically. The presented results indicate that the simplified equations appear to be valid approximations as the qualitative behaviour is wholly captured, but small quantitative discrepancies exist, which need to be taken into account when considering payload orbital transfer with tethers, for example. If the discrete formulation of the spinning motorised tether is employed, then a minimum number of point masses must be included.

Chapter 3

Derivation and Evaluation of Closed-Form Solutions for the Tethered Dumbbell

3.0 Introduction

In this chapter an approximate closed form solution is sought to the equations of motion governing a tethered dumbbell. The method of multiple scales has proved to be a very successful and powerful perturbation technique employed in many fields within mechanical engineering. Nayfeh (2000) gives an excellent introduction to the technique and presents numerous examples of the implementation and use of the multiple scales method. In addition to Nayfeh (2000), the treatment by Thomsen (1997) is very readable and easily understood. The method of multiple scales is employed in this chapter to obtain an approximate closed-form solution to the dumbbell's equations of motion, which are subsequently evaluated to assess the validity of the obtained equations.

3.1 2nd Order Method of Multiple Scales Analysis of the Tethered Dumbbell on an Elliptical Orbit

A 2nd order approximate solution of (2.33)-(2.34) is sought that is uniformly valid near $\psi = \alpha = 0$ and that accounts for nonlinear effects. To achieve this the trigonometric functions present in (2.33)-(2.34) are expanded using Taylor series and the first terms are retained. Consequently, (2.33)-(2.34) become

$$(1 + \varepsilon \bar{e} \cos \theta) \ddot{\psi} - 2(1 + \varepsilon \bar{e} \cos \theta) \alpha \dot{\alpha} - 2\varepsilon \bar{e} \sin \theta \dot{\psi} + \omega_{\psi}^2 \psi = 2\varepsilon \bar{e} \sin \theta \quad (3.1)$$

$$(1 + \varepsilon \bar{e} \cos \theta) \ddot{\alpha} + 2(1 + \varepsilon \bar{e} \cos \theta) \alpha \dot{\psi} - 2\varepsilon \bar{e} \sin \theta \dot{\alpha} + \varepsilon \bar{e} \cos \theta \alpha + \omega_{\alpha}^2 \alpha = 0 \quad (3.2)$$

where the natural frequency terms equal

$$\omega_{\psi} = \sqrt{3}, \quad \omega_{\alpha} = 2 \quad (3.3) \quad (3.4)$$

The necessary assumption is made that the orbit eccentricity is close to zero, representing therefore a nearly circular orbit. To denote the smallness of the orbit eccentricity, e , in (3.1) and (3.2) has been replaced with

$$e = \varepsilon \bar{e} \quad (3.5)$$

where the small parameter ε , $\varepsilon \ll 1$, is introduced to indicate the weak orbit eccentricity and serves merely as a book-keeping device. Following the method of multiple scales, the solution of (3.1) and (3.2) is approximated by uniformly valid expansions of the form

$$\psi(\theta, \varepsilon) = \varepsilon \psi_1(T_0, T_1) + \varepsilon^2 \psi_2(T_0, T_1) + O(\varepsilon^3) \quad (3.6)$$

$$\alpha(\theta, \varepsilon) = \varepsilon \alpha_1(T_0, T_1) + \varepsilon^2 \alpha_2(T_0, T_1) + O(\varepsilon^3) \quad (3.7)$$

where ψ_1 , ψ_2 , α_1 and α_2 are functions to be determined. Note that the zeroth order terms, ψ_0 and α_0 in this specific case, have to be assumed to be negligible to ensure that the lowest order perturbation equation yields a closed form solution. Without this assumption the method of multiple scales will not yield a solution to the given problem. The uniformly valid expansions are subject to independent time-scales where T_0 is the fast time and T_1 the slow time, such that

$$T_0 = \theta, \quad T_1 = \varepsilon \theta \quad (3.8) \quad (3.9)$$

Upon substituting (3.6) and (3.7) into (3.1) and (3.2) the derivatives with respect to θ are required which become partial derivatives with respect to the independent time scales, according to

$$\frac{d}{d\theta} = \frac{dT_0}{d\theta} \frac{\partial}{\partial T_0} + \frac{dT_1}{d\theta} \frac{\partial}{\partial T_1} = \frac{\partial}{\partial T_0} + \varepsilon \frac{\partial}{\partial T_1} = D_0 + \varepsilon D_1 \quad (3.10)$$

$$\frac{d^2}{d\theta^2} = \frac{\partial(D_0 + \varepsilon D_1)}{\partial T_0} + \varepsilon \frac{\partial(D_0 + \varepsilon D_1)}{\partial T_1} = D_0^2 + 2\varepsilon D_0 D_1 + \varepsilon^2 D_1^2 \quad (3.11)$$

where the partial differential operator has been defined through

$$D_i^j \equiv \frac{\partial^j}{\partial T_i^j} \quad (3.12)$$

Substituting (3.6), (3.7), (3.10) and (3.11) into (3.1) and (3.2), and equating to zero the coefficients to like powers of ε yields, to order ε^1 :

$$D_0^2 \psi_1 + \omega_\psi^2 \psi_1 = 0 \quad D_0^2 \alpha_1 + \omega_\alpha^2 \alpha_1 = 0 \quad (3.13) \quad (3.14)$$

and to order ε^2 :

$$D_0^2 \psi_2 + \omega_\psi^2 \psi_2 = 2\bar{e} \sin T_0 D_0 \psi_1 + 2\bar{e} \sin T_0 - \bar{e} \cos T_0 D_0^2 \psi_1 + 2\alpha_1 D_0 \alpha_1 - 2D_0 D_1 \psi_1 \quad (3.15)$$

$$D_0^2 \alpha_2 + \omega_\alpha^2 \alpha_2 = 2\bar{e} \sin T_0 D_0 \alpha_1 - \bar{e} \cos T_0 \alpha_1 - \bar{e} \cos T_0 D_0^2 \alpha_1 - 2\alpha_1 D_0 \psi_1 - 2D_0 D_1 \alpha_1 \quad (3.16)$$

The solutions to the undamped and unforced linear oscillators in (3.13) and (3.14) can be written in the complex exponential form

$$\psi_1 = A(T_1) e^{i\omega_\psi T_0} + \bar{A}(T_1) e^{-i\omega_\psi T_0} \quad \alpha_1 = B(T_1) e^{i\omega_\alpha T_0} + \bar{B}(T_1) e^{-i\omega_\alpha T_0} \quad (3.17) \quad (3.18)$$

where A and B are unknown complex-valued functions of the slow scale T_1 , and \bar{A} and \bar{B} are the respective complex conjugates. Substituting (3.17) and (3.18) into (3.15) and (3.16) gives

$$D_0^2 \psi_2 + \omega_\psi^2 \psi_2 = 2i\omega_\alpha B^2 e^{i2\omega_\alpha T_0} - 2i\omega_\psi D_1 A e^{i\omega_\psi T_0} - i\bar{e} e^{iT_0} + \frac{1}{2} \bar{e} \omega_\psi (\omega_\psi - 2) A e^{i(\omega_\psi - 1)T_0} + \frac{1}{2} \bar{e} \omega_\psi (\omega_\psi + 2) A e^{i(\omega_\psi + 1)T_0} + cc \quad (3.19)$$

$$D_0^2 \alpha_2 + \omega_\alpha^2 \alpha_2 = -2i\omega_\alpha D_1 B e^{i\omega_\alpha T_0} - 2i\omega_\psi A B e^{i(\omega_\alpha + \omega_\psi)T_0} + 2i\omega_\psi \bar{A} B e^{i(\omega_\alpha - \omega_\psi)T_0} + \frac{1}{2} \bar{e} (\omega_\alpha^2 + 2\omega_\alpha - 1) B e^{i(\omega_\alpha + 1)T_0} + \frac{1}{2} \bar{e} (\omega_\alpha^2 - 2\omega_\alpha - 1) B e^{i(\omega_\alpha - 1)T_0} + cc \quad (3.20)$$

where cc denotes the complex conjugates of the preceding terms. The term containing $e^{i\omega_\psi T_0}$ in (3.19) and the term containing $e^{i\omega_\alpha T_0}$ in (3.20), known as secular terms, resonantly excite their respective undamped oscillators at the natural frequency. However, as the ω_ψ and ω_α terms in (3.3) and (3.4) are constant, there are no other resonance conditions possible. Thus, to eliminate secular terms from (3.19) and (3.20), which will otherwise grow unbounded with time and thus violate the assumption of the uniformly valid expansion, the following conditions must hold

$$-2i\omega_\psi D_1 A = 0 \quad -2i\omega_\alpha D_1 B = 0 \quad (3.21) \quad (3.22)$$

which are commonly termed the solvability conditions for the multiple scales analysis. With the solvability conditions fulfilled, (3.19) and (3.20) constitute linear oscillators with multiple harmonic forcing terms. Inserting the assumed form of

$$\psi_2 = C(T_1) e^{i2\omega_\alpha T_0} + E(T_1) e^{iT_0} + F(T_1) e^{i(\omega_\psi - 1)T_0} + G(T_1) e^{i(\omega_\psi + 1)T_0} \quad (3.23)$$

$$\alpha_2 = H(T_1) e^{i(\omega_\alpha + \omega_\psi)T_0} + I(T_1) e^{i(\omega_\alpha - \omega_\psi)T_0} + J(T_1) e^{i(\omega_\alpha + 1)T_0} + K(T_1) e^{i(\omega_\alpha - 1)T_0} \quad (3.24)$$

into (3.19) and (3.20), the coefficients are found to be

$$C(T_1) = \frac{2i\omega_\alpha B^2}{\omega_\psi^2 - 4\omega_\alpha^2}, \quad E(T_1) = \frac{-i\bar{e}}{\omega_\psi^2 - 1} \quad (3.25) \quad (3.26)$$

$$F(T_1) = \frac{\bar{e} \omega_\psi (\omega_\psi - 2) A}{2(2\omega_\psi - 1)}, \quad G(T_1) = \frac{\bar{e} \omega_\psi (\omega_\psi + 2) A}{2(2\omega_\psi + 1)} \quad (3.27) \quad (3.28)$$

$$H(T_1) = \frac{2iAB}{2\omega_\alpha + \omega_\psi}, \quad I(T_1) = \frac{2i\bar{A}B}{2\omega_\alpha - \omega_\psi} \quad (3.29) \quad (3.30)$$

$$J(T_1) = -\frac{\bar{e}(\omega_\alpha^2 + 2\omega_\alpha - 1)B}{2(2\omega_\alpha + 1)}, \quad K(T_1) = \frac{\bar{e}(\omega_\alpha^2 - 2\omega_\alpha - 1)B}{2(2\omega_\alpha - 1)} \quad (3.31) \quad (3.32)$$

Hence, the particular solution is

$$\psi_2 = \frac{2i\omega_\alpha B^2}{\omega_\psi^2 - 4\omega_\alpha^2} e^{i2\omega_\alpha T_0} - \frac{i\bar{e}}{\omega_\psi^2 - 1} e^{iT_0} + \frac{\bar{e}\omega_\psi(\omega_\psi - 2)A}{2(2\omega_\psi - 1)} e^{i(\omega_\psi - 1)T_0} \quad (3.33)$$

$$+ \frac{\bar{e}\omega_\psi(\omega_\psi + 2)A}{2(2\omega_\psi + 1)} e^{i(\omega_\psi + 1)T_0} + cc$$

$$\alpha_2 = \frac{2iAB}{2\omega_\alpha + \omega_\psi} e^{i(\omega_\alpha + \omega_\psi)T_0} + \frac{2i\bar{A}B}{2\omega_\alpha - \omega_\psi} e^{i(\omega_\alpha - \omega_\psi)T_0} - \frac{\bar{e}(\omega_\alpha^2 + 2\omega_\alpha - 1)B}{2(2\omega_\alpha + 1)} e^{i(\omega_\alpha + 1)T_0} \quad (3.34)$$

$$+ \frac{\bar{e}(\omega_\alpha^2 - 2\omega_\alpha - 1)B}{2(2\omega_\alpha - 1)} e^{i(\omega_\alpha - 1)T_0} + cc$$

The A and B functions expressed in polar notation, are

$$A = \frac{1}{2} a e^{i\varphi_1}, \quad B = \frac{1}{2} b e^{i\varphi_2} \quad (3.35) \quad (3.36)$$

where a , b , φ_1 , φ_2 are real valued functions of T_1 . Substituting (3.35) and (3.36) into the solvability conditions of (3.21) and (3.22) yields upon separating the real components

$$\omega_\psi a D_1 \varphi_1 = 0, \quad \omega_\alpha b D_1 \varphi_2 = 0 \quad (3.37) \quad (3.38)$$

and imaginary parts

$$-\omega_\alpha D_1 a = 0, \quad -\omega_\alpha D_1 b = 0 \quad (3.39) \quad (3.40)$$

which are first order, ordinary differential equations and are readily solved to find

$$a = a_1, \quad b = a_2 \quad (3.41) \quad (3.42)$$

$$\varphi_1 = \phi_1, \quad \varphi_2 = \phi_2 \quad (3.43) \quad (3.44)$$

with a_1 , a_2 , ϕ_1 , ϕ_2 being arbitrary constants of integration. The second order approximate solution for the tether's three dimensional motion on an elliptical orbit can be assembled by substituting (3.17), (3.33), (3.35), (3.36) and (3.41)-(3.44) into (3.6)

$$\psi(T_0, \varepsilon) = \varepsilon \frac{1}{2} a_1 e^{i(\phi_1 + \omega_\psi T_0)} + \frac{1}{2} \frac{\varepsilon^2 i \omega_\alpha a_2^2}{\omega_\psi^2 - 4\omega_\alpha^2} e^{i(2\phi_2 + 2\omega_\alpha T_0)} - \frac{\varepsilon^2 i \bar{e}}{\omega_\psi^2 - 1} e^{iT_0} \quad (3.45)$$

$$+ \frac{1}{2} \frac{\varepsilon^2 \bar{e} \omega_\psi (\omega_\psi - 2) a_1}{2(2\omega_\psi - 1)} e^{i(\phi_1 + (\omega_\psi - 1)T_0)}$$

$$+ \frac{1}{2} \frac{\varepsilon^2 \bar{e} \omega_\psi (\omega_\psi + 2) a_1}{2(2\omega_\psi + 1)} e^{i(\phi_1 + (\omega_\psi + 1)T_0)} + cc + O(\varepsilon^3)$$

and substituting (3.18), (3.34), (3.35), (3.36) and (3.41)-(3.44) into (3.7)

$$\alpha(T_0, \varepsilon) = \varepsilon \frac{1}{2} a_2 e^{i(\phi_2 + \omega_\alpha T_0)} + \frac{1}{2} \frac{\varepsilon^2 i a_1 a_2}{2\omega_\alpha + \omega_\psi} e^{i(\phi_1 + \phi_2 + (\omega_\alpha + \omega_\psi)T_0)} \quad (3.46)$$

$$+ \frac{1}{2} \frac{\varepsilon^2 i a_1 a_2}{2\omega_\alpha - \omega_\psi} e^{i(\phi_2 - \phi_1 + (\omega_\alpha - \omega_\psi)T_0)} - \frac{1}{2} \frac{\varepsilon^2 \bar{e} (\omega_\alpha^2 + 2\omega_\alpha - 1) a_2}{2(2\omega_\alpha + 1)} e^{i(\phi_2 + (\omega_\alpha + 1)T_0)}$$

$$+ \frac{1}{2} \frac{\varepsilon^2 \bar{e} (\omega_\alpha^2 - 2\omega_\alpha - 1) a_2}{2(2\omega_\alpha - 1)} e^{i(\phi_2 + (\omega_\alpha - 1)T_0)} + cc + O(\varepsilon^3)$$

Finally, substituting (3.8) into (3.45) and (3.46) and converting the complex exponentials back into trigonometric functions, yields

$$\begin{aligned} \psi(\theta, \varepsilon) = & \varepsilon a_1 \cos(\phi_1 + \omega_\psi \theta) + \frac{\varepsilon^2 \omega_\alpha a_2^2}{\omega_\psi^2 - 4\omega_\alpha^2} \sin(2\phi_2 + 2\omega_\alpha \theta) + \frac{\varepsilon^2 2\bar{e}}{\omega_\psi^2 - 1} \sin \theta \\ & + \frac{\varepsilon^2 \bar{e} \omega_\psi (\omega_\psi - 2) a_1}{2(2\omega_\psi - 1)} \cos(\phi_1 + (\omega_\psi - 1)\theta) \\ & + \frac{\varepsilon^2 \bar{e} \omega_\psi (\omega_\psi + 2) a_1}{2(2\omega_\psi + 1)} \cos(\phi_1 + (\omega_\psi + 1)\theta) + O(\varepsilon^3) \end{aligned} \quad (3.47)$$

$$\begin{aligned} \alpha(\theta, \varepsilon) = & \varepsilon a_2 \cos(\phi_2 + \omega_\alpha \theta) + \frac{\varepsilon^2 a_1 a_2}{2\omega_\alpha + \omega_\psi} \sin(\phi_1 + \phi_2 + (\omega_\alpha + \omega_\psi)\theta) \\ & + \frac{\varepsilon^2 a_1 a_2}{2\omega_\alpha - \omega_\psi} \sin(\phi_2 - \phi_1 + (\omega_\alpha - \omega_\psi)\theta) \\ & - \frac{\varepsilon^2 \bar{e} (\omega_\alpha^2 + 2\omega_\alpha - 1) a_2}{2(2\omega_\alpha + 1)} \cos(\phi_2 + (\omega_\alpha + 1)\theta) \\ & + \frac{\varepsilon^2 \bar{e} (\omega_\alpha^2 - 2\omega_\alpha - 1) a_2}{2(2\omega_\alpha - 1)} \cos(\phi_2 + (\omega_\alpha - 1)\theta) + O(\varepsilon^3) \end{aligned} \quad (3.48)$$

where a_1, a_2, ϕ_1, ϕ_2 are determined by the initial conditions and ε now serves to indicate the assumed magnitude of the terms. The presented solutions were derived by hand but were also obtained with a *Mathematica* solver developed by Khanin *et al.* (2000) who automated the method of multiple scales. Both methods yielded identical solutions.

The closed-form solution given in (3.47) and (3.48) shows that the motion of a tether on a circular orbit will remain planar if there is no initial out-of-plane displacement or velocity. This is due to the nature of the coupling between the in and out-of-plane angles, which only exists when an out-of-plane displacement is present. Furthermore, a tether that is aligned along the gravity vector on a circular orbit will remain radial because all the terms in (3.47) and (3.48) evaluate to zero due to $e = 0$. However, the presence of the particular solution in (3.47), where the amplitude of oscillation is governed by the orbit eccentricity alone, implies that the tether cannot remain radial on an elliptical orbit and will, therefore, always be in motion. In the elliptical orbit case the qualitative interaction between the in and out-of-plane angles is identical to the circular case as the coupling terms are independent of the orbit eccentricity. Thus, out-of-plane motion on an elliptical orbit is only possible with an initial out-of-plane displacement or velocity. If the amplitudes of the in and out-of-plane angles are very small on a circular orbit, such that the terms to first order are only taken into account, then the tether's in and out-of-plane motions are uncoupled and librate at frequency of $\sqrt{3}$ and 2 times the orbital frequency, respectively. This is a well-known property of the

linearised tethered dumbbell, which Arnold (1987) derived by simpler means. Equation (3.47) suggests that the frequency spectrum associated with the motion of the in-plane angle on an elliptical orbit consists of the frequency of planar libration in a circular orbit, the orbital frequency, twice the frequency of the out-of-plane libration in a circular orbit, and modulation frequencies composed of the sum and difference between the frequency of planar libration in a circular orbit and the orbital frequency. The frequency spectrum associated with the motion in the out-of-plane angle on an elliptical orbit, according to (3.48), comprises the frequency of out-of-plane libration on a circular orbit, the sum and difference between the frequency of out-of-plane libration on a circular orbit and the orbital frequency, and finally the sum and difference between the in and out-of-plane libration frequency on a circular orbit.

3.2 Alternative Closed-Form Solutions for the Planar Tethered Dumbbell on Elliptical Orbits

The approximate solutions obtained in (3.47) and (3.48) are not the first attempt to derive closed-form solutions for the tethered dumbbell on an elliptical orbit. Modi and Brereton (1966) derived a closed form solution to (2.33) with $\alpha = 0$ using an approximation to the Wentzel-Kramers-Brillouin-Jeffreys (WKBJ) method. Their solution is only valid for the planar case and is stated in the following form

$$\psi(\theta) = A_1\psi_1 + A_2\psi_2 + \psi_3 \quad (3.49)$$

where

$$\psi_1 = \cos\sqrt{3}\theta - e\frac{5+2\sqrt{3}}{12}\cos(\sqrt{3}+1)\theta + e\frac{2\sqrt{3}-5}{12}\cos(\sqrt{3}-1)\theta \quad (3.50)$$

$$\psi_2 = \sin\sqrt{3}\theta - e\frac{5+2\sqrt{3}}{12}\sin(\sqrt{3}+1)\theta + e\frac{2\sqrt{3}-5}{12}\sin(\sqrt{3}-1)\theta \quad (3.51)$$

$$\psi_3 = e\sin\theta - \frac{e\sin\sqrt{3}\theta}{\sqrt{3}} \quad (3.52)$$

The constants A_1 and A_2 are determined by the initial conditions.

Combining the use of variation of parameters and a perturbation method with the expansion in terms of the orbit eccentricity, Anand *et al.* (1971) derived a closed form solution to (2.33) with $\alpha = 0$, again only valid for the planar case, which is given as

$$\psi(\theta) = A_0\cos(\sqrt{3}\theta - \phi) + eA_1 + e^2A_2 + \dots \quad (3.53)$$

where

$$\phi = \phi_0 - \frac{6\sqrt{3}e^2}{44}\theta \quad (3.54)$$

$$A_1 = \sin \theta + \frac{\sqrt{3}A_0}{2} [(\sqrt{3}-2)B_1^- - (\sqrt{3}+2)B_1^+] \quad (3.55)$$

$$A_2 = -\frac{3}{2} \sin(2\theta) + \frac{\sqrt{3}A_0}{16} [(\sqrt{3}-2)(\sqrt{3}-3)B_2^- + (\sqrt{3}+2)(\sqrt{3}+3)B_2^+] \quad (3.56)$$

and

$$B_j^\pm = \frac{\cos((\sqrt{3} \pm j)\theta - \phi)}{2\sqrt{3} \pm 1} \quad (3.57)$$

The constants A_0 and ϕ_0 are determined by the initial conditions.

Apart from a single trigonometric term in (3.56), describing a frequency component at twice the orbital frequency, there is no difference between the qualitative frequency spectrum predicted by the closed-form solutions when comparing the solutions obtained with the method of multiple scales to those obtained by Modi and Brereton (1966) and Anand *et al.* (1971). This suggests the multiple scales method is generating an approximate solution that is capturing the same part of the tether's motion as the previously published solutions. However, (3.47) and (3.48) have an important advantage over the solutions given by Modi and Brereton (1966) and Anand *et al.* (1971) in that they are more elegant and considerably more compact. The planar case in (3.47) constitutes only four terms in comparison to the eight terms in (3.49) and the seven terms in (3.53). Moreover, the presented analysis has extended previous work to also include the tether's out-of-plane motion.

3.3 3rd Order Method of Multiple Scales Analysis of the Tethered Dumbbell on a Circular Orbit

A third order approximate solution to (2.40)-(2.41) is sought that is uniformly valid near $\psi = \alpha = 0$ and that accounts for nonlinear effects. To this end the trigonometric functions are expanded using Taylor Series and the first two terms are retained. Consequently, (2.40)-(2.41) become

$$\ddot{\psi} - 2\alpha\dot{\alpha} - 2\alpha\dot{\alpha}\dot{\psi} + \xi_1\alpha^2\dot{\psi} + \xi_2\psi^3 + \omega_\psi^2\psi = 0 \quad (3.58)$$

$$\ddot{\alpha} + 2\alpha\dot{\psi} + \alpha\dot{\psi}^2 + \xi_3\alpha\dot{\psi}^2 + \xi_4\alpha^3 + \omega_\alpha^2\alpha = 0 \quad (3.59)$$

where

$$\omega_\psi^2 = \frac{3(r_C - 2(L_1 + L_2))}{r_C}, \quad \omega_\alpha^2 = \frac{2(2r_C - 3(L_1 - L_2))}{r_C} \quad (3.60) \quad (3.61)$$

$$\xi_1 = \frac{9(L_1 + L_2)}{2r_C}, \quad \xi_2 = \frac{17(L_1 + L_2) - 4r_C}{2r_C} \quad (3.62) \quad (3.63)$$

$$\xi_3 = \frac{3(7(L_1 - L_2) - 2r_C)}{2r_C}, \quad \xi_4 = \frac{51(L_2 - L_1) - 16r_C}{6r_C} \quad (3.64) \quad (3.65)$$

Following the method of multiple scales the solution of (3.58) and (3.59) are approximated by uniformly valid expansions

$$\psi(\theta, \varepsilon) = \varepsilon\psi_1(T_0, T_1, T_2) + \varepsilon^2\psi_2(T_0, T_1, T_2) + \varepsilon^3\psi_3(T_0, T_1, T_2) + O(\varepsilon^4) \quad (3.66)$$

$$\alpha(\theta, \varepsilon) = \varepsilon\alpha_1(T_0, T_1, T_2) + \varepsilon^2\alpha_2(T_0, T_1, T_2) + \varepsilon^3\alpha_3(T_0, T_1, T_2) + O(\varepsilon^4) \quad (3.67)$$

where ψ_1 , ψ_2 , ψ_3 , α_1 , α_2 and α_3 are functions to be determined. As before, the zeroth order terms, ψ_0 and α_0 in this specific case, have to be assumed to be negligible to ensure that the lowest order perturbation equation yields a closed form solution. Without this assumption the method of multiple scales will not yield a solution to the given problem. The uniformly valid expansions are subject to independent time-scales where T_0 is a fast time, T_1 equals a medium time scale and T_2 represents a slow time scale, such that

$$T_0 = \theta, \quad T_1 = \varepsilon\theta, \quad T_2 = \varepsilon^2\theta \quad (3.68) \quad (3.69) \quad (3.70)$$

Upon substituting (3.66) and (3.67) into (3.58) and (3.59) the derivatives with respect to θ are required, which become partial derivatives with respect to the independent time scales, according to

$$\frac{d}{d\theta} = \frac{dT_0}{d\theta} \frac{\partial}{\partial T_0} + \frac{dT_1}{d\theta} \frac{\partial}{\partial T_1} + \frac{dT_2}{d\theta} \frac{\partial}{\partial T_2} = \frac{\partial}{\partial T_0} + \varepsilon \frac{\partial}{\partial T_1} + \varepsilon^2 \frac{\partial}{\partial T_2} = D_0 + \varepsilon D_1 + \varepsilon^2 D_2 \quad (3.71)$$

$$\begin{aligned} \frac{d^2}{d\theta^2} &= \frac{\partial(D_0 + \varepsilon D_1 + \varepsilon^2 D_2)}{\partial T_0} + \varepsilon \frac{\partial(D_0 + \varepsilon D_1 + \varepsilon^2 D_2)}{\partial T_1} + \varepsilon^2 \frac{\partial(D_0 + \varepsilon D_1 + \varepsilon^2 D_2)}{\partial T_2} \\ &= D_0^2 + 2\varepsilon D_0 D_1 + 2\varepsilon^2 D_0 D_2 + \varepsilon^2 D_1^2 + 2\varepsilon^3 D_1 D_2 + \varepsilon^4 D_2^2 \end{aligned} \quad (3.72)$$

Substituting (3.66), (3.67), (3.71) and (3.72) into (3.58) and (3.59), and equating to zero the coefficients to like powers of ε yields, to order ε^1 :

$$D_0^2 \psi_1 + \omega_\psi^2 \psi_1 = 0 \quad D_0^2 \alpha_1 + \omega_\alpha^2 \alpha_1 = 0 \quad (3.73) \quad (3.74)$$

to order ε^2 :

$$D_0^2 \psi_2 + \omega_\psi^2 \psi_2 = 2\alpha_1 D_0 \alpha_1 - 2D_0 D_1 \psi_1 \quad (3.75)$$

$$D_0^2 \alpha_2 + \omega_\alpha^2 \alpha_2 = -2\alpha_1 D_0 \psi_1 - 2D_0 D_1 \alpha_1 \quad (3.76)$$

and to order ε^3 :

$$\begin{aligned} D_0^2 \psi_3 + \omega_\psi^2 \psi_3 &= 2\alpha_1 D_0 \alpha_1 D_0 \psi_1 + 2\alpha_2 D_0 \alpha_1 + 2\alpha_1 D_0 \alpha_2 + 2\alpha_1 D_1 \alpha_1 - 2D_0 D_1 \psi_2 \\ &\quad - 2D_0 D_2 \psi_1 - D_1^2 \psi_1 - \xi_1 \psi_1 \alpha_1^2 - \xi_2 \psi_1^3 \end{aligned} \quad (3.77)$$

$$\begin{aligned} D_0^2 \alpha_3 + \omega_\alpha^2 \alpha_3 &= -2D_0 D_1 \alpha_2 - 2D_0 D_2 \alpha_1 - D_1^2 \alpha_1 - \xi_3 \alpha_1 \psi_1^2 - \xi_4 \alpha_1^3 - 2\alpha_1 D_0 \psi_2 \\ &\quad - 2\alpha_1 D_1 \psi_1 - 2\alpha_2 D_0 \psi_1 - \alpha_1 (D_0 \psi_1)^2 \end{aligned} \quad (3.78)$$

The solutions to the undamped and unforced linear oscillators in (3.73) and (3.74) can be written in the complex exponential form

$$\psi_1 = A(T_1, T_2)e^{i\omega_\psi T_0} + \bar{A}(T_1, T_2)e^{-i\omega_\psi T_0} \quad (3.79)$$

$$\alpha_1 = B(T_1, T_2)e^{i\omega_\alpha T_0} + \bar{B}(T_1, T_2)e^{-i\omega_\alpha T_0} \quad (3.80)$$

where A and B are unknown complex-valued functions of the slow scales T_1 and T_2 , and \bar{A} and \bar{B} are the respective complex conjugates. Substituting (3.79) and (3.80) into (3.75) and (3.76) gives

$$D_0^2 \psi_2 + \omega_\psi^2 \psi_2 = 2i\omega_\alpha B^2 e^{i2\omega_\alpha T_0} - 2i\omega_\psi D_1 A e^{i\omega_\psi T_0} + cc \quad (3.81)$$

$$D_0^2 \alpha_2 + \omega_\alpha^2 \alpha_2 = 2i\omega_\psi \bar{A} B e^{i(\omega_\alpha - \omega_\psi) T_0} - 2i\omega_\alpha D_1 B e^{i\omega_\alpha T_0} - 2i\omega_\psi A B e^{i(\omega_\alpha + \omega_\psi) T_0} + cc \quad (3.82)$$

where cc denotes the complex conjugates of the preceding terms. The ω_ψ and ω_α terms in (3.60) and (3.61) are, in contrast to the second order treatment, not constant with respect to the orbital radius and tether length and, following from (3.81), could theoretically give rise to the internal resonance condition of

$$2\omega_\alpha = \omega_\psi \quad (3.83)$$

Substituting the square root of (3.60) and (3.61) into (3.83) leads to an expression that determines the length of L_1 required to create the internal resonance,

$$L_1 = \frac{13}{18} r_C + \frac{5}{3} L_2 \quad (3.84)$$

which states that L_1 must be at least 70% of r_C 's length. This not only violates the assumption of $L_1 \ll r_C$ made in the derivation of the equations of motion but is for practical reasons unrealistic. The identified internal resonance condition is, therefore, not of relevance. Thus, to eliminate secular terms from (3.81) and (3.82) the following conditions must hold

$$-2i\omega_\psi D_1 A = 0 \quad -2i\omega_\alpha D_1 B = 0 \quad (3.85) \quad (3.86)$$

which imply that $A = A(T_2)$ and $B = B(T_2)$. With the solvability conditions fulfilled, (3.81) and (3.82) constitute linear oscillators with harmonic forcing terms. Inserting the assumed form of

$$\psi_2 = C(T_1, T_2)e^{i2\omega_\alpha T_0} + cc \quad (3.87)$$

$$\alpha_2 = E(T_1, T_2)e^{i(\omega_\alpha + \omega_\psi) T_0} + F(T_1, T_2)e^{i(\omega_\alpha - \omega_\psi) T_0} + cc \quad (3.88)$$

into (3.81) and (3.82) results in the coefficients being found

$$C(T_1, T_2) = \frac{2i\omega_\alpha B^2}{-4\omega_\alpha^2 + \omega_\psi^2} \quad E(T_1, T_2) = \frac{2iAB}{2\omega_\alpha + \omega_\psi} \quad (3.89) \quad (3.90)$$

$$F(T_1, T_2) = \frac{2i\bar{A}B}{2\omega_\alpha - \omega_\psi} \quad (3.91)$$

Hence, the particular solution for ψ_2 and α_2 are

$$\psi_2 = \frac{2i\omega_\alpha B^2}{-4\omega_\alpha^2 + \omega_\psi^2} e^{i2\omega_\alpha T_0} + cc \quad (3.92)$$

$$\alpha_2 = \frac{2iAB}{2\omega_\alpha + \omega_\psi} e^{i(\omega_\alpha + \omega_\psi)T_0} + \frac{2i\bar{A}B}{2\omega_\alpha - \omega_\psi} e^{i(\omega_\alpha - \omega_\psi)T_0} + cc \quad (3.93)$$

Substituting (3.79), (3.80), (3.92) and (3.93) into (3.77) and (3.78) gives

$$\begin{aligned} D_0^2 \psi_3 + \omega_\psi^2 \psi_3 = & -\xi_2 A^3 e^{i3\omega_\psi T_0} - (4 + \xi_1 - 2\omega_\alpha \omega_\psi) \bar{A} B^2 e^{i(2\omega_\alpha - \omega_\psi)T_0} \\ & - (4 + \xi_1 + 2\omega_\alpha \omega_\psi) A B^2 e^{i(2\omega_\alpha + \omega_\psi)T_0} \\ & - \left[2\xi_1 A \bar{B} \bar{B} + 3\xi_2 A^2 \bar{A} + \frac{16\omega_\psi \omega_\alpha A \bar{B} \bar{B}}{4\omega_\alpha^2 - \omega_\psi^2} + 2i\omega_\psi D_2 A + D_1^2 A \right] e^{i\omega_\psi T_0} \\ & - 2 \frac{4\omega_\alpha^2 + \omega_\psi^2}{4\omega_\alpha^2 - \omega_\psi^2} B D_1 B e^{i2\omega_\alpha T_0} + 2\bar{B} D_1 B + cc \end{aligned} \quad (3.94)$$

$$\begin{aligned} D_0^2 \alpha_3 + \omega_\alpha^2 \alpha_3 = & - (2\xi_3 \omega_\alpha - 4\omega_\psi - \xi_3 \omega_\psi - 2\omega_\alpha \omega_\psi^2 + \omega_\psi^3) \frac{A^2 \bar{B}}{2\omega_\alpha - \omega_\psi} e^{i(2\omega_\psi - \omega_\alpha)T_0} \\ & - (2\xi_3 \omega_\alpha - 4\omega_\psi + \xi_3 \omega_\psi - 2\omega_\alpha \omega_\psi^2 - \omega_\psi^3) \frac{A^2 B}{2\omega_\alpha + \omega_\psi} e^{i(2\omega_\psi + \omega_\alpha)T_0} \\ & + \left[-\xi_4 B^3 + \frac{8B^3 \omega_\alpha^2}{-4\omega_\alpha^2 + \omega_\psi^2} \right] e^{i3\omega_\alpha T_0} \\ & - \frac{2(\omega_\psi B D_1 \bar{A} - 2(\omega_\alpha - \omega_\psi) \bar{A} D_1 B)}{2\omega_\alpha - \omega_\psi} e^{i(\omega_\alpha - \omega_\psi)T_0} \\ & + \frac{2(\omega_\psi B D_1 A + 2(\omega_\psi + \omega_\alpha) A D_1 B)}{2\omega_\alpha + \omega_\psi} e^{i(\omega_\alpha + \omega_\psi)T_0} \\ & + \left[-2\xi_3 A \bar{A} B - 3\xi_4 B^2 \bar{B} + \frac{4\omega_\psi A \bar{A} B}{2\omega_\alpha - \omega_\psi} - \frac{4\omega_\psi A \bar{A} B}{2\omega_\alpha + \omega_\psi} \right. \\ & \left. - 2\omega_\psi^2 A \bar{A} B + \frac{8B^2 \bar{B} \omega_\alpha^2}{-4\omega_\alpha^2 + \omega_\psi^2} - 2i\omega_\alpha D_2 B - D_1^2 B \right] e^{i\omega_\alpha T_0} + cc \end{aligned} \quad (3.95)$$

with $D_1 B = 0$ and $D_1 A = 0$, because A and B are now solely functions of T_2 due to (3.85) and (3.86), the equations (3.94) and (3.95) become

$$\begin{aligned} D_0^2 \psi_3 + \omega_\psi^2 \psi_3 = & -\xi_2 A^3 e^{i3\omega_\psi T_0} - (4 + \xi_1 - 2\omega_\alpha \omega_\psi) \bar{A} B^2 e^{i(2\omega_\alpha - \omega_\psi)T_0} \\ & - (4 + \xi_1 + 2\omega_\alpha \omega_\psi) A B^2 e^{i(2\omega_\alpha + \omega_\psi)T_0} \\ & - \left[2\xi_1 A \bar{B} \bar{B} + 3\xi_2 A^2 \bar{A} + \frac{16\omega_\psi \omega_\alpha A \bar{B} \bar{B}}{4\omega_\alpha^2 - \omega_\psi^2} + 2i\omega_\psi D_2 A \right] e^{i\omega_\psi T_0} + cc \end{aligned} \quad (3.96)$$

$$\begin{aligned}
D_0^2 \alpha_3 + \omega_\alpha^2 \alpha_3 = & - \left(2\xi_3 \omega_\alpha - 4\omega_\psi - \xi_3 \omega_\psi - 2\omega_\alpha \omega_\psi^2 + \omega_\psi^3 \right) \frac{A^2 \bar{B}}{2\omega_\alpha - \omega_\psi} e^{i(2\omega_\psi - \omega_\alpha)T_0} \\
& - \left(2\xi_3 \omega_\alpha - 4\omega_\psi + \xi_3 \omega_\psi - 2\omega_\alpha \omega_\psi^2 - \omega_\psi^3 \right) \frac{A^2 B}{2\omega_\alpha + \omega_\psi} e^{i(2\omega_\psi + \omega_\alpha)T_0} \\
& + \left[-\xi_4 B^3 + \frac{8B^3 \omega_\alpha^2}{-4\omega_\alpha^2 + \omega_\psi^2} \right] e^{i3\omega_\alpha T_0} \\
& + \left[\begin{aligned} & -2\xi_3 A \bar{A} B - 3\xi_4 B^2 \bar{B} + \frac{4\omega_\psi A \bar{A} B}{2\omega_\alpha - \omega_\psi} - \frac{4\omega_\psi A \bar{A} B}{2\omega_\alpha + \omega_\psi} \\ & - 2A \bar{A} B \omega_\psi^2 + \frac{8B^2 \bar{B} \omega_\alpha^2}{-4\omega_\alpha^2 + \omega_\psi^2} - 2i\omega_\alpha D_2 B \end{aligned} \right] e^{i\omega_\alpha T_0} + cc
\end{aligned} \tag{3.97}$$

The secular terms from (3.96) and (3.97) need to be eliminated, such that

$$2\xi_1 A B \bar{B} + 3\xi_2 A^2 \bar{A} + \frac{16\omega_\psi \omega_\alpha A B \bar{B}}{4\omega_\alpha^2 - \omega_\psi^2} + 2i\omega_\psi D_2 A = 0 \tag{3.98}$$

$$\begin{aligned}
-2\xi_3 A \bar{A} B - 3\xi_4 B^2 \bar{B} + \frac{4\omega_\psi A \bar{A} B}{2\omega_\alpha - \omega_\psi} - \frac{4\omega_\psi A \bar{A} B}{2\omega_\alpha + \omega_\psi} - 2A \bar{A} B \omega_\psi^2 \\
+ \frac{8B^2 \bar{B} \omega_\alpha^2}{-4\omega_\alpha^2 + \omega_\psi^2} - 2i\omega_\alpha D_2 B = 0
\end{aligned} \tag{3.99}$$

With the solvability conditions fulfilled, (3.96) and (3.97) constitute linear oscillators with harmonic forcing terms. Inserting the assumed form of the particular solution

$$\psi_3 = G(T_1, T_2) e^{i3\omega_\psi T_0} + H(T_1, T_2) e^{i(2\omega_\alpha - \omega_\psi)T_0} + I(T_1, T_2) e^{i(2\omega_\alpha + \omega_\psi)T_0} + cc \tag{3.100}$$

$$\alpha_3 = J(T_1, T_2) e^{i3\omega_\alpha T_0} + K(T_1, T_2) e^{i(2\omega_\psi - \omega_\alpha)T_0} + M(T_1, T_2) e^{i(2\omega_\psi + \omega_\alpha)T_0} + cc \tag{3.101}$$

into (3.96) and (3.97), where

$$G(T_1, T_2) = \frac{\xi_2 A^3}{8\omega_\psi^2} \quad H(T_1, T_2) = \frac{\bar{A} B^2 (4 + \xi_1 - 2\omega_\psi \omega_\alpha)}{4\omega_\alpha (\omega_\alpha - \omega_\psi)} \tag{3.102} \tag{3.103}$$

$$I(T_1, T_2) = \frac{A B^2 (4 + \xi_1 + 2\omega_\psi \omega_\alpha)}{4\omega_\alpha (\omega_\alpha + \omega_\psi)} \quad J(T_1, T_2) = \frac{\xi_4 B^3}{8\omega_\alpha^2} + \frac{B^3}{4\omega_\alpha^2 - \omega_\psi^2} \tag{3.104} \tag{3.105}$$

$$K(T_1, T_2) = - \left(2\xi_3 \omega_\alpha - 4\omega_\psi - \xi_3 \omega_\psi - 2\omega_\alpha \omega_\psi^2 + \omega_\psi^3 \right) \frac{A^2 \bar{B}}{4\omega_\psi (\omega_\alpha - \omega_\psi) (2\omega_\alpha - \omega_\psi)} \tag{3.106}$$

$$M(T_1, T_2) = \left(2\xi_3 \omega_\alpha - 4\omega_\psi + \xi_3 \omega_\psi - 2\omega_\alpha \omega_\psi^2 - \omega_\psi^3 \right) \frac{A^2 B}{4\omega_\psi (\omega_\alpha + \omega_\psi) (2\omega_\alpha + \omega_\psi)} \tag{3.107}$$

are found, leading to

$$\psi_3 = \frac{\xi_2 A^3}{8\omega_\psi^2} e^{i3\omega_\psi T_0} + \frac{\bar{A}B^2(4 + \xi_1 - 2\omega_\psi\omega_\alpha)}{4\omega_\alpha(\omega_\alpha - \omega_\psi)} e^{i(2\omega_\alpha - \omega_\psi)T_0} \quad (3.108)$$

$$+ \frac{AB^2(4 + \xi_1 + 2\omega_\psi\omega_\alpha)}{4\omega_\alpha(\omega_\alpha + \omega_\psi)} e^{i(2\omega_\alpha + \omega_\psi)T_0} + cc$$

$$\alpha_3 = -\frac{(2\xi_3\omega_\alpha - 4\omega_\psi - \xi_3\omega_\psi - 2\omega_\alpha\omega_\psi^2 + \omega_\psi^3)A^2\bar{B}}{4\omega_\psi(\omega_\alpha - \omega_\psi)(2\omega_\alpha - \omega_\psi)} e^{i(2\omega_\psi - \omega_\alpha)T_0} \quad (3.109)$$

$$+ \frac{(2\xi_3\omega_\alpha - 4\omega_\psi + \xi_3\omega_\psi - 2\omega_\alpha\omega_\psi^2 - \omega_\psi^3)A^2B}{4\omega_\psi(\omega_\alpha + \omega_\psi)(2\omega_\alpha + \omega_\psi)} e^{i(2\omega_\psi + \omega_\alpha)T_0}$$

$$+ \left[\frac{\xi_4 B^3}{8\omega_\alpha^2} + \frac{B^3}{4\omega_\alpha^2 - \omega_\psi^2} \right] e^{i3\omega_\alpha T_0} + cc$$

The A and B functions expressed in polar notation, are

$$A = \frac{1}{2} a e^{i\phi_1}, \quad B = \frac{1}{2} b e^{i\phi_2} \quad (3.110) \quad (3.111)$$

where a, b, ϕ_1, ϕ_2 are real valued functions of T_1 and T_2 . Substituting (3.110) and (3.111) into the solvability conditions of (3.98) and (3.99), yields upon separating the real components

$$D_2\phi_1 = \frac{1}{4\omega_\psi} \xi_1 b^2 + \frac{3}{8\omega_\psi} \xi_2 a^2 + \frac{2\omega_\alpha b^2}{4\omega_\alpha^2 - \omega_\psi^2} \quad (3.112)$$

$$D_2\phi_2 = \frac{1}{4\omega_\alpha} \xi_3 a^2 + \frac{3}{8\omega_\alpha} \xi_4 b^2 - \frac{1}{2\omega_\alpha} \frac{\omega_\psi a^2}{2\omega_\alpha - \omega_\psi} + \frac{1}{2\omega_\alpha} \frac{\omega_\psi a^2}{2\omega_\alpha + \omega_\psi} \quad (3.113)$$

$$+ \frac{1}{4\omega_\alpha} a^2 \omega_\psi^2 + \frac{b^2 \omega_\alpha}{4\omega_\alpha^2 - \omega_\psi^2}$$

and imaginary parts

$$\omega_\psi D_2 a = 0 \quad \omega_\alpha D_2 b = 0 \quad (3.114) \quad (3.115)$$

which are first order, ordinary differential equations and are readily solved to find

$$a = a_1 \quad b = a_2 \quad (3.116) \quad (3.117)$$

$$\phi_1 = \frac{\xi_1 a_2^2 T_2}{4\omega_\psi} + \frac{3\xi_2 a_1^2 T_2}{8\omega_\psi} + \frac{2\omega_\alpha a_1^2 T_2}{4\omega_\alpha^2 - \omega_\psi^2} + \phi_1 \quad (3.118)$$

$$\phi_2 = \frac{\xi_3 a_1^2 T_2}{4\omega_\alpha} + \frac{3\xi_4 a_2^2 T_2}{8\omega_\alpha} - \frac{\omega_\psi^2 a_1^2 T_2}{\omega_\alpha(4\omega_\alpha^2 - \omega_\psi^2)} + \frac{a_1^2 \omega_\psi^2 T_2}{4\omega_\alpha} + \frac{a_2^2 \omega_\alpha T_2}{4\omega_\alpha^2 - \omega_\psi^2} + \phi_2 \quad (3.119)$$

where a_1, a_2, ϕ_1, ϕ_2 are arbitrary constants of integration. The third order approximate solution for the tether's three dimensional motion on a circular orbit can be assembled by substituting (3.79), (3.92), (3.108), (3.110), (3.111), (3.116) and (3.117) into (3.66)

$$\begin{aligned}
\psi(T_0, \varepsilon) = & \frac{1}{2} \varepsilon a_1 e^{i(\varphi_1 + \omega_\psi T_0)} + \frac{1}{2} \varepsilon^2 \frac{i \omega_\alpha a_2^2}{-4\omega_\alpha^2 + \omega_\psi^2} e^{i2(\varphi_2 + \omega_\alpha T_0)} + \frac{\varepsilon^3 \xi_2 a_1^3}{64\omega_\psi^2} e^{i3(\varphi_1 + \omega_\psi T_0)} \quad (3.120) \\
& + \frac{\varepsilon^3 a_1 a_2^2 (4 + \xi_1 - 2\omega_\psi \omega_\alpha)}{32\omega_\alpha (\omega_\alpha - \omega_\psi)} e^{i(-\varphi_1 + 2\varphi_2 + (2\omega_\alpha - \omega_\psi) T_0)} \\
& + \frac{\varepsilon^3 a_1 a_2^2 (4 + \xi_1 + 2\omega_\psi \omega_\alpha)}{32\omega_\alpha (\omega_\alpha + \omega_\psi)} e^{i(\varphi_1 + 2\varphi_2 + (2\omega_\alpha + \omega_\psi) T_0)} + cc + O(\varepsilon^4)
\end{aligned}$$

and substituting (3.80), (3.93), (3.109), (3.110), (3.111), (3.116) and (3.117) into (3.67)

$$\begin{aligned}
\alpha(T_0, \varepsilon) = & \frac{1}{2} \varepsilon a_2 e^{i(\varphi_2 + \omega_\alpha T_0)} + \frac{1}{2} \frac{\varepsilon^2 i a_1 a_2}{2\omega_\alpha + \omega_\psi} e^{i(\varphi_1 + \varphi_2 + (\omega_\alpha + \omega_\psi) T_0)} \quad (3.121) \\
& + \frac{1}{2} \frac{\varepsilon^2 i a_1 a_2}{2\omega_\alpha - \omega_\psi} e^{i(-\varphi_1 + \varphi_2 + (\omega_\alpha - \omega_\psi) T_0)} \\
& - \frac{\varepsilon^3 (2\xi_3 \omega_\alpha - 4\omega_\psi - \xi_3 \omega_\psi - 2\omega_\alpha \omega_\psi^2 + \omega_\psi^3) a_1^2 a_2}{32\omega_\psi (\omega_\alpha - \omega_\psi) (2\omega_\alpha - \omega_\psi)} e^{i(2\varphi_1 - \varphi_2 + (2\omega_\psi - \omega_\alpha) T_0)} \\
& + \frac{\varepsilon^3 (2\xi_3 \omega_\alpha - 4\omega_\psi + \xi_3 \omega_\psi - 2\omega_\alpha \omega_\psi^2 - \omega_\psi^3) a_1^2 a_2}{32\omega_\psi (\omega_\alpha + \omega_\psi) (2\omega_\alpha + \omega_\psi)} e^{i(2\varphi_1 + \varphi_2 + (2\omega_\psi + \omega_\alpha) T_0)} \\
& + \frac{1}{8} \varepsilon^3 \left[\frac{\xi_4 a_2^3}{8\omega_\alpha^2} + \frac{a_2^3}{4\omega_\alpha^2 - \omega_\psi^2} \right] e^{i(3\varphi_2 + 3\omega_\alpha T_0)} + cc + O(\varepsilon^4)
\end{aligned}$$

Finally, substituting (3.68) and (3.70) into (3.120) and (3.121), and converting the complex exponential terms back into trigonometric functions, yields

$$\begin{aligned}
\psi(\theta, \varepsilon) = & \varepsilon a_1 \cos(\varphi_1 + \omega_\psi \theta) + \frac{\varepsilon^2 \omega_\alpha a_2^2}{-4\omega_\alpha^2 + \omega_\psi^2} \sin(2\varphi_2 + 2\omega_\alpha \theta) \quad (3.122) \\
& + \frac{\varepsilon^3 a_1 a_2^2 (4 + \xi_1 - 2\omega_\psi \omega_\alpha)}{16\omega_\alpha (\omega_\alpha - \omega_\psi)} \cos(-\varphi_1 + 2\varphi_2 + (2\omega_\alpha - \omega_\psi) \theta) \\
& + \frac{\varepsilon^3 a_1 a_2^2 (4 + \xi_1 + 2\omega_\psi \omega_\alpha)}{16\omega_\alpha (\omega_\alpha + \omega_\psi)} \cos(\varphi_1 + 2\varphi_2 + (2\omega_\alpha + \omega_\psi) \theta) \\
& + \frac{\varepsilon^3 \xi_2 a_1^3}{32\omega_\psi^2} \cos(3\varphi_1 + 3\omega_\psi \theta) + O(\varepsilon^4)
\end{aligned}$$

$$\begin{aligned}
\alpha(\theta, \varepsilon) = & \varepsilon a_2 \cos(\varphi_2 + \omega_\alpha \theta) + \frac{\varepsilon^2 a_1 a_2}{2\omega_\alpha + \omega_\psi} \sin(\varphi_1 + \varphi_2 + (\omega_\alpha + \omega_\psi)\theta) \\
& + \frac{\varepsilon^2 a_1 a_2}{2\omega_\alpha - \omega_\psi} \sin(-\varphi_1 + \varphi_2 + (\omega_\alpha - \omega_\psi)\theta) \\
& - \frac{\varepsilon^3 a_1^2 a_2 (2\xi_3 \omega_\alpha - 4\omega_\psi - \xi_3 \omega_\psi - 2\omega_\alpha \omega_\psi^2 + \omega_\psi^3)}{16\omega_\psi (\omega_\alpha - \omega_\psi) (2\omega_\alpha - \omega_\psi)} \cos(2\varphi_1 - \varphi_2 + (2\omega_\psi - \omega_\alpha)\theta) \\
& + \frac{\varepsilon^3 a_1^2 a_2 (2\xi_3 \omega_\alpha - 4\omega_\psi + \xi_3 \omega_\psi - 2\omega_\alpha \omega_\psi^2 - \omega_\psi^3)}{16\omega_\psi (\omega_\alpha + \omega_\psi) (2\omega_\alpha + \omega_\psi)} \cos(2\varphi_1 + \varphi_2 + (2\omega_\psi + \omega_\alpha)\theta) \\
& + \frac{1}{4} \varepsilon^3 \left[\frac{\xi_4 a_2^3}{8\omega_\alpha^2} + \frac{a_2^3}{4\omega_\alpha^2 - \omega_\psi^2} \right] \cos(3\varphi_2 + 3\omega_\alpha \theta) + O(\varepsilon^4)
\end{aligned} \tag{3.123}$$

where

$$\varphi_1 = \frac{\xi_1 a_2^2 \varepsilon^2 \theta}{4\omega_\psi} + \frac{3\xi_2 a_1^2 \varepsilon^2 \theta}{8\omega_\psi} + \frac{2\omega_\alpha a_1^2 \varepsilon^2 \theta}{4\omega_\alpha^2 - \omega_\psi^2} + \phi_1 \tag{3.124}$$

$$\varphi_2 = \frac{\xi_3 a_1^2 \varepsilon^2 \theta}{4\omega_\alpha} + \frac{3\xi_4 a_2^2 \varepsilon^2 \theta}{8\omega_\alpha} - \frac{\omega_\psi^2 a_1^2 \varepsilon^2 \theta}{\omega_\alpha (4\omega_\alpha^2 - \omega_\psi^2)} + \frac{a_1^2 \omega_\psi^2 \varepsilon^2 \theta}{4\omega_\alpha} + \frac{a_2^2 \omega_\alpha \varepsilon^2 \theta}{4\omega_\alpha^2 - \omega_\psi^2} + \phi_2 \tag{3.125}$$

The constants a_1 , a_2 , ϕ_1 , ϕ_2 are determined by the initial conditions and ε now merely indicates the assumed magnitude of the terms. The derivation of the 3rd order solutions was carried out by hand but was also obtained with the *Mathematica* solver developed by Khanin *et al.* (2000). Both methods again yielded identical solutions.

3.4 Evaluation and Comparison of the Derived Closed-Form Solutions

The validity and accuracy of the approximate uniformly valid solutions obtained from the multiple scales method to second and third order are evaluated in the following figures below, Figure 3.1 to Figure 3.15, by comparing the output from the closed-form solutions with the results obtained by numerically integrating equations (2.33)-(2.34) and (2.40)-(2.41). The approximate solutions to second and third order in equations (3.47) and (3.48), (3.122) and (3.123) with (3.124) and (3.125) appropriately substituted, were differentiated with respect to the true anomaly to allow the constants of integration at $\theta = 0$ to be determined numerically. The figures from Figure 3.8 to Figure 3.10 also contain the alternative closed-form solutions derived by Modi and Brereton (1966), given in (3.49)-(3.52), and Anand *et al.* (1971), stated in (3.53)-(3.57), which were similarly differentiated and evaluated to obtain the constants of integration at $\theta = 0$. The numerical integration was carried out with a fourth/fifth-order Fehlberg Runge-Kutta method. A typical low Earth orbit radius was selected, where $r_p = 7000$ km, and short tether lengths were used, with $L_1 = L_2 = 500$ m, to ensure the ratio between the tether length and orbital radius is kept well below

unity. In determining the constants of integration the initial velocity in both angles was assumed to be zero. Finally, ε was set to unity as the perturbation parameter now only relates to the assumed magnitude of the terms.

Figure 3.1 gives the in and out-of-plane response on a circular orbit to an initial angular displacement of $\psi = \alpha = 0.05$ rad in both angles and shows that the 2nd and 3rd order solutions completely overlap with the numerical results. Magnifying the results between the 4th and 5th orbit, as shown in Figure 3.2, confirms that the discrepancy between the analytical and numerical results is certainly small. Increasing the initial displacement in Figure 3.3 to $\psi = \alpha = 0.1$ rad, the approximate solutions are slightly out of phase with the numerical response but still manage to capture the motion of the system very well. On closer inspection both the second and third order approximations in Figure 3.4 are found to be equally out of phase with the numerical solution with no advantage to either order of solution. In Figure 3.5 the initial conditions are set to $\psi = \alpha = 0.2$ rad and a large discrepancy between the approximate solutions and the numerical integration has appeared in both the phase and amplitude of the response due to the higher order terms neglected in the expansion. This is seen very clearly in the higher resolution depicted in Figure 3.6. Since at this point the second and third order closed-form solutions fail to capture the system's quantitative response, there is little necessity to evaluate the performance of the approximate solutions to larger initial conditions. Hence, both the second and third order approximate solutions to equations (2.33)-(2.34) and (2.40)-(2.41) are only valid, as demonstrated by the comparisons, when the initial angular displacements in both the in and out-of-plane angles are less than 0.1 rad. Furthermore, the results show that despite the higher order expansion, the third order approximate solution does not significantly capture more of the system's response than the second order solution. In Figure 3.7, the fast Fourier transform of the time history in Figure 3.3 shows that there are really only two frequency components to capture for the in-plane and three for the out-of-plane motion. The second order analysis generated a solution, which already possessed this level of detail and, hence, explains why the third order analysis does not improve on simulating the tether's response.

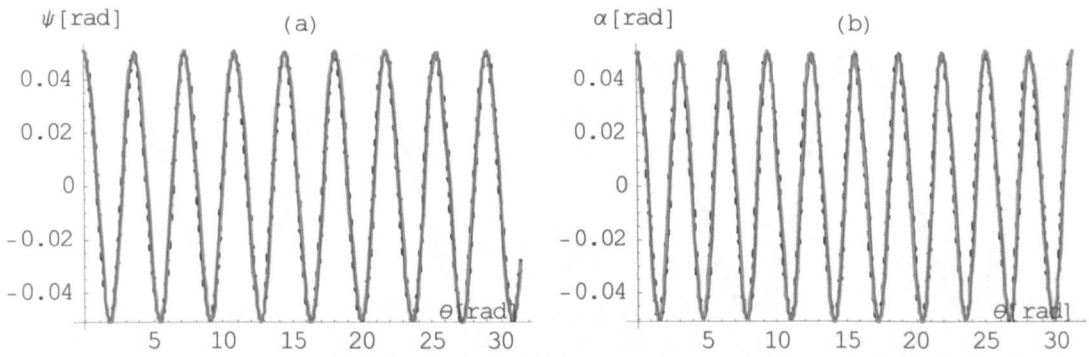


Figure 3.1 In-plane, (a), and out-of-plane, (b), angular response over 5 circular orbits against true anomaly with, $\dot{\psi}(0) = \dot{\alpha}(0) = 0$ and $\psi(0) = \alpha(0) = 0.05$ rad (solid black = numerical, solid grey = 2nd order analysis, dash = 3rd order analysis)

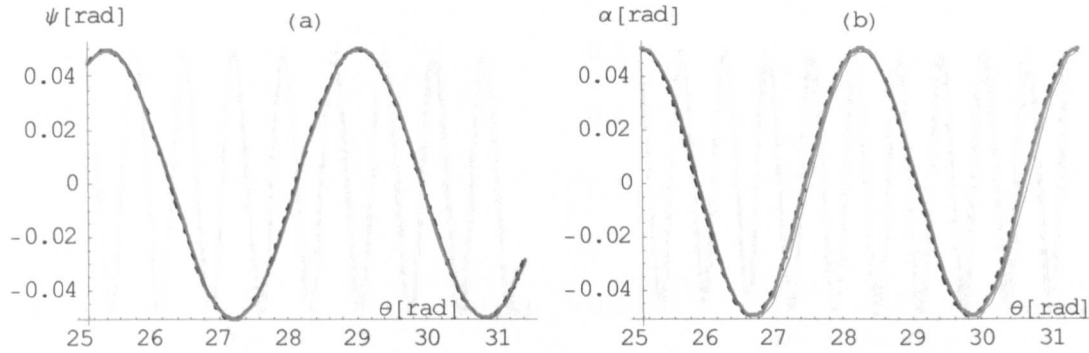


Figure 3.2 In-plane, (a), and out-of-plane, (b), angular response between the 4th and 5th circular orbit against true anomaly with $\dot{\psi}(0) = \dot{\alpha}(0) = 0$ and $\psi(0) = \alpha(0) = 0.05$ rad (solid black = numerical, solid grey = 2nd order analysis, dash = 3rd order analysis)

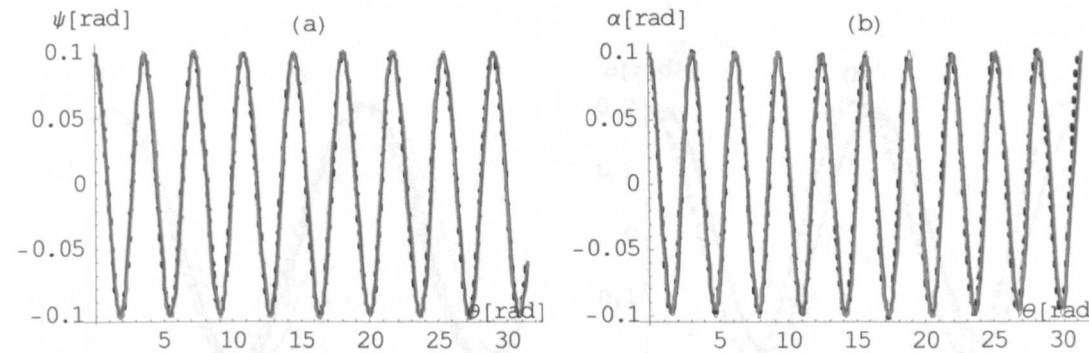


Figure 3.3 In-plane, (a), and out-of-plane, (b), angular response over 5 circular orbits against true anomaly with $\dot{\psi}(0) = \dot{\alpha}(0) = 0$ and $\psi(0) = \alpha(0) = 0.1$ rad (solid black = numerical, solid grey = 2nd order analysis, dash = 3rd order analysis)

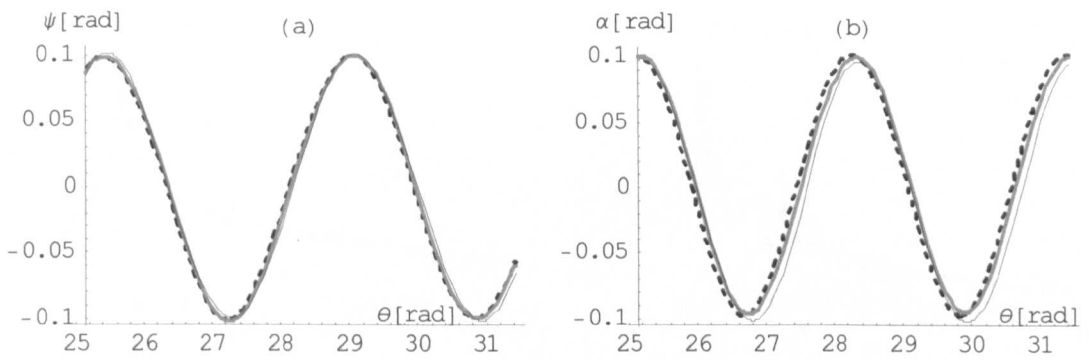


Figure 3.4 In-plane, (a), and out-of-plane, (b), angular response between the 4th and 5th circular orbit against true anomaly with $\dot{\psi}(0) = \dot{\alpha}(0) = 0$ and $\psi(0) = \alpha(0) = 0.1$ rad (solid black = numerical, solid grey = 2nd order analysis, dash = 3rd order analysis)

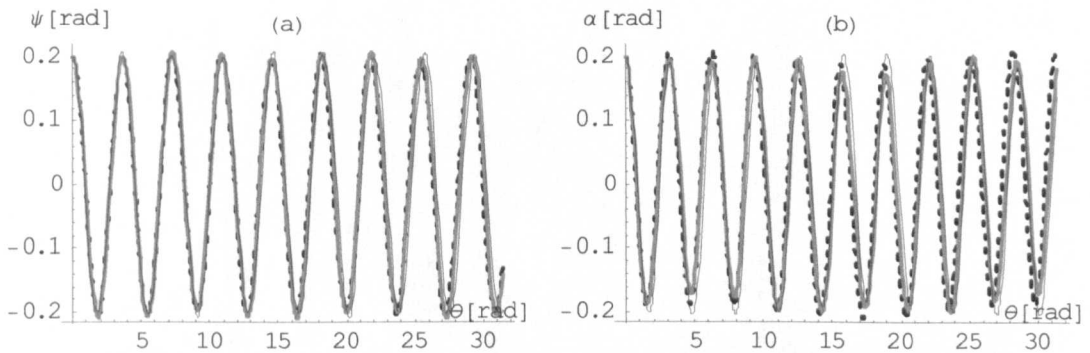


Figure 3.5 In-plane, (a), and out-of-plane, (b), angular response over 5 circular orbits against true anomaly with $\dot{\psi}(0) = \dot{\alpha}(0) = 0$ and $\psi(0) = \alpha(0) = 0.2$ rad (solid black = numerical, solid grey = 2nd order analysis, dash = 3rd order analysis)

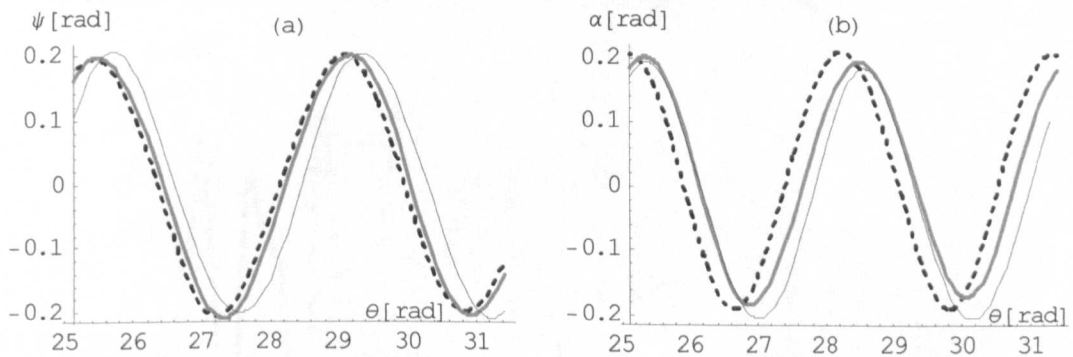


Figure 3.6 In-plane, (a), and out-of-plane, (b), angular response between the 4th and 5th circular orbit against true anomaly with $\dot{\psi}(0) = \dot{\alpha}(0) = 0$ and $\psi(0) = \alpha(0) = 0.2$ rad (solid black = numerical, solid grey = 2nd order analysis, dash = 3rd order analysis)

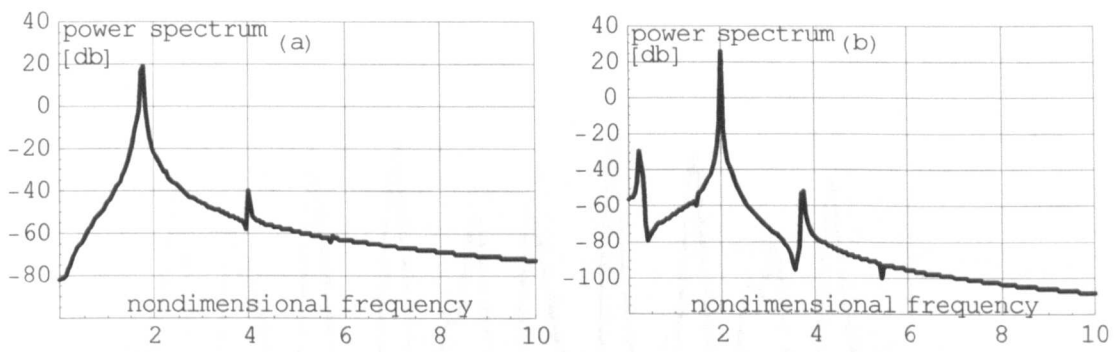


Figure 3.7 Power spectra of the in-plane, (a), and out-of-plane, (b), motion on a circular orbit with $\dot{\psi}(0) = \dot{\alpha}(0) = 0$ and $\psi(0) = \alpha(0) = 0.1$ rad

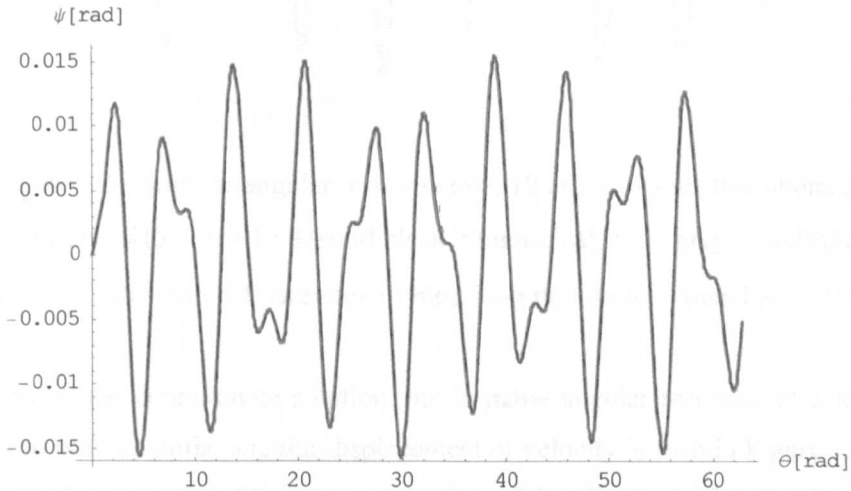


Figure 3.8 In-plane angular response over 10 orbits against true anomaly with $e = 0.01$ and $\dot{\psi}(0) = \dot{\psi}(0) = 0$ (solid black = numerical, solid grey = multiple scales, short thick dash = Modi & Brereton (1966), long thin dash = Anand *et al.* (1971))

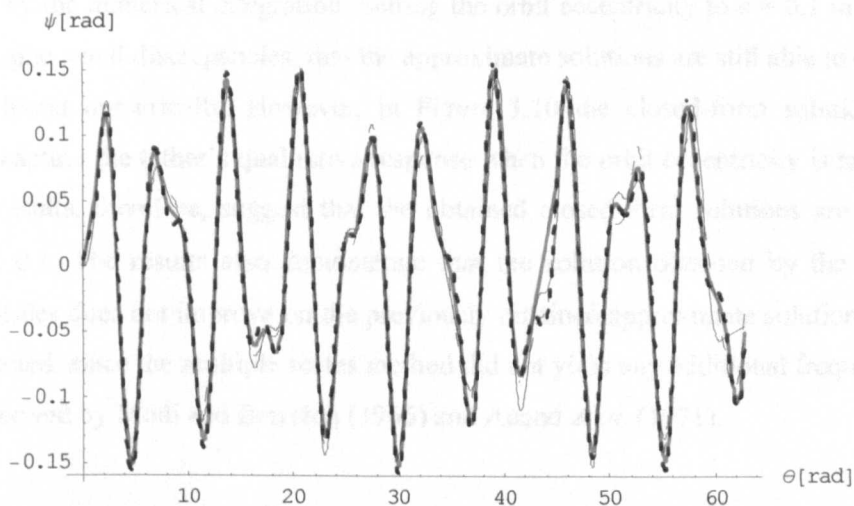


Figure 3.9 In-plane angular response over 10 orbits against true anomaly with $e = 0.1$ and $\dot{\psi}(0) = \dot{\psi}(0) = 0$ (solid black = numerical, solid grey = multiple scales, short thick dash = Modi & Brereton (1966), long thin dash = Anand *et al.* (1971))

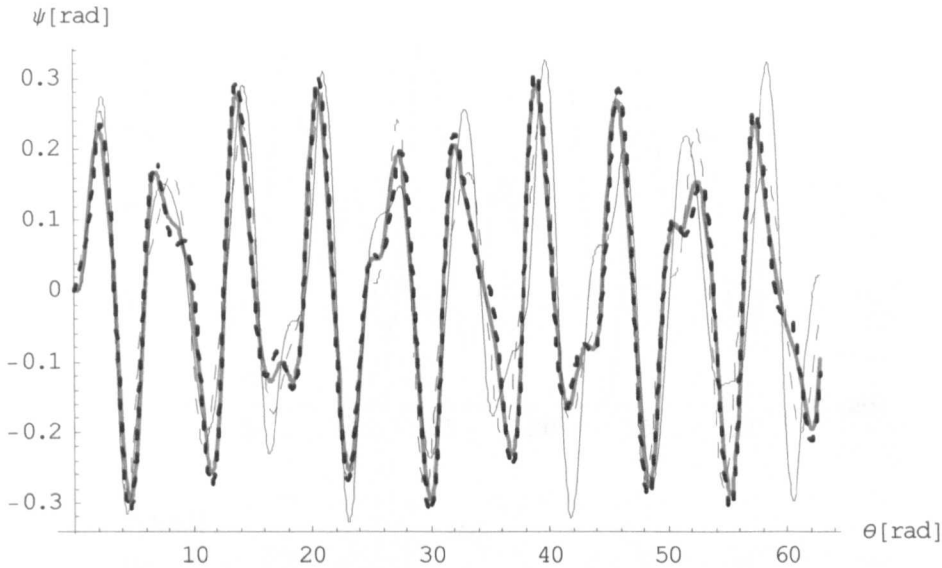


Figure 3.10 In-plane angular response over 10 orbits against true anomaly with $e = 0.2$ and $\dot{\psi}(0) = \psi(0) = 0$ (solid black = numerical, solid grey = multiple scales, short thick dash = Modi & Brereton (1966), long thin dash = Anand *et al.* (1971))

As predicted by the approximate solution, the in-plane angular response of a tether on an elliptical orbit with no initial angular displacement or velocity is seen in Figure 3.8 to Figure 3.10 to always be in motion. The constant forcing of the elliptical orbit simply does not let the tether align itself along the gravity vector. For a nearly circular orbit, Figure 3.8 demonstrates an excellent agreement between the closed form solutions obtained by the multiple scales method, Modi and Brereton (1966) and Anand *et al.* (1971), and those generated by the numerical integration. Setting the orbit eccentricity to $e = 0.1$ in Figure 3.9 shows, despite small discrepancies, that the approximate solutions are still able to capture the response found numerically. However, in Figure 3.10 the closed-form solutions are all unable to capture the tether's qualitative response when the orbit eccentricity is raised to $e = 0.2$. The results, therefore, suggest that the obtained closed-form solutions are only valid when $e < 0.1$. The results also demonstrate that the solution obtained by the method of multiple scales does not improve on the previously obtained approximate solutions, which is to be expected, since the multiple scales method did not yield any additional frequency terms to those derived by Modi and Brereton (1966) and Anand *et al.* (1971).

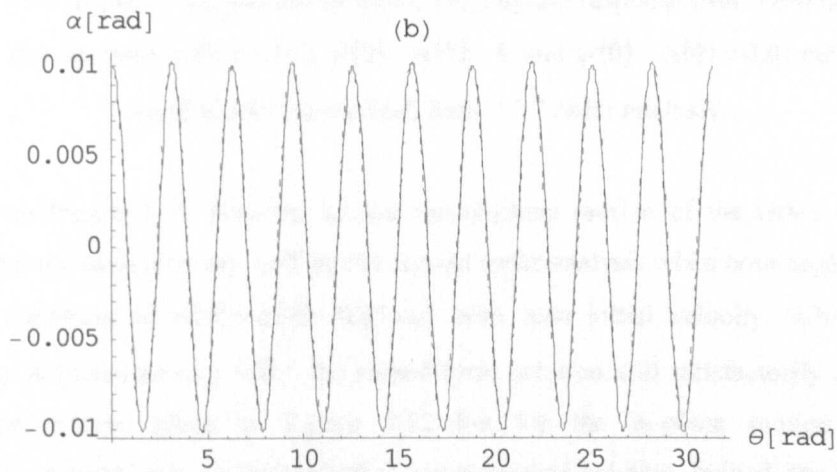
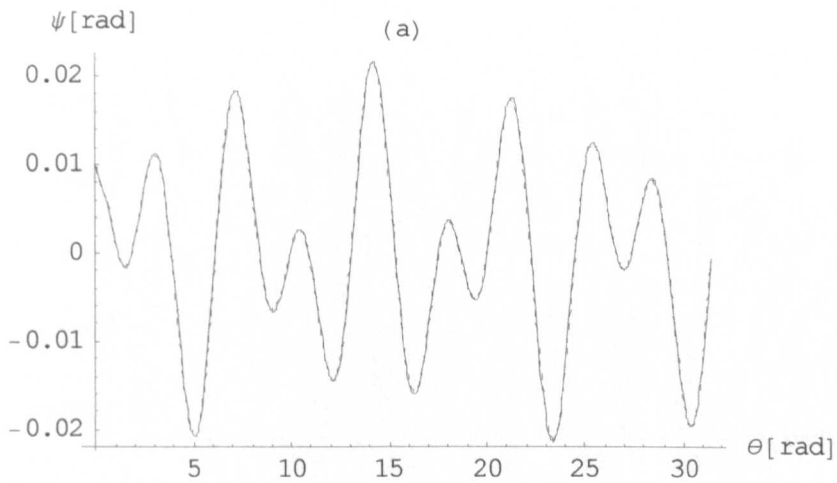
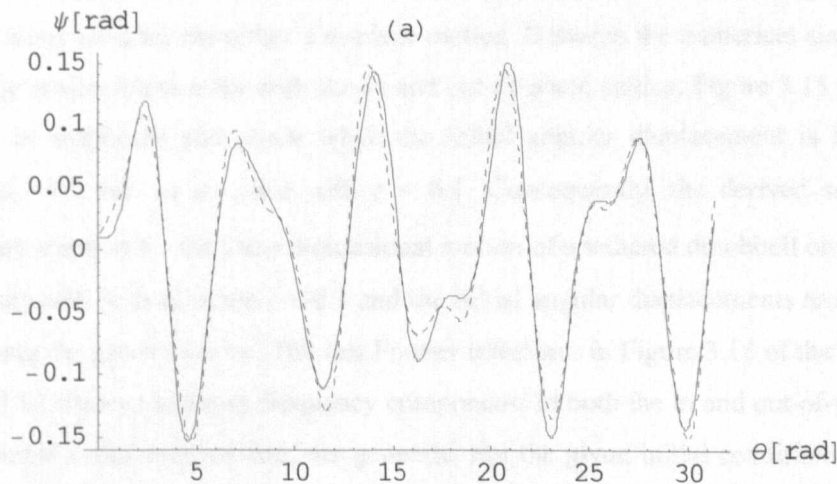


Figure 3.11 In-plane, (a), and out-of-plane, (b), angular response over 5 orbits against true anomaly with $e = 0.01$, $\dot{\psi}(0) = \dot{\alpha}(0) = 0$ and $\psi(0) = \alpha(0) = 0.01$ rad (solid black = numerical, dash = 2nd order analysis)



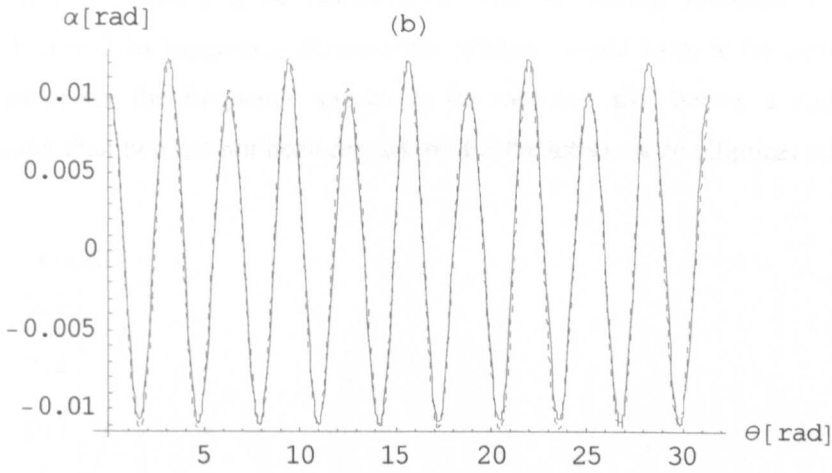


Figure 3.12 In-plane, (a), and out-of-plane, (b), angular response over 5 orbits against true anomaly with $e = 0.1$, $\dot{\psi}(0) = \dot{\alpha}(0) = 0$ and $\psi(0) = \alpha(0) = 0.01$ rad (solid black = numerical, dash = 2nd order analysis)

As shown in Figure 3.11, both the in and out-of-plane motion of the tether on a nearly circular orbit are captured very well by the second order analysis when both angles are given an initial condition of $\psi(0) = \alpha(0) = 0.01$ rad with zero initial velocity. When the orbit eccentricity is increased to $e = 0.1$ the closed-form solution still satisfactorily captures the out-of-plane motion given in Figure 3.12 but for the in-plane motion qualitative discrepancies appear between the analytical and numerical solution. Indeed, the approximate solution still fares well in capturing the out-of-plane motion when the orbit eccentricity is raised to $e = 0.2$ in Figure 3.13 and only when the eccentricity is set to $e = 0.3$ do large qualitative differences arise, as Figure 3.14 demonstrates. For the larger orbit eccentricities, however, the approximate solution is unable to reproduce the subtleties displayed by the numerical integration for the tether's in-plane motion. Between the numerical simulation and the multiple scales solution for both the in and out-of-plane angles, Figure 3.15 shows large deviations in amplitude and phase when the initial angular displacement is increased to $\psi(0) = \alpha(0) = 0.2$ rad on an orbit with $e = 0.1$. Consequently, the derived second order approximate solution for the three dimensional motion of a tethered dumbbell on an elliptical orbit appears only to hold when $e < 0.1$ and the initial angular displacements are both nearly aligned along the gravity vector. The fast Fourier transform in Figure 3.16 of the time history in Figure 3.12 shows numerous frequency components in both the in and out-of-plane angles that the second order analysis does not generate. For the given initial conditions the derived closed-form solution manages to represent the numerical solution but as soon as these are increased the additional frequency components begin to significantly contribute to the tether's motion. The algebra involved in carrying out the third order analysis for the tether on

a circular orbit is already quite cumbersome without having achieved a measurable advantage. Figure 3.16 suggests a closed-form solution would have to be carried out to a very high order for the frequency spectra to be captured and, hence, a multiple scales analysis greater than two has not been carried out for the tether on an elliptical orbit.

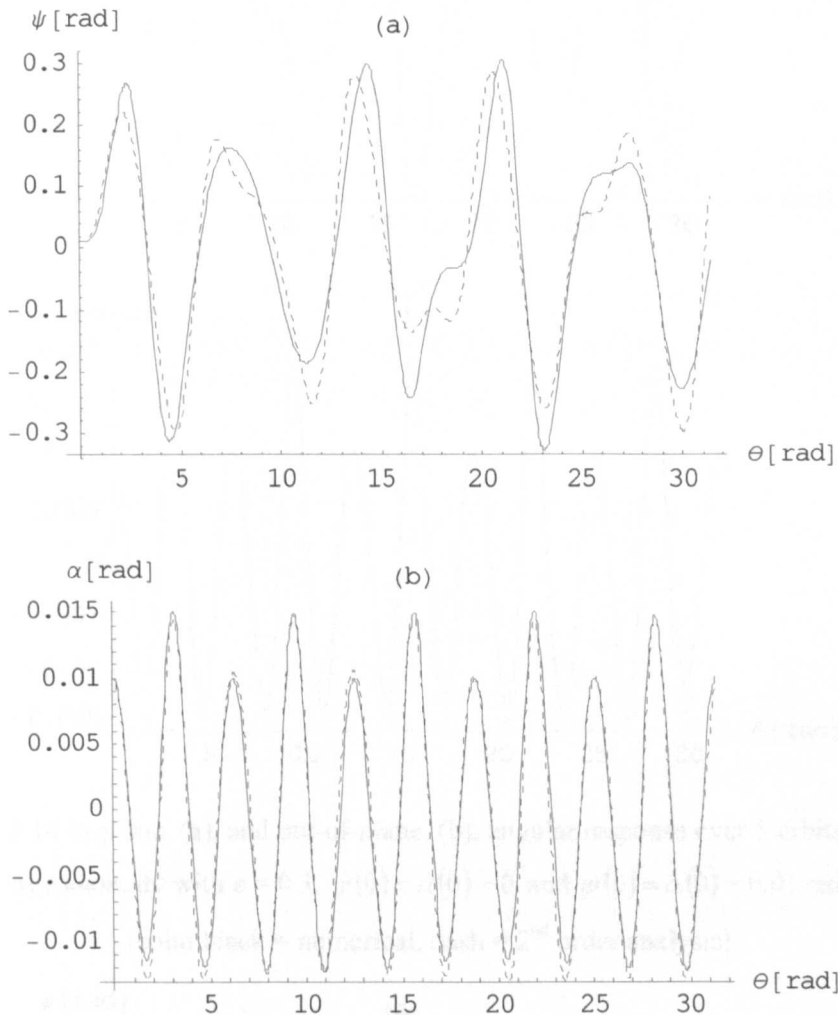


Figure 3.13 In-plane, (a), and out-of-plane, (b), angular response over 5 orbits against true anomaly with $e = 0.2$, $\dot{\psi}(0) = \dot{\alpha}(0) = 0$ and $\psi(0) = \alpha(0) = 0.01$ rad (solid black = numerical, dash = 2nd order analysis)

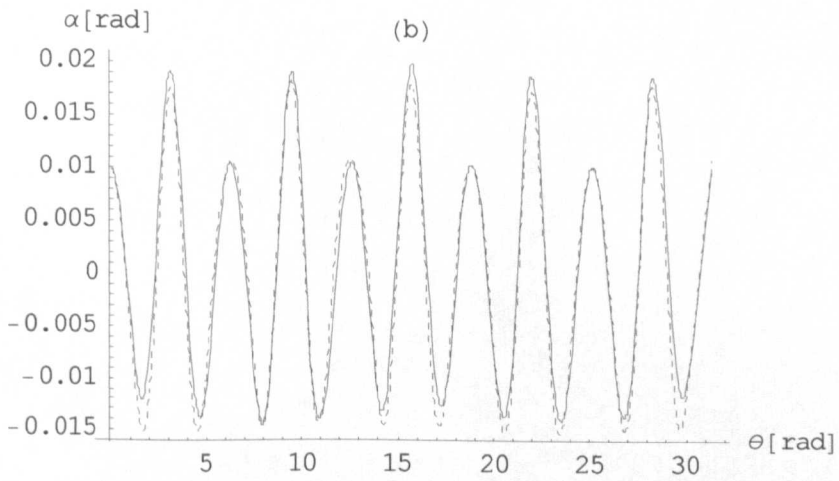
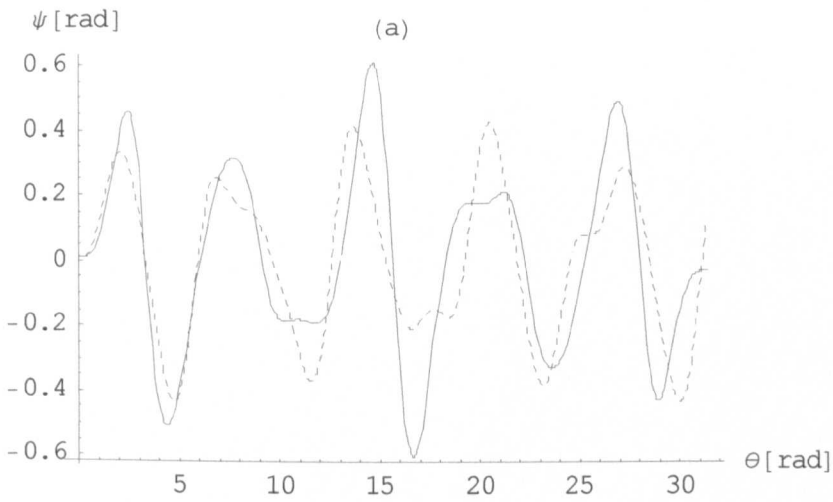
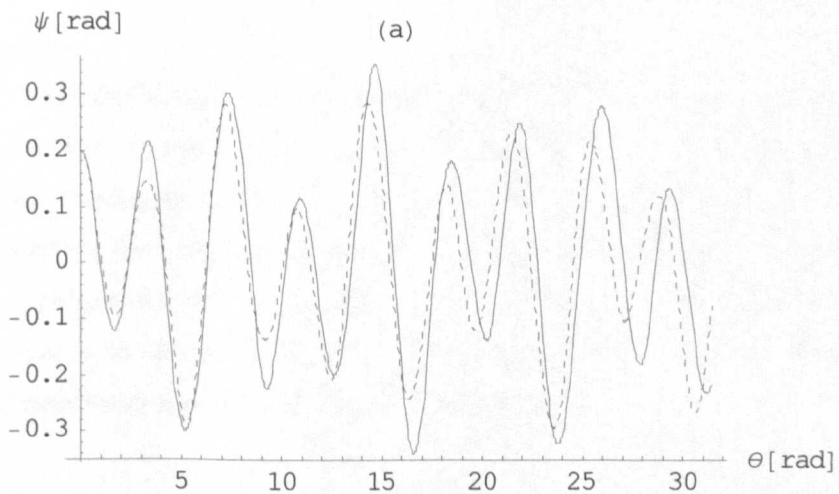


Figure 3.14 In-plane, (a), and out-of-plane, (b), angular response over 5 orbits against true anomaly with $e = 0.3$, $\dot{\psi}(0) = \dot{\alpha}(0) = 0$ and $\psi(0) = \alpha(0) = 0.01$ rad (solid black = numerical, dash = 2nd order analysis)



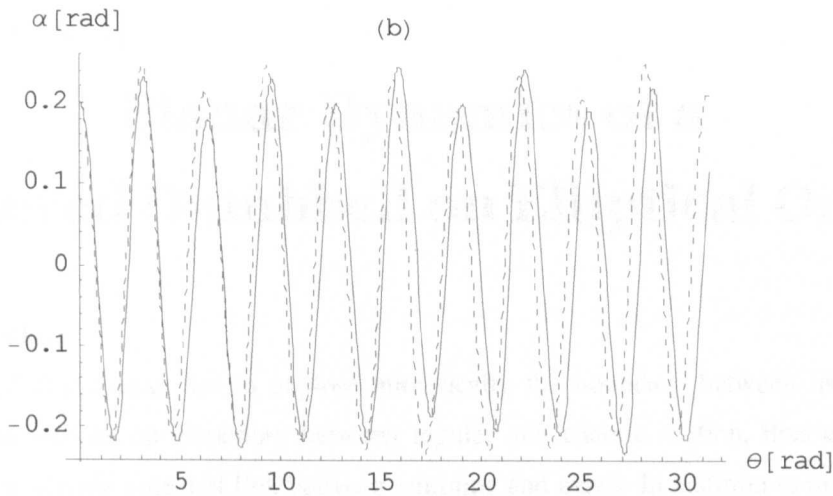


Figure 3.15 In-plane, (a), and out-of-plane, (b), angular response over 5 orbits against true anomaly with $e = 0.1$, $\dot{\psi}(0) = \dot{\alpha}(0) = 0$ and $\psi(0) = \alpha(0) = 0.2$ rad (solid black = numerical, dash = 2nd order analysis)

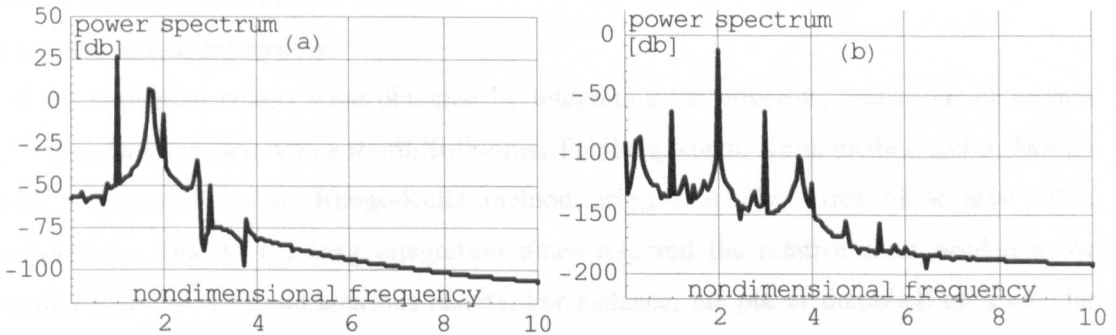


Figure 3.16 Power spectra of the in-plane, (a), and out-of-plane, (b), motion on an elliptical orbit with $e = 0.1$, $\dot{\psi}(0) = \dot{\alpha}(0) = 0$ and $\psi(0) = \alpha(0) = 0.01$ rad

3.5 Conclusions

The method of multiple scales has successfully generated a closed-form solution to the three dimensional motion of a tethered dumbbell on an elliptical orbit, which are valid for small initial angular displacements close to the gravity vector and orbit eccentricities less than $e < 0.1$. Moreover, the analytical solution has elegantly explained some of the fundamental principles of the tether's motion. However, numerical integration will have to be resorted to if the dynamics of the tether are to be comprehensively studied for values greater than the given initial conditions and those likely to be encountered in space.

Chapter 4

Planar Dynamics of a Tethered Dumbbell on Elliptical Orbits

4.0 Introduction

The aims of this chapter are to explore numerically the boundary between libration and tumbling, as well as the boundary between regular and chaotic motion, thus enabling an investigation into the potential link between tumbling and chaos. In addition to the long-term dynamics, the transient libration before the onset of tether rotation is studied in detail. The possibility of generating velocity increments through spin-orbit coupling of a freely moving dumbbell brings the chapter to a close.

4.1 Numerical Methods

4.1.1 Numerical Integration

All the numerical results were obtained by integrating the governing equations of motion (2.33) in *Mathematica* with a fourth/fifth-order Fehlberg Runge-Kutta method and in *Matlab* with a fourth/fifth-order Runge-Kutta method using a relative error of at least 10^{-11} , respectively. Due to the long integration times required the relative error needed to be smaller than 10^{-7} to avoid spurious results. For instance, the planar dumbbell on a circular orbit was found with time to begin tumbling for zero initial velocity but with an initial angular displacement near $\pi/2$ when the relative error was set to 10^{-6} . The lack of an energy input plus no initial velocity means the presence of tumbling clearly violates the expected physics of a tether on a circular orbit. This effect, which due to the build up of numerical errors, disappears by decreasing the relative error in the integrator. Additional checks were also initially carried out with a sixth/seventh-order Runge-Kutta method from the Numerical Algorithms Group libraries and an adaptive step-size fourth/fifth order Runge-Kutta method from Press *et al.* (1995). Very good agreement was found between the results from all integrators and results were found not to differ significantly when relative errors smaller than 10^{-8} were used.

4.1.2 Poincaré Map

A Poincaré map consists of a collection of discrete points obtained by numerically integrating the governing equations of motion and periodically sampling the state variables. In essence the Poincaré map represents a stroboscopic view of the phase plane and can

concisely represent a system's underlying dynamics. For example, a system oscillating at a single frequency will periodically return to the same point in the phase space and will manifest itself as a single point in the Poincaré map. Similarly a system vibrating at four different frequencies, say, will appear on the Poincaré map as four discrete points. A Poincaré map will produce a closed loop for a system undergoing regular motion but that is incommensurate with the sampling frequency. This motion is termed quasi-periodic and only occurs when the ratio between the frequency of the system's oscillations and the sampling frequency is irrational. When a deterministic nonlinear system becomes globally sensitive to initial conditions then the motion can be defined as being chaotic. Chaos manifests itself as an infinite number of frequencies and thus fills the Poincaré map with a cloud of dots. Moon (1992) states that the points in the Poincaré map of a Hamiltonian system do not form a fractal structure, as is the case for a non-conservative system. Thus, the map will be uniformly filled with points since chaotic orbits in conservative systems visit all parts of the phase plane. The Poincaré maps presented in this chapter sample the tethered dumbbell's angular displacement and velocity at each perigee crossing. In this manner the state variables are sampled every 2π of the true anomaly. The physical justification for this is that the perigee represents the point on the orbit in orbital transfer applications where the tether releases the payload. Consequently, the Poincaré map can provide valuable information about the practicalities of payload orbital transfer at the perigee of an elliptical orbit.

4.1.3 Bifurcation Diagram

A bifurcation diagram is produced by sampling a single state variable in the same way as for a Poincaré map and plotting it against a system parameter. The bifurcation diagram is a powerful numerical tool for observing period doubling and subharmonic bifurcations, as is shown by Moon (1992) in numerous examples. The bifurcation diagrams for the planar tethered dumbbell presented in this chapter show the tether's angular displacement sampled at each perigee crossing against the orbit eccentricity. Note that each column of data in the bifurcation diagram is generated by numerically integrating the system from the same initial conditions instead of slowly evolving the orbit eccentricity with time.

4.1.4 Lyapunov Exponents

Lyapunov exponents measure the sensitivity of a system to perturbations in the initial conditions by averaging the rate of convergence or divergence of nearby orbits in phase space. When the Lyapunov exponent is positive the nearby orbits separate exponentially. Thomsen (1997) explains that this causes a stretching of the phase space but since the phase space in real systems is bounded the separation cannot go on indefinitely. As a result the orbits have to repeatedly fold and stretch within the phase space but without ever actually

making contact. The infinitely repeated process of stretching and folding is in essence what defines chaos and thus a positive Lyapunov exponent when properly computed is one of the strongest indicators of chaotic dynamics. For each dimension of the system a Lyapunov exponent is calculated and the exponent with the largest magnitude is termed the first or largest Lyapunov exponent. When the largest exponent is zero or less than zero then the motion is deemed to be regular. The largest Lyapunov exponent can only be negative when the system is dissipative, as damping causes the perturbation between the two trajectories to decrease. Consequently for Hamiltonian systems the largest exponent is either positive or zero. For a nonlinear system to exhibit chaos the system must possess a minimum of three dimensions. One of the Lyapunov exponents will always be zero because there cannot be any divergence for a perturbed trajectory in the direction of the unperturbed trajectory. Karasopoulos and Richardson (1992) explain that the area of the phase space must be conserved in Hamiltonian systems and so the stretching in one direction is accompanied by an identical contraction in another direction. Thus in conservative systems the non-zero Lyapunov exponents appear as additive inverse pairs with equal magnitude but opposite sign.

If d_0 is a measure of the initial perturbation between two trajectories, then the distance between the two orbits after a short time interval is given by Moon (1992) as

$$d(t) = d_0 2^{\lambda(t-t_0)} \tag{4.1}$$

where λ is the Lyapunov exponent. Conceptually d_0 can, according to Moon (1992), be imagined as a small sphere containing the initial condition within the phase space and the Lyapunov exponent tracks the deformation of the sphere into an ellipse of maximum length d due to the system's dynamics. A single measurement does not however suffice and the calculation must be averaged over different regions of the phase space, which Moon (1992) gives as

$$\lambda = \lim_{N \rightarrow \infty} \frac{1}{N} \sum_{i=1}^N \frac{1}{t_i - t_{0i}} \log_2 \frac{d_i}{d_{0i}} \tag{4.2}$$

The seminal paper by Wolf *et al.* (1985) describes the algorithm required to obtain numerically the Lyapunov exponent for smooth dynamical systems governed by a system of 2nd order differential equations. The Lyapunov exponents were obtained in *Mathematica* by modifying the code produced by Sandri (1996). Rewriting the Lyapunov Exponents Toolbox in *Matlab* allowed the calculated exponents to be compared, thus providing an additional check. Before considering the case of the tethered dumbbell, the accuracy of the programs was investigated by revisiting many different systems considered by Moon (1992) for which he presents Lyapunov exponents. No qualitative differences and only small quantitative

discrepancies less than 1% were observed between the two programs and previous results in the literature.

4.2 Data and Tether Models

All the simulations presented in this chapter were carried out with the tether starting from the perigee. To investigate the influence of the initial position along the orbit some simulations were repeated with the tether starting at the apogee and for the few cases examined the qualitative effect on the tether's dynamics appears to be minor. Furthermore, the influence of the initial true anomaly on the long-term stability boundary is shown in Figure 4.1 to have no visible effect. This observation agrees with the findings of Crellin and Janssens (1996) who found the onset of tether spin occurred almost for the identical orbit eccentricity when the tether was started at either the perigee or apogee. Therefore, the effect of the starting position along the orbit appears to have little effect on the global dynamics of the dumbbell and consequently all the simulations were started from the perigee.

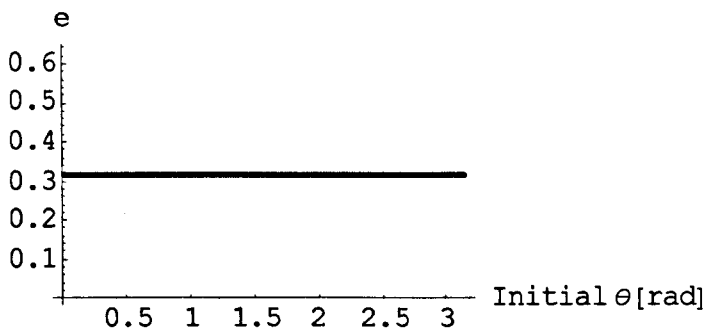


Figure 4.1 Effect of initial true anomaly on the long-term stability boundary on an elliptical orbit. 200 points in the interval between $0 \leq \theta \leq 2\pi$ and integrating for a duration of 30 completed orbits with $\dot{\psi}(0) = \psi(0) = 0$ and a step size in e of 0.0005.

(2.14)-(2.17) are dependent on the properties of the tether and orbital parameters. In order to compare the possible influence of the accuracy of the model (2.29)-(2.32) with the appropriate terms set to zero were integrated and compared to the results obtained for (2.33)-(2.34). Simulations were carried out for tethers with unequal end masses and different perigee altitudes for constant eccentricity and although the qualitative dynamics remained unchanged small but visible discrepancies were observed. This finding was also made by Crellin and Janssens (1996) who observed the onset of tumbling motion varied by 0.01 in the orbit eccentricity for different initial orbit radii. Since the qualitative attitude dynamics of the tethered dumbbell appears to be relatively unaffected by the accuracy of the tether modelling the results in this chapter are generated using (2.33) with $\alpha = 0$.

4.3 Transition from Libration to Spin

An initially radial and motionless tether placed on an elliptical orbit with an eccentricity of 0.1 is seen over thirty completed orbits to continuously librate in Figure 4.2. However, the tether may or may not librate for an indefinite period of time and as Figure 4.3 demonstrates a librating tether on an elliptical orbit may commence tumbling after completing numerous orbits. When the orbit eccentricity is increased to 0.32 for the initially radial and motionless tether, Figure 4.3 shows the tether librates for the first 11 orbits but during the 12th orbit the tether begins to tumble. For the case presented in Figure 4.3 the spinning does not continue indefinitely. Instead, the tether completes several revolutions before collapsing back into libration only to be followed by further rotation. This interplay between libration and spin is repeated many times over the 30 orbits. Thus, the orbit eccentricity is seen to have a large influence over the stability of the tether.

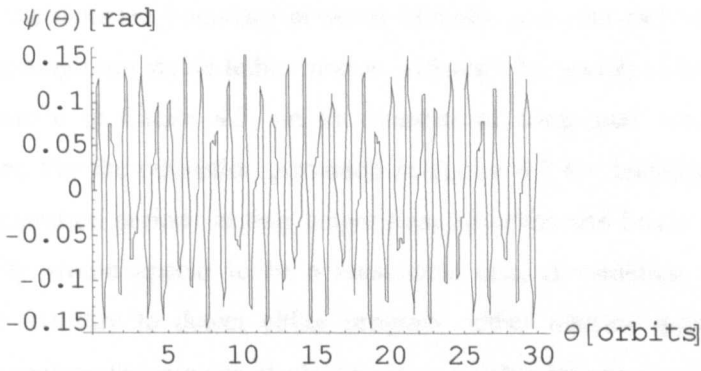


Figure 4.2 Time history of dumbbell's angular displacement over 30 orbits with $e = 0.1$ and $\dot{\psi}(0) = \psi(0) = 0$.

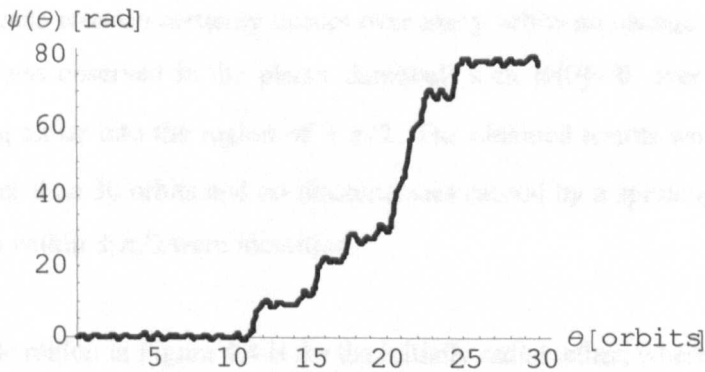


Figure 4.3 Time history of dumbbell's angular displacement over 30 orbits with $e = 0.32$ and $\dot{\psi}(0) = \psi(0) = 0$.

Figure 4.4 establishes the long-term boundary between libration and spin for an initial angular displacement but with $\dot{\psi}(0)=0$. For a given initial condition and orbit eccentricity (2.33) is numerically integrated for a duration of 30 orbits. Upon the 30th perigee crossing the tether's attitude displacement is evaluated and if the magnitude of the displacement ranges between $\pm \pi/2$ then the tether is deemed to be librating and if not then tether spin must have taken place. Starting from a zero orbit eccentricity this algorithm can be implemented to increment the eccentricity until the boundary between libration and spin is found for a given $\psi(0)$. Repeating this process for various values of $\psi(0)$ leads to the generation of Figure 4.4. Modi and Brereton (1966) were the first to generate this type of plot and the qualitative comparison between their results and Figure 4.4 is on the whole favourable. However, there do exist large quantitative discrepancies, which may possibly be accounted for by the lack of computing power in the 1960s causing a large round-off error in the floating-point number. The area below the depicted boundary between libration and spin can be interpreted as a region permitting long-term stable tether motion, although the notion of long-term is highly dependent, as shown in Figure 4.3, on the number of completed orbits the numerical integration covers. For the resolution presented in Figure 4.4 the boundary is found to be insensitive to integration periods lasting longer than 30 orbits and hence the perception of long-term stability would appear to be a reasonable one. A weakness of the presented algorithm is the inability to detect either prograde tether rotation quickly followed by retrograde spin to return the angular displacement to a value between $\pm \pi/2$ either during a single orbit or over the whole 30 orbit duration. Should this occur then the algorithm would falsely label this case as being stable even though rotation had clearly taken place. Intuitively, the perigee is the only position on the orbit that is capable of generating a large enough torque through the gravity gradient to reverse the tether's direction of rotation. Although retrograde rotation certainly occurs over many orbits no change from prograde to retrograde spin was observed in the planar dumbbell with $\dot{\psi}(0)=0$ over a single orbit to return a spinning tether into the region of $\pm \pi/2$. The obtained results were also integrated for periods longer than 30 orbits and no discrepancies caused by a spinning tether returning the value of ψ to within $\pm \pi/2$ were identified.

The largest stable region in Figure 4.4 is for the initially radial tether, where the onset of spin occurs for an eccentricity between 0.31 and 0.32. As soon as the initial angular displacement deviates from the local vertical the onset of spin is seen to commence for smaller eccentricities and the greater the displacement becomes the more tether spin is encouraged

on less elliptical orbits. The curve appears to be on the whole symmetrical about the local vertical and possesses visible features, such as “horns” near ± 0.5 rad and “humps” close to $\pm \pi/2$. The area around the left hump close to $-\pi/2$ is magnified in Figure 4.5 and a non-trivial boundary with discontinuous jumps, as well as complicated peaks and valleys, are uncovered. Moreover, the obtained results do not form a smooth and continuous line as they do in Figure 4.5 for $\psi(0) \geq -1.18$ rad. The equivalent “hump” on the right-hand side is zoomed in upon in Figure 4.6 and is clearly not a mirror image of the left-hand “hump”. Consequently, the detail of the libration-spin boundary is not perfectly symmetrical about the local vertical. For $\psi(0) \geq 1.18$ rad the boundary changes from a smooth line to a discrete collection of lines with complicated peaks and valleys. Magnifications of both of the “horns” from the left- and right-hand sides are presented in Figure 4.7 and Figure 4.8, respectively. As before, the areas are not mirror images of each other and discrete jumps, as well as non-trivial peaks and valleys, again form prominent features of the boundary. Hence, in addition to the orbit eccentricity the initial angular displacement is observed to affect the long-term stability boundary.

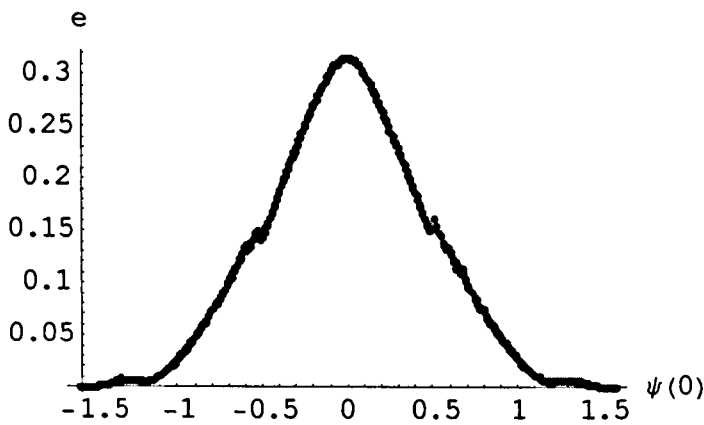


Figure 4.4 Effect of initial angular displacement on the long-term stability boundary on an elliptical orbit. 400 points in the interval between $-\pi/2 \leq \psi(0) \leq \pi/2$ and integrating for 30 perigee passings with a step size in e of 0.0005

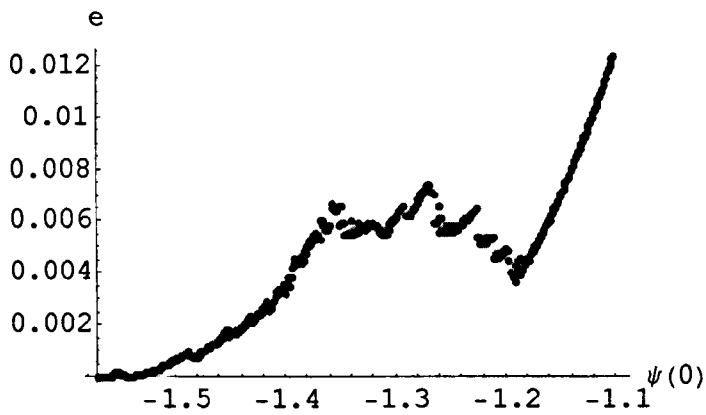


Figure 4.5 Effect of initial angular displacement on the long-term stability boundary on an elliptical orbit. 500 points in the interval between $-1.57 \leq \psi(0) \leq -1.1$ rad and integrating for 30 perigee passings with a step size in e of 0.00005.

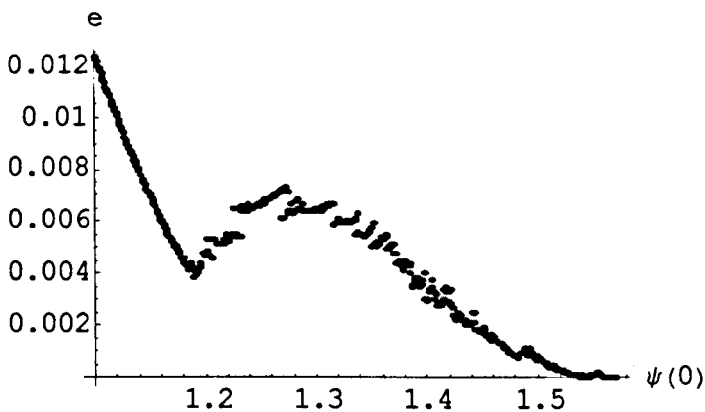


Figure 4.6 Effect of initial angular displacement on the long-term stability boundary on an elliptical orbit. 500 points in the interval between $1.1 \leq \psi(0) \leq -1.57$ rad and integrating for 30 perigee passings with step size in e of 0.00005.

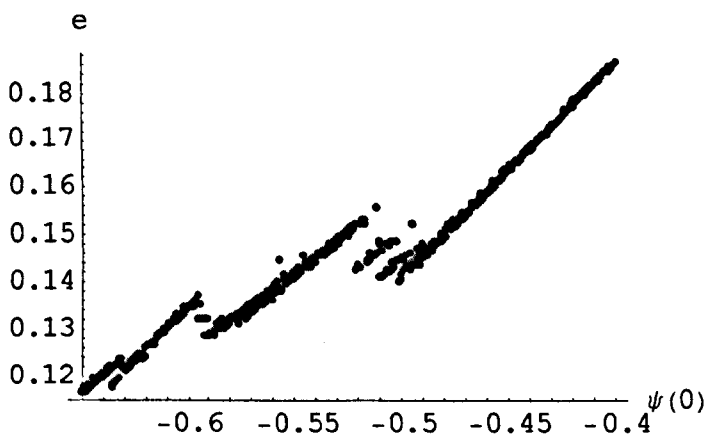


Figure 4.7 Effect of initial angular displacement on the long-term stability boundary on an elliptical orbit. 500 points in the interval between $-0.65 \leq \psi(0) \leq -0.4$ rad and integrating for 30 perigee passings with a step size in e of 0.0005.

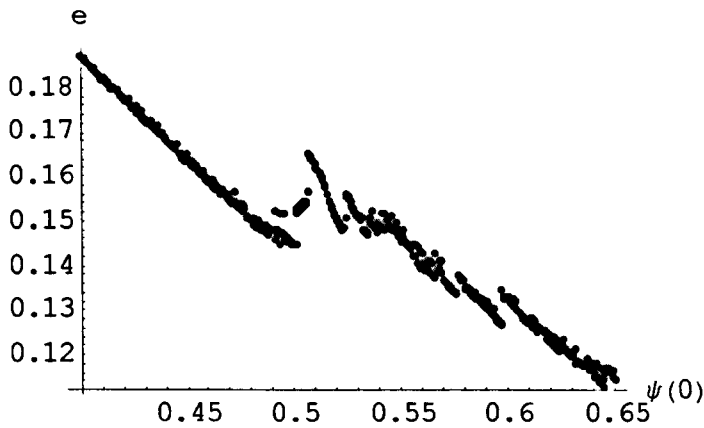


Figure 4.8 Effect of initial angular displacement on the long-term stability boundary on an elliptical orbit. 500 points in the interval between $0.4 \leq \psi(0) \leq 0.65$ rad and integrating for 30 perigee passings (starting at the perigee) step size in e of 0.0005.

The adopted approach to detect the onset of spin does not investigate whether stable attitude motion exists for orbit eccentricities greater than the boundary. Consequently, the algorithm used to produce Figure 4.4 - Figure 4.8 was rerun but with the duration of integration limited to a single orbit. The aim of this methodology was to identify when the tether commenced rotation during the first completed orbit. The black line shown in Figure 4.9 was generated by starting with a circular orbit and incrementing the eccentricity until the tether starts spinning but can be equally obtained by starting with $e = 1$ and reducing the eccentricity until only tether libration exists during the first orbit. In stark contrast to the long-term stability boundary the onset of spin during the first orbit, presented in Figure 4.9, is asymmetrical with a local and global maximum encountered near $\psi(0) \approx 0.45$ rad and $\psi(0) \approx 1.1$ rad, respectively. The grey curve in Figure 4.9 represents the last steady-state tether libration observed before the first tether tumbling is encountered for larger orbit eccentricities. The grey boundary does not, however, preclude that steady-state libration cannot exist for larger orbit eccentricities between the grey and black curves. Hence, the region fenced in between the two curves in Figure 4.9 represents a zone for the dumbbell where either steady-state libration occurs or where the libration is a transient, which eventually gives way to tumbling.

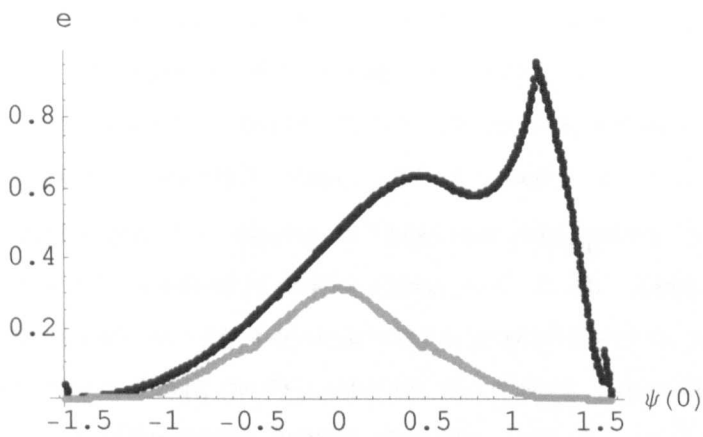


Figure 4.9 Comparison between the onset of tether spin during first orbit (black) and the long-term stability boundary (grey) up to 30 perigee passings. 750 points between $-\pi/2 \leq \psi(0) \leq \pi/2$ with a step size in e of 0.001.

Crellin and Janssens (1996) were the first to consider how many orbits an initially radial tether with $\dot{\psi}(0) = 0$ completes before libration gives way to spin on an elliptical orbit and their results are reproduced as the grey dots in Figure 4.10. At each perigee crossing the integration of (2.33) for given initial conditions and orbit eccentricity is paused to examine whether tether spin has begun and if not the integration is repeatedly advanced to the next perigee until spin is finally encountered. The last perigee passing prior to the onset of spin is recorded as the quantity η . Thus, for each investigated orbit eccentricity η is a discrete and whole number measurement of the number of completed orbits for which continued librational motion occurs before the onset of spin. The results of Crellin and Janssens (1996) do not cover the whole region between the long-term stability boundary and the onset of spin during the first orbit for a radial tether, as determined by Figure 4.9. Consequently, η is determined throughout the whole interval and at a much finer resolution than that employed by Crellin and Janssens (1996). Comparing the obtained results with those of Crellin and Janssens (1996) suggests, apart from a handful of cases, that very good qualitative and quantitative agreement exists between the two. Figure 4.10 only required 20 perigee passings to differentiate between steady state and transient librational motion, hence, $\eta_{\max} = 20$ implies the dumbbell is in steady state libration. The line of points on the left-hand side of Figure 4.10 indicates the end of the long-term boundary between libration and spin, whereas the line of points on the right-hand side marks the onset of the tether spinning during the first orbit. The zone between these two limits for the radial tether has three large distinct plateaux at values of five, three and unity for η . In between these three plateaux plus the two boundaries there exists a formation of dots that clearly distinguish the regions. The arrangement of the dots is very complex with no obvious underlying structure. For example,

at $e = 0.38582$ η is determined to be 4, whereas for $e = 0.38616$ η is found to be 10. Moreover, increasing e yet again to 0.3865 causes η to change to 5. Hence, within this region η appears to be very sensitive to e . Integrating through the zone in Figure 4.9 for the initial conditions of $\psi(0)=0.5$ rad and $\dot{\psi}(0)=0$ has a profound change on η when compared to the initially radial tether. Figure 4.11 displays a single prominent plateau for $\eta = 1$ with an immediately adjacent but considerably smaller plateau at $\eta = 2$. The complex arrangement of points is again a feature between the long-term stability boundary and the plateaux as well as between the onset of spin during the first orbit and the plateau. Notice that η_{\max} had to be increased to 200 to aid differentiation between the steady state and transient librations. η_{\max} has to be increased to 500 to be able to differentiate between transient and steady state libration in Figure 4.12. The change in the initial condition is seen again to greatly affect the dumbbell's dynamics between the stability boundary and onset of spin during the first orbit. Zones again exist, which do not possess an obvious structure between the two visible plateaux and the previously defined boundaries. Moreover, many orbits have to be completed before tumbling is initiated and even after 500 orbits there are still many orbit eccentricities within the bounded zone that have not yielded rotation.

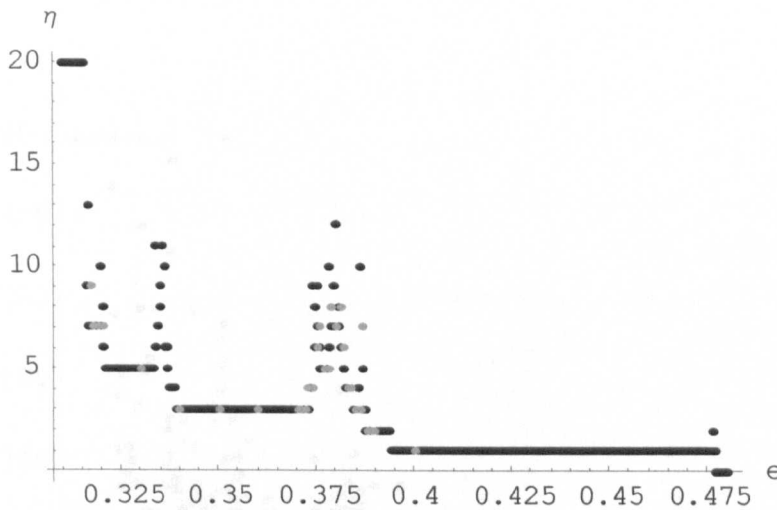


Figure 4.10 Number of orbit passing before tether begins to spin, η , against orbit eccentricity for $\dot{\psi}(0)=\psi(0)=0$ with $\eta_{\max} = 20$. 500 points between 0.31 and 0.48 with a step size of 0.00034. Grey = Crellin and Janssens (1996); black = numerical integration of (2.33).

The discrete measure proposed for η may possibly contribute artificially to the nature of the results reported in Figure 4.10 - Figure 4.12. To dispel any concern, the results were rerun with the value for η recorded at the point along the orbit where the angular displacement precisely equals $\pi/2$ instead of noting the last completed perigee. Figure 4.13 shows the precisely calculated η for the case presented in Figure 4.10, where very little quantitative difference is observed. Thus, the original definition of η appears to be acceptable.

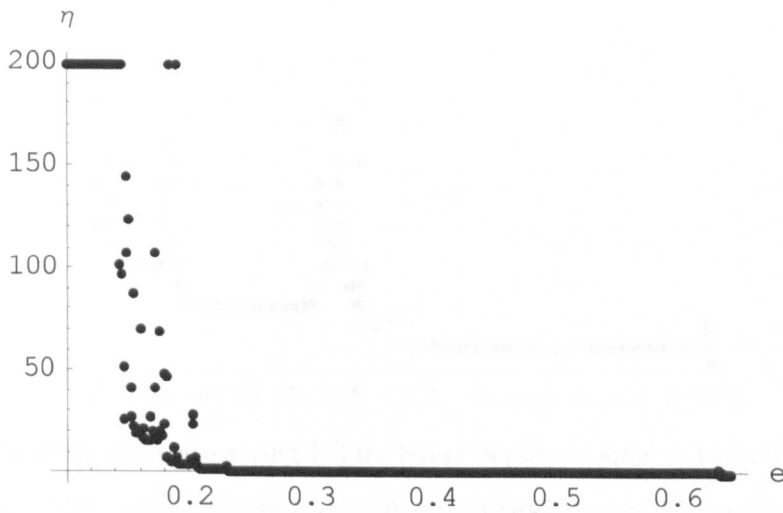


Figure 4.11 Number of orbit passing before tether begins to spin, η , against orbit eccentricity for $\dot{\psi}(0)=0$ and $\psi(0)=0.5rad$ with $n_{max} = 200$. 500 points between 0.13 and 0.645 with a step size of 0.00103.

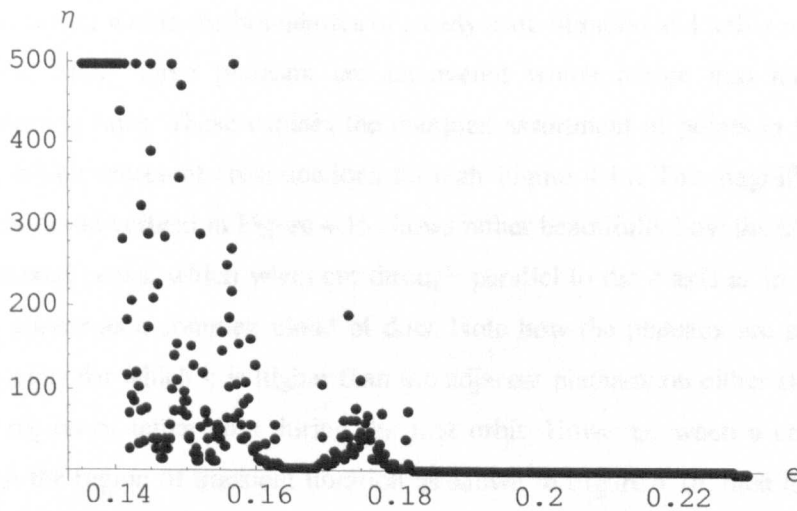


Figure 4.12 Number of orbit passing before tether begins to spin, η , against orbit eccentricity for $\dot{\psi}(0)=0$ and $\psi(0)=-0.5rad$ with $\eta_{max} = 500$. 500 points between 0.135 and 0.23 with a step size of 0.00019.

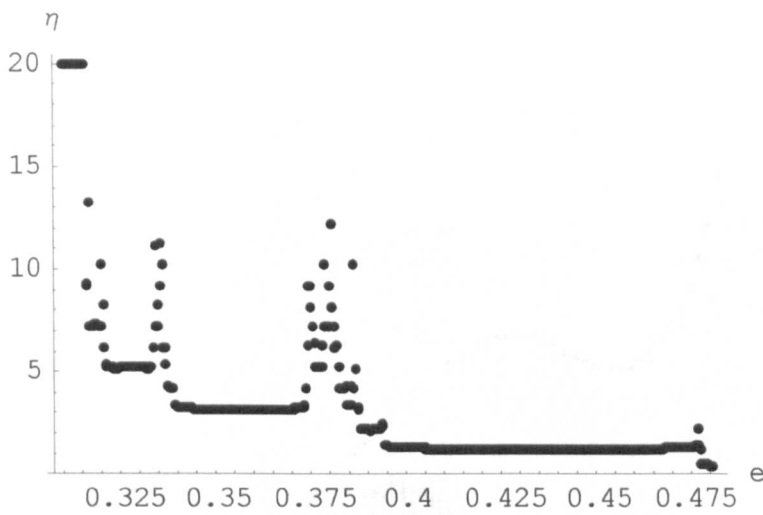


Figure 4.13 Number of orbit passing before tether begins to spin, η (exact), against orbit eccentricity for $\dot{\psi}(0) = \psi(0) = 0$ with $\eta_{\max} = 20$. 500 points between 0.31 and 0.48 with a step size of 0.00034.

In an attempt to understand the full effect of the initial conditions and the orbit eccentricity on η , the identified region in Figure 4.9 is numerically evaluated to determine η , the results of which are presented in Figure 4.14. Figure 4.14 yields a truly remarkable, clear and unexpected structure within the boundaries of steady state libration and tether rotation during the first orbit. Many large plateaux are uncovered which merge into narrow regions eventually forming lines. These explain the complex assortment of points in Figure 4.10 – Figure 4.12, which represent cross-sections through Figure 4.14. The magnification of the area around the local vertical in Figure 4.15 shows rather beautifully how the plateaux merge to form structured peaks, which when cut through parallel to the e axis as in Figure 4.10 – Figure 4.12, appear as a complex cloud of dots. Note how the plateaux are separated by a thin line of points for which η is higher than the adjacent plateaux on either side, especially prior to the region of tether spin during the first orbit. However, when a cross-section is taken through the region of transient libration as shown in Figure 4.16, then the obtained η , for the values of $\psi(0)$ and e along the cross-section from left to right, are presented in Figure 4.17. A more definitive structure emerges in Figure 4.17 between the plateaux in the form of peaks compared to Figure 4.10 – Figure 4.12. The fact that the dots are not perfectly ordered is likely to be a result of the cross-section not optimally slicing the peaks seen in Figure 4.15.

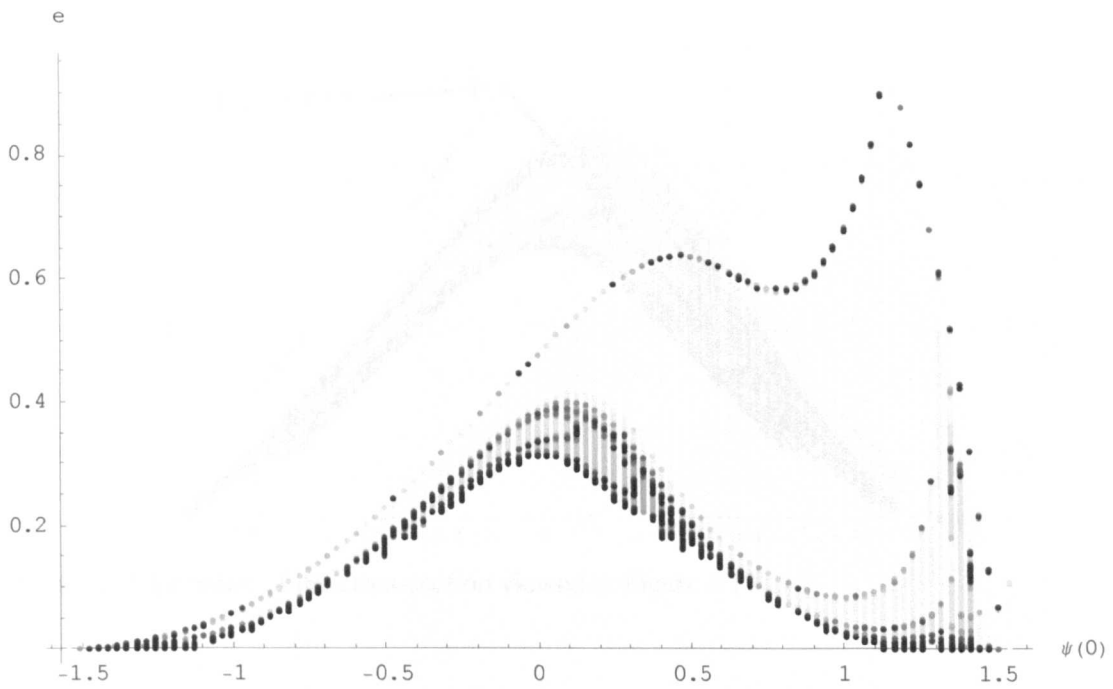


Figure 4.14 Number of completed orbits before the onset of tumbling within the identified zone of transient libration. The magnitude of η , ranging between zero and 20, is converted into a grey scale where a darker grey tone is assigned to a higher value for η , as given by:

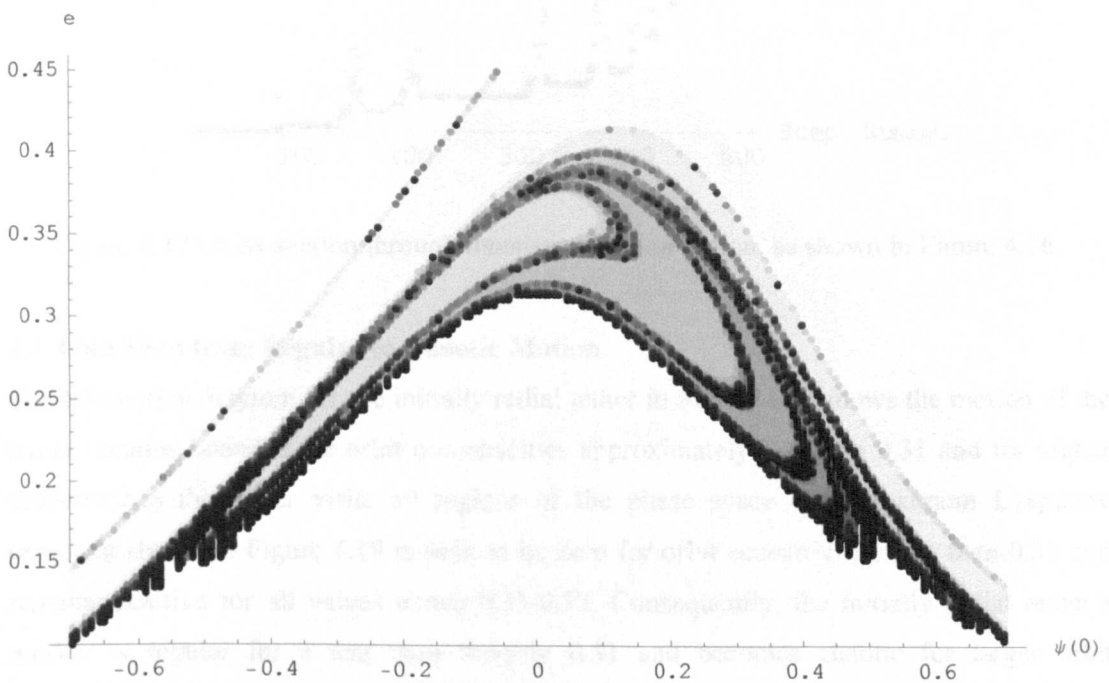
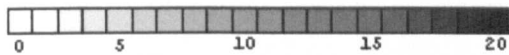


Figure 4.15 Number of completed orbits before the onset of tumbling within the identified zone of transient libration. η , ranging between zero and 20, is converted into a grey scale where a darker grey tone is assigned to a higher value for η , as assigned above.

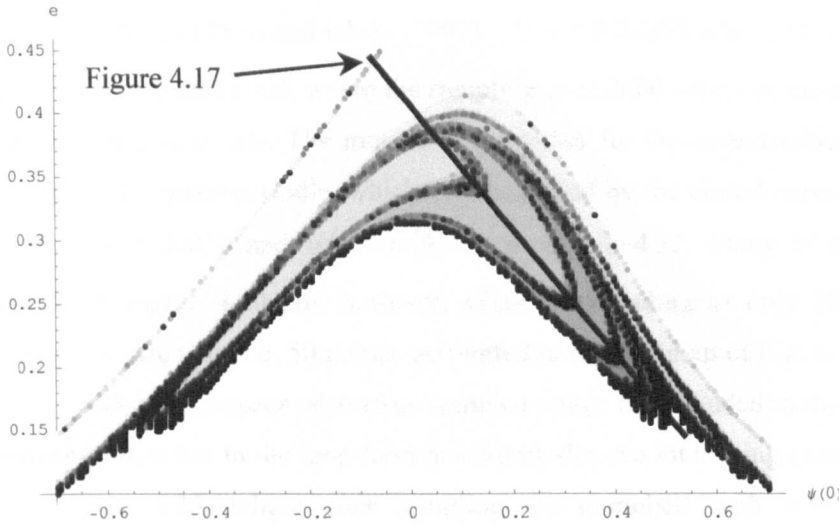


Figure 4.16 Location of the cross-section viewed in Figure 4.17

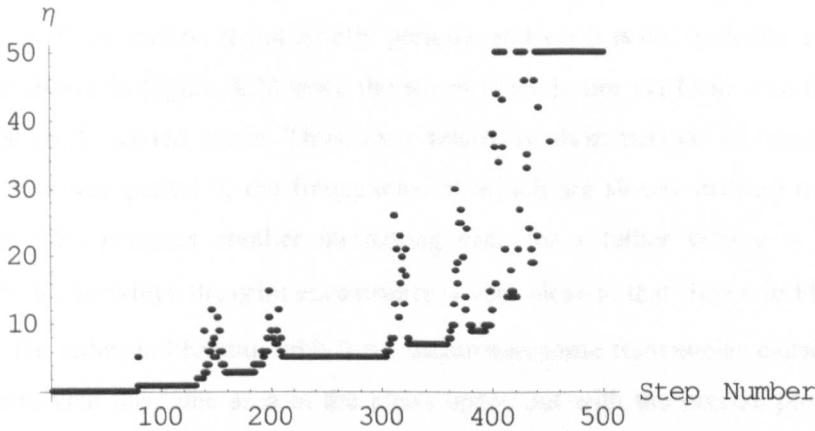


Figure 4.17 Cross-section through transient libration region, as shown in Figure 4.16.

4.4 Transition from Regular to Chaotic Motion

The bifurcation diagram for the initially radial tether in Figure 4.18 shows the motion of the tether remains bounded for orbit eccentricities approximately less than 0.31 and for higher eccentricities the tether visits all regions of the phase space. The maximum Lyapunov exponent shown in Figure 4.19 is seen to be zero for orbit eccentricities less than 0.31 and remains positive for all values above 0.31-0.32. Consequently, the initially radial tether's motion is regular for e less than roughly 0.31 and becomes chaotic for larger orbit eccentricities. The region in the bifurcation diagram for $0 \leq e \leq 0.3$ is magnified in Figure 4.20 and yields a structure depicting periodic windows and bands of points between the bounded regions. The general conical shape of the bifurcation diagram emanates from a single point at $e = 0$ where a period-1 attractor exists, representing the gravity gradient

stabilised tether on a circular orbit. Note, this is the only period-1 attractor for this system when $\dot{\psi}(0) = 0$. Both these bifurcation diagrams agree with those obtained by Karasopoulos and Richardson (1992) and Fujii and Ichiki (1997). At $e = 0.24955$ with $\dot{\psi}(0) = \psi(0) = 0$ a genuine period-3 orbit is identified, where the sampling over 2000 orbits as shown in Figure 4.21 returns three precise points. The motion of the tether for the eccentricities plotted in Figure 4.20 is typically quasi-periodic, which is exemplified by the closed curve seen in the Poincaré map for $e = 0.072$ and $\dot{\psi}(0) = \psi(0) = 0$ in Figure 4.22. Many of the periodic windows visible in Figure 4.20 are, however, slightly misleading as only 50 points are sampled for the Poincaré map, i.e. 50 points are plotted in each column of Figure 4.20. Many of the periodic windows disappear once more sampled points are included in the bifurcation diagram indicating these are in the long-term quasi-periodic. An interesting example though is shown in Figure 4.23, where after sampling the dumbbell with $e = 0.147$ and $\dot{\psi}(0) = \psi(0) = 0$ for 50 orbits the Poincaré map suggests the tether is librating very nearly on a 7-period orbit. However, as Figure 4.24 demonstrates, when the number of samples is increased to 1000 the motion is not strictly periodic and yet it is not typically quasi-periodic like the case shown in Figure 4.22 since the seven lines do not yet form with the additional samples a perfectly closed curve. Thus, over relatively short periods of time the tether is librating with a near period 7, the frequencies of which are slowly drifting over the long-term. Figure 4.25 presents another interesting case for a tether with $e = 0.24795$ and $\dot{\psi}(0) = \psi(0) = 0$, for which the orbit eccentricity is very close to that shown in Figure 4.21. In Figure 4.25 the tether is librating with three incommensurate frequencies causing the tether to periodically visit the same area in the phase space but with the precise position drifting quasi-periodically.

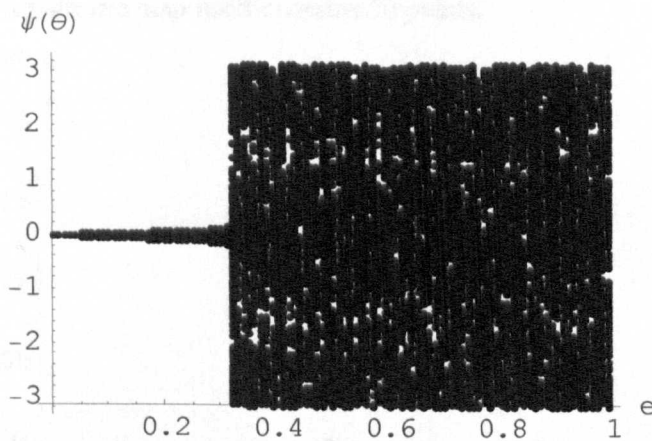


Figure 4.18 Bifurcation Diagram of the angular displacement with respect to the orbit eccentricity. Initial conditions are $\dot{\psi}(0) = \psi(0) = 0$ with a step size in e of 0.01. Each column of results contains 200 points.

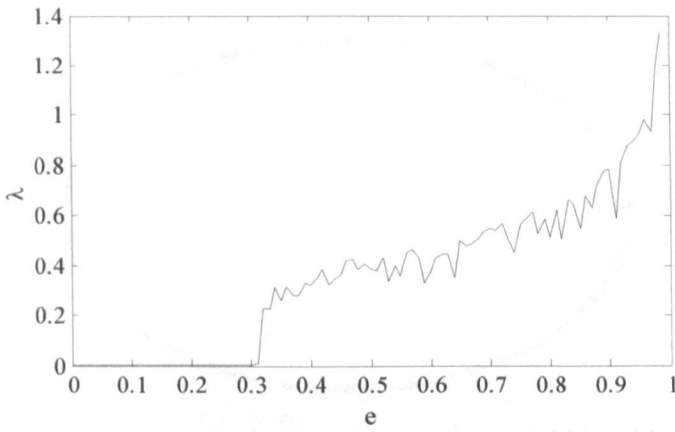


Figure 4.19 First Lyapunov exponent for a tether with $\dot{\psi}(0)=\psi(0)=0$. 100 points are plotted, each calculated over 40 orbits, with a stepsize in e of 0.01.

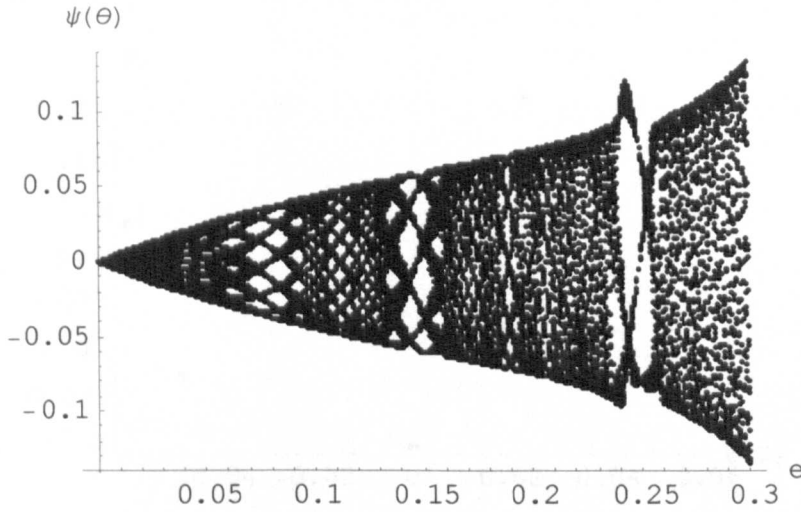


Figure 4.20 Bifurcation diagram of the angular displacement with respect to the orbit eccentricity. Initial conditions are $\dot{\psi}(0)=\psi(0)=0$ with a step size in e of 0.00075. Each column in essence a Poincaré map itself contains 50 points.

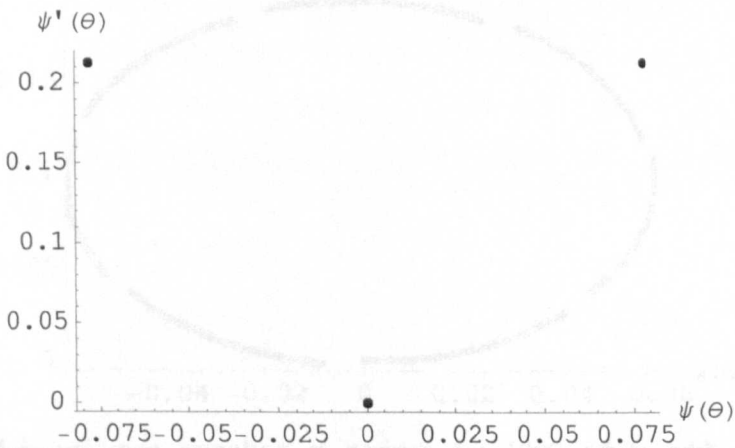


Figure 4.21 Poincaré map sampling at each perigee crossing for 2000 orbits with $e = 0.24955$ and $\dot{\psi}(0)=\psi(0)=0$.

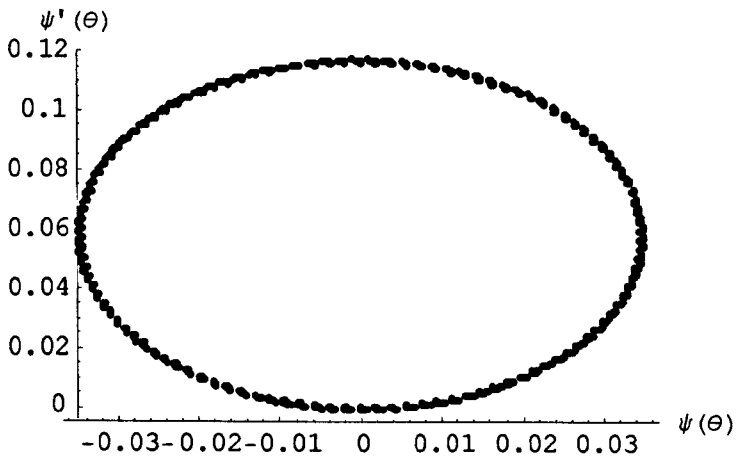


Figure 4.22 Poincaré map sampling at each perigee crossing for 1000 orbits with $e = 0.072$ and $\dot{\psi}(0) = \psi(0) = 0$.

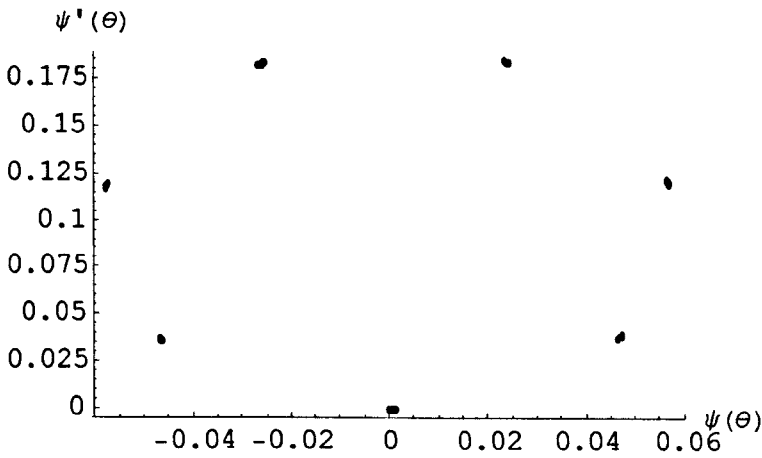


Figure 4.23 Poincaré map sampling at perigee for 50 orbits with $e = 0.147$ and $\dot{\psi}(0) = \psi(0) = 0$.

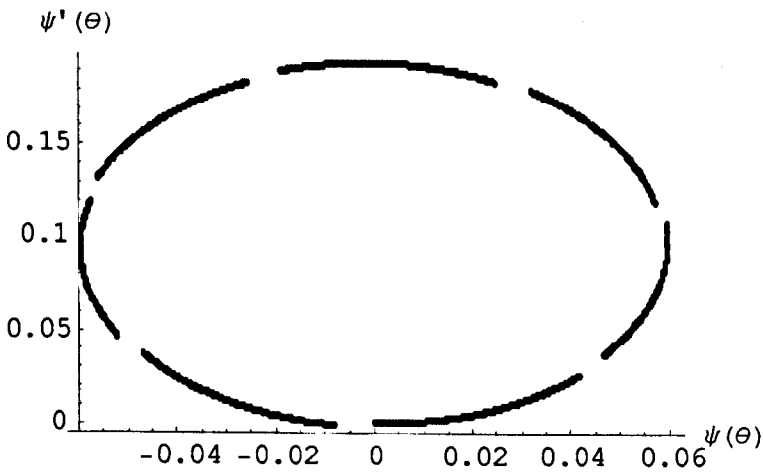


Figure 4.24 Poincaré map sampling at perigee for 1000 orbits with $e = 0.147$ and $\dot{\psi}(0) = \psi(0) = 0$.

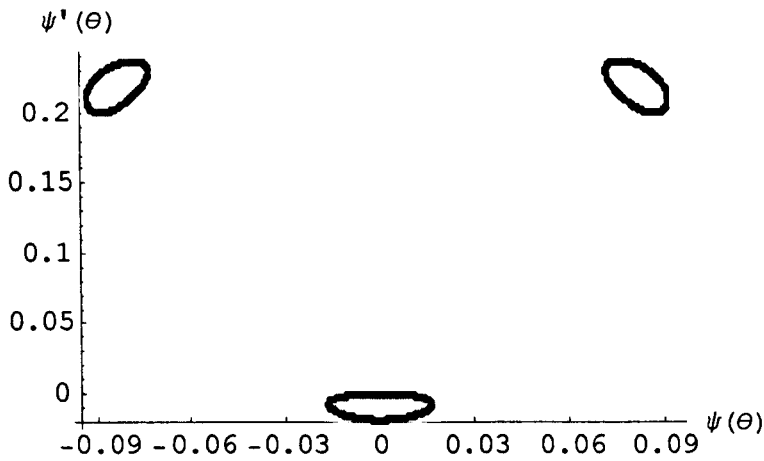


Figure 4.25 Poincaré map sampling at each perigee crossing for 1000 orbits with $e = 0.24795$ and $\dot{\psi}(0) = \psi(0) = 0$.

The bifurcation diagram shown in Figure 4.26 magnifies the region ranging between $0.31 \leq e \leq 0.315$ for a tethered dumbbell with $\dot{\psi}(0) = \psi(0) = 0$ and is the part of the bifurcation diagram just prior to where the tether visits all parts of the phase space. A period-7 window is visible in Figure 4.26, which after taking 2000 samples the Poincaré map in Figure 4.27 confirms to be a genuine period-7 orbit for a dumbbell with $e = 0.313025$ and $\dot{\psi}(0) = \psi(0) = 0$. When the orbit eccentricity is increased to $e = 0.33$ for an initially radial tether then the Poincaré map becomes freely populated with points, as shown in Figure 4.28, suggesting the tether is undergoing chaotic motion, which is confirmed by the positive Lyapunov exponent in Figure 4.19. The global onset of chaos is seen to commence for the radial tether upon orbit eccentricities of 0.3144. However, weakly chaotic motions as indicated by the small but positive first Lyapunov exponent in Figure 4.29 exist for e around 0.314. These results and observations agree with those made by Karasopoulos and Richardson (1992).

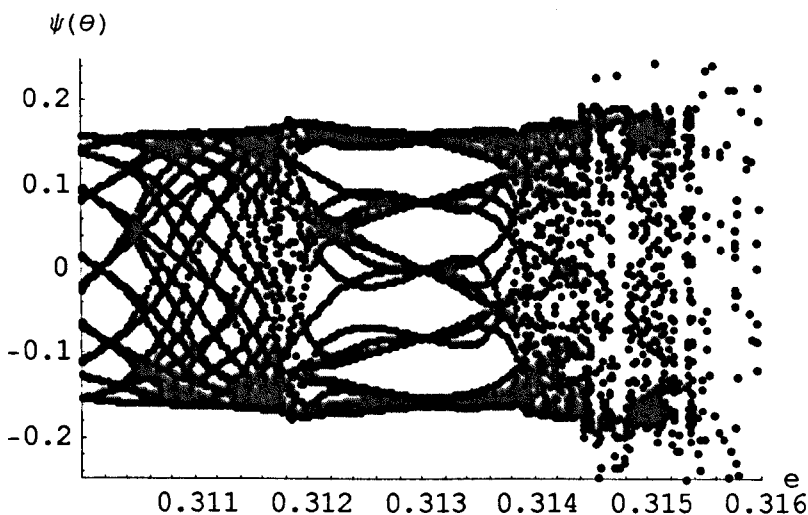


Figure 4.26 Bifurcation Diagram of the angular displacement with respect to the orbit eccentricity. Initial conditions are $\dot{\psi}(0)=0$ and $\psi(0)=0$ rad with a step size in e of 0.000025. Each column of results contains 50 points.

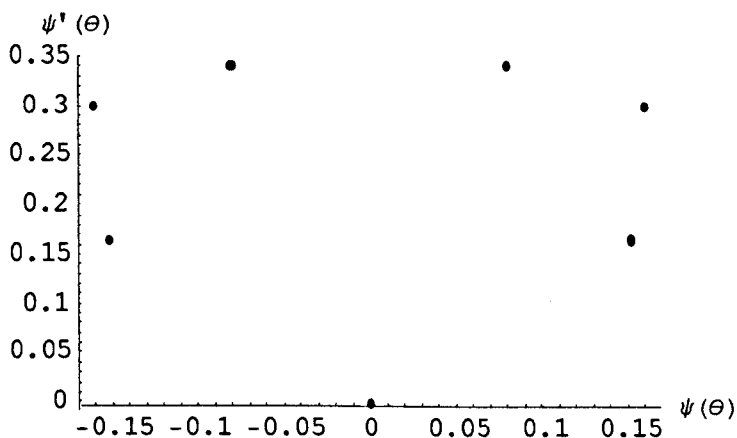


Figure 4.27 Poincaré map sampling at each perigee crossing for 2000 orbits with $e = 0.313025$ and $\dot{\psi}(0)=\psi(0)=0$.

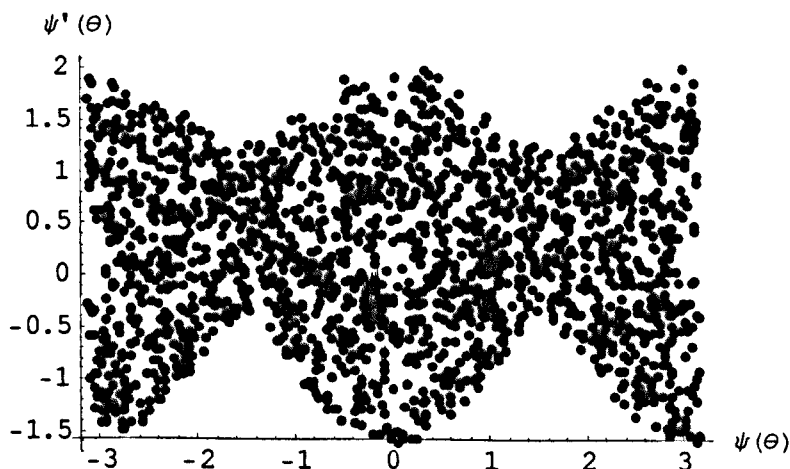


Figure 4.28 Poincaré map sampling at each perigee crossing for 1000 orbits with $e = 0.33$ and $\dot{\psi}(0)=\psi(0)=0$.

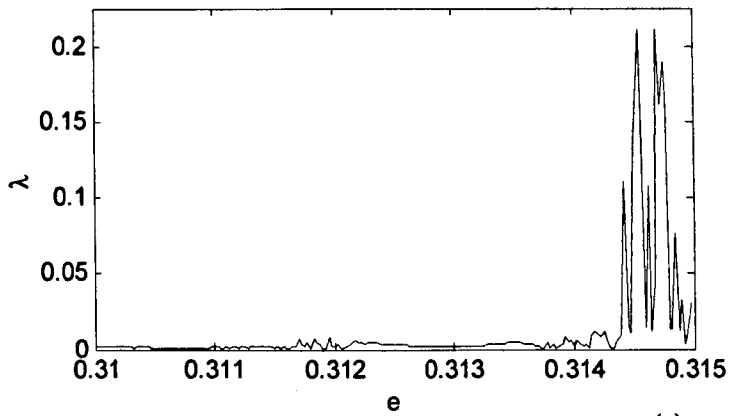


Figure 4.29 First Lyapunov exponent for a tether with $\dot{\psi}(0)=\psi(0)=0$ between $0.31 \leq e \leq 0.315$. 200 points are plotted, each calculated over 80 orbits, with a stepsize in e of 0.000025.

By introducing an initial angular displacement away from the local vertical the conical shape to the bifurcation diagram at low eccentricities is seen to disappear in Figure 4.30 and Figure 4.32. Moreover, the point at which the tether commences to visit all regions of the phase space reduces from $e \approx 0.31$ to $e \approx 0.14$ for both initial conditions of $\psi(0) = \pm 0.5$ rad. The first Lyapunov exponent in Figure 4.31 and Figure 4.33 confirms the motion of the dumbbell above eccentricities of ~ 0.14 to be chaotic. Consequently, the initial angular displacement is seen in addition to the orbit eccentricity to have a strong influence on the onset of chaos. The magnification of the region $0.14 \leq e \leq 0.145$ in Figure 4.34 and Figure 4.35 for $\psi(0) = 0.5$ rad shows it is not a mirror image of the same magnified zone in Figure 4.36 and Figure 4.37 for $\psi(0) = -0.5$ rad. The largest Lyapunov exponent for $\psi(0) = \pm 0.5$ rad in Figure 4.35 and Figure 4.37 suggest the global onset of chaos occurs in both cases slightly below $e = 0.141$.

Figure 4.38 presents the largest Lyapunov exponent calculated for any given orbit eccentricity and initial angular displacement. All the previously presented Lyapunov exponents represent cross-sections through Figure 4.38. The use of the colour red indicates a value of zero for the largest Lyapunov exponent and the remaining colours portray from yellow to purple a positive first Lyapunov exponent. The figure clearly shows the Lyapunov exponent growing for larger values of e and that the largest zone of regular motion occurs for a tether initially close to the local vertical. The shape of the red area of regular motion is strikingly similar to the region of long-term tether libration in Figure 4.4. Thus, there appears to be a strong correlation between regular and libration motion of the tether, as well as between tumbling and chaotic motion. Hence, the results suggest a planar tether with

$\dot{\psi} = 0$ on an elliptical orbit does not indefinitely librate in a chaotic manner and does not tumble in a periodic manner.

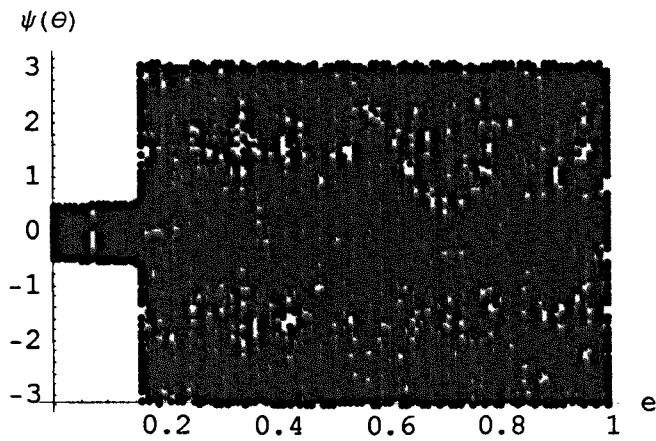


Figure 4.30 Bifurcation diagram of the angular displacement with respect to the orbit eccentricity. Initial conditions are $\dot{\psi}(0) = 0$ and $\psi(0) = 0.5$ rad and the step size in e is 0.01. Each column of results contains 200 points.

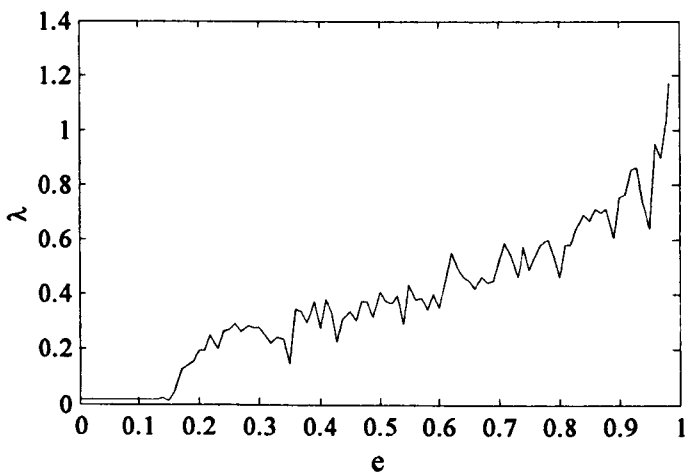


Figure 4.31 First Lyapunov exponent for a tether with $\dot{\psi}(0) = 0$ and $\psi(0) = 0.5$ rad. 100 points are plotted, each calculated over 40 orbits, with a stepsize in e of 0.01.

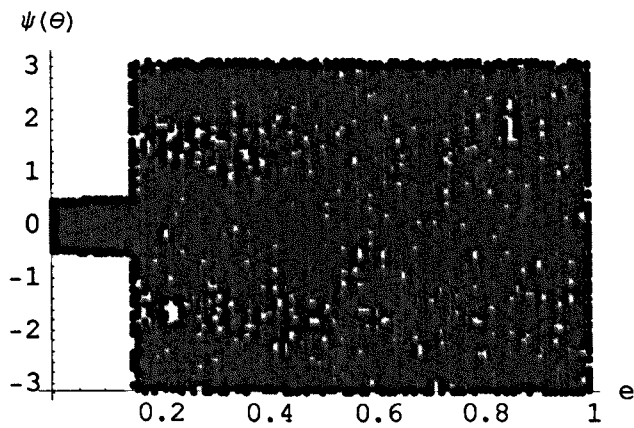


Figure 4.32 Bifurcation diagram of the angular displacement with respect to the orbit eccentricity. Initial conditions are $\dot{\psi}(0)=0$ and $\psi(0)=-0.5$ rad and the step size in e is 0.01. Each column of results contains 200 points.

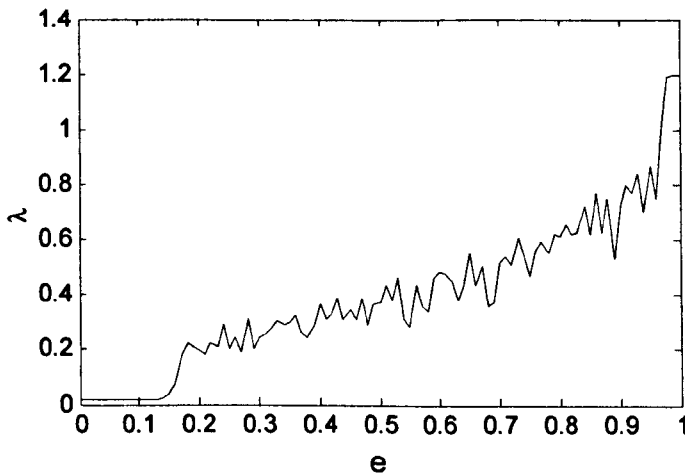


Figure 4.33 First Lyapunov exponent for a tether with $\dot{\psi}(0)=0$ and $\psi(0)=-0.5$ rad. 100 points are plotted, each calculated over 40 orbits, with a stepsize in e of 0.01.

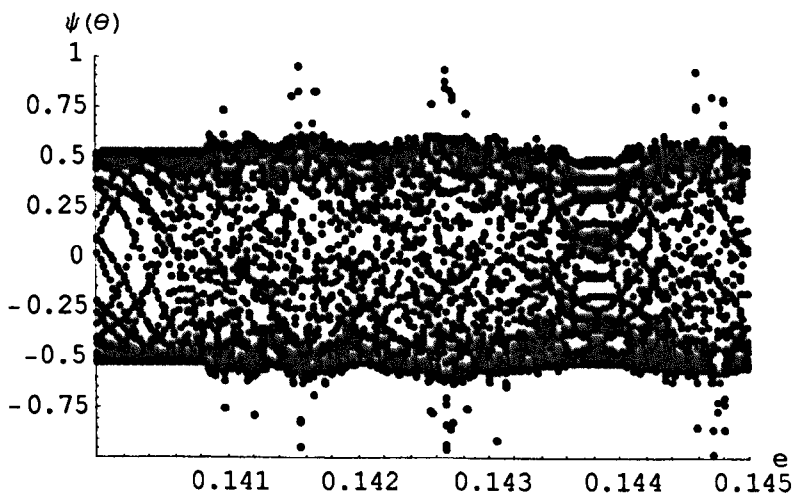


Figure 4.34 Bifurcation diagram of the angular displacement with respect to the orbit eccentricity. Initial conditions are $\dot{\psi}(0)=0$ and $\psi(0)=0.5$ rad and the step size in e is 0.000025. Each column of results contains 50 points.

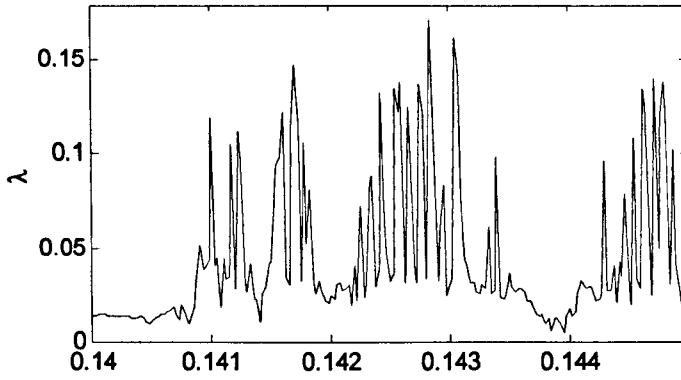


Figure 4.35 First Lyapunov exponent for a tether with $\dot{\psi}(0)=0$ and $\psi(0)=0.5$ rad. 200 points are plotted, each calculated over 80 orbits, with a stepsize in e of 0.000025.

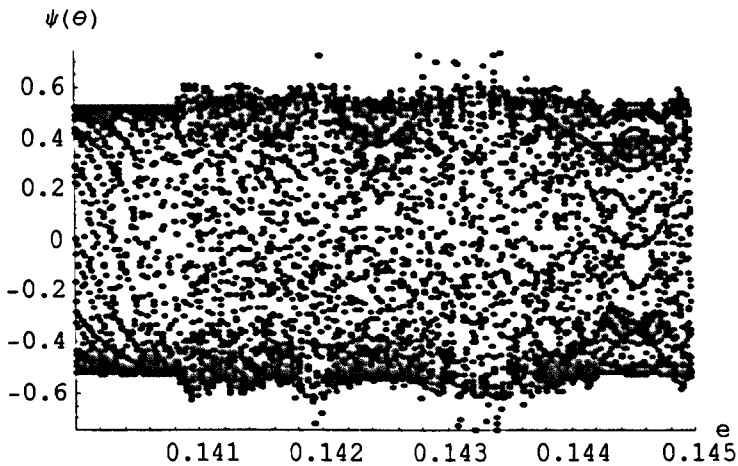


Figure 4.36 Bifurcation diagram of the angular displacement with respect to the orbit eccentricity. Initial conditions are $\dot{\psi}(0)=0$ and $\psi(0)=-0.5$ rad and the step size in e is 0.000025. Each column of results contains 50 points.

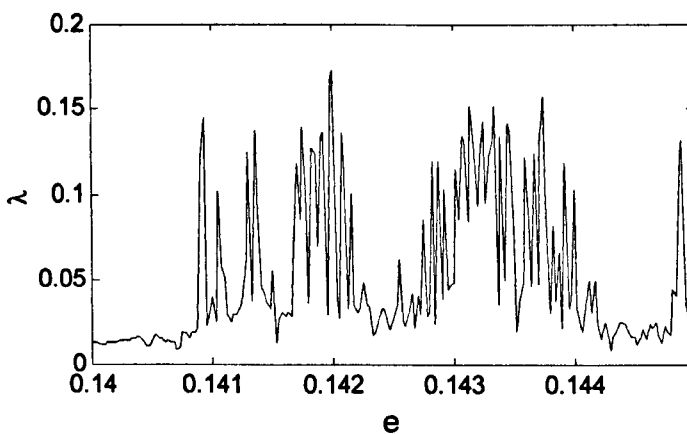


Figure 4.37 First Lyapunov exponent for a tether with $\dot{\psi}(0)=0$ and $\psi(0)=-0.5$ rad. 200 points are plotted, each calculated over 80 orbits, with a stepsize in e of 0.000025.

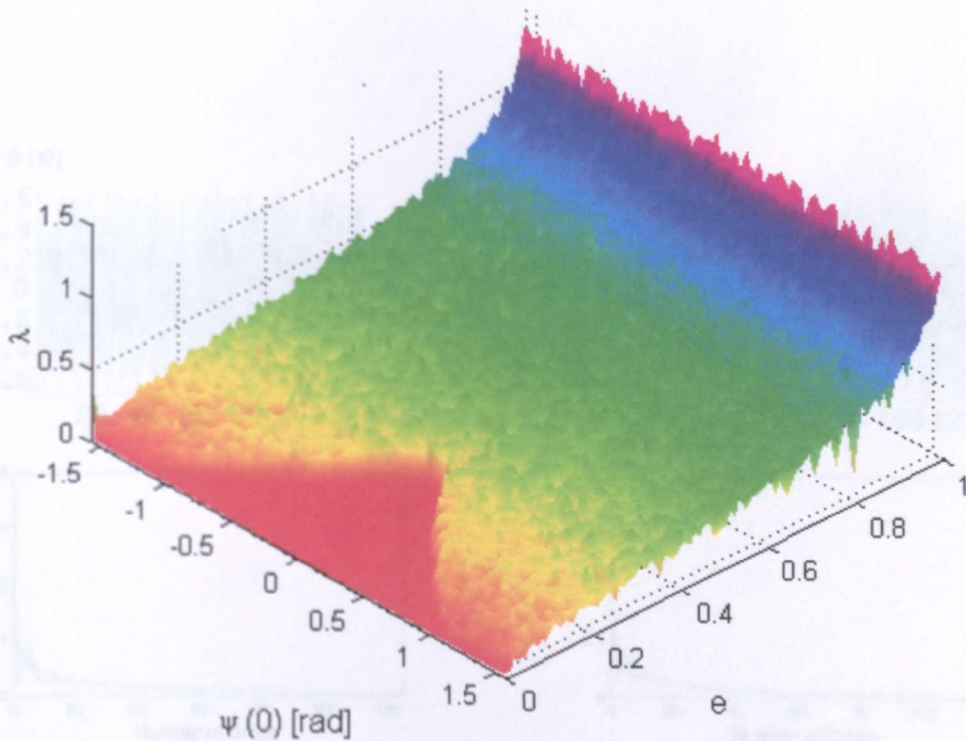


Figure 4.38 First Lyapunov exponent with respect to $\psi(0)$ and e .

4.5 Comparison between the Onset of Spin and Chaos

Figure 4.39-Figure 4.46 compare the time history, first Lyapunov exponent, Poincaré map and power spectrum for an initially motionless and radial tether on eight different orbit eccentricities, namely 0.31, 0.312, 0.313, 0.314, 0.314425, 0.3145, 0.315 and 0.316. The range of eccentricities is representative of the range between regular and chaotic motion, as well as the boundary between libration and tumbling. For e equal to 0.31, 0.312, 0.313 and 0.314 in Figure 4.39-Figure 4.42, the tether is librating during the 125 completed orbits and the first Lyapunov exponent is converging towards zero over the same period of time. Thus, the response is regular. Moreover, the 125 sampled points in the Poincaré maps are beginning to form closed curves and numerous but discrete peaks exist in the power spectra, which suggests the motion is quasi-periodic. Figure 4.40 is important as Karasopoulos and Richardson (1992) claim to find weakly chaotic motion below $e = 0.312$. Indeed positive Lyapunov exponents were also obtained for eccentricities in this region but the numerical integration with tighter relative and absolute errors yields Lyapunov exponents that converge towards zero, as shown.

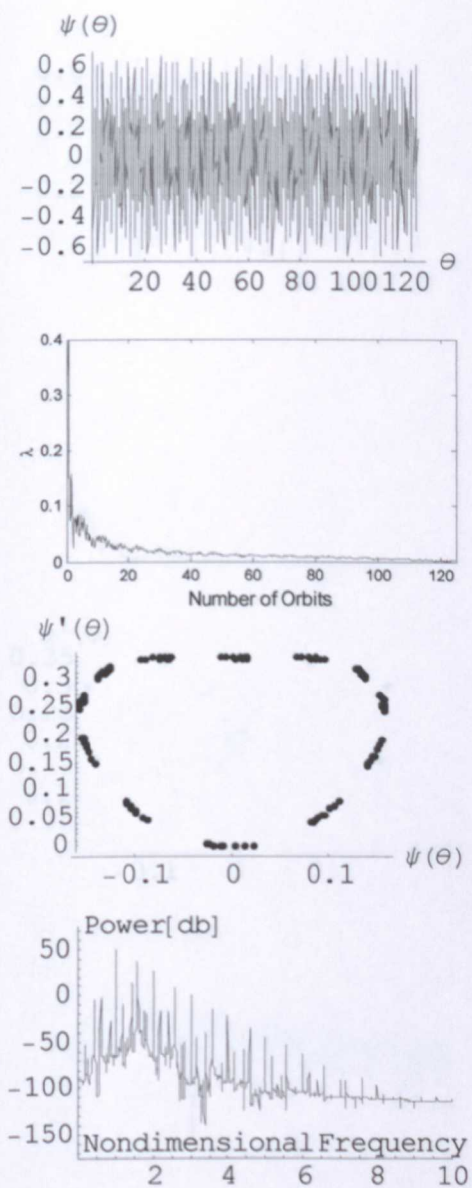


Figure 4.39 Time history, first Lyapunov exponent, Poincaré map and power spectrum of the tether with $e = 0.31$ and $\psi(0) = \dot{\psi}(0) = 0$.

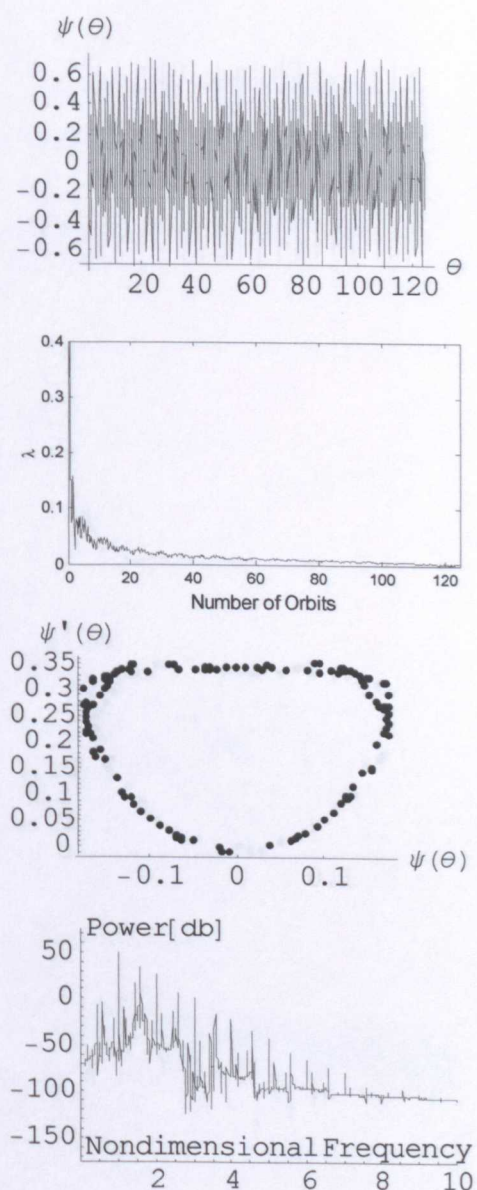


Figure 4.40 Time history, first Lyapunov exponent, Poincaré map and power spectrum of the tether with $e = 0.312$ and $\psi(0) = \dot{\psi}(0) = 0$.

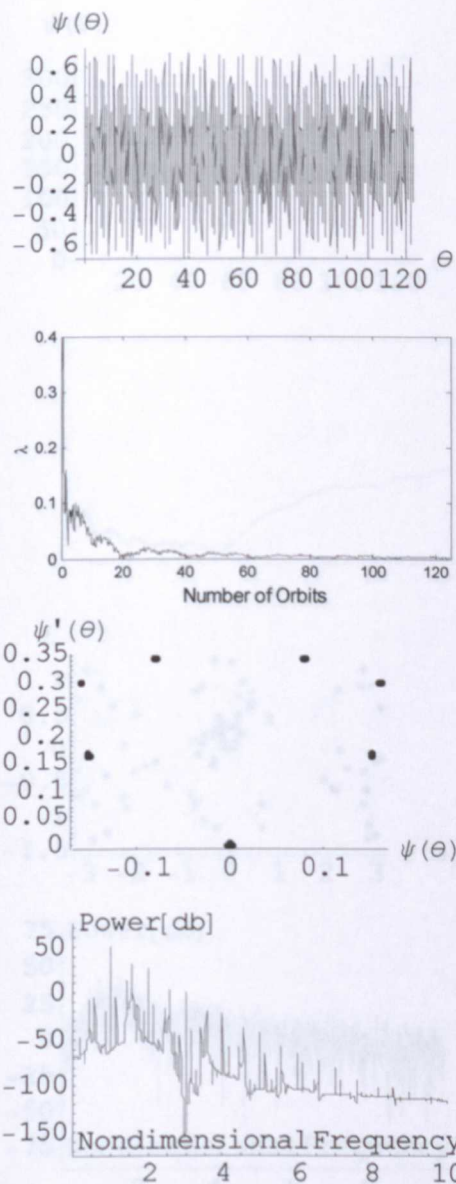


Figure 4.41 Time history, first Lyapunov exponent, Poincaré map and power spectrum of the tether with $e = 0.313$ and $\dot{\psi}(0) = \psi(0) = 0$.

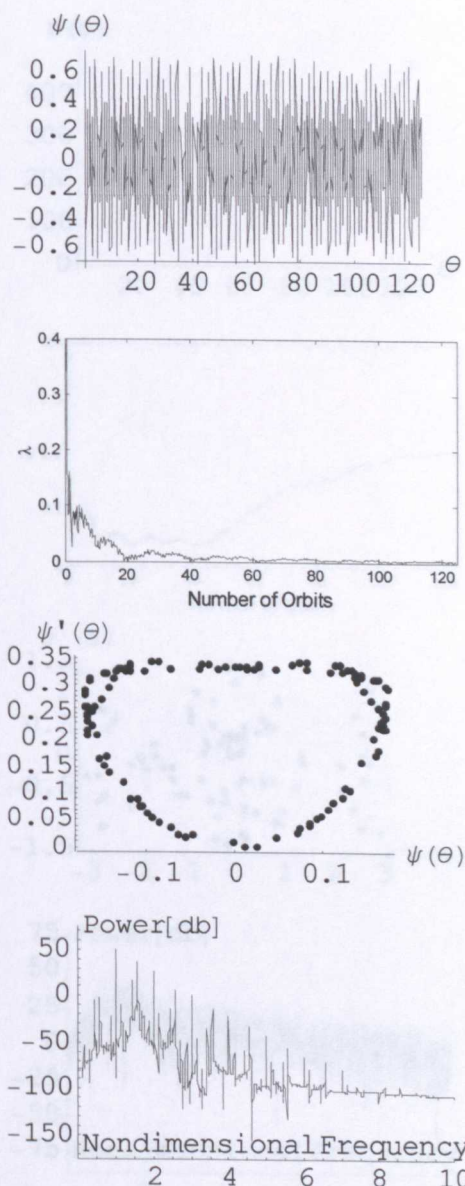


Figure 4.42 Time history, first Lyapunov exponent, Poincaré map and power spectrum of the tether with $e = 0.314$ and $\dot{\psi}(0) = \psi(0) = 0$.

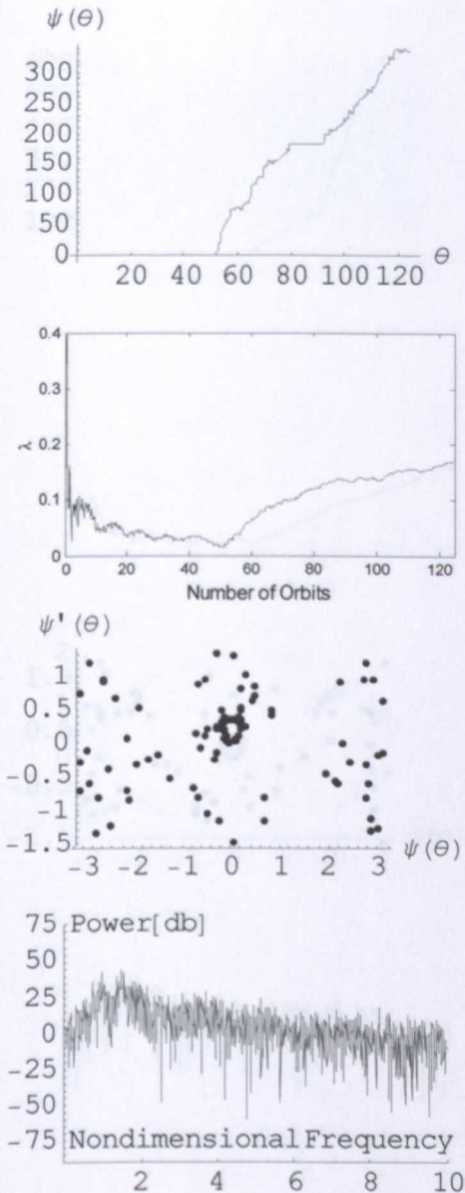


Figure 4.43 Time history, first Lyapunov exponent, Poincaré map and power spectrum of the tether with $e = 0.314425$ and $\dot{\psi}(0) = \psi(0) = 0$.

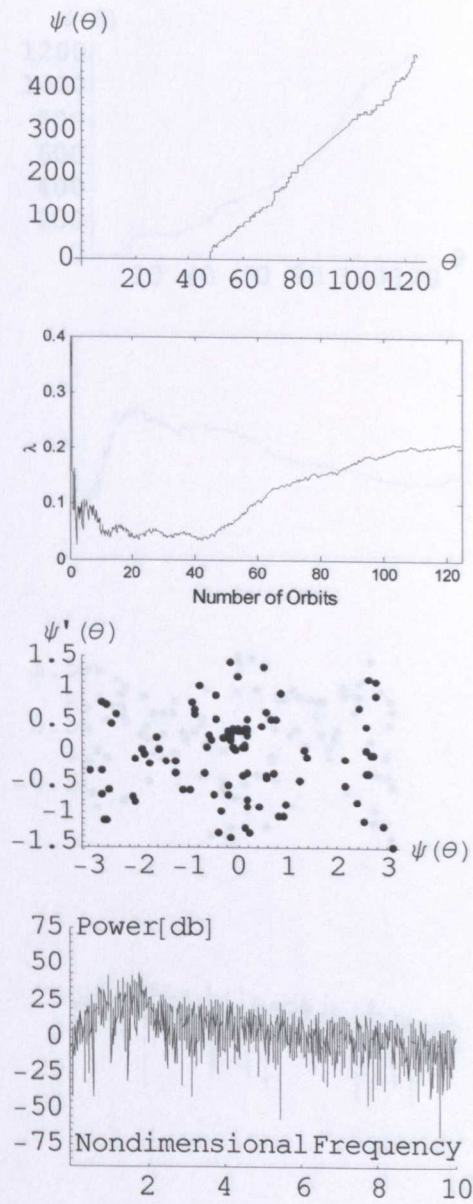


Figure 4.44 Time history, first Lyapunov exponent, Poincaré map and power spectrum of the tether with $e = 0.3145$ and $\dot{\psi}(0) = \psi(0) = 0$.

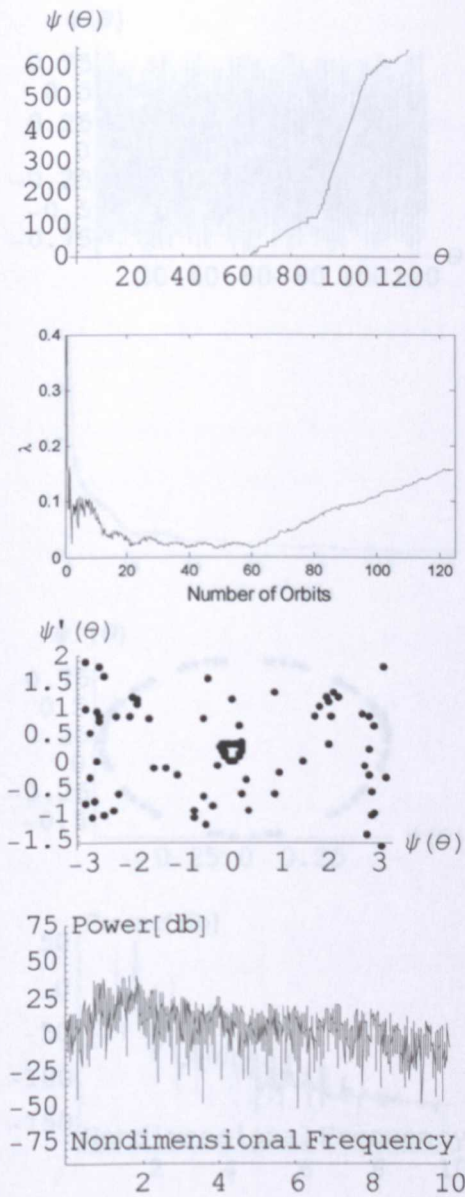


Figure 4.45 Time history, first Lyapunov exponent, Poincaré map and power spectrum of the tether with $e = 0.315$ and $\dot{\psi}(0) = \psi(0) = 0$.

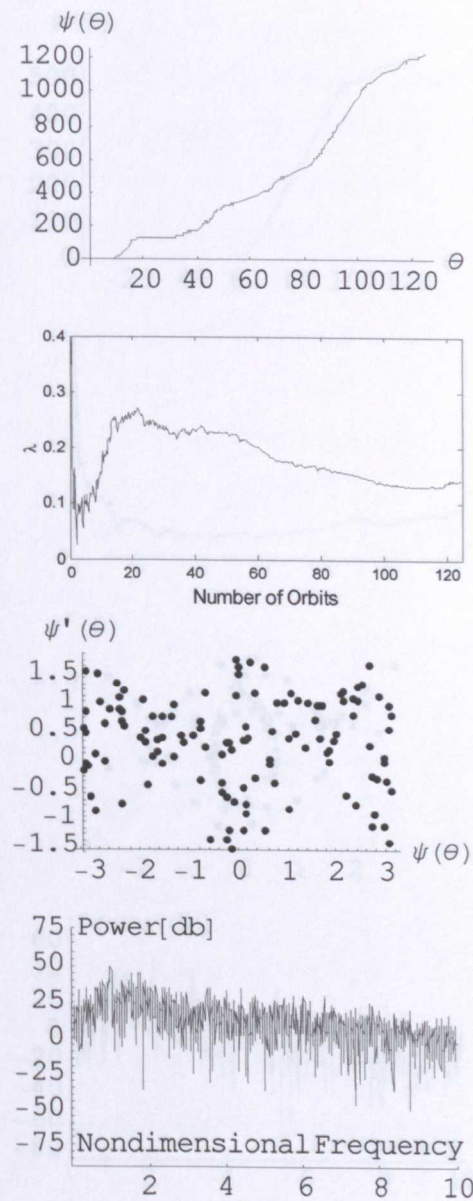


Figure 4.46 Time history, first Lyapunov exponent, Poincaré map and power spectrum of the tether with $e = 0.316$ and $\dot{\psi}(0) = \psi(0) = 0$.

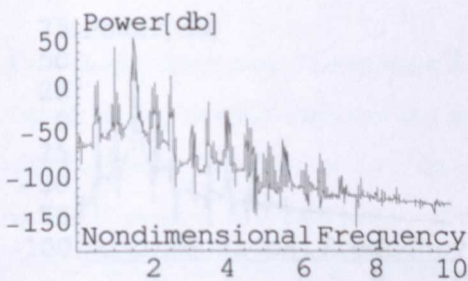
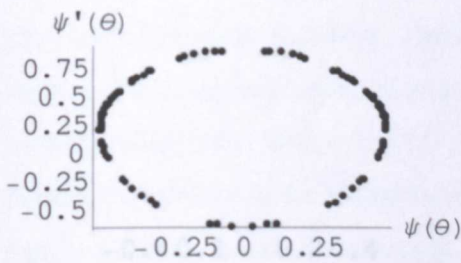
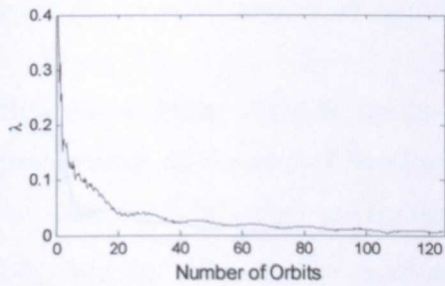
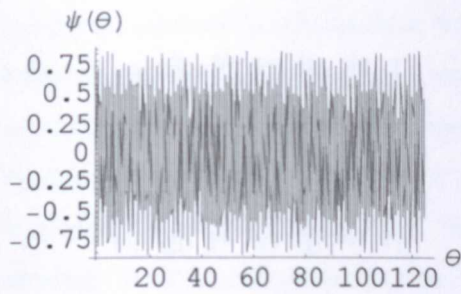


Figure 4.47 Time history, first Lyapunov exponent, Poincaré map and power spectrum of the tether with $e = 0.1405$, $\dot{\psi}(0) = 0$ and $\psi(0) = -0.5$.

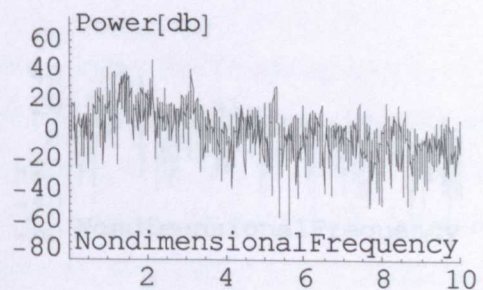
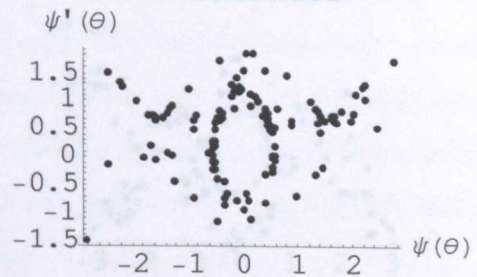
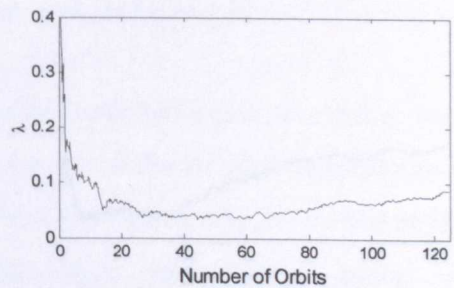
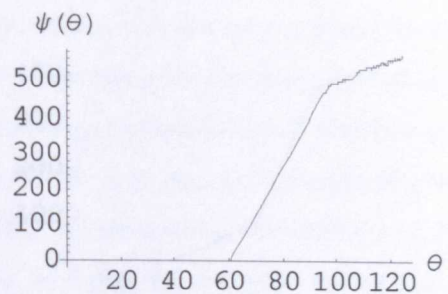


Figure 4.48 Time history, first Lyapunov exponent, Poincaré map and power spectrum of the tether with $e = 0.1415$, $\dot{\psi}(0) = 0$ and $\psi(0) = -0.5$.

The dumbbell's motion changes rather dramatically for orbit eccentricities above 0.316425. Figure 4.43-Figure 4.46 show the tether starting to tumble after librating for numerous orbits. During the period of initial tether libration the largest Lyapunov exponent slowly decays although whether the point of convergence is zero remains unclear. However, the first

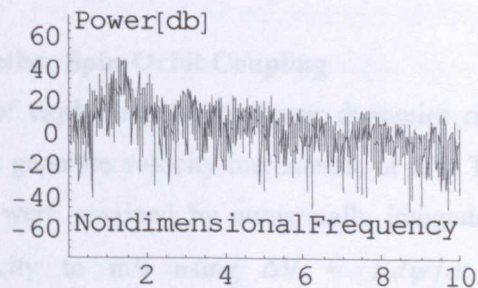
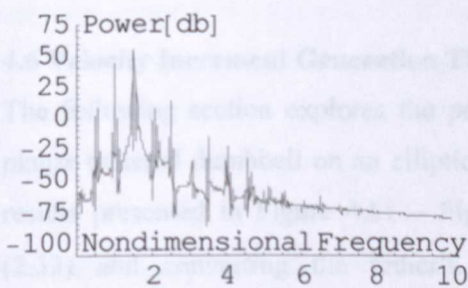
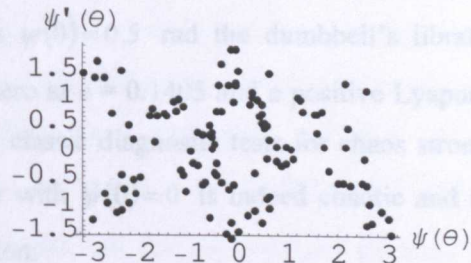
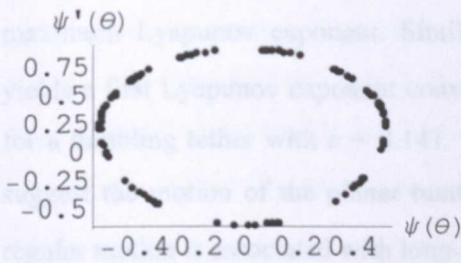
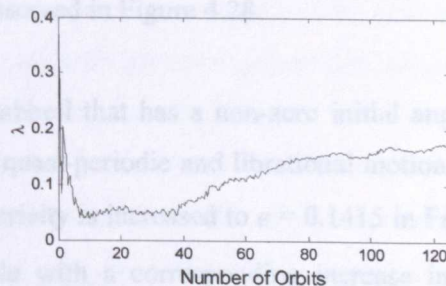
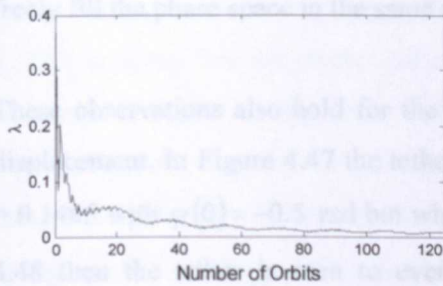
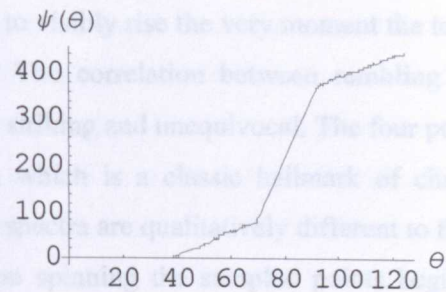
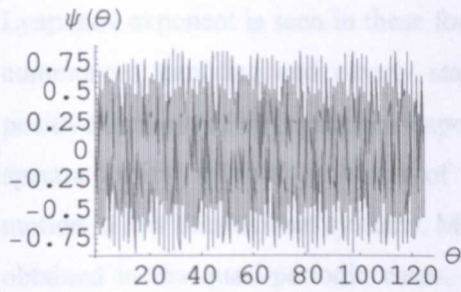


Figure 4.49 Time history, first Lyapunov exponent, Poincaré map and power spectrum of the tether with $e = 0.1405$, $\dot{\psi}(0)=0$ and $\psi(0)=0.5$.

Figure 4.50 Time history, first Lyapunov exponent, Poincaré map and power spectrum of the tether with $e = 0.141$, $\dot{\psi}(0)=0$ and $\psi(0)=0.5$.

The dumbbell's motion changes rather dramatically for orbit eccentricities above 0.314425. Figure 4.43-Figure 4.46 show the tether starting to tumble after librating for numerous orbits. During the period of initial tether libration the largest Lyapunov exponent slowly decays although whether the point of convergence is zero remains unclear. However, the first Lyapunov exponent is seen in these four examples to visibly rise the very moment the tether commences tumbling and clearly stays positive. The correlation between tumbling and positive increase of the Lyapunov exponent is very striking and unequivocal. The four power spectra exhibit a broad spectrum of frequencies, which is a classic hallmark of chaotic motion in low dimensional systems. Moreover, the spectra are qualitatively different to those obtained in the quasi-periodic cases. Finally, upon spinning the sampled points begin to freely fill the phase space in the same manner as observed in Figure 4.28.

These observations also hold for the tethered dumbbell that has a non-zero initial angular displacement. In Figure 4.47 the tether undergoes quasi-periodic and librational motion at $e = 0.1405$ with $\psi(0) = -0.5$ rad but when the eccentricity is increased to $e = 0.1415$ in Figure 4.48 then the tether is seen to eventually tumble with a corresponding increase in the maximum Lyapunov exponent. Similarly, when $\psi(0) = 0.5$ rad the dumbbell's libration yields a first Lyapunov exponent converging to zero at $e = 0.1405$ and a positive Lyapunov for a tumbling tether with $e = 0.141$. Hence, the classic diagnostic tests for chaos strongly suggest the motion of the planar tumbling tether with $\dot{\psi}(0) = 0$ is indeed chaotic and that regular motion is associated with long-term libration.

4.6 Velocity Increment Generation Through Tether Spin-Orbit Coupling

The following section explores the possibility of exploiting the nonlinear dynamics of a planar tethered dumbbell on an elliptical orbit to generate velocity increments, or ΔV . The results presented in Figure 4.51 – Figure 4.58 were obtained by numerically integrating (2.33) and converting the tether's tip velocity to m/s using $\Delta V = L d\psi/dt = L(\mu(1+e)/r^3)^{1/2} d\psi/d\theta$, where $\mu = 3.9877848 \times 10^{14} \text{ m}^3\text{s}^{-2}$, $r = 7000 \text{ km}$, and $L = 100 \text{ km}$. The numerical simulations were started at perigee with zero angular velocity and a given initial pitch angle ranging between $-\pi/2 \leq \psi(0) \leq \pi/2$, therefore utilising the spin-orbit coupling to generate the required libration or rotation. After completing a full orbit the pitch angle and ΔV were recorded upon return to perigee. The tether is assumed to be librating when the pitch angle at perigee, ψ_p , lies between $-\pi/2 \leq \psi_p \leq \pi/2$.

The ΔV and ψ_p obtained at perigee with respect to e is given in Figure 4.51 and Figure 4.52 for $\psi(0) = 0$ rad. The results suggest that the radial tether starts to spin after one full orbit at $e = 0.4796$, which agrees with Figure 4.9, and that the maximum ΔV for the prograde librating and spinning tether is 114.4 m/s and 117.0 m/s with $\psi_p = -0.35$ and 2.75 rad at $e = 0.4232$ and 0.48, respectively. Crellin and Janssens (1996) investigated the ΔV generated by a 100 km long tether moving freely on an elliptical orbit and their results are not identical but quantitatively similar to those in Figure 4.51. In the majority of cases the spinning tether is, due to the negative ΔV , undergoing retrograde motion at perigee and, in addition, Figure 4.51 shows that the magnitude of the retrograde ΔV is larger than that of the prograde motion. Furthermore, the largest positive ΔV for the spinning tether occurs shortly after the tether has begun to rotate and tapers off, along with the maximum negative ΔV , with larger e . This suggests that a spinning tether does not necessarily generate greater ΔV within the first orbit at higher e . The tether may have an initial angular displacement at the time of payload capture, thus requiring the payload, however, to be delivered to a higher altitude by the ground launcher. The ΔV and ψ_p achievable at perigee with $-\pi/2 \leq \psi(0) \leq \pi/2$ is given in Figure 4.53 and Figure 4.54 for $e = 0.1$. The result suggests that a positive $\psi(0)$ delays the onset of spin whereas a negative $\psi(0)$ encourages tether rotation, as is also observed in Figure 4.9. Figure 4.55 to Figure 4.58, which display the ΔV and ψ_p obtained at perigee with respect to e for $\psi(0) = \pm 0.3$ rad, confirm these observations. The tether, in Figure 4.53 and Figure 4.54, is found to spin when $-\pi/2 \leq \psi(0) \leq -0.841$ rad, $1.484 \leq \psi(0) \leq 1.515$ rad and $1.538 \leq \psi(0) \leq \pi/2$ rad. When $e = 0.1$ the maximum ΔV for the prograde librating and spinning tether is 162 m/s and 195.6 m/s, with $\psi(0) = -0.72$ and -1.49 rad, and $\psi_p = -0.13$ and 6.23 rad, respectively. The results show that the largest positive ΔV at perigee does not necessarily occur when the payload is above the facility with the tether aligned along the gravity vector.

For optimum payload transfer of an incoming payload from Earth, the largest possible positive ΔV is required when $\psi_p = \pm(\pi + 2n\pi)$ rad, where $n = 0, 1, 2, \dots$. The radial tether can deliver the payload at perigee close to the vertical above the facility with $n = 0$, $\psi_p = 3.15$ rad, $e = 0.482$ and $\Delta V = 5.6$ m/s in a window where prograde rotation occurs within $0.4796 \leq e \leq 0.482$. The following data gives the next three opportunities for delivering the payload as required: $n = 1$, $\psi_p = 9.43$ rad, $e = 0.5692$ and $\Delta V = 52.8$ m/s in a window where prograde rotation occurs within $0.5652 \leq e \leq 0.5712$; $n = 2$, $\psi_p = 15.7$ rad, $e = 0.6372$ and $\Delta V = 4.6$ m/s in a window where prograde rotation occurs within $0.632 \leq e \leq 0.6372$; $n = 3$, $\psi_p = 21.99$ rad, $e = 0.6828$ and $\Delta V = 15.3$ m/s in a window where prograde rotation occurs within $0.6792 \leq e \leq 0.6832$. When the tether has an initial angular displacement at the time

of payload capture then the payload can be delivered above the facility close to the vertical for the following sole case: $\psi(0) = -0.842$ rad, $e = 0.1$, $\psi_p = 3.17$ rad and $\Delta V = 177$ m/s. However, a small change in the given $\psi(0)$ leads to values for ψ_p that are not close to π and hence the practical implementation of this initial condition is questionable. The results above show it is difficult to find initial conditions that allow the payload to be released above the facility at perigee when the spinning tether is aligned exactly along the gravity vector at perigee, a problem which is not encountered on circular orbits. This small discrepancy reduces the effective tangential velocity of the payload imparted on release and causes a change in the released payload's orbital elements due to the ΔV vector not being aligned with the tangential orbital velocity vector. Furthermore, once all the environmental perturbations are taken into account, and observing the nature of the spinning tether depicted in Figure 4.51 – Figure 4.58 along with the small windows in which prograde rotation occurs, it becomes questionable whether the spin-orbit coupling of the tether is a viable method of generating ΔV . Moreover, mission analyses envisage the tethers to be reused, thus becoming competitive with chemical propulsion, and therefore remaining in orbit over longer periods of time. From the results above the motion of an initial radial tethered dumbbell is chaotic for orbit eccentricities greater than approximately 0.314. Hence, the orbit eccentricities that are greater than 0.314 are impractical for a freely moving dumbbell as the tether position and ΔV cannot be predicted in the long-term for payload rendezvous or release.

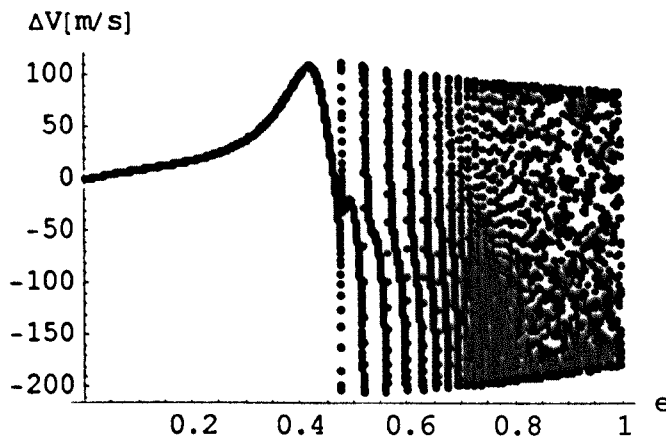


Figure 4.51 ΔV obtained at perigee after a full orbit with respect to e for $\psi(0) = 0$ rad. Plot contains 5000 points with a step size in e of 0.0002.

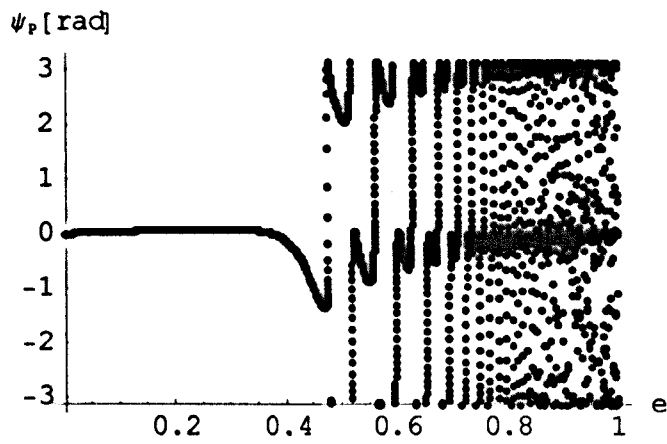


Figure 4.52 ψ_p (modulus 2π where $\psi_p \in [-\pi, \pi)$) obtained at perigee after a full orbit with respect to e for $\psi(0) = 0$ rad. Plot contains 5000 points with a step size in e of 0.0002.

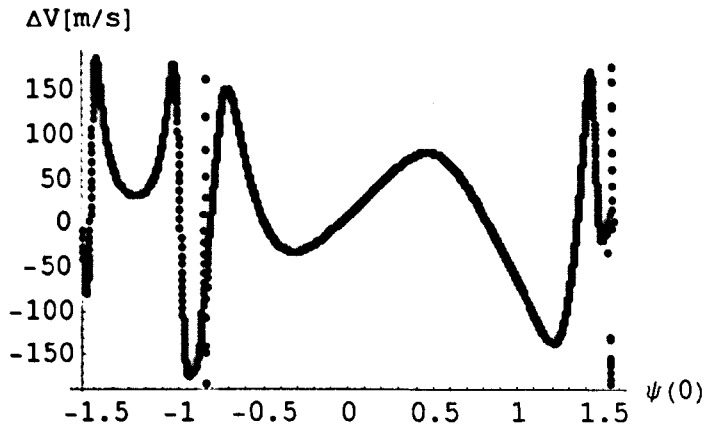


Figure 4.53 ΔV obtained at perigee after a full orbit with respect to $\psi(0)$ for $e = 0.1$. Plot contains 2500 points with a step size in $\psi(0)$ of $\pi/2500$ rad.

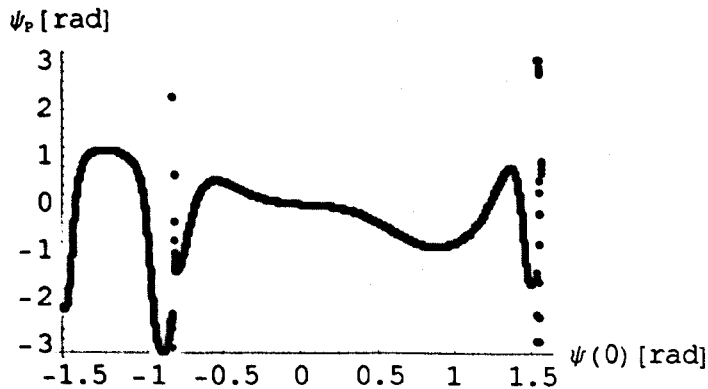


Figure 4.54 ψ_p obtained at perigee after a full orbit with respect to $\psi(0)$ for $e = 0.1$. Plot contains 2500 points with a step size in $\psi(0)$ of $\pi/2500$ rad.

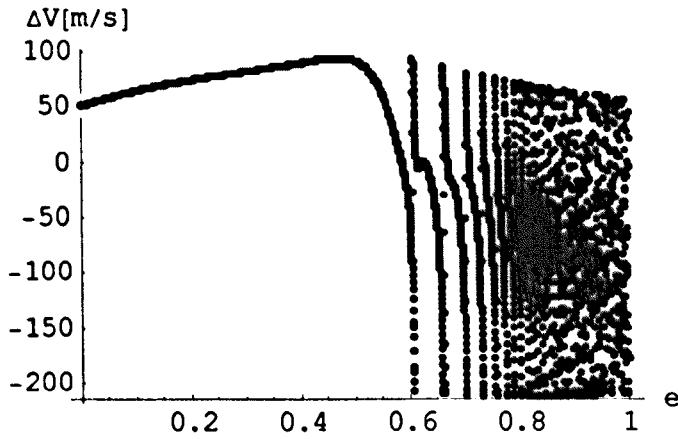


Figure 4.55 ΔV obtained at perigee after a full orbit with respect to e for $\psi(0) = 0.3$ rad. Plot contains 5000 points with a step size in e of 0.0002.

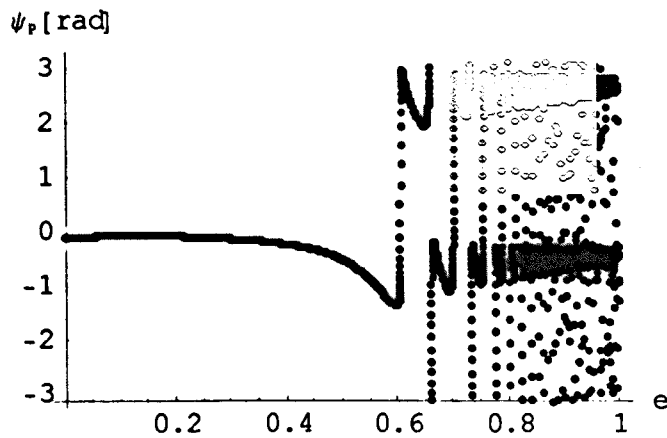


Figure 4.56 ψ_p (modulus 2π where $\psi_p \in [-\pi, \pi)$) obtained at perigee after a full orbit with respect to e for $\psi(0) = 0.3$ rad. Plot contains 5000 points with a step size in e of 0.0002.

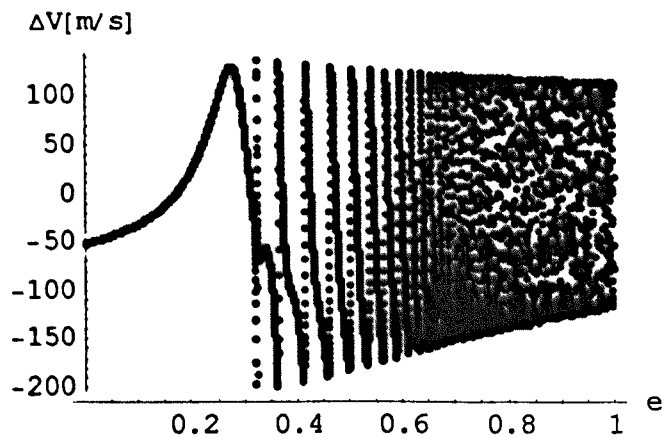


Figure 4.57 ΔV obtained at perigee after a full orbit with respect to e for $\psi(0) = -0.3$ rad. Plot contains 5000 points with a step size in e of 0.0002.

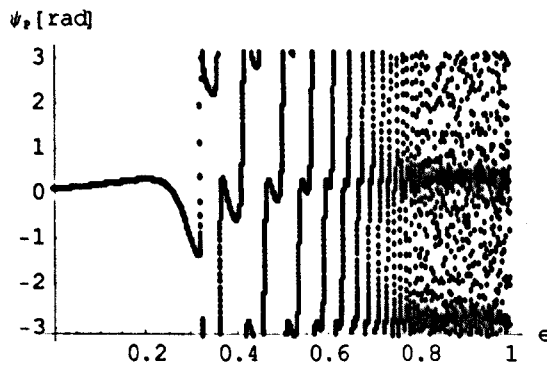


Figure 4.58 ψ_p (modulus 2π where $\psi_p \in [-\pi, \pi)$) obtained at perigee after a full orbit with respect to e for $\psi(0) = -0.3$ rad. Plot contains 5000 points with a step size in e of 0.0002.

4.7 Conclusions

The planar attitude dynamics of a tethered dumbbell on an elliptical orbit have been numerically explored in this chapter. The orbit eccentricity and initial angular displacement were found to affect the boundary between long-term libration and tumbling. The largest stable region exists for a tether with no initial angular velocity and initially positioned close to the local vertical. The long-term libration-tumbling boundary is globally symmetrical about the local vertical but is not found in all cases to be a clearly defined and continuous curve since some regions exhibited discontinuities. A further asymmetrical boundary was discovered for the onset of spin during the first completed orbit, which results in a positive initial angular displacement delaying the onset of tumbling, whereas a negative initial condition encourages tether rotation. The two identified boundaries describe a region where tether libration occurs as a transient and a remarkable structure is uncovered within the region that governs the duration of the transient. The onset of chaos was similarly found to be a function of orbit eccentricity and initial angular displacement. The first Lyapunov exponent with respect to the orbit eccentricity and initial condition yielded a region corresponding to the area of long-term libration. The correlation between tumbling and positive increase of the Lyapunov exponent is found to be very striking and unequivocal. The results suggest a planar tether with $\dot{\psi} = 0$ on an elliptical orbit does not indefinitely librate in a chaotic manner and does not tumble in a periodic manner. Finally, the generation of velocity increments upon completion of a single orbit through the spin-orbit coupling on an elliptical orbit is not found to be of particular use. Few initial conditions exist that allow the payload to be reliably released above the facility when the spinning tether is aligned exactly along the gravity vector at perigee. Moreover, the largest positive ΔV of a couple of hundred metres per second at perigee does not necessarily occur when the payload is above the facility with the tether aligned along the gravity vector, thus releasing the payload in a non-optimum configuration in relation to the orbital velocities.

Chapter 5

Three-Dimensional Dynamics of a Tethered Dumbbell on Circular and Elliptical Orbits

5.0 Introduction

The previous chapter focussed on the planar dynamics of the tethered dumbbell on elliptical orbits. This chapter will remove the constraint of the tether moving within the orbital plane and investigate how an initial angular displacement out of the orbital plane affects the dumbbell's motion. In particular the chapter aims to map the boundary at which the tether commences tumbling and to assess whether chaotic motion is associated with tether tumbling. Following the discovery in the previous chapter of a structured zone of transient libration prior to tumbling, the tether's three-dimensional transient behaviour will also be investigated.

5.1 Steady-state Boundary between Libration and Spin

The graphs in Figure 5.1-Figure 5.4 are generated by numerically integrating (2.33)-(2.34) for a duration of 50 orbits and subsequently checking at every perigee and apogee whether the tether has tumbled. In contrast to the planar tether the three-dimensional motion is equally prone to both prograde and retrograde motion where prograde rotation was generally found to dominate the planar dumbbell. Moreover, the dumbbell with an out-of-plane initial condition is observed in many cases to quite readily switch from prograde to retrograde tumbling or vice versa. Hence, the introduction of additional evaluations at every perigee and apogee to ensure tether rotation is recorded after the completion of 50 orbits. If tumbling is observed for a given pair of initial angular displacements within or out of the orbital plane then a point is plotted in the graphs. If after 50 orbits the tether has not tumbled then the tether is considered to be librating indefinitely, which for the resolution in Figure 5.1-Figure 5.4 is found to be satisfactory. The results are symmetric about the axis defined by $\alpha(0) = 0$ and hence only the results for positive $\alpha(0)$ are presented.

Figure 5.1 shows that a relatively large number of initial conditions exist for which the dumbbell undergoes steady-state libration on a circular orbit. The results are largely symmetrical about the $\psi(0) = 0$ axis but when looked at in detail the boundary is not found to be a precise mirror image. The maximum initial out-of-plane displacement that yields

libration is when the tether is initially aligned along the local vertical. The larger the initial angular displacement is in ψ the smaller $\alpha(0)$ has to be for libration to exist. Increasing the orbit eccentricity from zero to 0.1, as depicted in Figure 5.2, causes the number of initial conditions giving rise to libration to significantly decrease. The boundary between steady-state libration and spin is not trivial with many islands of initial conditions causing the tether to tumble within the general area of libration. In detail the boundary is clearly not symmetrical about the local vertical. The libration-spin boundary becomes more straightforward upon increasing the orbit eccentricity to 0.2, as seen in Figure 5.3. The zone of steady-state libration is further reduced with the majority of initial conditions giving way to tumbling. When the eccentricity is yet further increased to 0.3 only a small number of initial conditions remain that let the tether librate. Furthermore, Figure 5.1-Figure 5.4 indicate that a relatively small out-of-plane initial displacement does not cause the tethered dumbbell to behave qualitatively different from the planar case. The dumbbell deviates from the planar tether's qualitative behaviour only when $\alpha(0)$ becomes sufficiently large. The maximum permissible out-of-plane angle for stable motion exists when the tether is initially aligned along the local vertical.

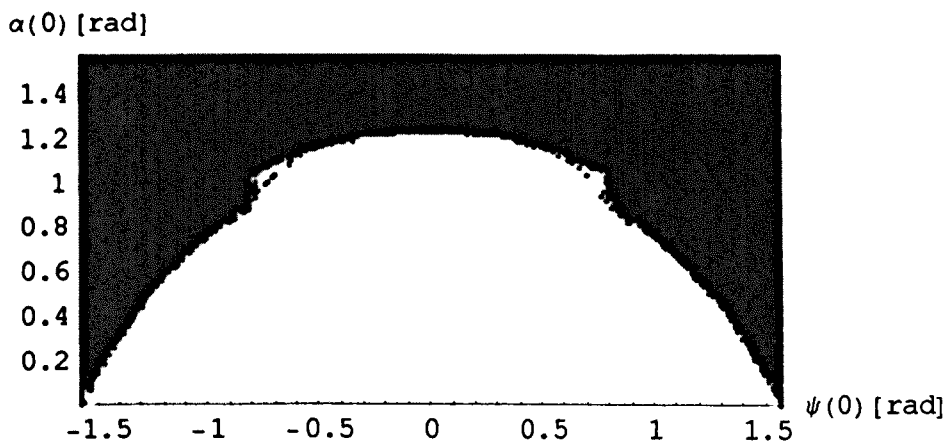


Figure 5.1 Effect of initial in- and out-of-plane angular displacement on tether libration (white) and tumbling (black) over 50 completed orbits with $e = 0$. Plot contains 80000 points with a step size of $\pi/400$ for both $\psi(0)$ and $\alpha(0)$, respectively.

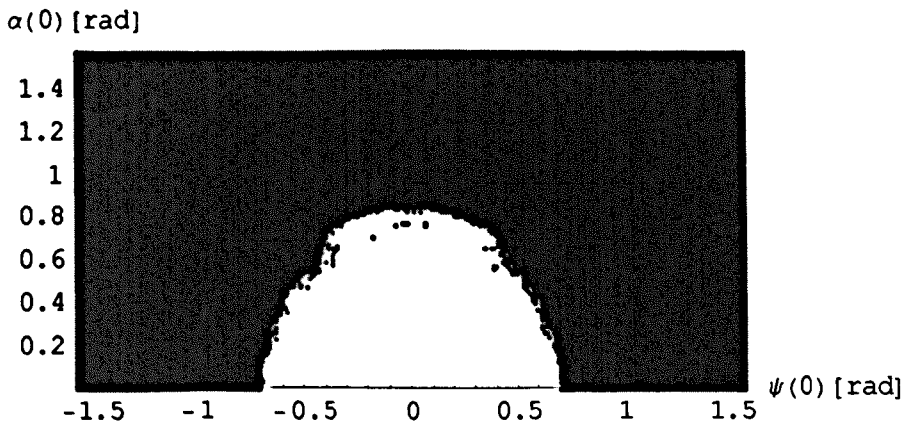


Figure 5.2 Effect of initial in- and out-of-plane angular displacement on tether libration (white) and tumbling (black) over 50 completed orbits with $e = 0.1$. Plot contains 80000 points with a step size of $\pi/400$ for both $\psi(0)$ and $\alpha(0)$, respectively.

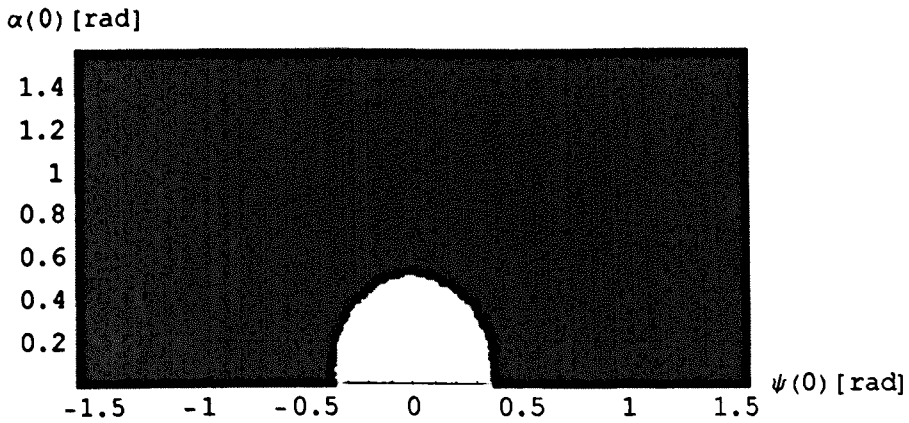


Figure 5.3 Effect of initial in- and out-of-plane angular displacement on tether libration (white) and tumbling (black) over 50 completed orbits with $e = 0.2$. Plot contains 80000 points with a step size of $\pi/400$ for both $\psi(0)$ and $\alpha(0)$, respectively.

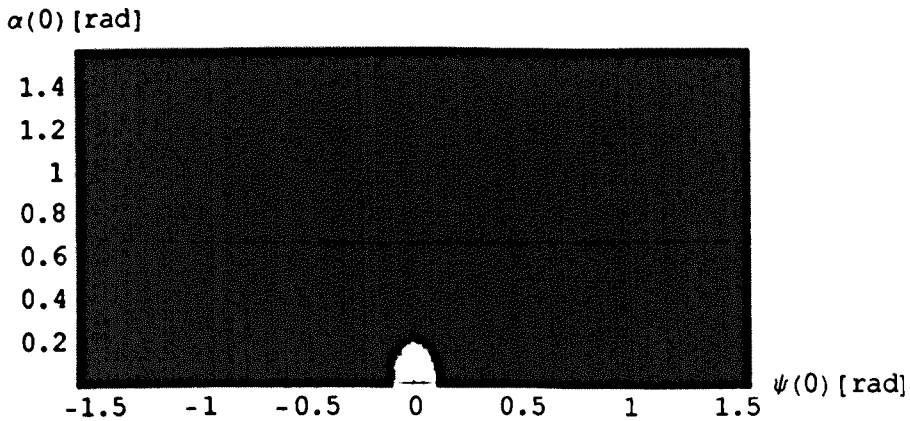


Figure 5.4 Effect of initial in- and out-of-plane angular displacement on tether libration (white) and tumbling (black) over 50 completed orbits with $e = 0.3$. Plot contains 80000 points with a step size of $\pi/400$ for both $\psi(0)$ and $\alpha(0)$, respectively.

5.2 Tether Tumbling during First Completed Orbit

Figure 5.5-Figure 5.8 explore the pairs of initial conditions that give rise to tether tumbling within the first completed orbit. (2.33)–(2.34) are numerically integrated for a single orbit and the angular displacements are evaluated at the perigee, as well as the apogee, to test whether $\pm \pi/2$ has been breached. In contrast to Figure 5.1-Figure 5.4 the results shown in Figure 5.5-Figure 5.8 are asymmetrical. The motion of a tether on a circular orbit is largely seen in Figure 5.5 to be libration. For very large out-of-plane angular displacements the dumbbell undergoes rotation before the first perigee pass, as well as for most out-of-plane displacements where $\psi(0)$ is near $-\pi/2$. Two additional islands exist for the initial conditions where tumbling occurs during the first orbit with one adjacent to the zone of rotation near $\psi(0) = -\pi/2$ and the other close to $\psi(0) = \pi/2$. Placing the dumbbell onto an elliptical orbit of 0.1 has a major influence on the islands but no effect on the boundary for very large $\alpha(0)$. The island in the left-hand quadrant increases more rapidly than the one on the right-hand side leaving most initial conditions with a negative $\psi(0)$ to tumble. Increasing the eccentricity to 0.2 causes the islands to grow even further but still separated by a zone of libration. However, for $e = 0.3$ the islands merge to form a zone separated by a thin line when $\alpha(0)$ is relatively large and a zone of libration around the local vertical for small out-of-plane angular displacements. Starting with $e = 0.1$ a small island of libration forms near $\psi(0) = \pi/2$, which still endures when $e = 0.3$. The graphs in Figure 5.5-Figure 5.8 indicate that a positive initial condition in $\psi(0)$ resists tumbling within the first orbit and that an increase in the orbit eccentricity encourages the tether to tumble. In general a larger initial condition in $\alpha(0)$ promotes tether rotation although a narrow band exists for large $\alpha(0)$ where the tether is found to librate during the first completed orbit.

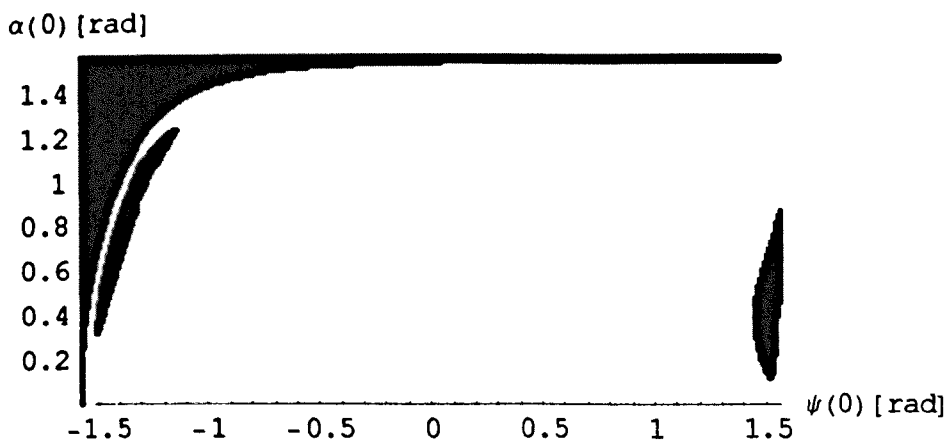


Figure 5.5 Effect of initial in- and out-of-plane angular displacement on tether libration (white) and tumbling (black) over a single completed orbit with $e = 0$. Plot contains 45000 points with a step size of $\pi/300$ for both $\psi(0)$ and $\alpha(0)$, respectively.

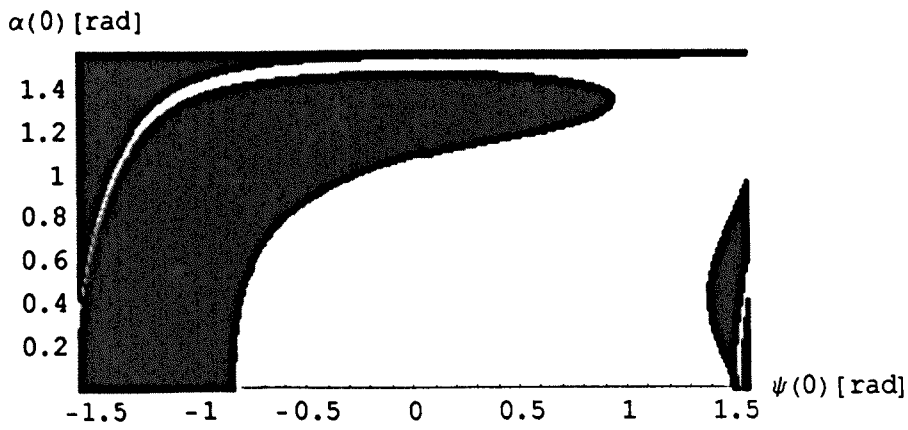


Figure 5.6 Effect of initial in- and out-of-plane angular displacement on tether libration (white) and tumbling (black) over a single completed orbit with $e = 0.1$. Plot contains 45000 points with a step size of $\pi/300$ for both $\psi(0)$ and $\alpha(0)$, respectively.

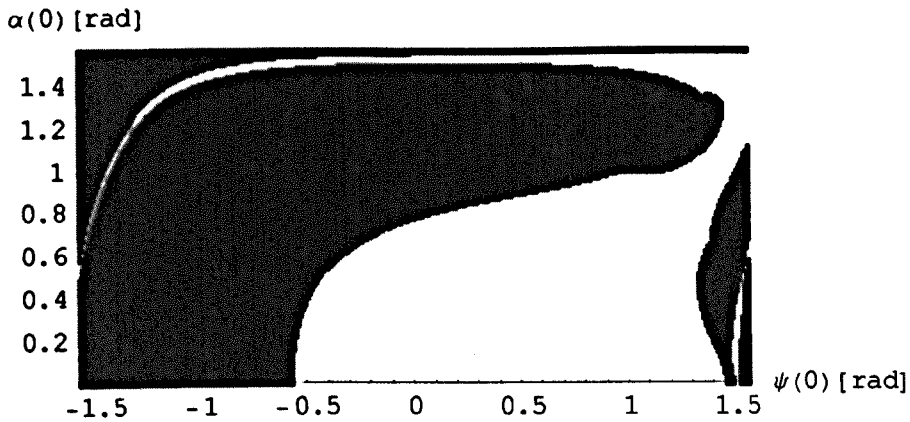


Figure 5.7 Effect of initial in- and out-of-plane angular displacement on tether libration (white) and tumbling (black) over a single completed orbit with $e = 0.2$. Plot contains 45000 points with a step size of $\pi/300$ for both $\psi(0)$ and $\alpha(0)$, respectively.

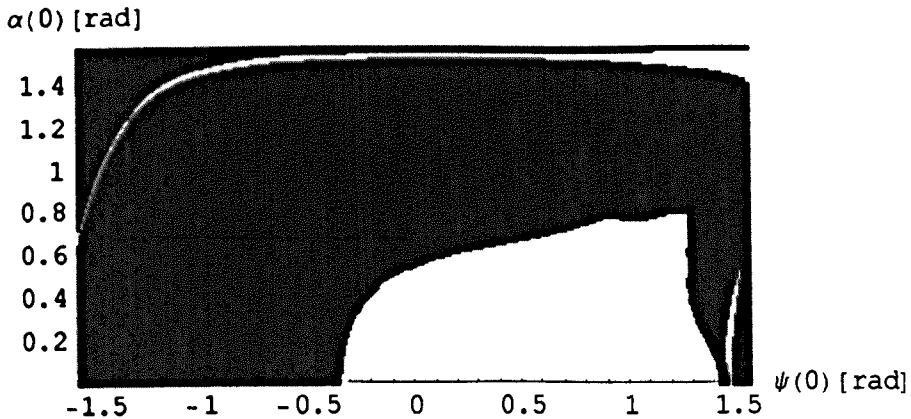


Figure 5.8 Effect of initial in- and out-of-plane angular displacement on tether libration (white) and tumbling (black) over a single completed orbit with $e = 0.3$. Plot contains 45000 points with a step size of $\pi/300$ for both $\psi(0)$ and $\alpha(0)$, respectively.

5.3 Duration of Transient Librations

The existence of libration during the first completed orbit in Figure 5.5-Figure 5.8 does not imply that the librational motion endures into the steady state, seen in Figure 5.1-Figure 5.4. Thus, the libration forms a transient that eventually gives way to tether tumbling. The number of perigee passes where libration occurs can be recorded to examine when tumbling commences and as defined in Chapter 4 this discrete quantity is denoted η . The graphs in Figure 5.9-Figure 5.12 represent η as a grey scale with black and white representing $\eta = 20$ and $\eta = 0$, respectively. The numerical integration of (2.33)-(2.34) was halted at 20 perigee passes because a larger number of completed orbits become increasingly difficult to differentiate with the grey scale. The transient dynamics of the tethered dumbbell on a circular orbit is seen in Figure 5.9 to be rather complex. A multitude of plateaux exist where the same number of orbits are completed before tumbling ensues. The boundary between two plateaux is never a simple discrete jump but instead a peak is formed between two regions where more orbits are completed before spin occurs. Many of the plateaux in Figure 5.9 merge to form a boundary between two further plateaux at another part of the initial condition parameter space. Placing the dumbbell on an elliptical orbit of $e = 0.1$ reduces the number of different plateaux and the transient libration is seen in the majority of cases to endure in Figure 5.10 for only one or two perigee crossings. Around the region of steady-state libration the transient libration remains complex with many plateaux merging to form a multitude of peaks. Increasing the orbit eccentricity to 0.2 in Figure 5.11 causes the tether to predominantly librate only for a single orbit before tumbling. The band around the steady-state libration region has increased to exhibit a complex merging of plateaux. Increasing the eccentricity to 0.3 encourages the tether to tumble fairly rapidly in Figure 5.12. There are few initial conditions about the region of steady-state libration that allow the tether to librate for 20 orbits when compared to Figure 5.11. The structure of initial conditions yielding the transient libration is less complicated with far fewer plateaux than the case of the dumbbell placed on a circular orbit.

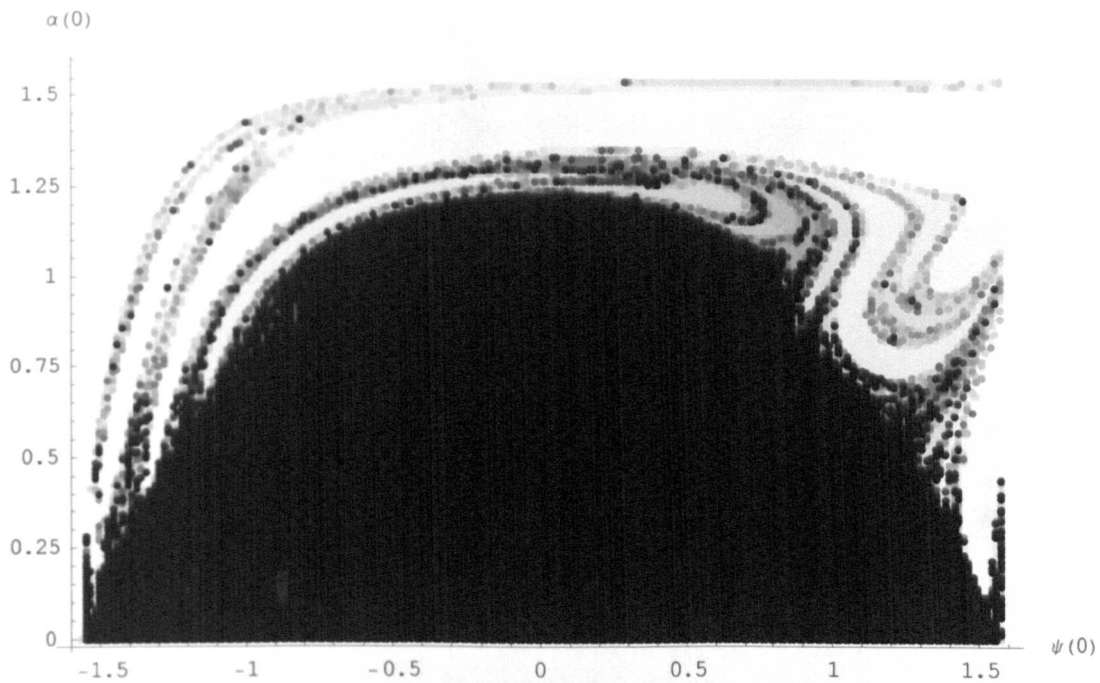
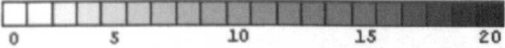


Figure 5.9 Number of completed orbits before the onset of tumbling within the identified zone of transient libration for $e = 0$. The magnitude of η , ranging between zero and 20, is converted into a grey scale where a darker grey tone is assigned to a higher value for η , as

given by: 

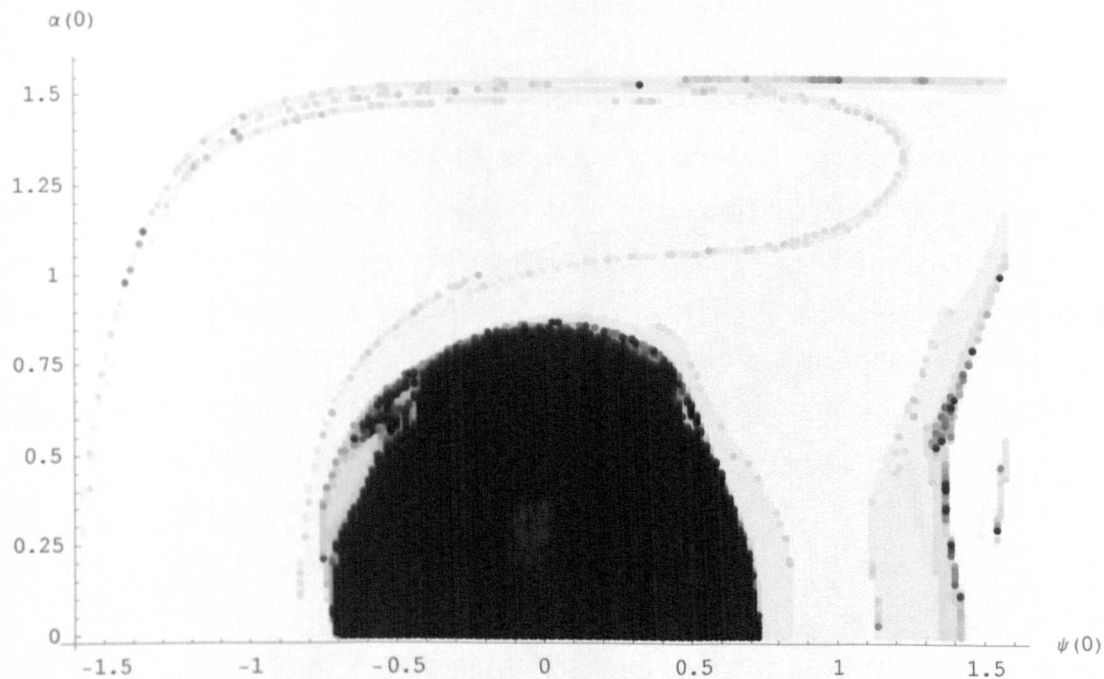
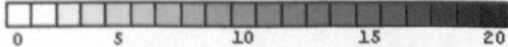


Figure 5.10 Number of completed orbits before the onset of tumbling within the identified zone of transient libration for $e = 0.1$. The magnitude of η , ranging between zero and 20, is converted into a grey scale where a darker grey tone is assigned to a higher value for η , as

given by: 

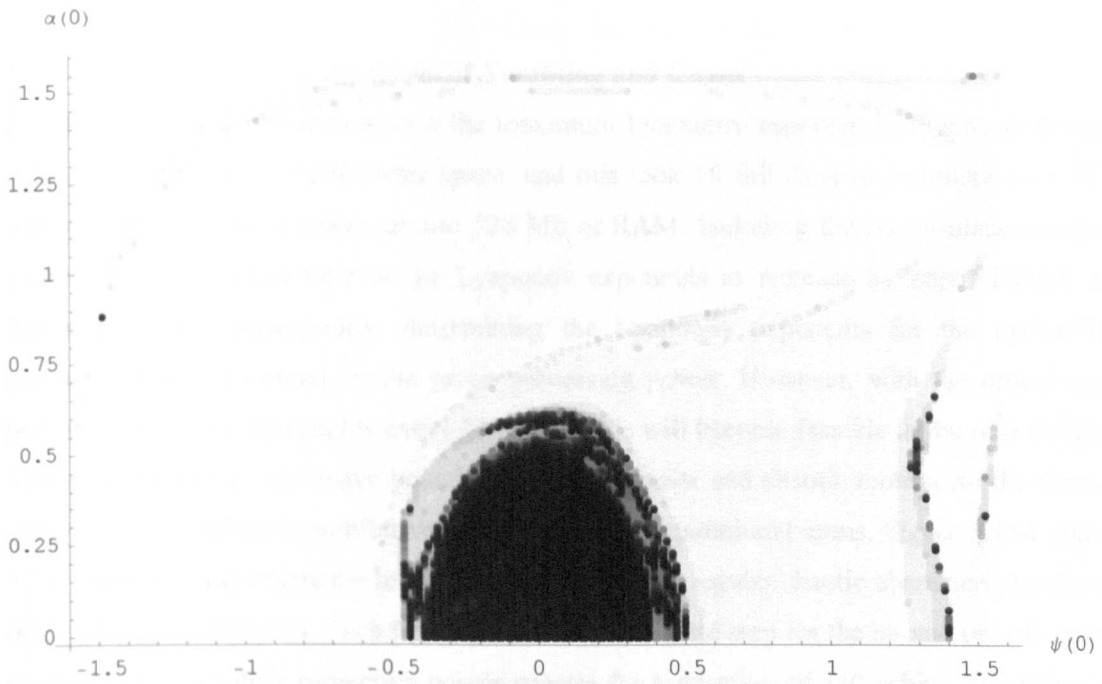


Figure 5.11 Number of completed orbits before the onset of tumbling within the identified zone of transient libration for $e = 0.2$. The magnitude of η , ranging between zero and 20, is converted into a grey scale where a darker grey tone is assigned to a higher value for η , as

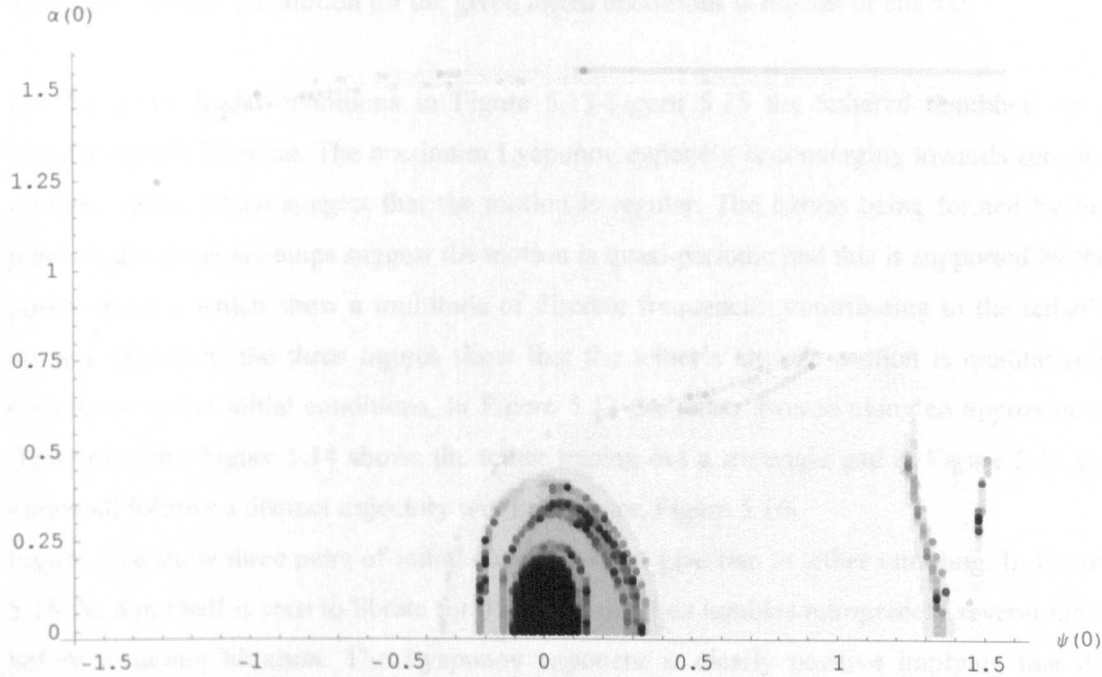
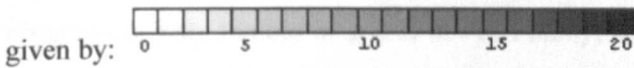
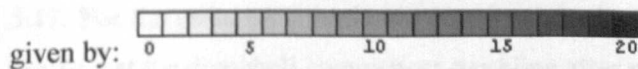


Figure 5.12 Number of completed orbits before the onset of tumbling within the identified zone of transient libration for $e = 0.3$. The magnitude of η , ranging between zero and 20, is converted into a grey scale where a darker grey tone is assigned to a higher value for η , as



5.4 Comparison between the Onset of Tumbling and Chaos

For the case of the planar dumbbell the maximum Lyapunov exponent in Figure 4.38 was computed for the $\psi(0)$ - e parameter space, and this took 18 full days to complete on a PC with a 1.4 GHz Athlon processor and 528 Mb of RAM. Including the out-of-plane motion causes the computation time of the Lyapunov exponents to increase by approximately a factor of three. Consequently, determining the Lyapunov exponents for the $\psi(0)$ - $\alpha(0)$ parameter space is limited by the given processing power. However, with the processing power of PCs doubling roughly every 18 months this will become feasible in the near future. Thus, determining a conclusive boundary between regular and chaotic motion for the three-dimensional dumbbell is prohibitively expensive in computational terms. Figure 5.13-Figure 5.24, therefore, investigate the tether's libration/spin and regular/chaotic characteristics for a range of initial conditions. Each figure presents the Poincaré map for the in- and out-of-plane motion as well as their respective power spectra for a duration of 150 orbits. The tether's attitude position is plotted onto a unit sphere, as well as a projection of the unit sphere onto a 2D plane, to aid visualising the tether's motion within the relative rotating x_0 - y_0 - z_0 coordinate frame. The in-plane angular response over time is presented as the dumbbell is observed to only tumble in ψ and not α . Finally, the first Lyapunov exponent is shown to determine whether the motion for the given initial conditions is regular or chaotic.

For the given initial conditions in Figure 5.13-Figure 5.15 the tethered dumbbell on a circular orbit is librating. The maximum Lyapunov exponent is converging towards zero for all three cases, which suggest that the motion is regular. The curves being formed by the points in the Poincaré maps suggest the motion is quasi-periodic and this is supported by the power spectra, which show a multitude of discrete frequencies contributing to the tether's motion. However, the three figures show that the tether's attitude motion is qualitatively dependent on the initial conditions. In Figure 5.13 the tether sweeps along an approximate figure-of-eight, Figure 5.14 shows the tether tracing out a rectangle and in Figure 5.15 the dumbbell follows a distinct trajectory within a square. Figure 5.16-

Figure 5.18 show three pairs of initial conditions that give rise to tether tumbling. In Figure 5.16 the dumbbell is seen to librate for 65 orbits and then tumbles retrogradely several times before resuming libration. The Lyapunov exponent is clearly positive implying that the tether's motion is chaotic. The dense power spectra in both the in- and out-of-plane is indicative of chaos and the Poincaré map is being filled with a cloud of dots. An earlier made observation of the motion not being mirrored about the $\psi(0) = 0$ axis is confirmed by Figure 5.17. For the same magnitude but positive initial conditions as in Figure 5.16, Figure 5.17 shows that the dumbbell commences tumbling after roughly 200 completed orbits and rotates

in the prograde direction. The motion is chaotic due to the positive first Lyapunov exponent, which the power spectra and Poincaré maps support. The results in Figure 5.17 agree with those obtained by Misra and Nixon (2001), who only considered initial conditions where $\psi(0) = \alpha(0) = \text{constant}$. For the initial conditions in Figure 5.18 the dumbbell is rotating predominately in the retrograde direction and due to the positive Lyapunov exponent is again chaotic.

Placing the tethered dumbbell on an elliptical orbit with an eccentricity of 0.1 introduces more frequencies into the power spectra in Figure 5.19 than the equivalent initial conditions on the circular orbit shown in Figure 5.13. The tether in Figure 5.19 undergoes libration with the Lyapunov exponent converging towards zero. Thus, the motion is regular and quasi-periodic due to the closed curves forming in the Poincaré maps. However, for the initial conditions in Figure 5.20 the tether is found to tumble progradely after completing 28 orbits of libration. The first Lyapunov exponent rises distinctly at the onset of tumbling and is clearly positive thus implying chaos. The Poincaré maps and power spectra show the expected characteristics for chaos and thus support the finding of the Lyapunov exponents. Increasing the orbit eccentricity to 0.2 introduces yet further frequency components in the power spectra of

Figure 5.21 but the librational motion is regular according to the maximum Lyapunov exponent. The Poincaré maps again suggest the libration is quasi-periodic. The tumbling observed in Figure 5.22 is accompanied by a positive Lyapunov exponent, where the power spectra lift off the zero-axes and the Poincaré maps are filled with a cloud of dots. The initial conditions of $\psi(0) = 0$ and $\alpha(0) = 0.5$ rad yield libration when the orbit eccentricity ranges between 0 and 0.2. However, when the eccentricity is set 0.3 the tether is seen to tumble in Figure 5.24. The motion is seen to be chaotic and tumbling at times progradely and retrogradely. A very small set of initial conditions gives rise to steady-state libration when $e = 0.3$ of which one of these is depicted in Figure 5.23. The Poincaré maps begin to form closed curves and the Lyapunov exponent settles to zero, suggesting the motion is quasi-periodic. In summary a strong connection is established between libration and regular tether motion and between chaos and a tumbling dumbbell. Of all the cases investigated and presented no set of initial conditions was identified that yielded a chaotically librating tether or a periodically tumbling tether.

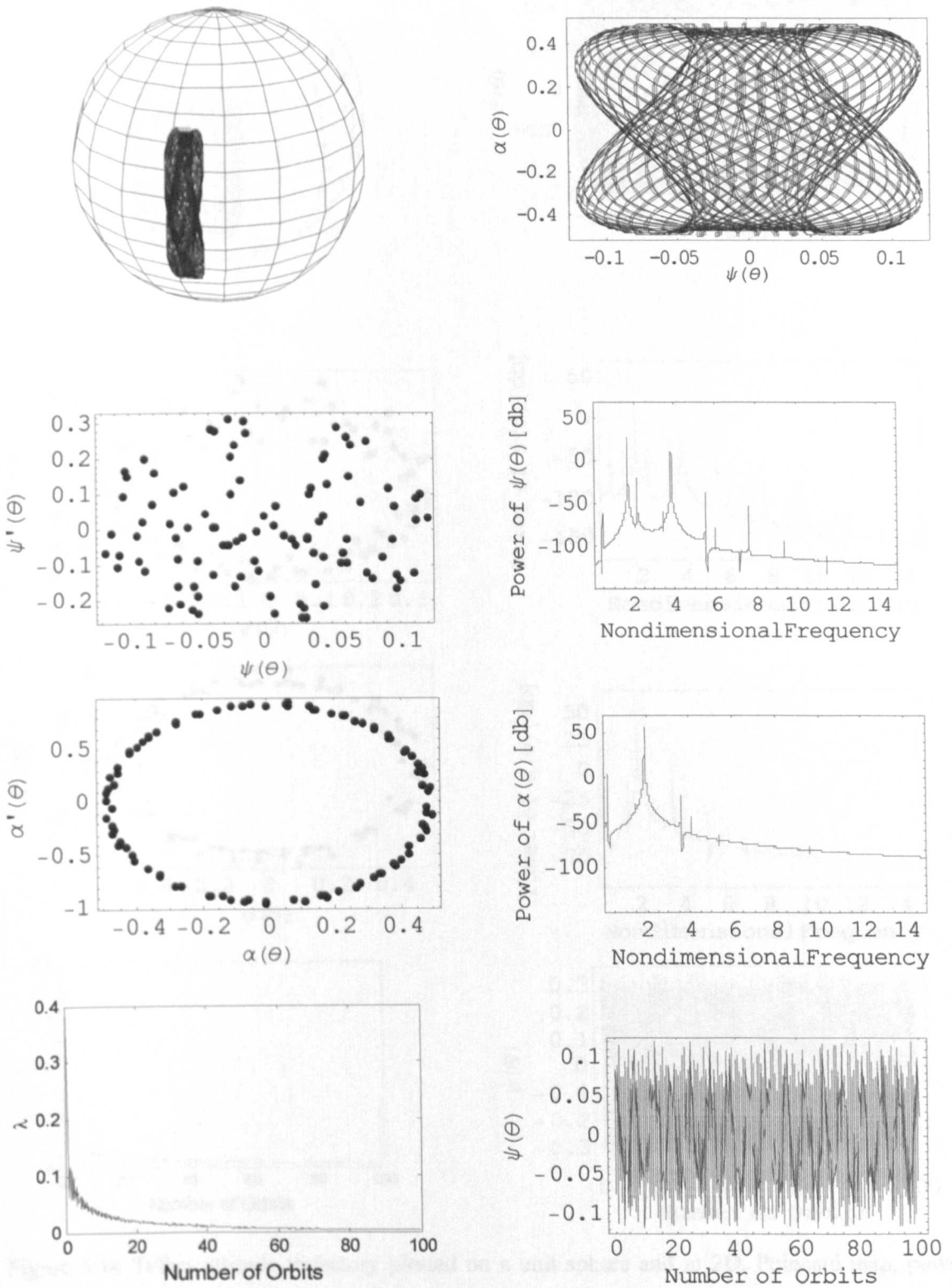


Figure 5.13 Tether attitude trajectory plotted on a unit sphere and in 2D, Poincaré map, power spectra, first Lyapunov exponent and time history of tether's pitch motion with $e = 0$, $\dot{\psi}(0) = \dot{\alpha}(0) = 0$, $\psi(0) = 0$ rad and $\alpha(0) = 0.5$ rad.

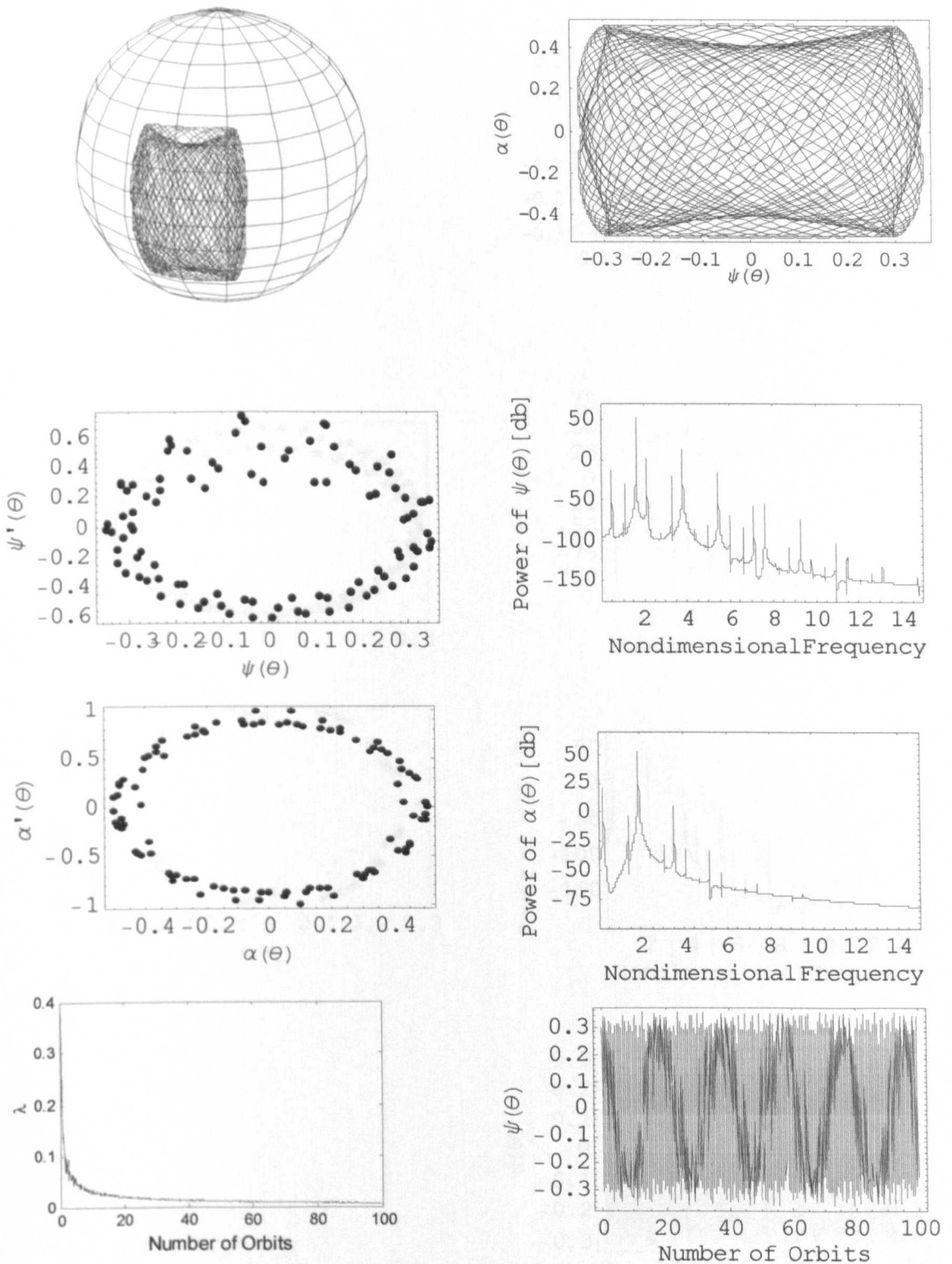


Figure 5.14 Tether attitude trajectory plotted on a unit sphere and in 2D, Poincaré map, power spectra, first Lyapunov exponent and time history of tether's pitch motion with $e = 0$, $\dot{\psi}(0) = \dot{\alpha}(0) = 0$, $\psi(0) = 0.3$ rad and $\alpha(0) = 0.5$ rad.

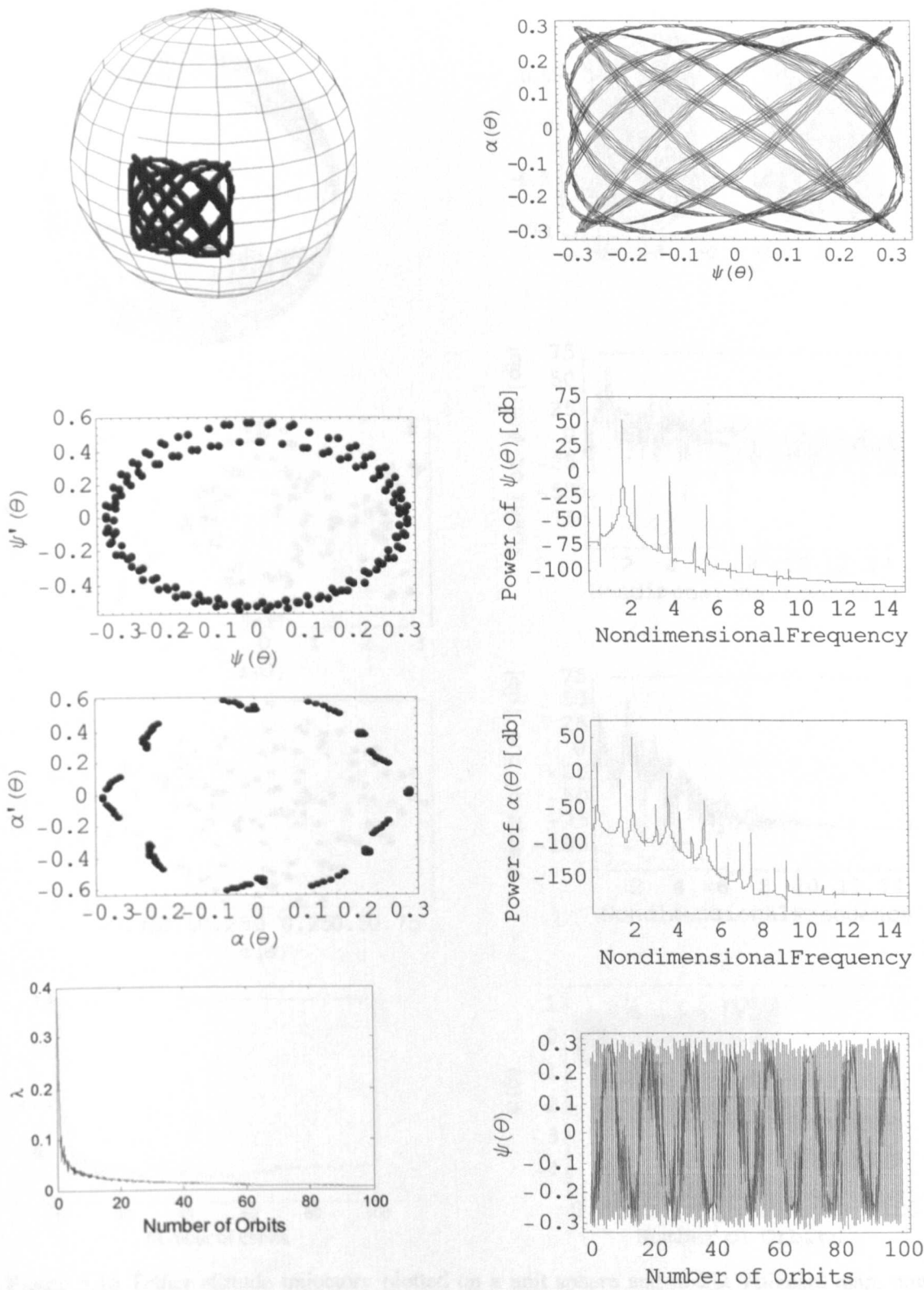


Figure 5.15 Tether attitude trajectory plotted on a unit sphere and in 2D, Poincaré map, power spectra, first Lyapunov exponent and time history of tether's pitch motion with $e = 0$, $\dot{\psi}(0) = \dot{\alpha}(0) = 0$, $\psi(0) = -0.3$ rad and $\alpha(0) = 0.3$ rad.

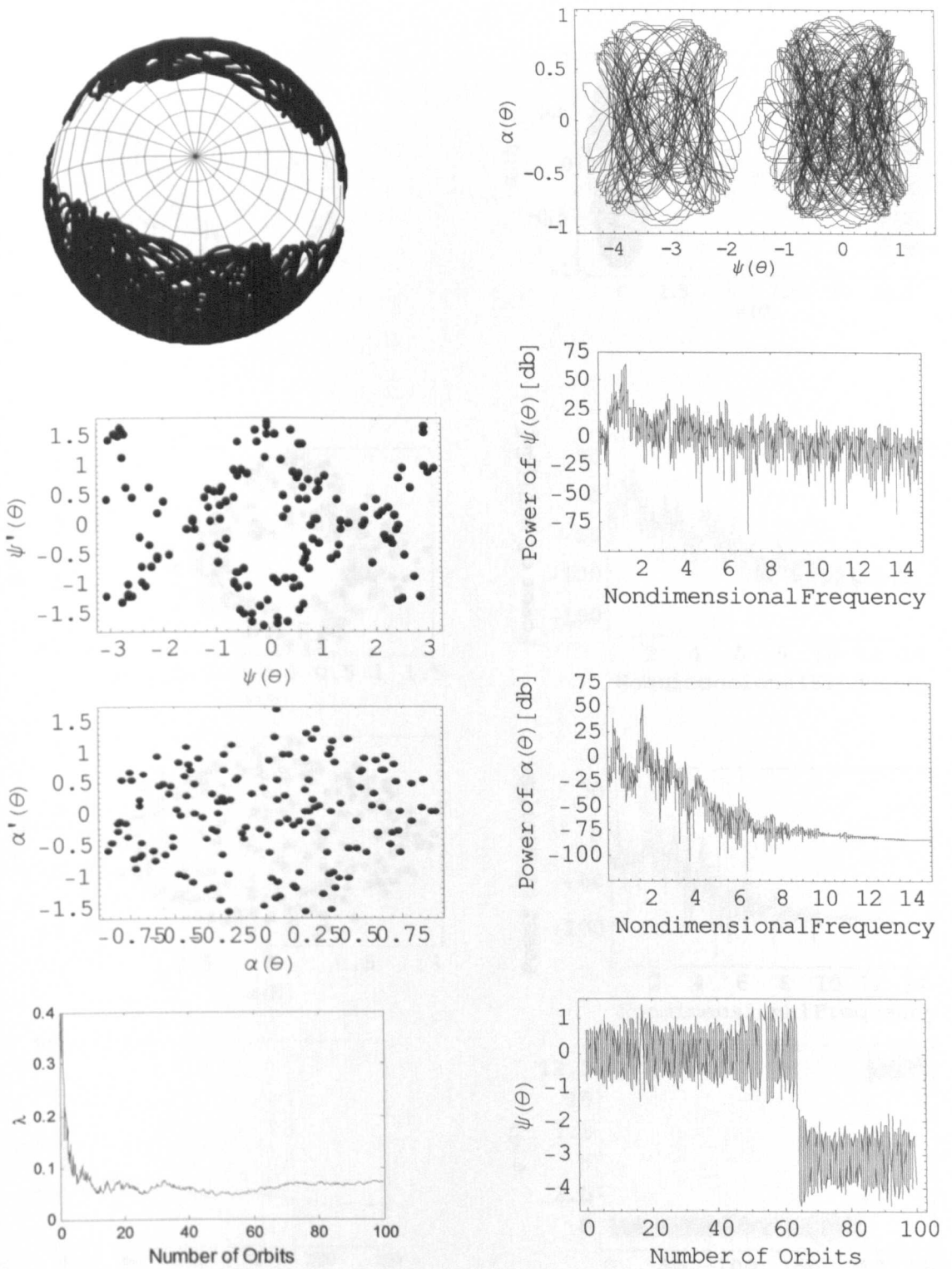


Figure 5.16 Tether attitude trajectory plotted on a unit sphere and in 2D, Poincaré map, power spectra, first Lyapunov exponent and time history of tether's pitch motion with $e = 0$, $\dot{\psi}(0) = \dot{\alpha}(0) = 0$, $\psi(0) = -0.86$ rad and $\alpha(0) = 0.86$ rad.

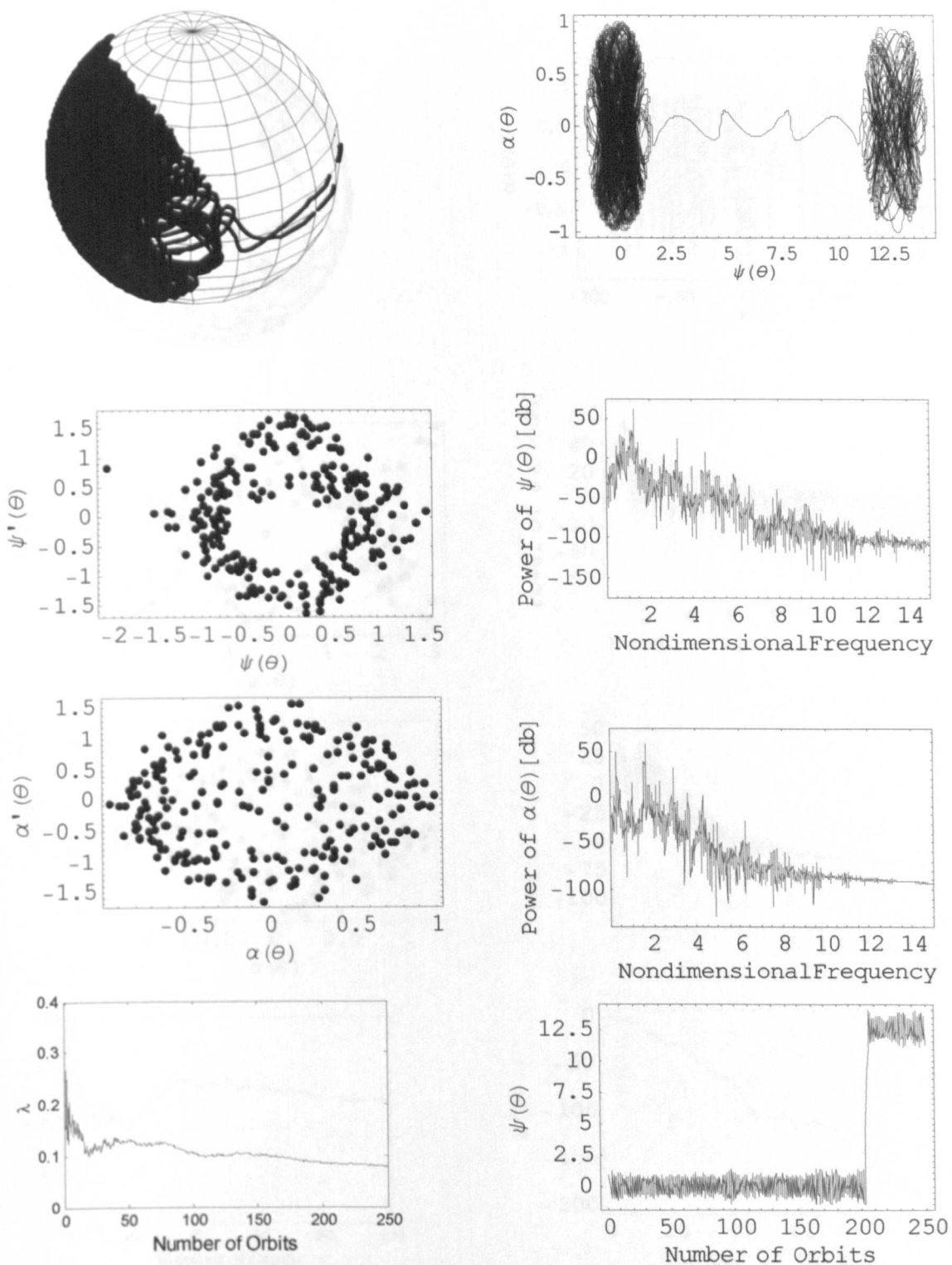


Figure 5.17 Tether attitude trajectory plotted on a unit sphere and in 2D, Poincaré map, power spectra, first Lyapunov exponent and time history of tether's pitch motion with $e = 0$, $\dot{\psi}(0) = \dot{\alpha}(0) = 0$, $\psi(0) = 0.86$ rad and $\alpha(0) = 0.86$ rad.

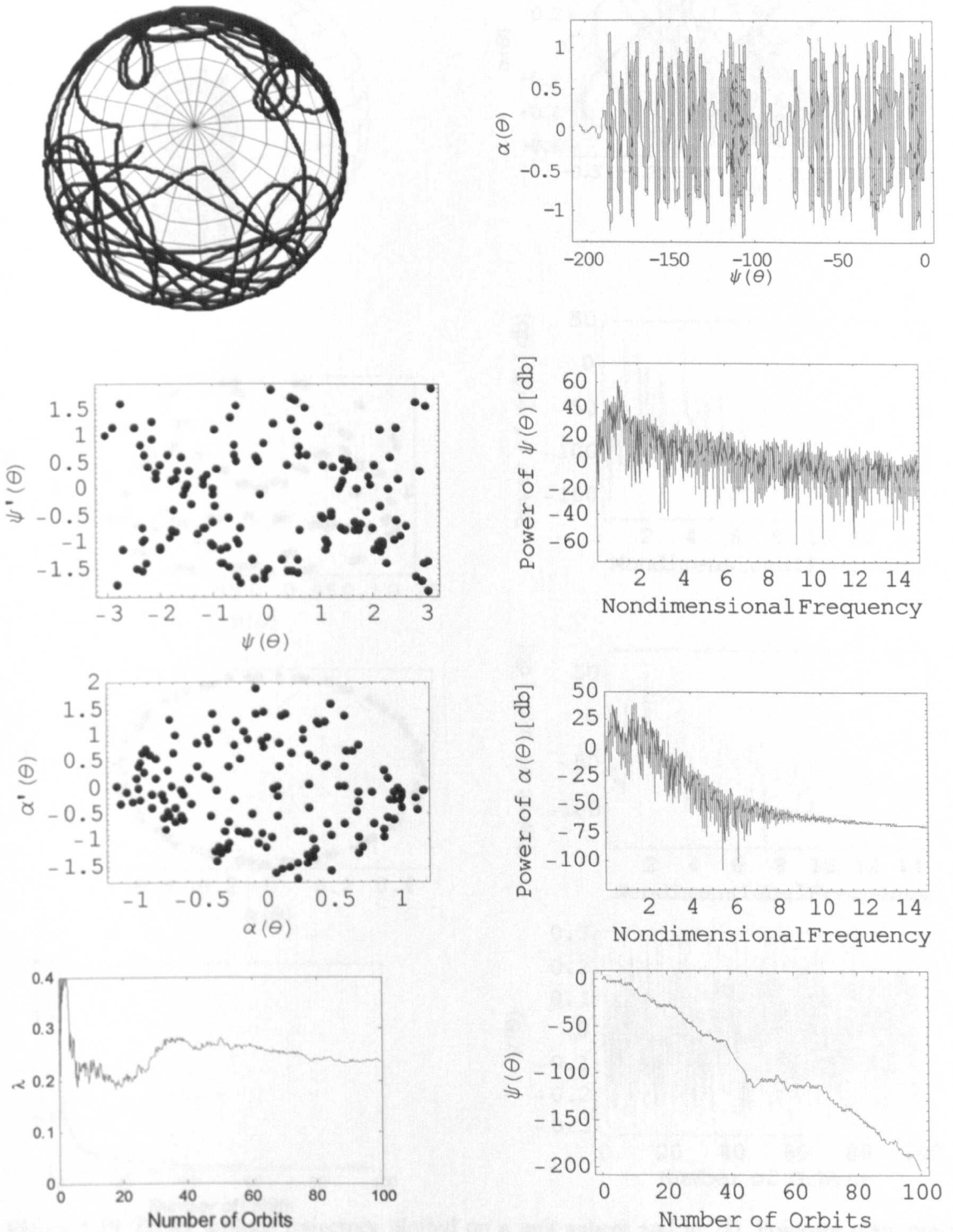


Figure 5.18 Tether attitude trajectory plotted on a unit sphere and in 2D, Poincaré map, power spectra, first Lyapunov exponent and time history of tether's pitch motion with $e = 0$, $\dot{\psi}(0) = \dot{\alpha}(0) = 0$, $\psi(0) = -1.0$ rad and $\alpha(0) = 1.2$ rad.

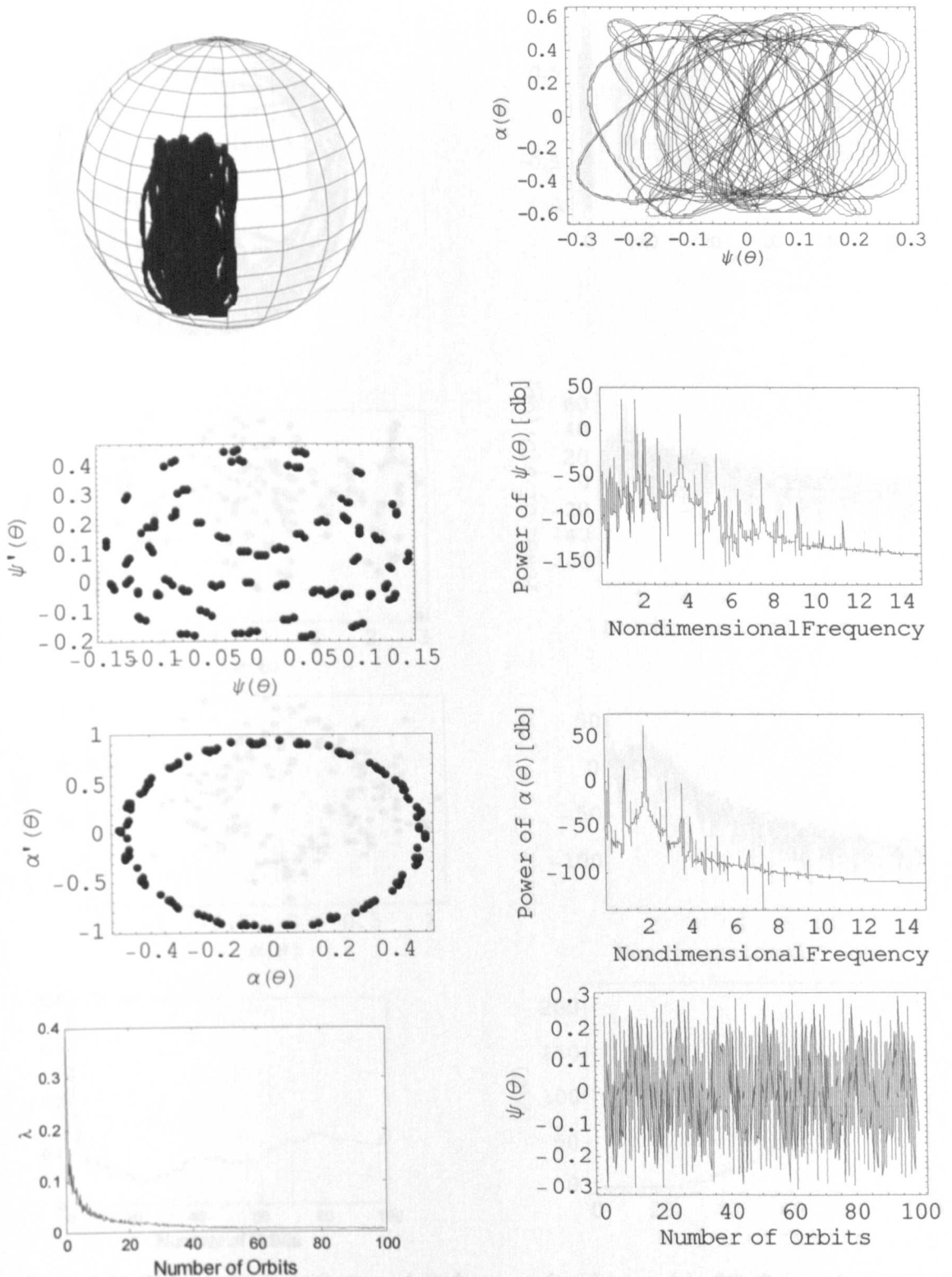


Figure 5.19 Tether attitude trajectory plotted on a unit sphere and in 2D, Poincaré map, power spectra, first Lyapunov exponent and time history of tether's pitch motion with $e = 0.1$, $\dot{\psi}(0) = \dot{\alpha}(0) = 0$, $\psi(0) = 0$ rad and $\alpha(0) = 0.5$ rad.

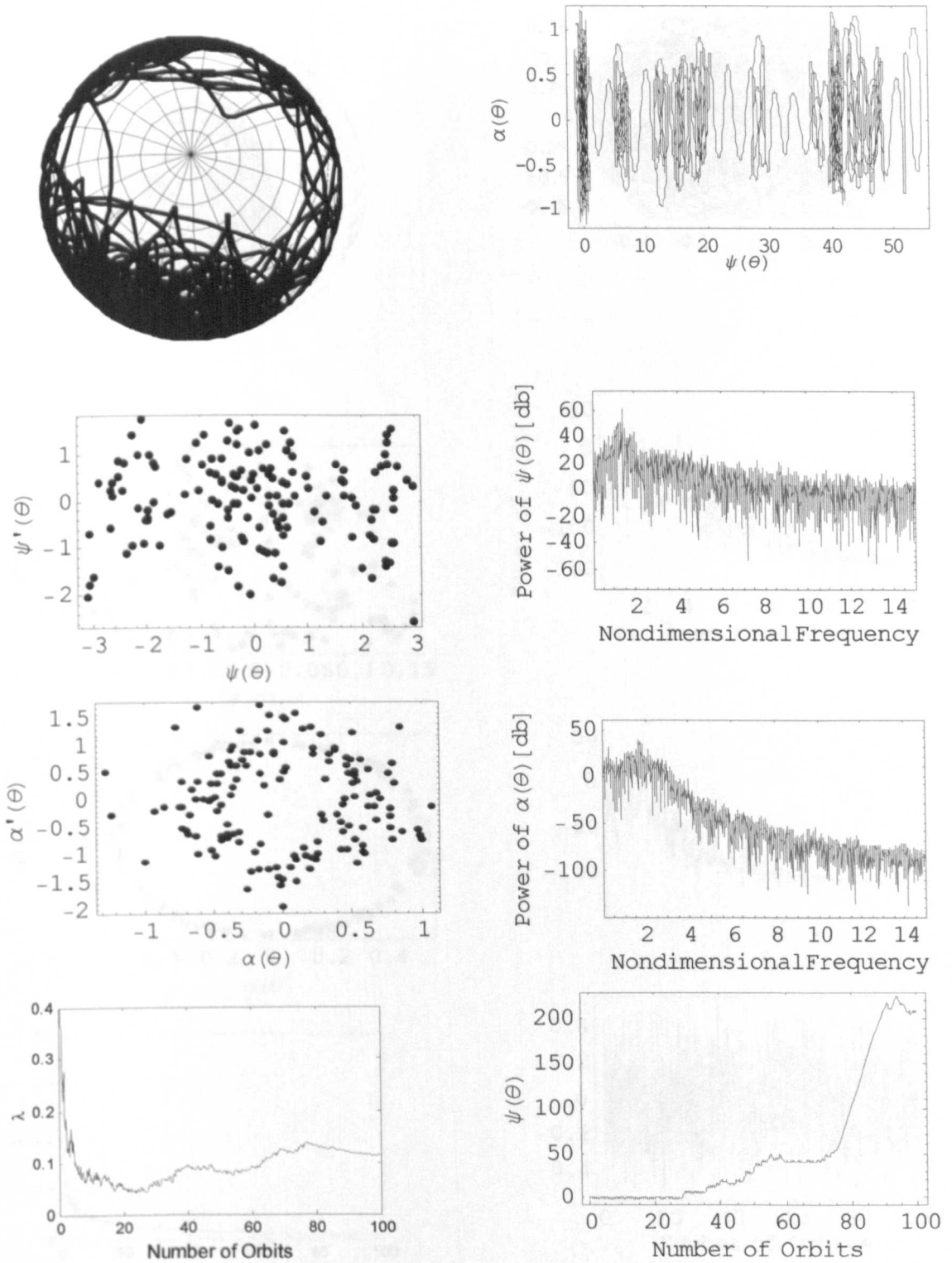


Figure 5.20 Tether attitude trajectory plotted on a unit sphere and in 2D, Poincaré map, power spectra, first Lyapunov exponent and time history of tether's pitch motion with $e = 0.1$, $\dot{\psi}(0) = \dot{\alpha}(0) = 0$, $\psi(0) = -0.5$ rad and $\alpha(0) = 0.65$ rad.

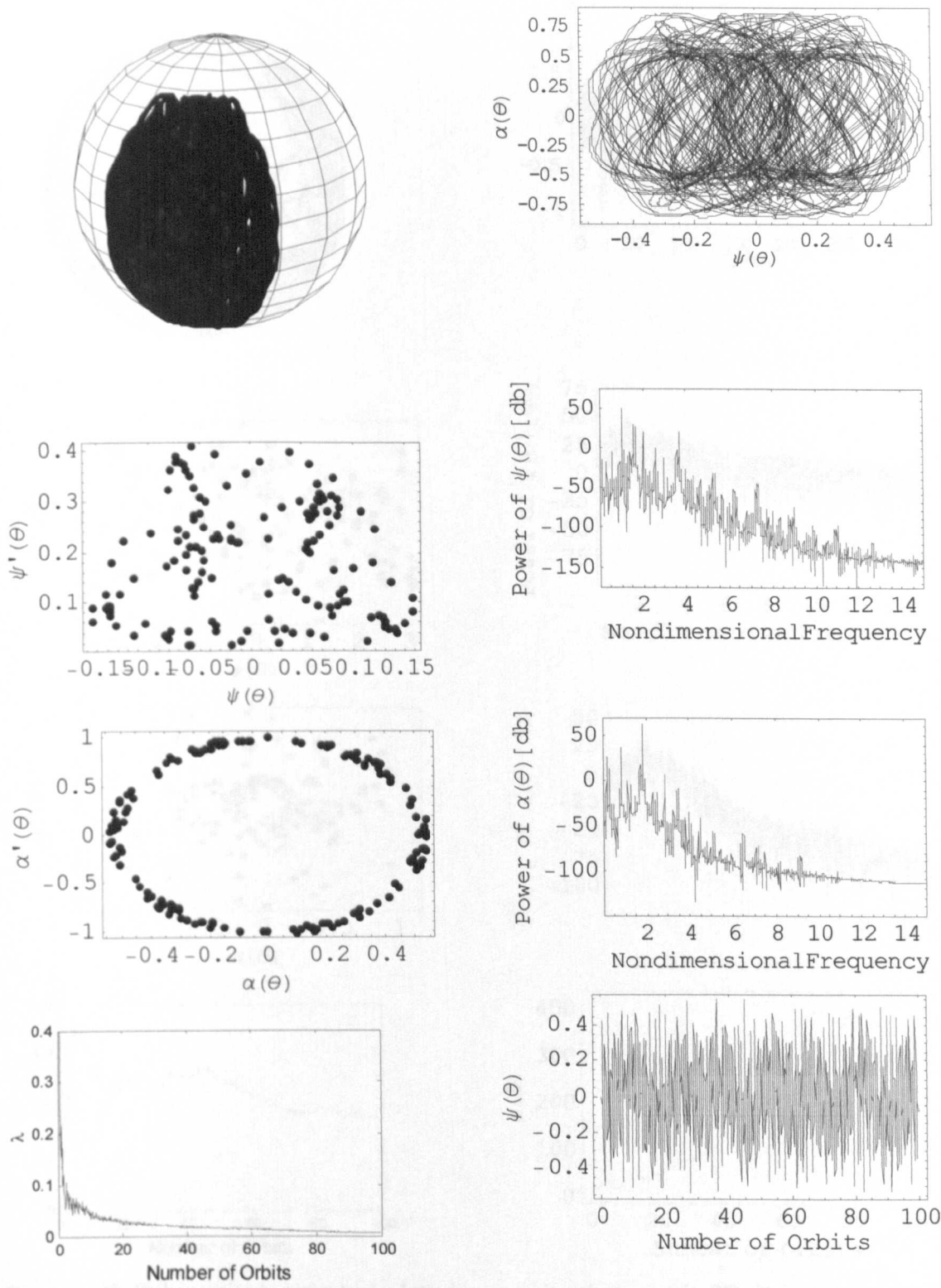


Figure 5.21 Tether attitude trajectory plotted on a unit sphere and in 2D, Poincaré map, power

Figure 5.21 Tether attitude trajectory plotted on a unit sphere and in 2D, Poincaré map, power spectra, first Lyapunov exponent and time history of tether's pitch motion with $e = 0.2$, $\dot{\psi}(0) = \dot{\alpha}(0) = 0$, $\psi(0) = 0$ rad and $\alpha(0) = 0.5$ rad.

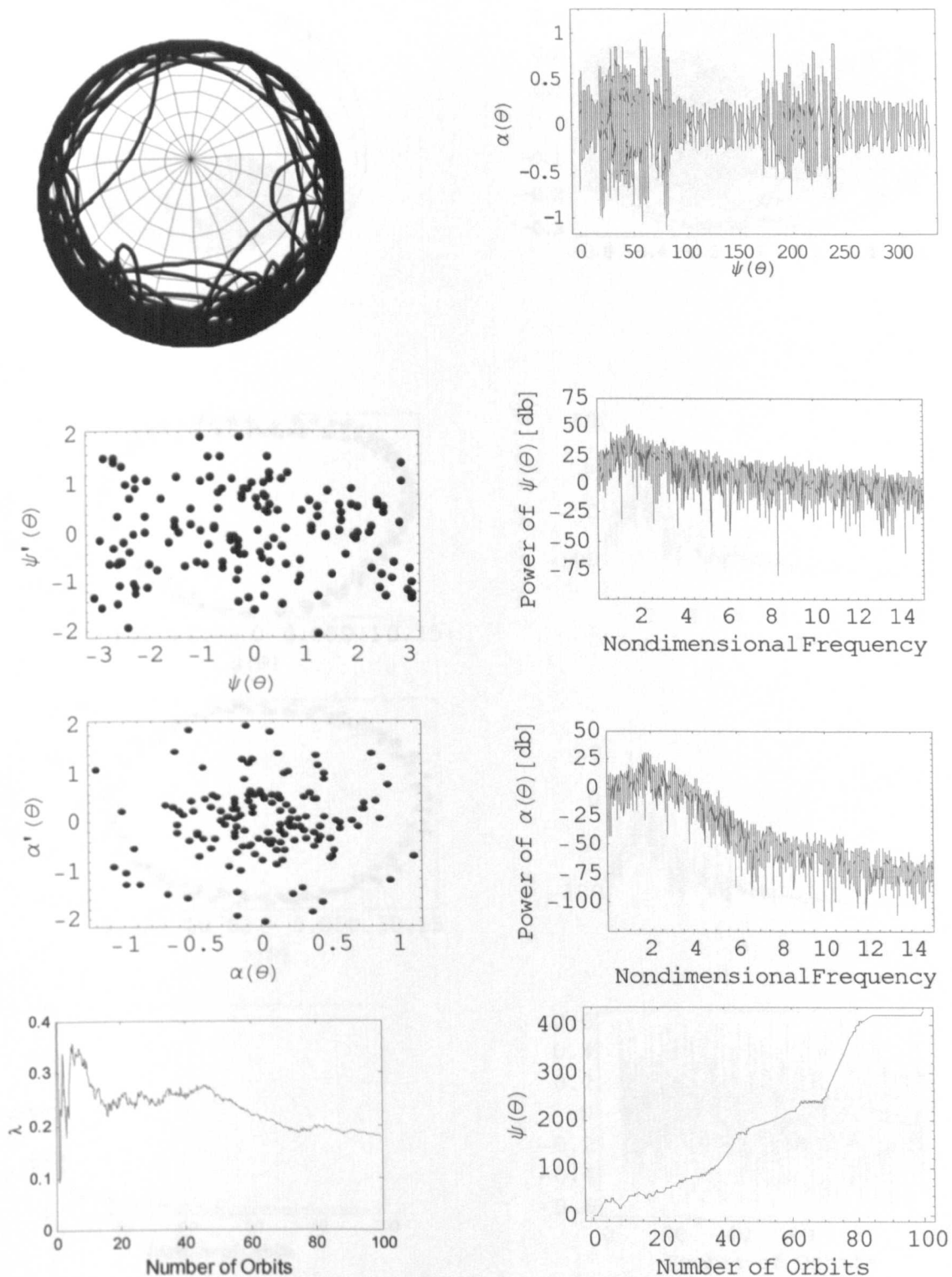


Figure 5.22 Tether attitude trajectory plotted on a unit sphere and in 2D, Poincaré map, power spectra, first Lyapunov exponent and time history of tether's pitch motion with $e = 0.2$, $\dot{\psi}(0) = \dot{\alpha}(0) = 0$, $\psi(0) = 1.0$ rad and $\alpha(0) = 0.5$ rad.

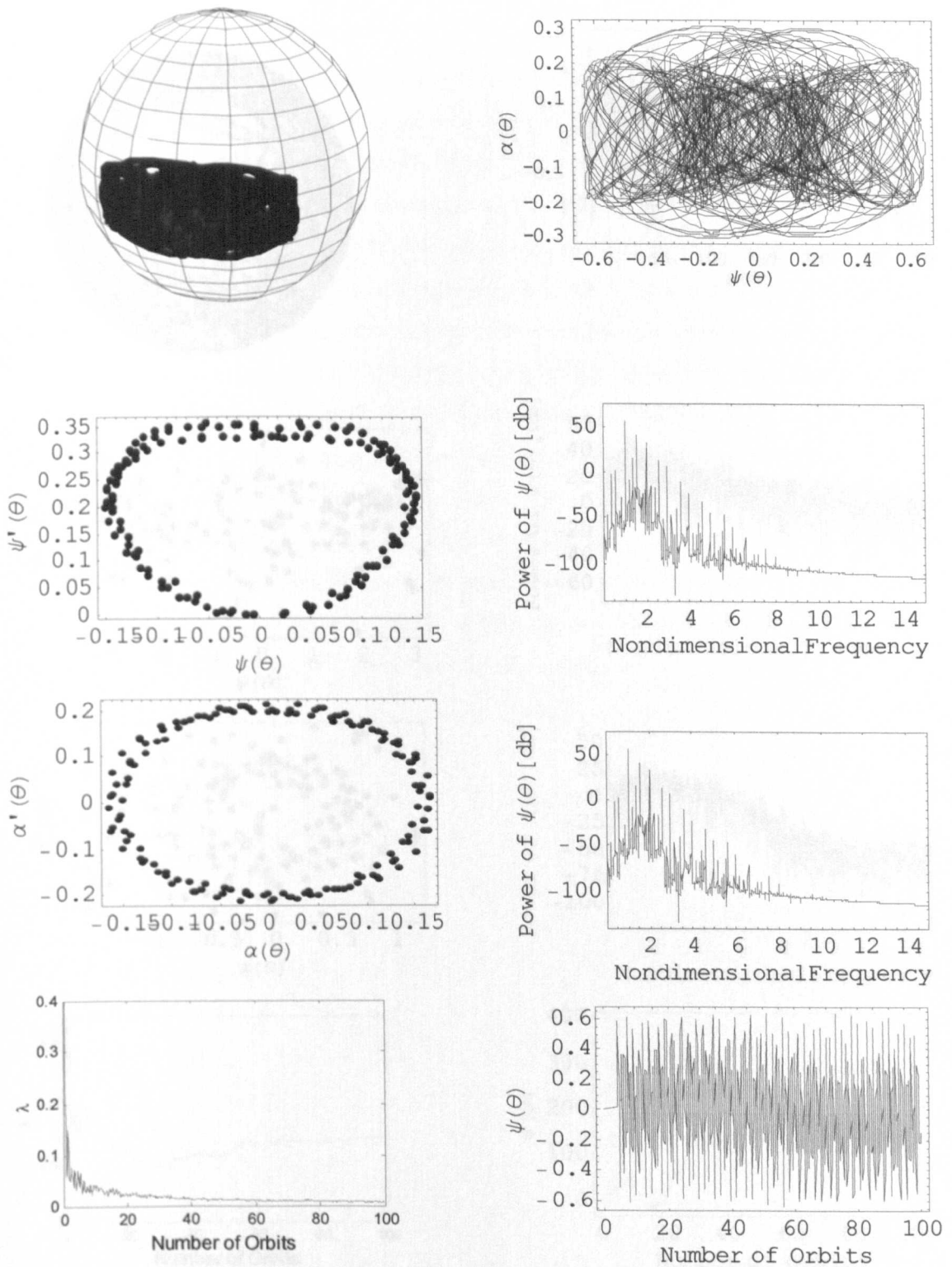


Figure 5.23 Tether attitude trajectory plotted on a unit sphere and in 2D, Poincaré map, power spectra, first Lyapunov exponent and time history of tether's pitch motion with $e = 0.3$, $\dot{\psi}(0) = \dot{\alpha}(0) = 0$, $\psi(0) = 0$ rad and $\alpha(0) = 0.15$ rad.

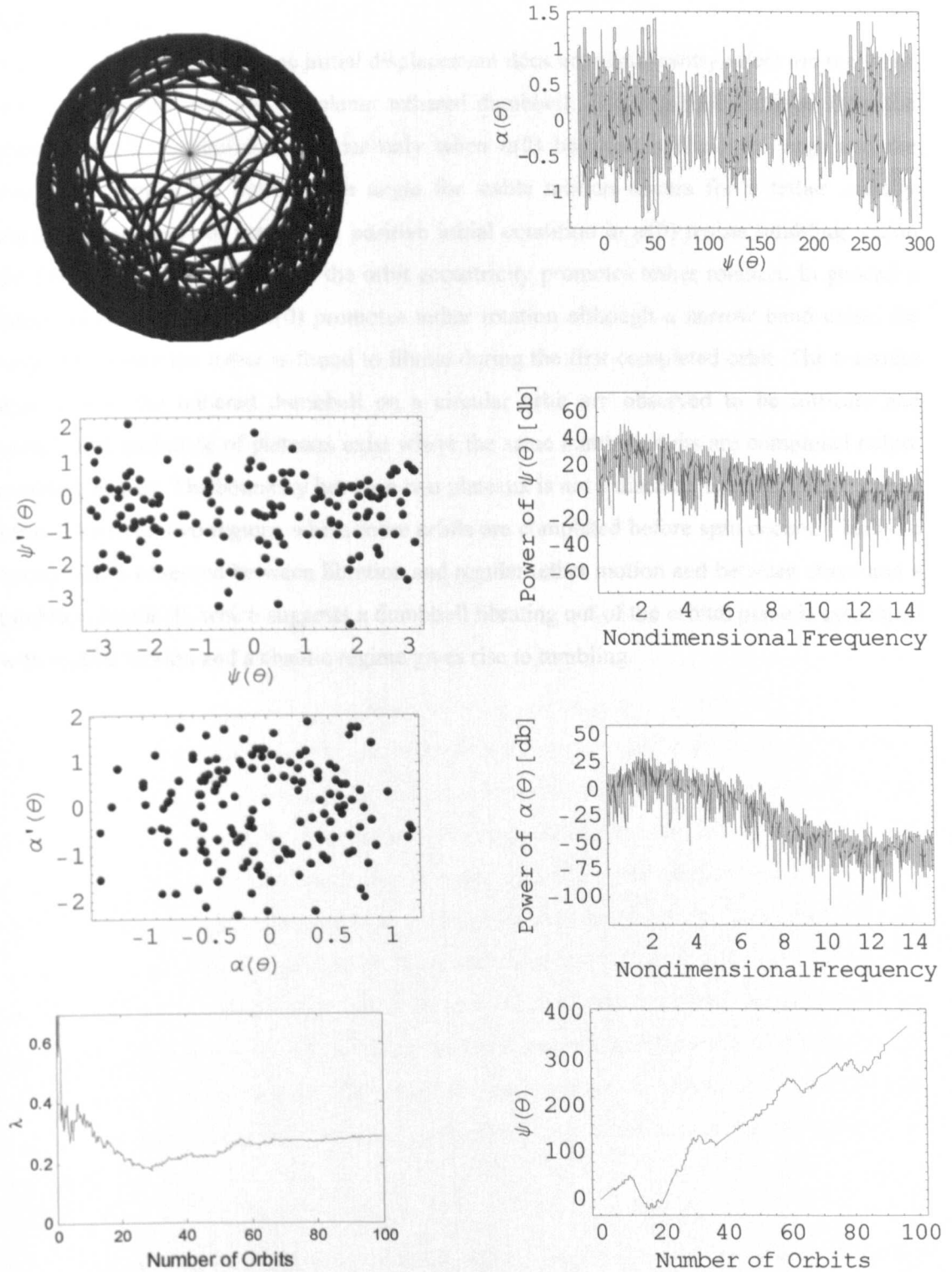


Figure 5.24 Tether attitude trajectory plotted on a unit sphere and in 2D, Poincaré map, power spectra, first Lyapunov exponent and time history of tether's pitch motion with $e = 0.3$, $\dot{\psi}(0) = \dot{\alpha}(0) = 0$, $\psi(0) = 0$ rad and $\alpha(0) = 0.5$ rad.

5.4 Conclusions

A relatively small out-of-plane initial displacement does not significantly affect the region of stable motion observed for the planar tethered dumbbell. The dumbbell deviates from the planar tether's qualitative behaviour only when $\alpha(0)$ becomes sufficiently large and the maximum permissible out-of-plane angle for stable motion occurs for a tether initially aligned along the local vertical. A positive initial condition in $\psi(0)$ resists tumbling within the first orbit but an increase in the orbit eccentricity promotes tether rotation. In general a larger initial condition in $\alpha(0)$ promotes tether rotation although a narrow band exists for large $\alpha(0)$ where the tether is found to librate during the first completed orbit. The transient dynamics of the tethered dumbbell on a circular orbit are observed to be intricate and complex. A multitude of plateaux exist where the same number orbits are completed before tumbling ensues. The boundary between two plateaux is not a discrete jump but rather a peak formed between two regions where more orbits are completed before spin occurs. Finally, a strong link is observed between libration and regular tether motion and between chaos and a tumbling dumbbell, which suggests a dumbbell librating out of the orbital plane is associated with regular motion and a chaotic regime gives rise to tumbling.

Chapter 6

Payload Orbital Transfer with Motorised Tethers

6.0 Introduction

This chapter considers the release of both the upper and lower payloads from a hanging and librating tether, as well as a spinning motorised tether. This is an important step in the conceptual evaluation of the motorised tether's performance and can only be fully appreciated in comparison with the release conditions obtained from hanging or librating tether configurations. Moreover, the literature survey identified the need to derive accurate expressions governing the orbital elements of a released payload to allow a valid comparison to be made.

6.1 Orbital Elements of the Payload after Tether Release

The motorised tether facility is assumed to orbit the Earth on a circular path and it is also assumed that the Earth's gravitational field is spherical, environmental perturbations are negligible, the tether's motion is coplanar with the orbital plane, the tethers are rigid, the cross-sectional area of the tether is constant and the tethers are fully deployed before payload release is considered. Apart from the last two assumptions, which are dependent on the tether's design and operation, there is little physical justification for the above assumptions since the real environmental conditions in space will affect the released payload's orbit. However, the presented analysis is a preliminary evaluation of the motorised tether's performance at payload orbital transfer. If the analysis demonstrates that the motorised tether concept is attractive for payload orbital transfer then a more realistic analysis should be considered. The effort involved in taking the environmental conditions into account would not be warranted if the concept possesses poor performance characteristics. Consequently, although not ideal, choosing a relatively unsophisticated model for an initial feasibility is justifiable.

If the payload is released when the tether is aligned along the gravity vector then, assuming the released payload has not reached escape velocity, the release point will either be the perigee or apogee of the payload's elliptical orbit. This release condition is the most desirable for orbit raising or lowering since the full component of the velocity vectors are summed or subtracted. However, there is no guarantee that the payload can be released at the instant when the tether is in line with the gravity vector. Any misalignment between the

tether and gravity vector at payload release will cause a reduction in the maximum achievable altitude gain and the apogee of the released payload's orbit will no longer coincide with that of the ideal or planned release scenario. Hence, in deriving the orbital elements of a released payload the obtained expressions must be general enough to encompass not only the ideal release conditions but also non-ideal scenarios.

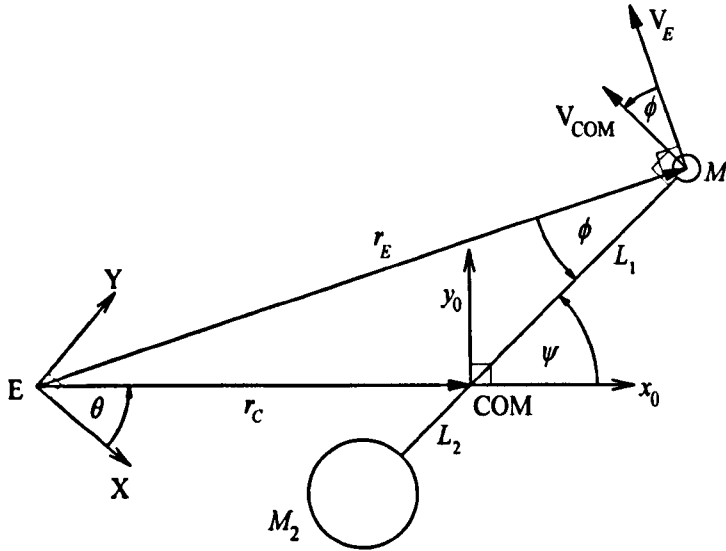


Figure 6.1 Geometry of a general planar release

The general equation for the radius r on an elliptical orbit is of the form

$$r = \frac{p}{1 + e \cos \Theta} \quad (6.1)$$

and is classically derived in the mathematics describing conic sections. The orbit eccentricity is denoted e , the released payload's position on the orbit is given by the true anomaly Θ , and p is the orbit's semilatus rectum. From (6.1) the following relationships in (6.2) can be derived between p , the semimajor axis a , orbit eccentricity, the periapsis radius r_{PE} , and the apoapsis radius r_{AP} .

$$p = a(1 - e^2) = r_{PE}(1 + e) = r_{AP}(1 - e) \quad (6.2)$$

Rearranging (6.2) allows the periapsis and apoapsis radius to be determined in terms of the semimajor axis and eccentricity. The periapsis is, thus, described by

$$r_{PE} = a(1 - e) \quad (6.3)$$

and, similarly, for the apoapsis

$$r_{AP} = a(1 + e) \quad (6.4)$$

Hence, to determine the orbital elements of a payload released from a tether, expressions need to be derived that link the release conditions and tether alignment to the semimajor axis and the eccentricity.

The semimajor axis can be obtained by squaring the expression in (6.5), which originates, as Chobotov (1996) shows, from the vis-viva equation,

$$V = \sqrt{\mu \left[\frac{2}{r_E} - \frac{1}{a} \right]} \quad (6.5)$$

and rearranges to yield

$$a = \frac{\mu r_E}{2\mu - V^2 r_E} \quad (6.6)$$

where μ = the product of the gravitational constant G and the planet's mass, which in this case is Earth, r_E = the distance from the Earth's centre to the payload M_1 , and V = payload's total velocity at release. The distance from the Earth's centre to the payload M_1 is obtained by considering the geometry in Figure 6.1:

$$r_E = \sqrt{r_C^2 + L_1^2 + 2r_C L_1 \cos \psi} \quad (6.7)$$

where r_C = circular orbit radius to the tether's COM, L_1 = the tether length from the COM to the released payload, and ψ = angle between the tether and gravity vector. The velocity in (6.6) comprises the normal and radial velocity components of M_1 along r_E :

$$V = \sqrt{V_N^2 + V_R^2} \quad (6.8)$$

The radial velocity is composed of the component of the tether's tip velocity about its centre of mass V_{COM} :

$$V_R = V_{COM} \sin \phi \quad (6.9)$$

and the normal velocity component is described by the payload's orbital velocity V_E plus the tether's tip velocity about the COM:

$$V_N = V_E + V_{COM} \cos \phi \quad (6.10)$$

The velocities V_E and V_{COM} are given by

$$V_E = r_E \theta' = r_E \sqrt{\frac{\mu}{r_C^3}} \quad (6.11)$$

and

$$V_{COM} = L_1 \psi' \quad (6.12)$$

where θ' = orbital angular velocity of the tethered system about the Earth and ψ' = tether angular velocity about the COM. The angle ϕ measures the angle between V_{COM} and V_E , and can be found in terms of ψ by employing the sine rule:

$$\phi = \sin^{-1} \left[\frac{r_C}{r_E} \sin \psi \right] \quad (6.13)$$

Substituting (6.11)-(6.13) into (6.9) and (6.10) yields

$$V_R = \frac{L_1 r_C}{r_E} \psi' \sin \psi \quad (6.14)$$

and

$$V_N = r_E \sqrt{\frac{\mu}{r_C^3}} + L_1 \psi' \cos \left[\sin^{-1} \left(\frac{r_C}{r_E} \sin \psi \right) \right] \quad (6.15)$$

The semi-major axis can now be obtained with (6.7), (6.14) and (6.15). The final term to be found in (6.3) and (6.4) is the orbit eccentricity, which Chobotov (1996) gives as

$$e = \sqrt{1 - \frac{p}{a}} \quad (6.16)$$

Chobotov (1996) also shows the semilatus rectum can be expressed in terms of the angular momentum, H :

$$p = \frac{H^2}{\mu} = \frac{(V_N r_E)^2}{\mu} \quad (6.17)$$

This completes all the required expressions needed to determine the orbital elements of a payload released for any initial condition within the orbital plane from a rigid tether. A further quantity of interest is the position of the payload within its transfer orbit at the point of release. A non-optimum release will not necessarily guarantee that the point of release is either the apoapsis or periapsis of the orbit. Thus, the transfer orbit's true anomaly at the point of release Θ_0 , is stated by Chobotov (1996) to be:

$$\Theta_0 = \sin^{-1} \left[\frac{p V_R}{e H} \right] \quad (6.18)$$

The shift in the orbit's apoapsis or periapsis in relation to the ideal periapsis or apoapsis is portrayed in Figure 6.2 for the release of the upper payload and determined by

$$\Phi = \psi - \phi - \Theta_0 \quad (6.19)$$

The apoapsis of an orbit-raised payload represents, as part of a continuous interplanetary payload exchange with tethers, the point of rendezvous between the incoming payload and the catching cable end of another tether. To obtain the orbital radius of a non-optimally released payload at the location of the ideal or required apoapsis, the orbit's true anomaly defining this position is given by

$$\Theta_{\Delta\pi, apo} = \pi - \Phi \quad (6.20)$$

Similarly for a non-optimum release of the lower payload the transfer orbit's true anomaly at the position of the ideal periapsis is given by

$$\Theta_{\Delta\pi, per} = \pi - \psi - \phi - \Theta_0 \quad (6.21)$$

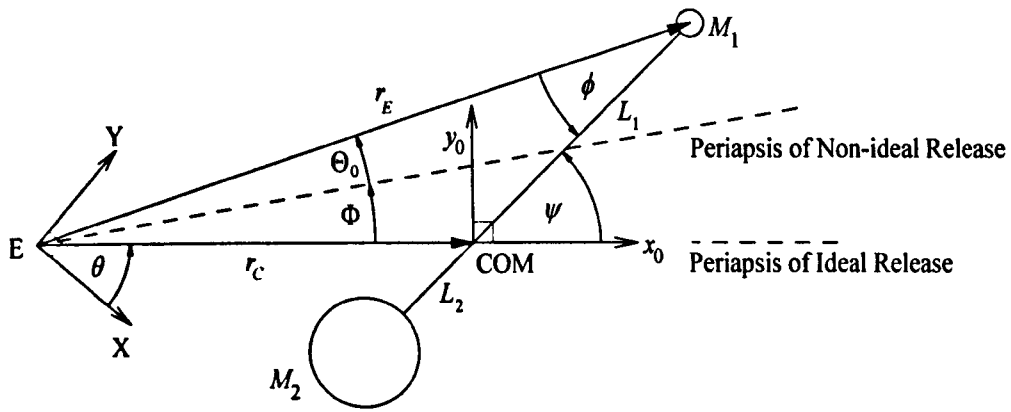


Figure 6.2 Comparison of periapsis from an ideal and non-ideal release

6.2 Altitude Gain or Drop of a Payload Released from a Tether Aligned Along the Gravity Gradient

The distance, half an orbit after the tether has released the payload, between the payload and the facility's circular orbit at the time of release is of primary interest when considering payload orbital transfer with tethers. The literature denotes this distance Δr_{π} , as shown in Figure 1.1. The optimum release condition is met when the point of release occurs along the local vertical. Thus, with $\psi = 0$ and inserting (6.2), (6.6)-(6.8) and (6.14)-(6.17) into (6.1) gives Δr_{π} for the release of the upper payload from a hanging tether, i.e. $\psi' = 0$,

$$\Delta r_{\pi} = \frac{(r_c + L)^4}{2r_c^3 - (r_c + L)^3} - r_c \quad (6.22)$$

and similarly for the lower payload

$$\Delta r_{\pi} = \frac{(r_c - L)^4}{2r_c^3 - (r_c - L)^3} - r_c \quad (6.23)$$

Carrying out the same substitution for a prograde swinging or spinning tether gives for the upper payload

$$\Delta r_{\pi} = \frac{(r_c + L)^2 [(r_c + L)\theta' + L\psi']^2}{2\mu - (r_c + L)[(r_c + L)\theta' + L\psi']^2} - r_c \quad (6.24)$$

and similarly for the lower payload

$$\Delta r_{\pi} = \frac{(r_c - L)^2 [(r_c - L)\theta' - L\psi']^2}{2\mu - (r_c - L)[(r_c - L)\theta' - L\psi']^2} - r_c \quad (6.25)$$

Assuming $L \ll r_c$ implies $\delta \ll 1$, where $\delta = L/r_c$ and allows a binomial expansion to be applied to (6.22)-(6.25), giving to $O(\delta)$

$$\Delta r_{\pi} \approx 7L \quad (6.26)$$

$$\Delta r_x \approx -7L \quad (6.27)$$

$$\Delta r_x \approx (7 + 4\psi'/\theta')L \quad (6.28)$$

$$\Delta r_x \approx -(7 + 4\psi'/\theta')L \quad (6.29)$$

and to $O(\delta^2)$

$$\Delta r_x \approx (7 + 30L/r_C)L \quad (6.30)$$

$$\Delta r_x \approx (-7 + 30L/r_C)L \quad (6.31)$$

$$\Delta r_x \approx (7 + 30L/r_C + 4\psi'/\theta' + 2Lr_C^2\psi'(18\theta' + 5\psi')/\mu)L \quad (6.32)$$

$$\Delta r_x \approx (-7 + 30L/r_C - 4\psi'/\theta' + 2Lr_C^2\psi'(18\theta' + 5\psi')/\mu)L \quad (6.33)$$

respectively. As can be seen, the above derivation obtains the identical expressions in (6.26) and (6.28) to those in the literature discussed in Chapter 1, (1.1) and (1.5). In contrast to (6.26), which is linear and solely dependent on L , (6.22) is a nonlinear expression and a function of r_C and L . Equation (6.24), moreover, is dependent on r_C , L , μ , ψ' , and θ' whereas (6.28) is solely dependent on L , ψ' , and θ' . Note that the second order simplification in (6.30) and (6.31) gives a mission designer a better insight into the most effective orbital position for the hanging tether than the first order terms in (6.26) and (6.27). To obtain ψ' for an expression above, it is necessary to distinguish between cases where the motor is on or off.

6.3 Tether Angular Velocity, Tether Strength and Spin-up Criterion

An untorqued tethered system on a circular orbit will hang, librate or spin depending on the tether's initial conditions. However, this chapter only considers the hanging and librating cases as the untorqued tether is presumed to have no initial angular velocity. ψ' has to be obtained when the tether is precisely aligned along its gravity vector, i.e. when the tether is vertical, so that (6.24), (6.25), (6.28), (6.29), (6.32) and (6.33) can be evaluated. An analytical expression for ψ' is desirable and the equation of motion of the motorised tether is derived in Chapter 2. Thus, integrating (2.95) or (2.99) with respect to ψ , assuming the tether starts from rest on a circular orbit, gives

$$\psi' = \pm \sqrt{\frac{2((\psi_1 - \psi_0)\tau - U[\psi_1] + U[\psi_0])}{M_M r_M^2/2 + M_P(2L^2 + r_{Payload}^2) + \rho AL(4L^2 + 3(r_{To}^2 + r_{Ti}^2))}}/6} \quad (6.34)$$

where the subscripts 0 and 1 represent the beginning and end states, respectively, and the square brackets the evaluation of the total potential energy U at each of these states. Equation (6.34) allows Δr_x to be determined analytically, and numerically integrating (2.95)-(2.97) provides a numerical answer for comparison. Libration results are obtained from (2.95)-(2.97) and (6.34) by setting the motor torque τ to zero.

When the tether is torqued, ψ' can be obtained analytically from (6.34) or by numerically integrating (2.95)–(2.97). This approach gives the conditions under which the tether can be spun, the nature of the spin-up and the time required to reach a desired velocity but it does not give the maximum achievable velocity. For this an expression is needed which incorporates the tether's strength. A tether, holding a payload at one end and rotating about the other, will experience centripetal acceleration and a resulting tensile force. Equating the two, whilst assuming the gravity gradient effects are negligible, gives

$$M_p L \psi'^2 + \rho A \psi'^2 \int_0^L dl = F_{tension} = \sigma A \quad (6.35)$$

yielding

$$\psi' = \sqrt{\frac{\sigma A}{L(M_p + \rho A L/2)}} \quad (6.36)$$

Equation (6.36) can be used to determine the orbital elements of a payload after release from a motorised tether facility, which unjustifiably assumes that the velocity obtained from (6.36) can be achieved when the tether aligns itself along the gravity vector. However, as the relatively slow dynamics occur over a large period of time the difference between the prediction of (6.36) and ψ' at the last vertical position before reaching the value from (6.36), which will be within one full rotation, is very small. Nonetheless, the results obtained using (6.36) will represent the maximum achievable orbital elements for the given configuration. Using (6.36), furthermore, presumes that an initial condition exists where the tether is able to spin-up. The Earth's gravity exerts a force on the tether and payload masses, which acts through the tether length, depending on the tether's orientation and direction of motion, as either an additive or resistive torque on the motor. If the motor's torque is not large enough to override the resulting gravity torque the tether will simply librate rather than spin-up. A symmetrical double-ended motorised tether with an initial starting angle between $-\pi/2 \leq \psi_0 \leq \pi/2$ will spin-up in a prograde manner as long as ψ' from (6.34) is positive and real at $\psi_1 = \pi/2$. Thus, the analytical spin-up criterion is given by

$$(\pi/2 - \psi_0)r - U[\pi/2] + U[\psi_0] > 0 \quad (6.37)$$

where due to symmetry only $-\pi/2 \leq \psi_0 < \pi/2$ needs to be considered.

6.4 Definition of Performance and Efficiency Indices

Δr_π gives the distance, half an orbit after the tether releases the payload, between the payload and the facility's orbit at the time of release. Essentially Δr_π describes how well the tether facility performs at transferring the payload. In the case of apogee altitude gain the larger Δr_π is, the better the tether's performance in payload raising, and in the case of perigee altitude

loss, the smaller Δr_π is, the better the tether's performance in payload lowering. Hence, Δr_π can be defined as the tether's performance index. It is also of interest to know how well the tether is performing in relation to its own length. A new ratio, $\Delta r_\pi/L$, is introduced here and defines the tether's efficiency index. In the case of apogee altitude gain, a more efficient tether will have a larger $\Delta r_\pi/L$ whereas in the case of perigee altitude loss $\Delta r_\pi/L$ will be smaller. With this distinction made, a further aim of the chapter is to investigate the validity of the literature's prediction of the efficiency index for given configurations.

6.5 Results and Discussion for Optimum Release of Payload

Unless stated otherwise all the results were generated with the following system parameters: $\mu = 3.9877848 \times 10^{14} \text{ m}^3 \text{ s}^{-2}$, $M_P = 1000 \text{ kg}$, $M_M = 5000 \text{ kg}$, $r_M = r_{\text{Payload}} = 0.5 \text{ m}$, $L = 50 \text{ km}$, $r_C = 6870 \text{ km}$, $r_n = 4 \text{ mm}$, $r_{T0} = 6 \text{ mm}$, $A = 62.83 \text{ mm}^2$, $\rho = 970 \text{ kgm}^{-3}$, $\sigma = 3.25 \text{ GPa}$, safety factor ($S.F.$) = 2, $\psi_0 = -0.9 \text{ rad}$, $\psi_1 = 0$. The data for the tether are based on Spectra 2000. Numerical results were obtained by integrating (2.95)–(2.97) with $\tau = 0$ in *Mathematica* with a fourth/fifth-order Fehlberg Runge-Kutta method and in *Matlab* with a fourth/fifth-order Runge-Kutta method using a relative error of 10^{-8} and 10^{-10} , respectively. Very good agreement was found between the results from both integrators and results were found not to significantly differ when relative errors smaller than 10^{-8} were used.

6.5.1 Hanging Tether

The hanging tether results for the upper, Figure 6.3, and lower, Figure 6.4, payload release show the analytical, first and second order approximations of the performance and efficiency indices, (6.22), (6.26), (6.30) and (6.23), (6.27), (6.31), respectively. The efficiency and performance of the upper payload released from a hanging tether increases with larger L . As r_C increases the indices are found to decrease, tailing off for larger r_C , which suggests the most efficient and best performing hanging tether for payload raising is one which is as close as possible to Earth with the longest possible length. Such a configuration would have to be optimised as this position in orbit experiences the greatest atmospheric drag. However, a change in L has a greater effect on performance and efficiency than altering the orbital radius and thus it is L that dominates the design of the hanging tether. The constant efficiency index of seven predicted by (6.26) is, as Figure 6.3(c) and Figure 6.3(d) shows, a lower bound.

The results in Figure 6.4 show that the requirements for high efficiency and performance in payload deorbiting from a hanging tether are different to those of payload raising. The performance of a lower payload release improves with larger L and r_C , whereas the efficiency drops with larger L and increases with greater r_C . A high performance hanging tether for payload deorbit would, therefore, be as far as possible from Earth with a large

tether length. Similarly, for efficient payload deorbit the tether is as far as possible from Earth but with a tether length that is as short as possible. As before, altering L has a greater effect on performance and efficiency than changing the orbital radius. The constant efficiency index of negative seven predicted by (6.27) is, as Figure 6.4 (c) and Figure 6.4(d) show, an upper bound.

The first order approximation is independent of L when considering the tether's efficiency and also of r_c , for both payload raising and lowering from a hanging tether, and therefore differs qualitatively from the full analytical solution. When L is less than 50 km, (6.26) and (6.27), according to Figure 6.3(a) and Figure 6.4(a), agree qualitatively and quantitatively with the full solution but due to their linearity are not able to capture the curve exhibited by (6.22) and (6.23) when L is greater than 50 km. The second order approximation is qualitatively similar to the performance index of the full analytical solution. The quantitative discrepancy between the second order approximation and the full solution, seen in Figure 6.3(b), Figure 6.3(d), Figure 6.4(b) and Figure 6.4(d), is small due to the choice of L and increases when L is larger. When L is less than 150 km (6.30) and (6.31) are in good agreement with the Δr_π of (6.22) and (6.23). Similarly, when L is less than 50 km, (6.30) and (6.31) are in good agreement with the $\Delta r_\pi/L$ of (6.22) and (6.23). However, as L moves above these thresholds the discrepancy between the solutions grows with increasing L . The results presented in Figure 6.3-Figure 6.12, show that the first and second order approximations quantitatively under predict the tether's performance and efficiency at payload raising, whereas the first and second order approximations, respectively, over and under predict the tether's performance and efficiency at payload deorbiting. In all cases the second order approximation is, as expected, quantitatively closer to the analytical solution than the first order approximation and is superior to the first order simplifications in capturing the qualitative behaviour of the full nonlinear expressions.

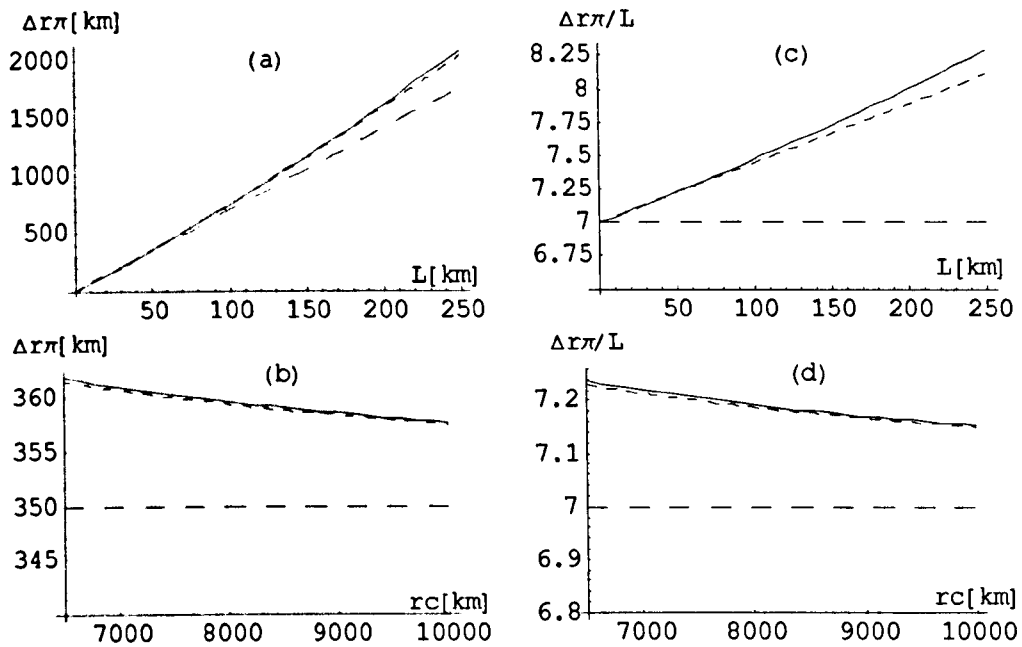


Figure 6.3 Performance and efficiency of upper payload released from a hanging tether: solid = analytical, (6.22); long dash = 1st order approximation, (6.26); short dash = 2nd order approximation, (6.30).

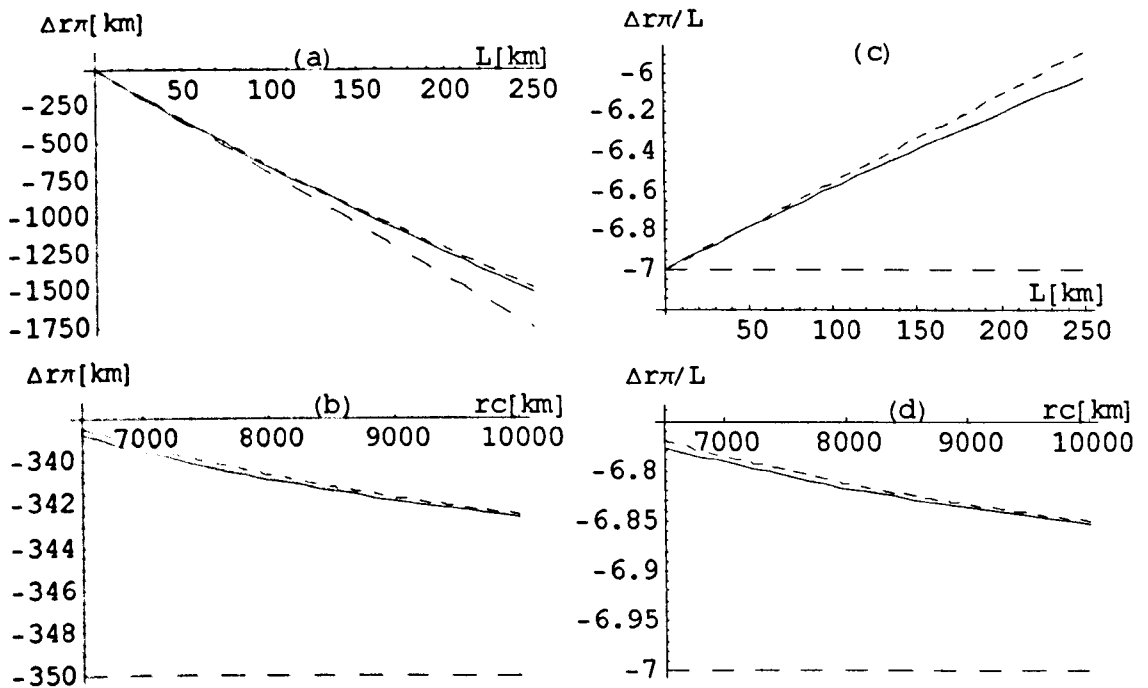


Figure 6.4 Performance and efficiency of lower payload released from a hanging tether: solid = analytical, (6.23); long dash = 1st order approximation, (6.27); short dash = 2nd order approximation, (6.31).

6.5.2 Librating Tether

The results of the performance and efficiency of a prograde librating tether at payload raising and deorbiting are presented in Figure 6.5-Figure 6.8, which combine the numerical simulation results, (1.4), and the full analytical solution, (6.24) and (6.25), along with its first and second order approximations, (6.28), (6.29) and (6.32), (6.33), respectively. These results show there is hardly any discrepancy between the full analytical and numerical results and between (1.4) and the first order approximation. Despite quantitative differences, the first order approximation is qualitatively similar to the full analytical solution when ψ_0 and M_p is varied but independent of L with regard to efficiency and r_C and thus differs qualitatively from the analytical results. When L is less than 50 km, there is good quantitative and qualitative agreement between the performance predictions of the analytical solution and its first order approximation, but due to its linearity, the approximation is unable to follow the curve of the full solution when this threshold is exceeded. The discrepancy between the analytical solution and its second order approximation, shown in Figure 6.5(a), Figure 6.5 (c), Figure 6.5 (d), Figure 6.6(a), Figure 6.6(c), Figure 6.6(d), Figure 6.7(a), Figure 6.7(c), Figure 6.7 (d), Figure 6.8(a), Figure 6.8(c) and Figure 6.8(d), is relatively small because of the choice of L and increases with larger L . Good agreement exists between the full solution and the second order approximation for efficiency and performance when L is less than 50 km and 150 km, respectively. However, a discrepancy between these two occurs when these thresholds are exceeded and this discrepancy increases with larger L .

The performance and efficiency of a librating tether at payload transfer improves but also levels off with larger ψ_0 , see Figure 6.5(a), Figure 6.6(a), Figure 6.7(a) and Figure 6.8(a). The results in Figs. Figure 6.5(b), Figure 6.6(b) and Figure 6.8(b) show the performance at payload lowering and performance and efficiency at payload raising increases with larger L but as shown in Figure 6.7(b) larger L decreases the efficiency at payload lowering. The performance and efficiency of payload raising and lowering decreases and increases, respectively, as r_C is increased, as shown in Figure 6.5(c), Figure 6.6(c), Figure 6.7(c) and Figure 6.8(c), and is found to tail off the larger r_C becomes. The results shown in Figure 6.5(d), Figure 6.6(d), Figure 6.7(d) and Figure 6.8(d) demonstrate that M_p does not significantly affect the performance nor the efficiency of the librating tether's ability at payload transfer. However, on closer inspection M_p is found to influence the numerical results, the analytical solution and both its approximations but not (1.4). The performance and efficiency of payload transfer for both upper and lower payload release improves very slightly with larger M_p . For payload raising the most efficient and best performing prograde librating tether is found to be one which has the largest possible maximum libration angle and tether length as well as orbiting Earth as closely as possible. A prograde librating tether

facility that has a large maximum libration angle and is situated as far as possible from Earth is very efficient and performs well at payload lowering. A long tether improves the performance whereas a short tether improves the efficiency at payload lowering. The maximum efficiency index of fourteen as quoted from the literature in (1.2) is not found to hold according to Figure 6.5(a) and Figure 6.5(b) because values above fourteen are readily seen to be obtained. The results show that the prograde librating tether improves, up to roughly a factor of two, on the performance and efficiency of the hanging tether.

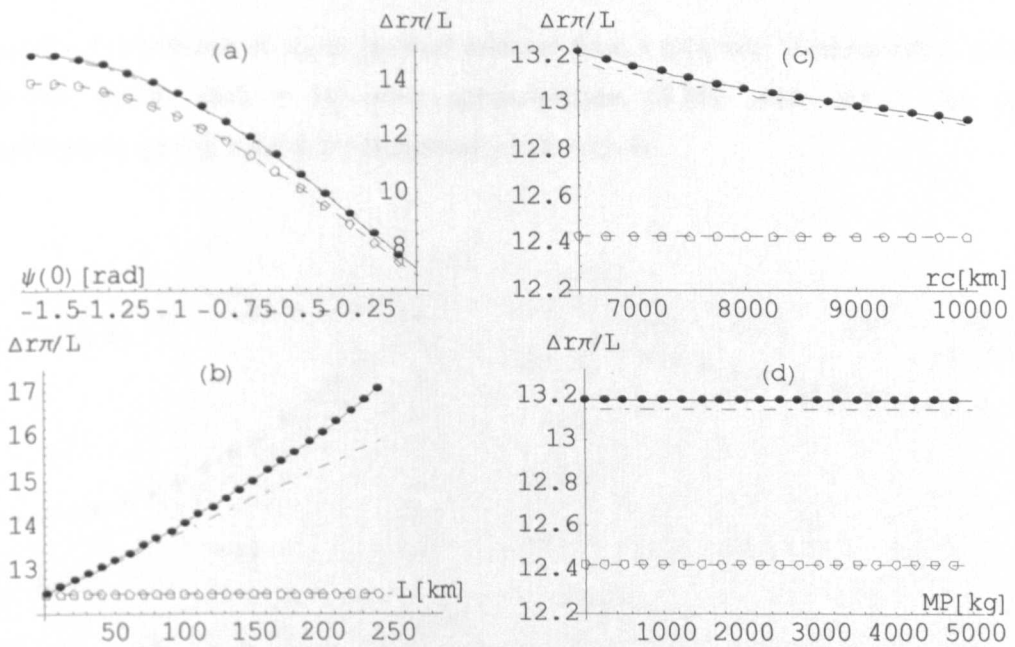


Figure 6.5 Efficiency of upper payload released from a prograde librating tether: solid = analytical, (6.24); dash = 1st order approximation, (6.28); chain dot = 2nd order approximation, (6.32); solid dot = numerical; circle = (1.4).

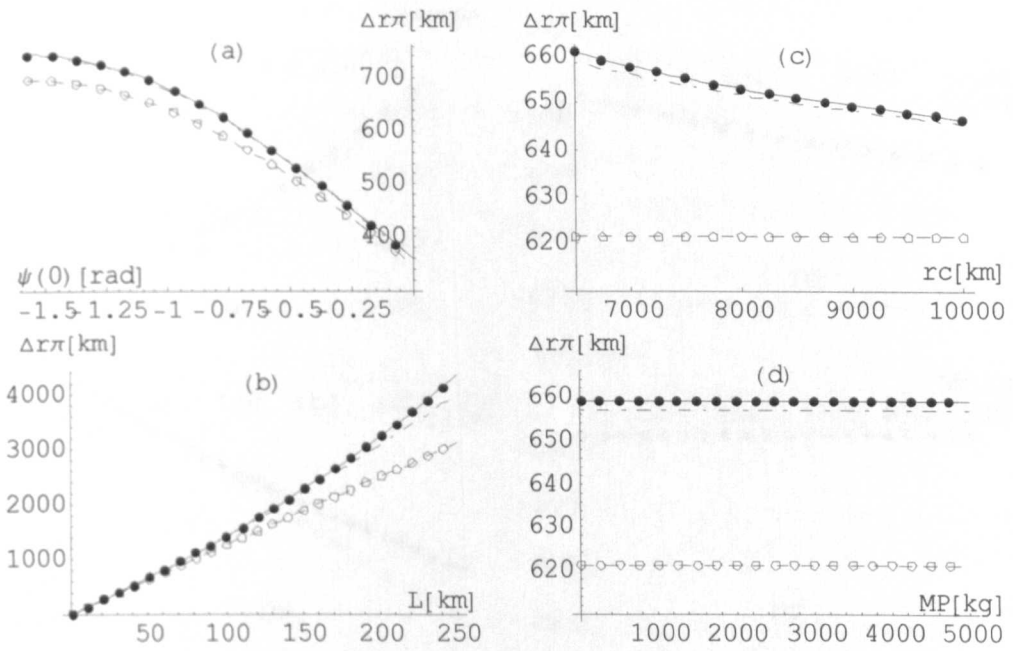


Figure 6.6 Performance of upper payload released from a prograde librating tether: solid = analytical, (6.24); dash = 1st order approximation, (6.28); chain dot = 2nd order approximation, (6.32); solid dot = numerical; circle = (1.4).

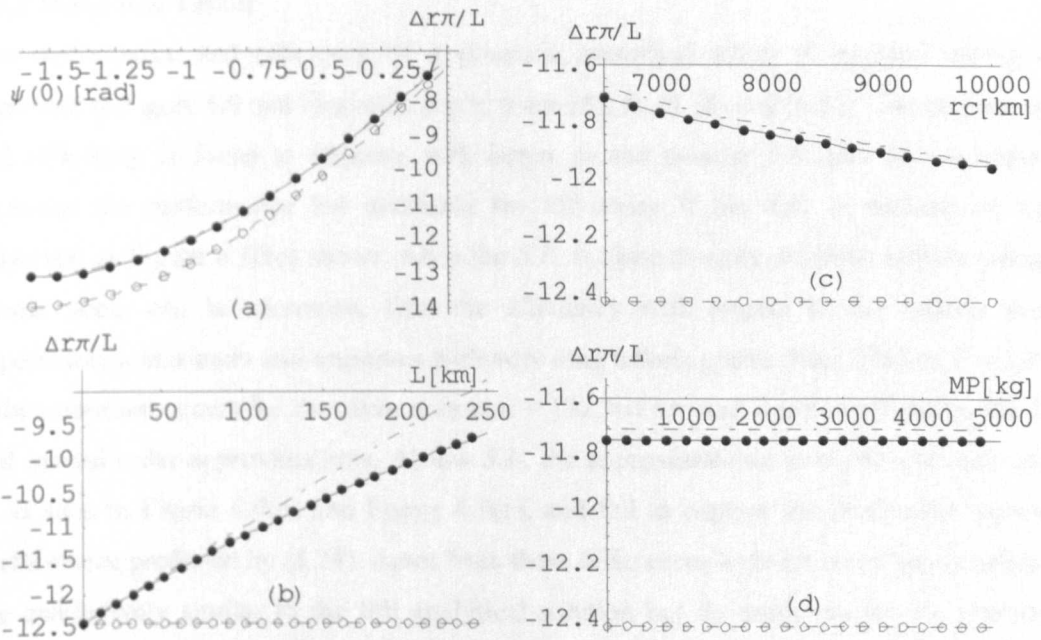


Figure 6.7 Efficiency of lower payload released from a prograde librating tether: solid = analytical, (6.25); dash = 1st order approximation, (6.29); chain dot = 2nd order approximation, (6.33); solid dot = numerical; circle = (1.4).

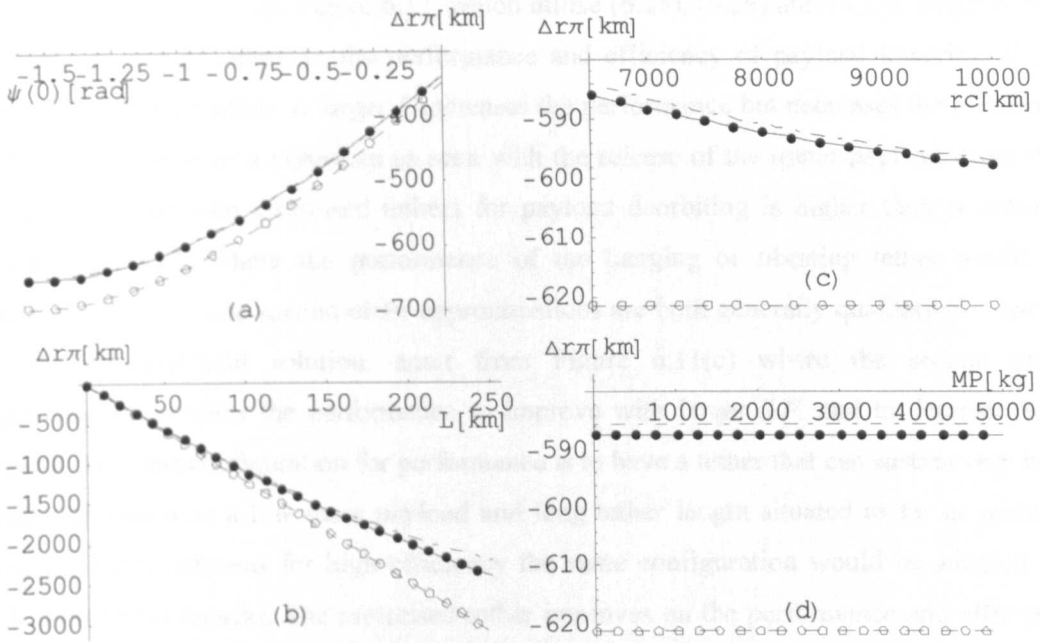


Figure 6.8 Performance of lower payload released from a prograde librating tether: solid = analytical, (6.25); dash = 1st order approximation, (6.29); chain dot = 2nd order approximation, (6.33); solid dot = numerical; circle = (1.4).

6.5.3 Motorised Tether

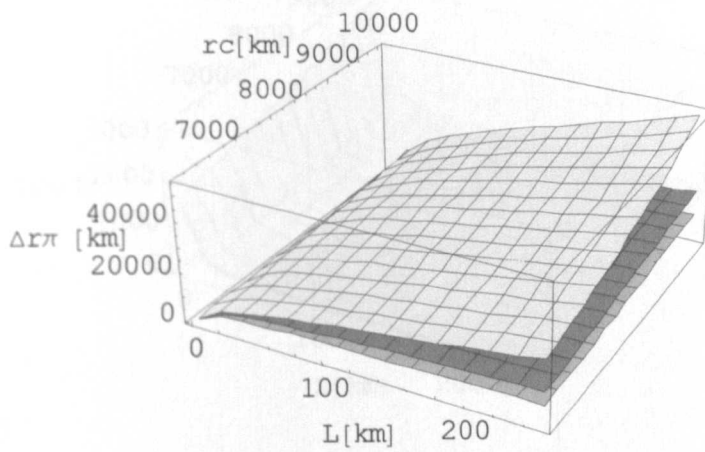
The performance and efficiency of a prograde motorised tether at payload raising are presented in Figure 6.9 and Figure 6.10 which use (6.24), (6.28) and (6.32). The performance and efficiency is found to improve with larger r_C and smaller $S.F.$ and M_p . A larger L increases the performance but decreases the efficiency if the $S.F.$ is medium or high. However, as Figure 6.10(c) shows, when the $S.F.$ is close to unity, or if the tether's ultimate tensile stress can be increased, then the efficiency with respect to the tether's length experiences a minimum and improves with very long tethers greater than 200 km. For $S.F. = 1$ the minimum occurs for the given data at $L = 132.561$ km and is not predicted by the first and second order approximations. At low $S.F.$ the approximations level off with increasing L , as seen in Figure 6.9(b) and Figure 6.9(c), and fail to capture the drastically improved performance predicted by (6.24). Apart from these differences both orders of approximations are qualitatively similar to the full analytical solution but do under predict the motorised tether's performance and efficiency quantitatively. The best performing motorised tether is one that can sustain very high tensile stress with a lightweight payload mass and long tether length, situated as far as possible from Earth. Unless tether lengths very much greater than 200 km are used the most efficient motorised tether has the same configuration as for highest performance but with tether lengths that are as short as possible.

As seen in Figure 6.11 and Figure 6.12, which utilise (6.25), (6.29) and (6.33), larger r_C and smaller $S.F.$ and M_p improve the performance and efficiency of payload lowering of the prograde motorised tether. A larger L increases the performance but decreases the efficiency with no appearance of a minimum as seen with the release of the upper payload. Note that the Δr_x achieved with motorised tethers for payload deorbiting is higher than is actually necessary in LEO where the performance of the hanging or librating tether would be sufficient. The first and second order approximations are both generally qualitatively similar to the full analytical solution, apart from Figure 6.11(c) where the second order approximation predicts the performance to improve with larger $S.F.$ and to decrease with larger L . The best configuration for performance is to have a tether that can sustain very high tensile stresses with a low mass payload and long tether length situated as far as possible from the Earth, whereas for high efficiency the same configuration would be adopted but with short tether lengths. The motorised tether improves on the performance and efficiency of the hanging and librating tether by two orders of magnitude.

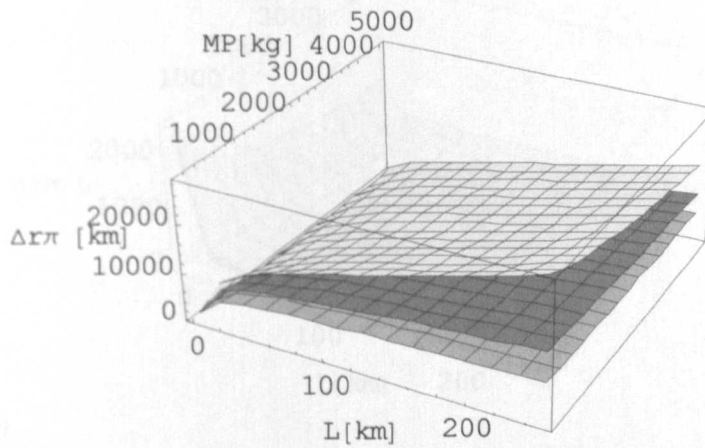
For orbital transfer, the results demonstrate that either for payload raising or lowering the motorised tether performs best and is the most efficient out of the three fundamental tether motions investigated in this chapter. Figure 6.9(c) shows that by using long tethers an upper payload can be propelled by a motorised tether in a circular LEO to GEO. A motorised tether using the above data along with $P = 5.5$ kW, $\tau = 464720$ Nm, $S.F. = 1.2$ and $L = 139.122$ km can achieve $\Delta r_x = 35467.38$ km but requires a very large motor torque and puts great demands on the tether's strength. Here the relationship of $P = \tau \psi'$ is employed and a rating of 5.5 kW appears reasonable, if not a little conservative, as the solar panels on satellites being currently launched are able to generate 10-12.5 kW. Increasing the $S.F.$ requires larger L and higher values of motor torque to deliver the payload to GEO. Hence, unless expendable tethers are used, multiple tether stages or tethers on elliptical orbits will have to be considered. Multiple tether stages could utilise long tethers which are greater than 10 km, but Figure 6.10 and Figure 6.11 suggest that the more efficient shorter tethers, roughly 1 km in length, are worthy of consideration. Despite the poor performance, short tethers have the advantage of being lighter, therefore, costing less to deliver into orbit, less susceptible to being severed due to the reduced area exposed to space debris, easier to manufacture and requiring less material, thereby, reducing costs. Generating the same tangential velocity with short tethers as achieved with long tethers requires an increase in ψ' and a reduction in motor torque if the available power remains constant. Hence, the central facility's mass can be reduced as a lesser amount of torque utilises a smaller gearbox.

The results of numerically integrating (2.95)-(2.97) to obtain the angular pitch displacement achieved from different ψ_0 over 50000 seconds, are shown in Figure 6.13. In general, when the tether is librating then $-\pi/2 < \psi_{50000} < \pi/2$ and if it is spinning progradely then $\psi_{50000} > \pi/2$. The threshold between libration and spin-up is obtained from (6.37) and shows very good agreement with the numerical results. The 50 km long tether in Figure 6.13(a) spins up for $-\pi/2 \leq \psi_0 \leq -1.3977$ rad and $1.5608 \leq \psi_0 \leq \pi/2$ rad using $P = 5.5$ kW, whereas a 1km long tether driven by the same power source spins up for all ψ_0 in Figure 6.13(b). If $P = 55$ W then the 1 km tether, shown in Figure 6.13(c), spins up for $-\pi/2 \leq \psi_0 \leq -1.2108$ rad and $1.5262 \leq \psi_0 \leq \pi/2$ rad which is a larger region than that of the 50 km tether. Thus, a further advantage of short tethers is the ability to spin-up for any ψ_0 , as in Figure 6.13(b), and a larger region of ψ_0 for which spin-up is possible if the power source is reduced, thereby, ruling out sophisticated, vulnerable and expensive orientational controls for start-up that would be required for motorised tethers using long tethers. The disadvantage is of course the increase in risk of losing a payload due to the additionally required transfers.

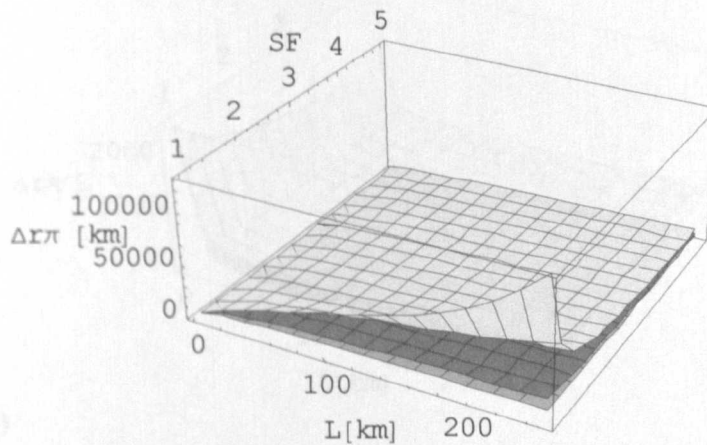
Rather than deploying the tethers fully before energising the motor to spin the system, the results in Figure 6.13 suggest that the motor should be energised prior to deploying the tethers. The reaction to the centripetal acceleration caused by the spinning rotor should aid deployment and increase the range of ψ_0 enabling spin-up, if not altogether avoiding the problems with the resistive gravity torque at start-up. Further work should model the proposed deployment and investigate the effects of tether flexibility and deployment on the performance and efficiency of the tether mediated payload orbital transfer.



(a)



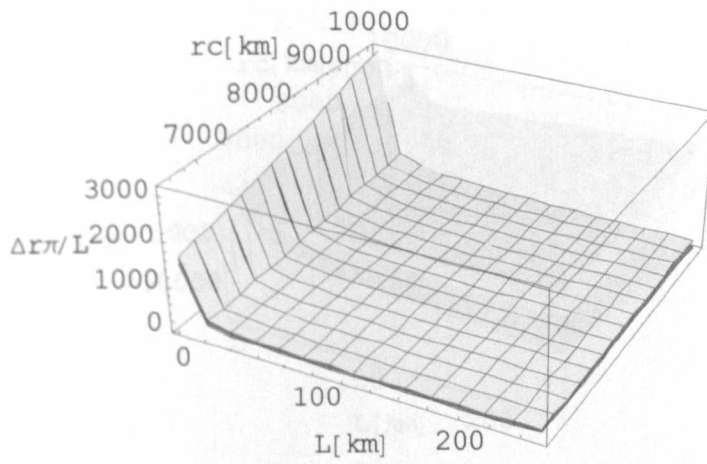
(b)



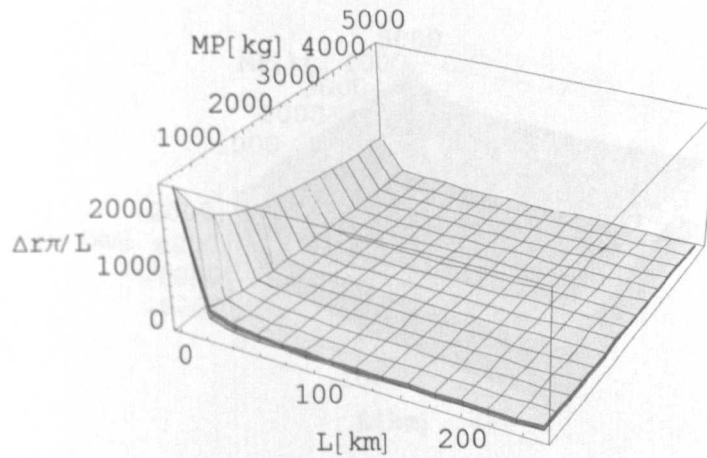
(c)

Figure 6.16 Efficiency of upper payload released from a prograde motorised tether.

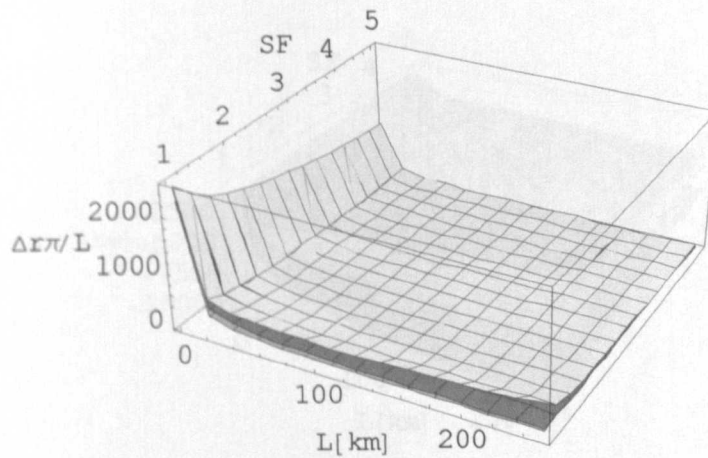
Figure 6.9 Performance of upper payload released from a prograde motorised tether: light grey = analytical, (6.24); medium grey = 1st order approximation, (6.28); dark grey = 2nd order approximation, (6.32).



(a)

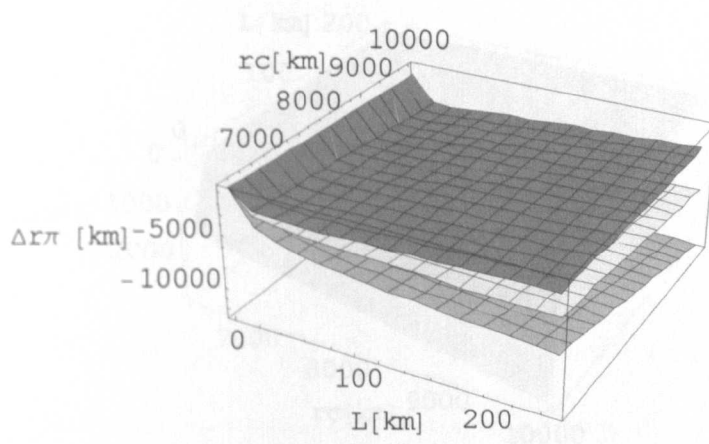


(b)

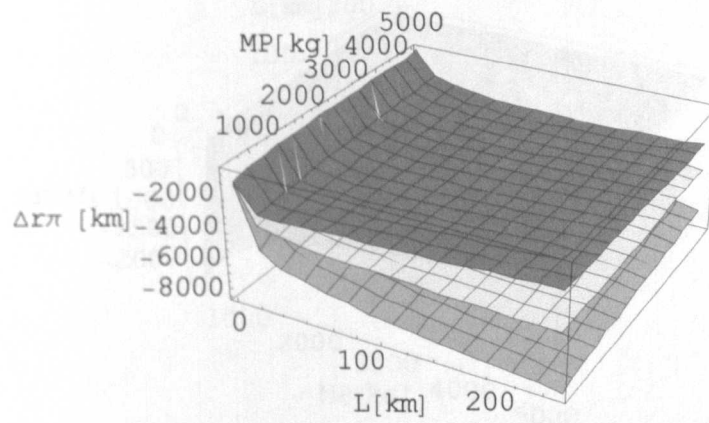


(c)

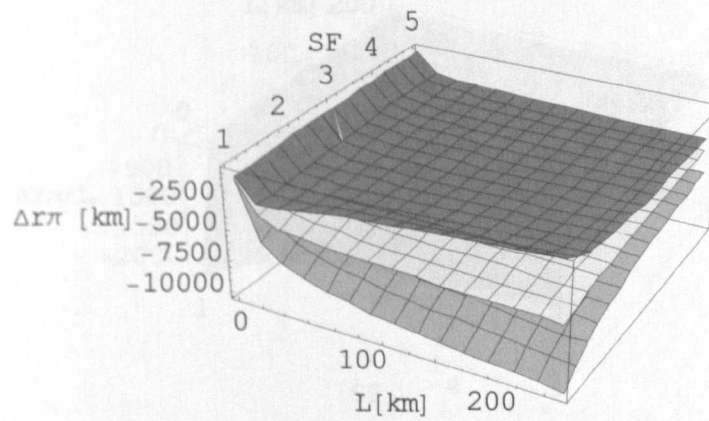
Figure 6.10 Efficiency of upper payload released from a prograde motorised tether: light grey = analytical, (6.24); medium grey = 1st order approximation, (6.28); dark grey = 2nd order approximation, (6.32).



(a)

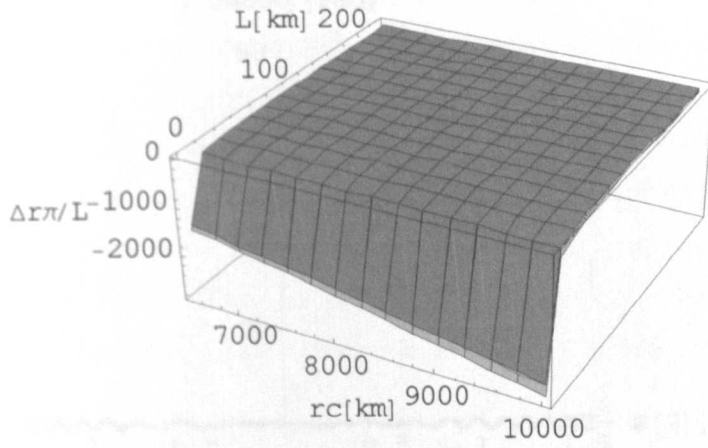


(b)

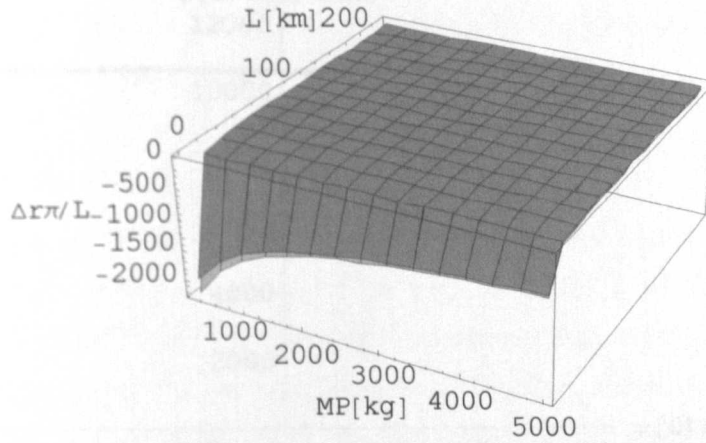


(c)

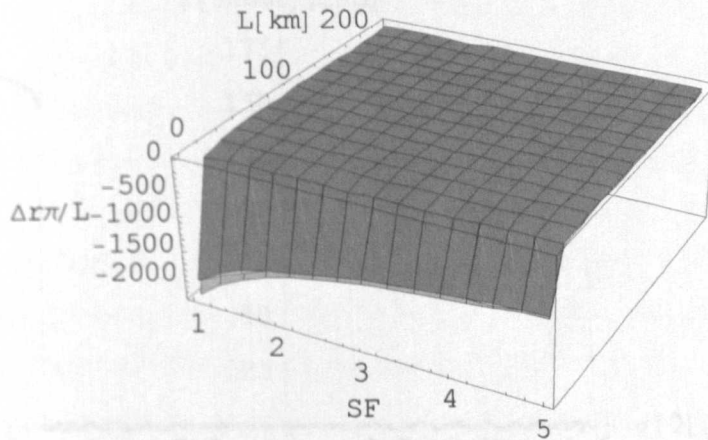
Figure 6.11 Performance of lower payload released from a prograde motorised tether: light grey = analytical, (6.25); medium grey = 1st order approximation, (6.29); dark grey = 2nd order approximation, (6.33).



(a)



(b)



(c)

Figure 6.12 Efficiency of lower payload released from a prograde motorised tether: light grey = analytical, (6.25); medium grey = 1st order approximation, (6.29); dark grey = 2nd order approximation, (6.33).

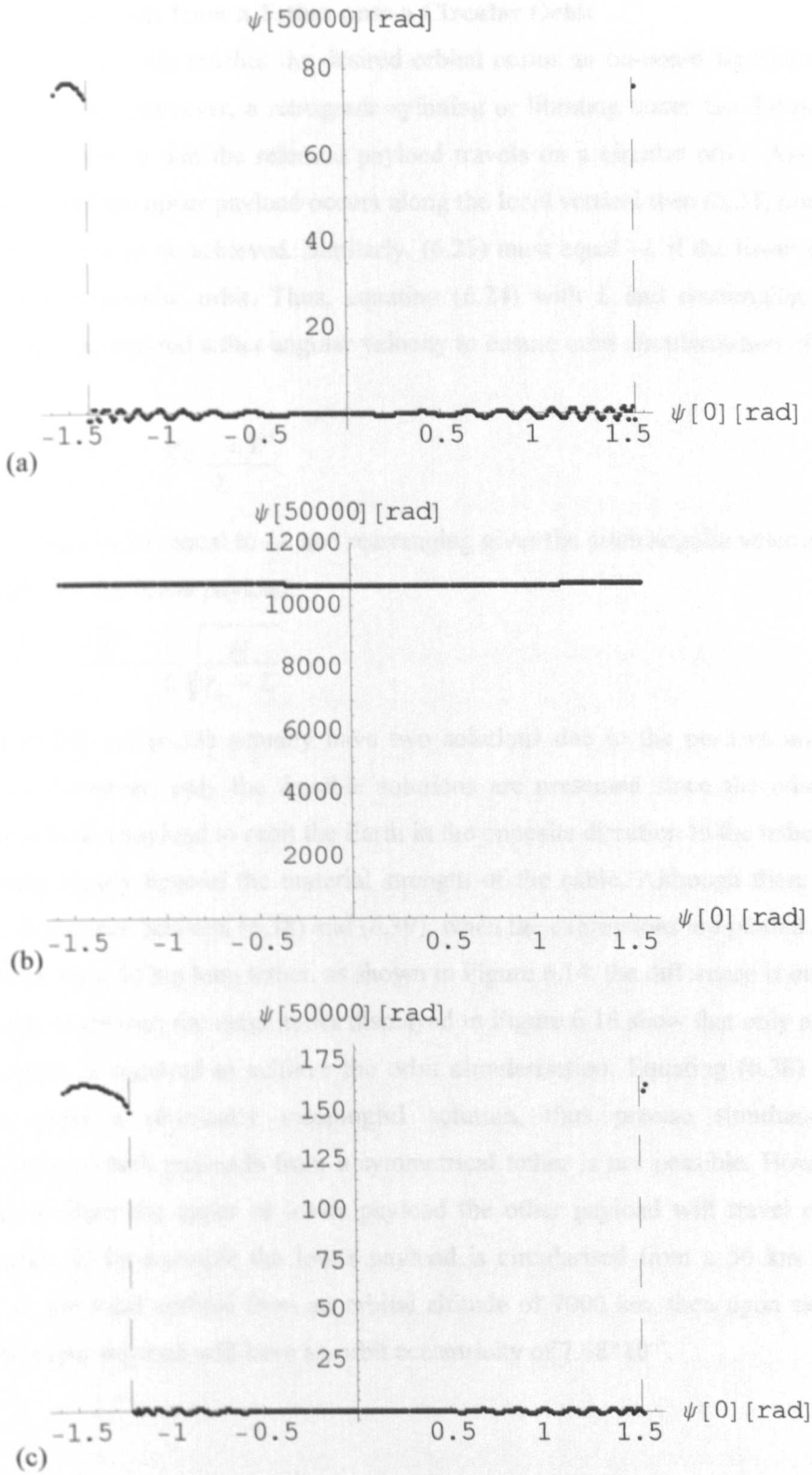


Figure 6.13 Motorised tether spin-up dependency on initial angular displacement: dot = numerical; dashed = analytical criterion, (6.37); (a) $L = 50$ km, $P = 5.5$ kW, $\tau = 193353$ Nm; (b) $L = 1$ km, $P = 5.5$ kW, $\tau = 17473.1$ Nm; (c) $L = 1$ km, $P = 55$ W, $\tau = 174.731$ Nm.

6.6 Release of Payloads from a Tether onto a Circular Orbit

Once a payload currently reaches the desired orbital radius an on-board thruster is fired to circularise the orbit. However, a retrograde spinning or librating tether has the potential of releasing a payload so that the released payload travels on a circular orbit. Assuming the point of release of the upper payload occurs along the local vertical then (6.24) must equal L if a circular orbit is to be achieved. Similarly, (6.25) must equal $-L$ if the lower payload is released on to a circular orbit. Thus, equating (6.24) with L and rearranging yields an expression for the required tether angular velocity to ensure orbit circularisation of the upper payload,

$$\psi' = \frac{1}{L} \sqrt{\frac{\mu}{r_c + L}} - \frac{(r_c + L)\theta'}{L} \quad (6.38)$$

Similarly, setting (6.25) equal to $-L$ and rearranging gives the pitch angular velocity for orbit circularisation of the lower payload,

$$\psi' = \frac{(r_c - L)\theta'}{L} - \frac{1}{L} \sqrt{\frac{\mu}{r_c - L}} \quad (6.39)$$

Note that (6.38) and (6.39) actually have two solutions due to the positive and negative square root. However, only the feasible solutions are presented since the other solution causes the released payload to orbit the Earth in the opposite direction to the tether, which is a manoeuvre clearly beyond the material strength of the cable. Although there is a small numerical difference between (6.38) and (6.39), when the expressions are plotted against the orbital radius for a 50 km long tether, as shown in Figure 6.14, the difference is on the whole rather small. Moreover, the magnitudes displayed in Figure 6.14 show that only a retrograde librating tether is required to achieve the orbit circularisation. Equating (6.38) and (6.39) does not yield a physically meaningful solution, thus precise simultaneous orbit circularisation of both payloads from a symmetrical tether is not possible. However, upon circularising either the upper or lower payload the other payload will travel on a nearly circular orbit. If for example the lower payload is circularised from a 50 km long tether precisely at the local vertical from an orbital altitude of 7000 km, then upon simultaneous release the upper payload will have an orbit eccentricity of 7.68×10^{-5} .

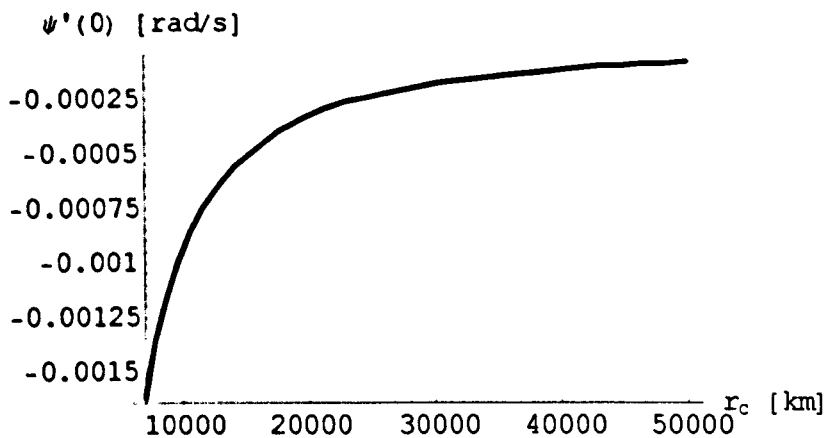


Figure 6.14 ψ' required for orbit circularisation of the released payload from a 50 km long tether with the orbital radius is prescribed.

6.7 Effect of Non-optimum Release on Payload Orbital Transfer with Tethers

The literature and the above analysis have assumed the release of the payload occurs whilst the tether is parallel to the local vertical or gravity vector. This represents the ideal release conditions for payload raising or lowering as the full component of the relevant velocity vectors are in line with each other. Moreover, investigating the perfect release conditions allows the full potential of tethers to be quantified. However, studying the effect of a non-optimum release on the payload transfer with tethers is equally important as this indicates how the performance of tethers will be affected by the inaccuracies at release and can specify how accurate the payload release has to be. In the context of continuous interplanetary payload exchange the examination of non-optimum release will also give an insight into how large the distance between an incoming payload and the catching tether tip might be and what problems a catch mechanism would have to overcome.

The following considers some non-optimum release conditions for a hanging, librating and spinning tether. Instead of releasing the payload from a hanging tether the payload might be cut from a tether that is slightly librating. This scenario is not unrealistic as the final libration angle on the SEDS-2 mission in 1994 was controlled to within 4° . The point of release could occur at the maximum libration angle, whilst the tether is aligned along the gravity vector, or perhaps somewhere in between. For a swinging or spinning release there is no guarantee that the payload will be released upon the tether reaching the local vertical. A slight error in the timing of the release or perhaps a delay in the mechanism severing the contact between the payload and cable can cause the point of release to drift either side of the local vertical.

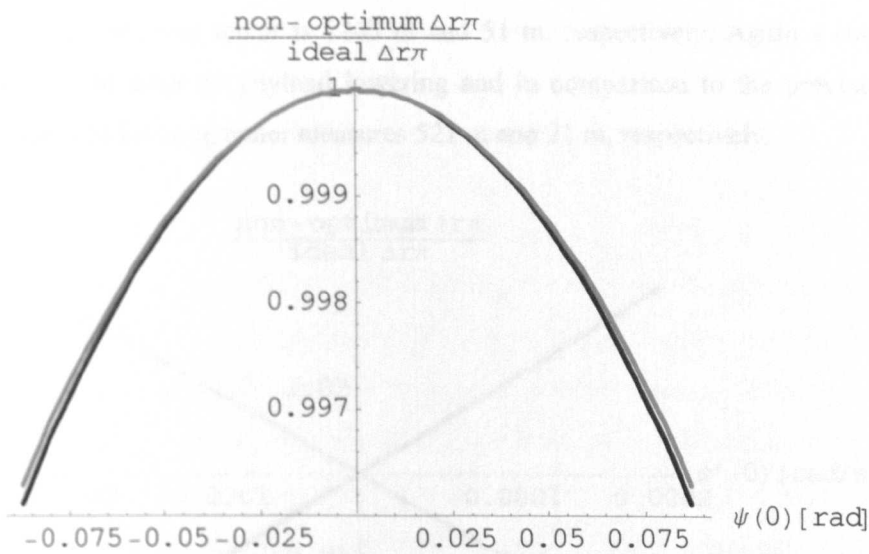


Figure 6.15 Comparison of the effect of releasing the upper (black) and lower (grey) payload from a hanging tether and a tether displaced from the local vertical with $\psi(0) = 0$.

Figure 6.15 displays the effect of releasing the upper and lower payload, respectively, from a slightly librating tether where the point of release occurs at the largest libration angle with $\psi' = 0$. The ratio of Δr_π for the non-optimum and perfect release is formed and plotted against a maximum libration angle ranging between $\pm 5^\circ$. As this release scenario does not cause a radial velocity along the payload's orbital radius, the point of release for payload raising becomes the periapsis and similarly the apoapsis for payload lowering. However, the position of the periapsis and apoapsis shifts relative to those of the ideal release according to (6.20) and (6.21) but upon inspection is found to be less than a thousandth of a radian for payload raising and lowering, which is negligibly small. Consequently, the difference between the orbital radius at the payload's apogee or perigee and the payload's orbital radius in line with the location of the ideal apogee or perigee measures 3 cm for payload raising and 1 mm for payload lowering, and is therefore equally negligible. Figure 6.15 shows the difference between the ideal and non-optimum Δr_π drops off in a parabolic fashion with increasing libration angle and measures less than 1% within the $\pm 5^\circ$ window. Although not shown, both depicted curves are found to be insensitive to different tether lengths.

The absolute difference in Δr_π between a hanging tether and a 50 km long tether releasing the upper payload at an angle of 5° with $\psi' = 0$ is 1407 m. If the angle reduces to 1° then the difference measures 56 m. These values are primarily dependent on the tether length and the discrepancy will be smaller with a shorter tether. For example, the discrepancy in Δr_π for a 20 km long tether reduces to 544 m and 22 m for the same release conditions. Similarly, the variation between a 50 km long tether with $\psi' = 0$ releasing the lower payload at an angle of

5° and 1°, and a hanging tether is 1263 m and 51 m, respectively. Again a shorter tether length reduces the error on payload lowering and in comparison to the previous data the difference for a 20 km long tether measures 521 m and 21 m, respectively.

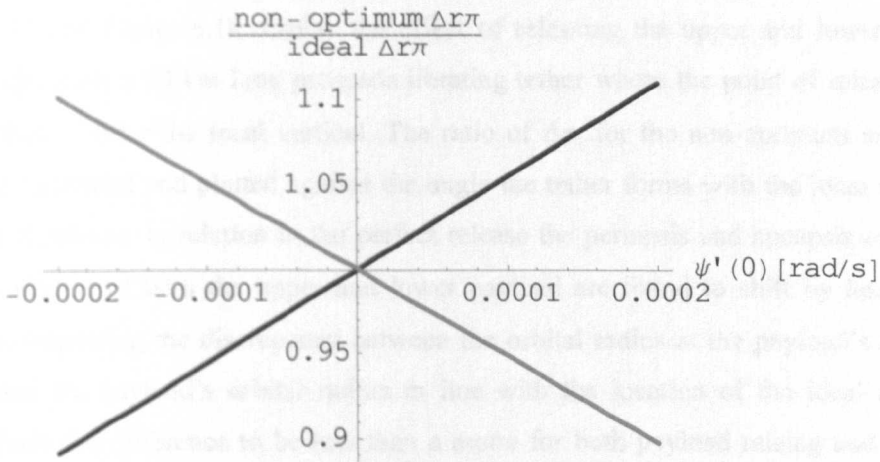


Figure 6.16 Comparison of the effect of releasing the upper (black) and lower (grey) payload from a hanging and a slightly librating tether aligned along the gravity gradient.

Figure 6.16 explores the effect of releasing the upper or lower payload along the local vertical but with an initial angular velocity of ± 0.0002 rad/s about the COM, which equates to a tether librating with a maximum angular displacement of $\pm 5^\circ$. By plotting the ratio of the non-optimum and ideal Δr_π , Figure 6.16 shows that the error varies linearly between $\pm 10\%$ with the initial angular velocity. Altering the tether length is found to have little effect on the qualitative and quantitative shape of the line. When the tether has a prograde velocity the upper payload gains a greater Δr_π than for the ideal release and conversely for a retrograde velocity the Δr_π is less than the ideal altitude gain, as would be expected. Similarly, the lower payload attains a greater Δr_π for prograde rotation and less Δr_π with retrograde motion than the perfect release from a hanging tether. The absolute difference between a hanging tether and a 50 km long tether with a libration angle of 5° releasing the upper payload in line with the local vertical is 33.9 km. If the maximum libration angle reduces to 1° then the difference is 6773 m. As before, these values are primarily dependent on the tether length and the discrepancy will be smaller with a shorter tether. For the same release condition as before the discrepancy for a 20 km long tether reduces to 13 km and 2604 m, respectively. When the release of the lower payload from a hanging tether and a 50 km long librating tether is considered, where the angular velocity is equivalent to a libration angle of 5° and the tether cut occurs in line with the local vertical, then the difference is found to be 29.8 km. If for this given release scenario the maximum libration angle reduces to 1° then the

difference becomes 5955 m. If the error from a shorter tether is investigated for the identical scenarios then the discrepancy reduces for a 20 km long tether to 12.4 km and 2473 m, respectively.

Figure 6.17 and Figure 6.18 display the effect of releasing the upper and lower payload, respectively, from a 50 km long prograde librating tether where the point of release occurs either before or after the local vertical. The ratio of Δr_x for the non-optimum and perfect release is calculated and plotted against the angle the tether forms with the local vertical at the point of release. In relation to the perfect release the periapsis and apoapsis of the non-optimum release of both the upper and lower payload are found to shift by less than 1° . Similarly, inspecting the discrepancy between the orbital radius at the payload's apogee or perigee and the payload's orbital radius in line with the location of the ideal apogee or perigee finds the difference to be less than a metre for both payload raising and lowering. The effect of these can probably be discounted since the error caused by the non-optimum release portrayed in Figure 6.17 and Figure 6.18 are larger by at least an order of magnitude. Furthermore, the curves presented in Figure 6.17 and Figure 6.18 were found to be largely unaffected by different tether lengths. Four maximum libration angles are presented: -25° , -20° , -15° , and -10° , with the negative sign indicating a prograde rotation. For both payload raising and lowering the larger the maximum libration angle is the less the percentage difference is on the ratio between the perfect and non-optimum release. Moreover, the error between the desired and non-optimum release increases in a parabolic fashion the earlier the payload is released before the local vertical. The difference between a 50 km long tether with a maximum libration angle of -25° releasing the upper payload at 1° before the local vertical compared to a perfect release is 227 m. When the maximum libration angle is reduced to -10° the difference between the two release conditions rises to 412 m. For a 20 km long tether, however, this drops for the same conditions to 86 m and 158 m, respectively. Similarly, when the lower payload is released from a 50 km long tether with maximum libration angles measuring -25° and -10° at 1° prior to the local vertical the difference between optimum and non-optimum release is found to be 191 m and 356 m. These decrease to 80 m and 149 m, respectively, for a 20 km long tether with the same release conditions as before.

The ratio of the non-optimum over the ideal Δr_x is investigated in Figure 6.19 for a prograde spinning tether and is seen not to be particularly informative, as there is little discrepancy between the three tether lengths of 10 km, 25 km and 50 km. Furthermore, the small difference in percent observed over the $\pm 5^\circ$ angle prior to the local vertical at which the

payload is released hides the fact that a few percent of a large Δr_{π} represents a large absolute error. Hence, when the non-optimum Δr_{π} is subtracted from the ideal Δr_{π} , as shown in Figure 6.20 and Figure 6.21, the drop in performance from a non-optimum release measures several kilometres. Moreover, the longer the tether is the larger the error becomes between a perfect and non-optimum release of the upper or lower payload. In addition to this, the error between the two release conditions increases in a parabolic manner the earlier the payload is released prior to the local vertical. For the case of the spinning tether release the discrepancy between the orbital radius at the payload's apogee or perigee and the payload's orbital radius in line with the location of the ideal apogee or perigee is found to be significant and therefore cannot be neglected for payload raising or lowering. The perigee of the non-optimum release is additionally found to shift relative to the ideal perigee by several degrees. The difference between a 50 km long tether spinning at 0.01 rad/s and releasing the upper payload at 5° before the local vertical compared to a perfect release is 12 km, and drops to 494 m when the angle prior to the local vertical reduces to 1°. For a 10 km long tether the differences are in comparison 40-43 m and 162 m, respectively. Likewise, the difference between a 50 km long tether spinning at 0.01 rad/s and releasing the lower payload at 5° before the local vertical compared to a perfect release is 5792 m, and reduces to 232 m when the error drops to 1°. The differences for a 10 km long tether in comparison measure 2942 m and 118 m, respectively.

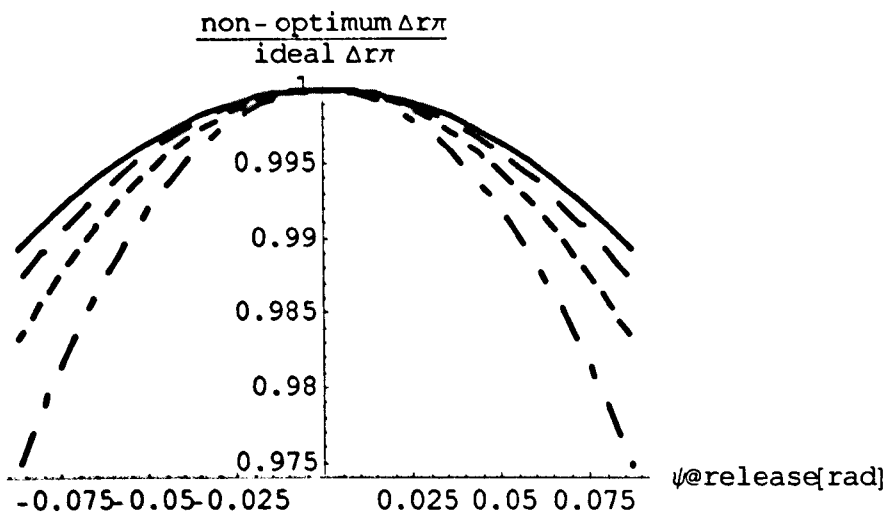


Figure 6.17 Ratio of non-optimum over perfect release of the upper payload from a librating tether. Solid: $\psi(0) = -25^\circ$, long dashed: $\psi(0) = -20^\circ$, short dashed: $\psi(0) = -15^\circ$, and chain dashed: $\psi(0) = -10^\circ$.

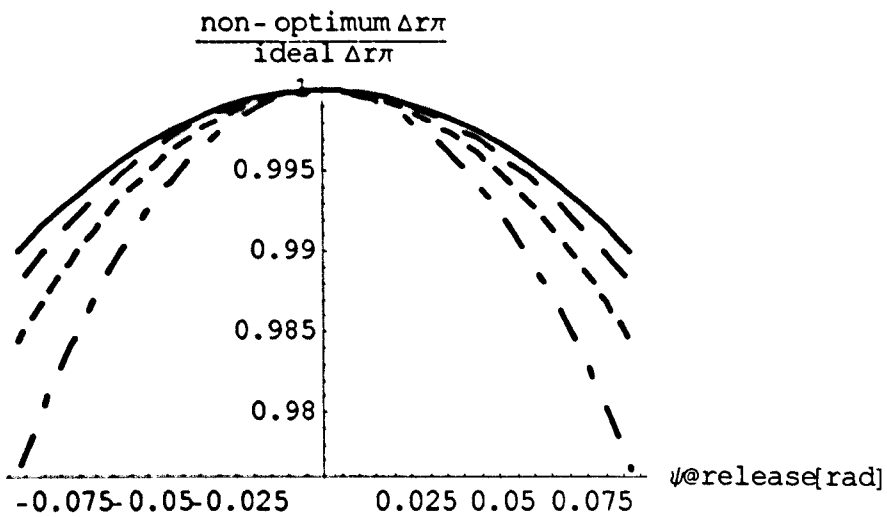


Figure 6.18 Ratio of non-optimum over perfect release of the lower payload from a librating tether. Solid: $\psi(0) = -25^\circ$, long dashed: $\psi(0) = -20^\circ$, short dashed: $\psi(0) = -15^\circ$, and chain dashed: $\psi(0) = -10^\circ$.

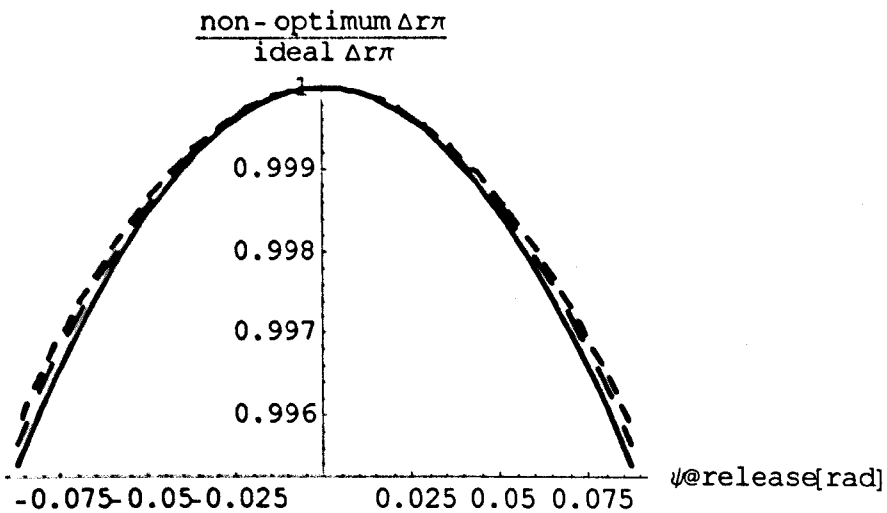


Figure 6.19 Ratio of non-optimum over perfect release of the upper payload from a spinning tether with a non-zero angular displacement relative to the local vertical. Solid: $L = 50$ km, long dashed: $L = 25$ km, short dashed: $L = 10$ km.

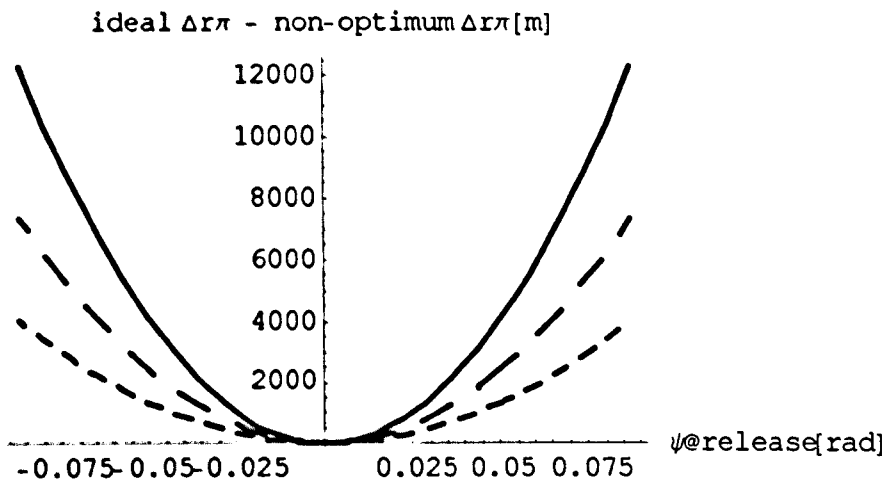


Figure 6.20 Effect of releasing the upper payload from a spinning tether with a non-zero angular displacement relative to the local vertical. Solid: $L = 50$ km, long dashed: $L = 25$ km, short dashed: $L = 10$ km.

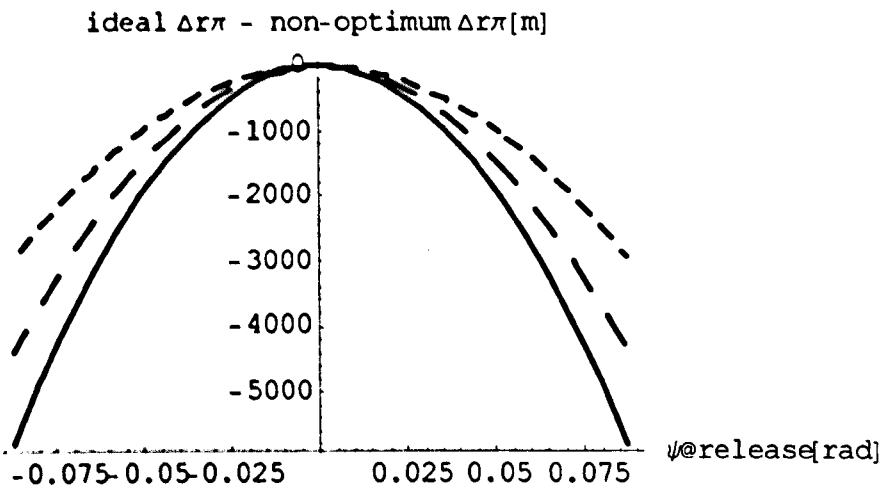


Figure 6.21 Effect of releasing the lower payload from a spinning tether with a non-zero angular displacement relative to the local vertical. Solid: $L = 50$ km, long dashed: $L = 25$ km, short dashed: $L = 10$ km.

The results presented in Figure 6.15-Figure 6.19 demonstrate that a non-optimum release of the payload has a significant impact on the performance of payload transfer with tethers. The absolute difference between the ideal and non-optimum Δr_x ranges anything from a few tens of metres to several kilometres. The results emphasise the importance of a very precise and accurately timed release since missing the point of release by a single degree with a spinning tether, say, can cause the payload to entirely undershoot its target orbit or rendezvous.

Consequently, future work on designing the payload release mechanism must deliver a very accurate and reliable methodology as well as hardware. The results also show that a payload release from a hanging tether must carefully control the librations of the tether, as well as any tether vibrations. If payload lowering with a hanging tether is attempted from the International Space Station, say, then any unwanted librations could cause the payload to either under- or overshoot the required orbit by several kilometres.

Hoyt (2000a) discusses the use of a grapple mechanism for catching an incoming payload. The amount of separation between the tether tip and the payload that the grapple mechanism can overcome is not entirely clear but a presented graph in the paper suggests a few metres discrepancy can be corrected by deploying the grapple at the end of a cable. Hoyt (2000b) presents another proposal for a catch mechanism consisting of a net and a harpoon. From the tether tip a large net structure is deployed, thus giving the incoming payload a large target area into which a harpoon can be fired to establish the connection between the two. The use of mechanical capture mechanisms will in most cases rely on the separation between the tether tip and the incoming payload being probably in the region of perhaps a few tens of metres or more. However, unless an ingenious concept is found the above results suggest the reduction in orbital altitude due to a non-optimum release will most likely have to be overcome by firing rocket thrusters within the payload instead of employing a mechanical catching device.

6.8 Conclusions

Three fundamental tether motions investigated in this chapter were considered for payload orbital transfer: hanging, prograde libration and prograde motorised spin. The symmetrical double-ended motorised spinning tether performs best and is most efficient, improving by two orders of magnitude on the librating tether which in turn improves on the hanging tether by roughly a factor of two. An upper payload using long tethers with a motorised tether on a circular orbit can be transferred from a low to a geostationary Earth orbit by employing relatively high motor torque and a safety factor on the tether strength close to unity. Multiple tethered stages or tethers on elliptic orbits will, therefore, have to be considered for geostationary payload transfer unless expendable tethers are employed. Despite their poor performance, short tethers are worth considering for use in conjunction with the multiple tethered stages because of their efficiency, overall system mass reduction, cost effectiveness, better survivability and greater range of initial conditions for which spin-up is possible. Consequently, the motor should be spun prior to tether deployment rather than deploying the tethers fully before commencing spin-up. Two common literature results, the constant efficiency index of seven for a hanging tether upper payload release and the maximum

efficiency index of fourteen for an upper payload released from a prograde librating tether, are found to be a lower bound and quite readily breached, respectively. Orbit circularisation through tether release is found to be feasible with retrograde librating tethers. Moreover, upon circularising either the upper or lower payload the payload released from the other end of a symmetrical tether will travel on a nearly circular orbit. When the point of release does not occur along the local vertical then a non-optimum release of the payload is found to severely reduce the performance of payload transfer with tethers. Consequently, a very precise and accurately timed release is important for the success of payload orbital transfer with tethers since missing the point of release by a single degree with a spinning tether, say, can cause the payload to miss its required target. The large discrepancies in orbit transfer between ideal and non-optimum release scenarios call into question the use of mechanical catch mechanisms and therefore released payloads will most likely have to correct the inaccuracy at release by firing rocket thrusters.

Chapter 7

Design Considerations and Dynamics of a Symmetrical Motorised Tether

7.0 Introduction

The previous chapter compared the performance of motorised tethers at payload orbital transfer with that achieved by hanging and librating tethers. An important observation was made that for long tether lengths the motor torque may not be large enough to overcome the gravity gradient torque, therefore, not permitting the system to spin-up. Although this is undesirable for the motor's rotor, which is trying to generate as much ΔV as possible for the payloads, trapping the stator in the potential well may be a possible design solution for the outrigger system. Furthermore, the previous chapter made several unsubstantiated assumptions about the motorised tether's dynamics, such as the spin-up of the tether being regular and periodic, thus allowing the payloads to be released at the desired point on orbit with the tether in line with the gravity vector. Consequently, the evaluation of the motorised tether concept is continued in this chapter by investigating the design of the outrigger system and the planar spin-up of the motorised tether, as well as the effect of the motor's orientation and out-of-plane initial conditions on the process of tether spin-up.

7.1 Design of Outrigger System

Flywheels are employed in satellites to obtain the desired attitude orientation in space. The following explores if a solid flywheel wheel can be used to provide the necessary reaction to allow the propulsive tethers to spin up. The ability to replace the outrigger tethers would be an advantage, as the motorised tether possesses the inherent risk of a catastrophic clash occurring between the propulsion and outrigger tethers. The critical issue though is whether a spinning disc can withstand the hoop and radial stresses or whether the disc will fail at the required angular velocities. Lamé's equations, as discussed by Polter (1967), allow the maximum stress due to the constant angular velocity of a homogeneous, uniformly thick disc to be determined, and is given by

$$\sigma_{\max} = \frac{3 + \nu}{8} \rho_{\text{disc}} r_{\text{disc}}^2 \beta'^2 \quad (7.1)$$

where β' = in-plane outrigger angular velocity, r_{disc} = radius of the reaction wheel, ρ_{disc} = material density, σ_{\max} = ultimate tensile strength, ν = Poisson's ratio. Note that Lamé's

equations do not strictly apply to the case of the motorised tether since the reaction wheel would be accelerating and thus not spinning at a constant angular velocity. However, applying Lamé's equations provides a rough estimate as to whether a flywheel could provide the necessary resistive torque. Rearranging (7.1) gives the maximum permissible angular velocity

$$\beta' = \sqrt{\frac{8\sigma_{max}}{(3+\nu)\rho_{disc}r_{disc}^2}} \quad (7.2)$$

Assuming a flywheel is composed of steel, where $\rho_{disc} = 7850 \text{ kg/m}^3$, $\sigma_{max} = 450 \text{ MPa}$ and $\nu = 0.3$, then (7.2) gives the maximum velocity the flywheel can withstand for a given disc radius. The amount of time required for the flywheel with a thickness of 0.2 m to reach β' for a given torque of 50 kNm, say, is obtained by integrating Newton's 2nd law once with respect to time, where the result is plotted against r_{disc} in Figure 7.1. A larger disc radius is seen to allow the flywheel to spin-up longer before attaining the critical stress. With a motor torque of 50 kNm, which for the motorised tether is rather conservative, the critical stress is arrived at in less than 60 seconds for disc radii less than 1.5 m. In comparison to the orbital period this is simply too short since the motorised tether will need more than an orbit revolution to impart the necessary ΔV . A flywheel with a radius of 2.5 m will reach the critical stresses due to rotation in less than 5 minutes, a duration of time which is still too short. Moreover, such a flywheel with the given dimensions would have an impractical mass of 30,827 kg. Changing the material for the flywheel does increase the duration of spin-up time but is not significant enough to allow the motor to spin-up the rotor. Hence, the reaction wheel is not a viable means of providing the resistive torque for the motorised tether.

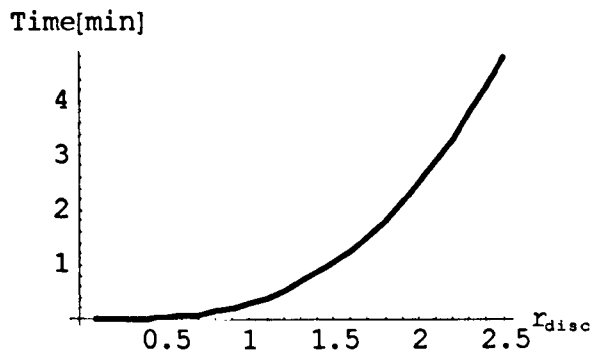


Figure 7.1 Time required for a steel flywheel to reach a maximum sustainable angular velocity for a specified disc radius.

A more effective means of providing the necessary resistive torque is to deploy two further tethers from the stator drum, which are identical to the propulsive tethers and terminate in end masses. If the effect of the gravity gradient is not employed to aid in the design of the outrigger, then the outrigger's mass moment of inertia must equal or exceed that of the

propulsive side. An unequal mass moment of inertia implies one side must spin faster than the other, which is not acceptable for the outrigger as it would reach the maximum allowable stress before the propulsive side. Thus, if the outrigger tethers are shorter than the propulsive tethers then the outrigger's end masses must be larger than the payloads to equate the propulsive side's mass moment of inertia. Outrigger tethers equal in length to the propulsive tethers would require the outrigger end masses to be identical to the payloads. Outrigger tethers longer than the propulsive tethers would permit smaller end masses to be attached to the outrigger tips. Shorter outrigger tethers have the advantage of exposing less surface area to micrometeorites and should therefore survive the space environment for longer. Their disadvantage is the need to deliver more mass into orbit in the form of the end bodies for the motorised tether to operate, which increases the mission's launch costs. Longer outrigger tethers increase the stator's mass moment of inertia more effectively without a huge mass penalty but are more exposed to micrometeorites. Equal propulsive and outrigger end masses and tethers are probably only a serious option if the outrigger masses are additional payloads.

The gravity gradient exerts through the tether mass and end masses a torque about the tether's centre of mass. Depending on the orientation of the tether about the local vertical the torque will either resist or assist the motor torque's sense of direction. However, as seen in Chapter 6 the gravity gradient can exert such a large resistive torque that the motor is unable to spin-up the tether. Exploiting the gravity gradient could therefore provide a means of reducing the mass of the outrigger's end bodies plus reduce the outrigger tether length, thus decreasing the surface area exposed to high velocity particles. A similar analysis to that in Chapter 6 is required to determine the necessary tether length required to trap the outrigger in the gravitational potential well. The equation of motion governing the outrigger is

$$I_{out} \beta'' + \frac{\partial U_{out}}{\partial \beta} = \tau \quad (7.3)$$

where β = angular displacement of outrigger system defined positive in the opposite direction to ψ , I_{out} = mass moment of inertia of outrigger and U_{out} = potential energy of outrigger system. Integrating (7.3) with respect to β and assuming the initial outrigger angular velocity is zero at the point of initiating the motor torque, gives

$$\beta'_2 = \sqrt{2 \frac{\tau(\beta_2 - \beta_1) + U_{out}[\beta_1] - U_{out}[\beta_2]}{I_{out}}} \quad (7.4)$$

If the outrigger is to spin up then the velocity β'_2 has to be positive and real at $\beta_2 = \pi/2$.

Hence,

$$\tau(\pi/2 - \beta_1) + U_{out}[\beta_1] - U_{out}[\pi/2] > 0 \quad (7.5)$$

where U_{out} is obtained from (2.94) or (2.98). Note, that this criterion is independent of the tether's mass moment of inertia. The torque's magnitude is determined by the propulsive tether side through the strength consideration in (6.35). With the motor torque selected, the criterion in (7.5) can be used to determine the minimum outrigger length required for a given initial condition to keep the outrigger trapped within the potential well.

Figure 7.2 compares the tether length of a spinning outrigger tether with the identical mass moment of inertia as the propulsive side, to an outrigger captured by the gravity gradient within the potential well. The motorised tether's dimensions and properties are: $M_M = 2500$ kg, $M_P = 500$ kg, $M_{out} =$ outrigger end masses = 50 kg, $r_t = 0.001$ m, $r_M = r_{payload} = 0.5$ m, $r_C = 7000$ km, $\sigma_{max} = 1.625$ GPa, $\rho = 970$ kg/m³, and $P = 5.5$ kW. Employing the motor torque as a variable allows the possible pitch velocity to be determined using the relationship $P = \tau\psi'$, which subsequently allows (6.35) to determine the propulsive tether length. The tether length of the spinning outrigger can consequently be determined by equating the outrigger's mass moment of inertia with that of the propulsive side and the tether length of the gravity gradient captured outrigger is obtained from (7.5). Figure 7.2 shows that the spinning outrigger is always larger than the propulsive tether, whereas the captured outrigger is longer than the propulsive tether for low torque values and shorter for higher magnitudes. For very low torque values a spinning outrigger is shorter in length than a gravity gradient captured outrigger system. However, for the majority of torque values and especially those of practical interest the captured outrigger is significantly shorter than a spinning outrigger tether, thereby exposing less surface area to the environment and requiring less tether mass to be delivered into orbit. Moreover, the captured outrigger is significantly shorter than the propulsive tether for large torque values.

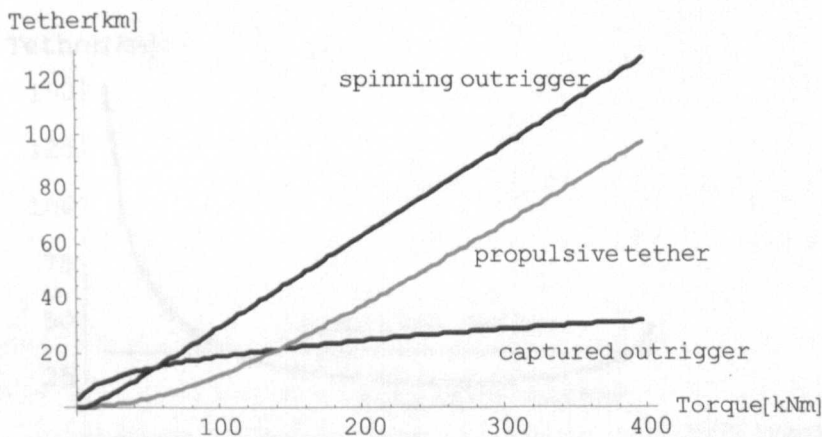


Figure 7.2 Comparison between a spinning and gravity gradient captured outrigger system in relation to the propulsive tether length for a given motor torque with $\beta(0) = 0$ rad.

The graph in Figure 7.2 was generated by assuming a zero initial angular displacement in the outrigger tether. As Figure 7.3 shows, the initial angular displacement of the outrigger has a noteworthy effect on the required length necessary to ensure the tether remains captured within the potential well. Initiating the motor torque with a large libration angle present in the outrigger will require the outrigger to have several tens of kilometres of additional tether length. The optimum tether length is not, however, obtained for $\beta(0)=0$ rad. Figure 7.4 shows for an applied torque of 200 kNm the shortest outrigger length is obtained for $\beta(0)\approx 0.4$ rad. On the whole it is favourable to have a positive initial angular displacement rather than a large negative one.

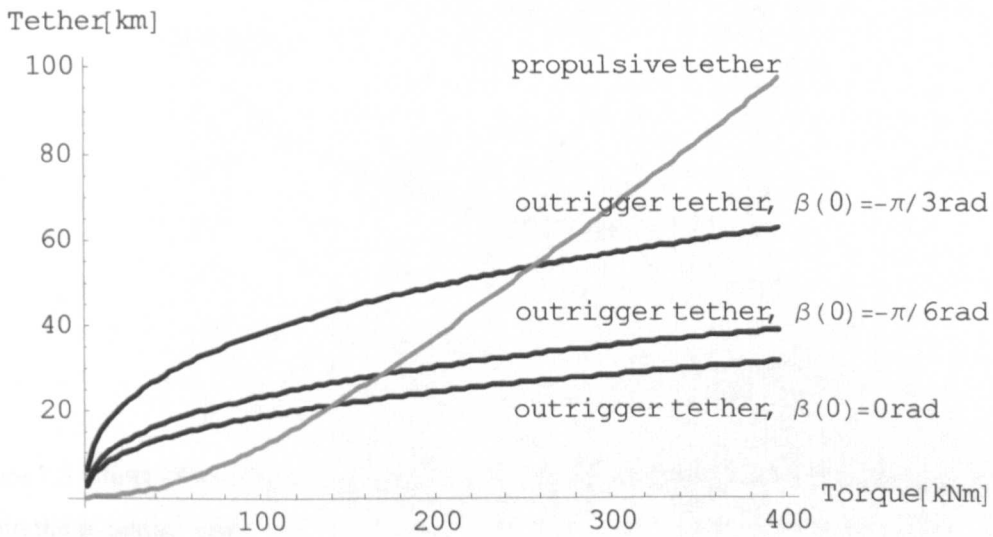


Figure 7.3 Propulsive and outrigger tether length required for a given motor torque, where the outrigger system is trapped inside the potential well.

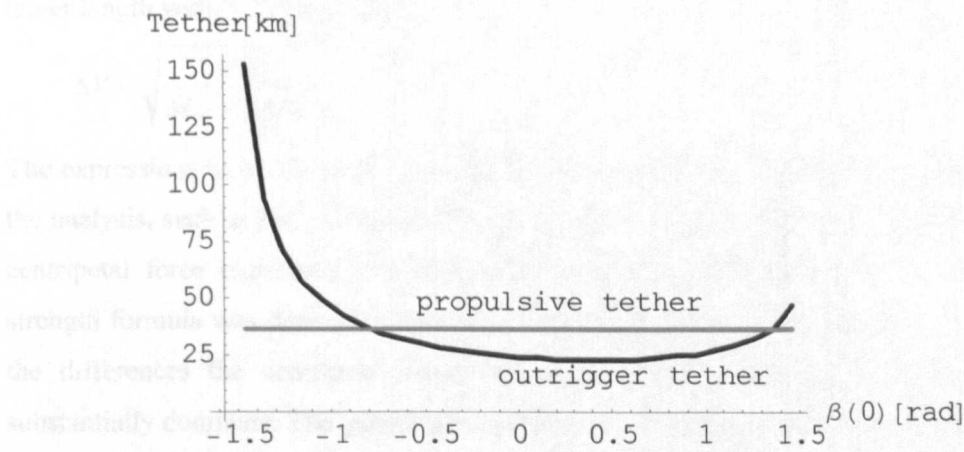


Figure 7.4 Effect of initial angular displacement on the outrigger tether length required to keep the system trapped within the potential well.

In Figure 7.5 the effect of the outrigger end body mass on the necessary tether length is investigated for gravity gradient capture. As would be expected an increase in the mass of the end body causes a decrease in the required outrigger tether length. Increasing M_{out} from 50 to 500 kg yields, for the given data and $\tau = 200$ kNm, a corresponding decrease in tether length of approximately 10 km. In other words, increasing M_{out} by 450 kg only decreases the tether mass by roughly 30 kg but exposes 10 km less to the environment. Increasing M_{out} would therefore appear to unnecessarily add to the launch costs and may be best kept as low as possible. However, only a risk analysis quantifying the reduction in tether severing by micrometeorites would be able to definitively quantify and conclude whether the cost of the additional launch mass is worth an increase in predicted tether lifetime.

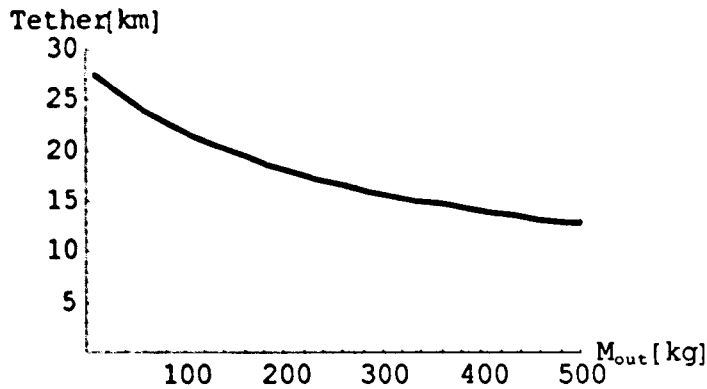


Figure 7.5 Effect of outrigger end mass on required tether length to contain outrigger system within the potential well.

7.2 Design Data for the Motorised Tether

The amount of ΔV a motorised tether is able to generate, can be estimated by multiplying the tether length with (6.35) to obtain

$$\Delta V = \sqrt{\frac{\alpha L}{M_p + \rho A L / 2}} \quad (7.6)$$

The expressions in (6.35) or (7.6) are not wholly accurate as several forces are neglected in the analysis, such as the gravitational force acting on the end body and tether masses or the centripetal force experienced by the system whilst orbiting the Earth. A more detailed strength formula was derived to take account of these forces on the tether but in comparing the differences the centripetal force about the tether's centre of mass was found to substantially dominate. The quantitative difference was found to affect the second significant digit after the decimal point, which is negligibly small.

To maximise the possible ΔV in (7.6) the material used to manufacture the tether should have a very high yield strength but a low density. The tether should be as long as possible with the payloads having a low mass if the ΔV is to be as large as possible. The magnitudes of ΔV attainable with a motorised tether using Spectra 2000, where $r_t = 0.001$ m, $\sigma_{max} = 1.625$ GPa and $\rho = 970$ kg/m³, are presented in Figure 7.6 and Figure 7.7. For the given data a ΔV in the region of 400-600 m/s can be imparted to a payload with a mass of 1000 kg, whereas for a payload of 100 kg the maximum ΔV ranges between 1-1.4 km/s depending on the tether length. Figure 7.7 shows that a maximum ΔV of 1.4-1.75 km/s can be achieved for very small payload mass, e.g. $M_p = 10$ kg, if a suitably long tether is selected. In summary, Figure 7.6 and Figure 7.7 suggest a motorised tether can generate a ΔV in the region of 1 km/s for a payload mass that is of practical interest and a realistic tether length. In future, greater ΔV can be expected with the emergence of stronger but lighter materials.

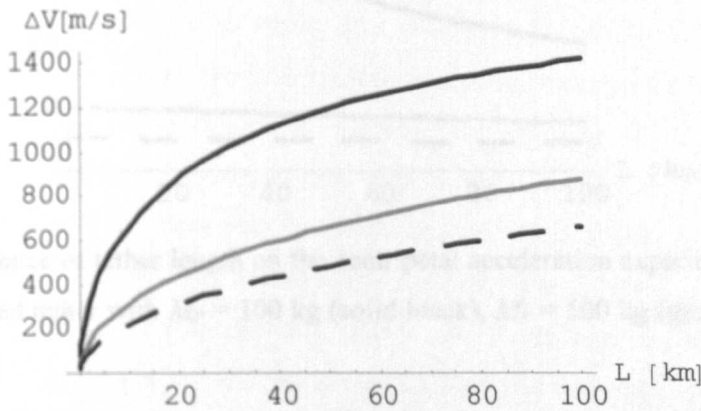


Figure 7.6 Influence of tether length on the ΔV from a motorised tether with $M_p = 100$ kg (solid black), $M_p = 500$ kg (grey), and $M_p = 1000$ kg (dashed).

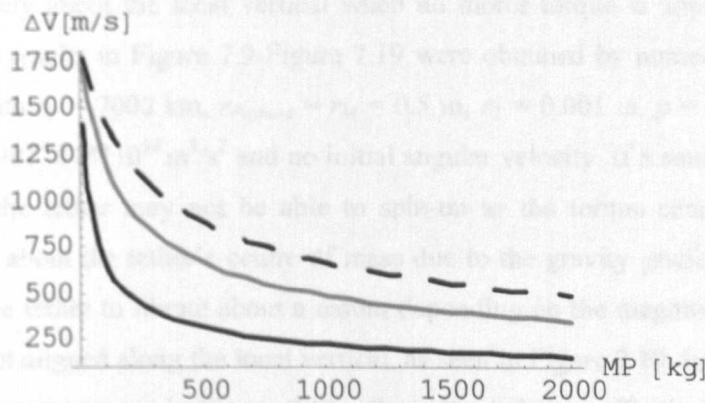


Figure 7.7 Influence of payload mass on the ΔV from a motorised tether with $L = 10$ km (solid black), $L = 50$ km (grey), and $L = 100$ km (dashed).

Figure 7.8 presents the centripetal acceleration experienced by a body at the tether's tip. A body with a mass of 1000 kg will experience half a g, where $g = 9.81$ m/s², at the point of

release and is independent of the tether length. The 500 kg mass is also largely unaffected by the tether length and feels a 1 g acceleration upon approaching the release conditions. A payload of 100 kg is, however, greatly affected by the tether length and can experience an acceleration between 2-5 g depending on the tether length. The longer the tether the smaller the acceleration is on the relatively light end mass. Due to the amount of mass that can be handled by a motorised tether at its tip, the nature of the payload will be in practice therefore restricted to cargo, although in theory a human could easily survive the levels of acceleration seen in Figure 7.8.

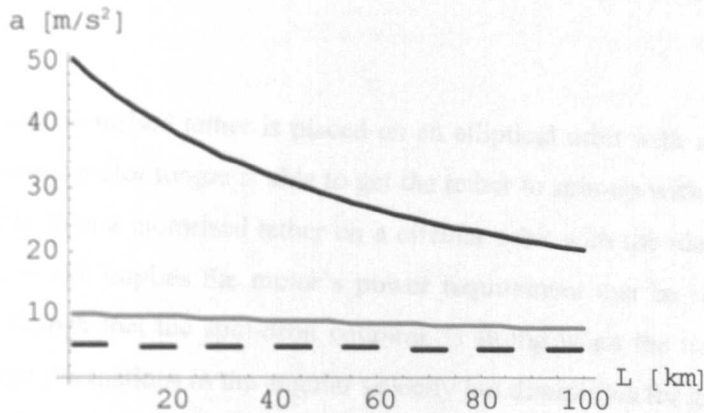


Figure 7.8 Influence of tether length on the centripetal acceleration experienced at the tether tip of a motorised tether with $M_p = 100$ kg (solid black), $M_p = 500$ kg (grey), $M_p = 1000$ kg (dashed).

7.3 Spin-Up Dynamics of a Motorised Tether

A planar motorised tether with a non-zero initial angular displacement on a circular orbit will librate indefinitely about the local vertical when no motor torque is applied, as shown in Figure 7.9. The results in Figure 7.9-Figure 7.19 were obtained by numerically integrating (2.95)-(2.97) with $r_p = 7000$ km, $r_{payload} = r_M = 0.5$ m, $r_T = 0.001$ m, $\rho = 970$ kg/m³, $M_M = 1000$ kg, $\mu = 3.9877848 \cdot 10^{14}$ m³/s² and no initial angular velocity. If a small motor torque is provided then the tether may not be able to spin-up as the torque cannot overcome the resistive torque about the tether's centre of mass due to the gravity gradient. However, the motor causes the tether to librate about a datum depending on the magnitude of the applied torque that is not aligned along the local vertical, as seen in Figure 7.10. In fact, choosing an appropriate motor torque, as in Figure 7.11, allows the tether to effectively shift a hanging tether from the local vertical to a near constant position with an angular offset. This may have useful applications in tethered interferometry where the field of view can be altered by the motor whilst maintaining a stable configuration. Once the gravity gradient torque threshold is breached, as depicted in Figure 7.12, the motor causes the tether to spin up with a net increase in the tether's angular velocity. When the magnitude of the applied torque is

slightly greater than the torque exerted by the gravity gradient then the gravity gradient's effect is clearly evident in the motorised tether's angular velocity, shown in Figure 7.12. However, a significantly larger torque exerted by the motor on the tether causes this effect to lessen, as is evident in Figure 7.13. Longer tethers and heavier end masses increase the gravity gradient's torque on the motorised tether and thus the initial angular displacement plays an important role as to whether the tether can spin-up. For example, the negative initial angular displacement in Figure 7.12 aids the motorised tether to spin, whereas the same but positive initial angular displacement in Figure 7.14 does not permit any build up of tether rotation.

When the planar motorised tether is placed on an elliptical orbit with an eccentricity of 0.1 then a much lower motor torque is able to get the tether to spin-up with a net increase in the angular velocity than a motorised tether on a circular orbit with the identical initial angular displacement, which implies the motor's power requirement can be reduced. Figure 7.15 demonstrates though that the spin-orbit coupling is strong when the motor's torque is low and causes large fluctuations in the angular velocity but diminishes for greater torque values, as shown in Figure 7.16. Note that the tether in Figure 7.16 appears to be spinning faster since a greater angular velocity is attained during the first 5 orbits. As the orbital period increases with larger orbit eccentricities Figure 7.16 cannot conclusively state whether the elliptical orbit causes an actual increase in angular velocity because there is more time for a tether to spin-up over a set number of orbits when comparing elliptical to circular orbits. As is evident by Figure 7.17, the elliptical orbit provides the motorised tether, as an alternative to the reduction in power requirement, more initial conditions that permit tether spin-up, where for the same initial conditions the motorised tether does not spin on a circular orbit. Figure 7.18 demonstrates that for the given motorised tether a larger orbit eccentricity of 0.2 allows the motor to spin up the tether for all initial angular displacements. Moreover, the greater orbit eccentricity allows the magnitude of the applied torque to be reduced, as exemplified by Figure 7.19, whilst still being able to spin-up from all initial displacements.

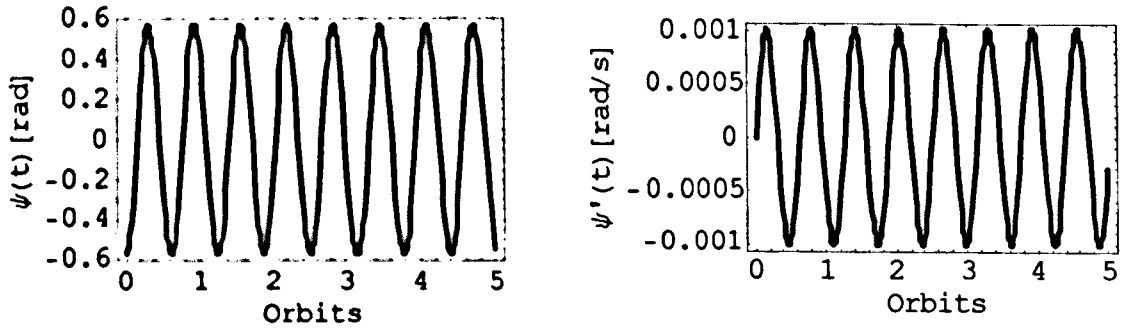


Figure 7.9 Response of angular displacement and velocity of an untorqued planar motorised tether on a circular orbit over 5 orbits with $M_p = 500$ kg, $L = 20$ km, $\psi(0) = -0.575$ rad.

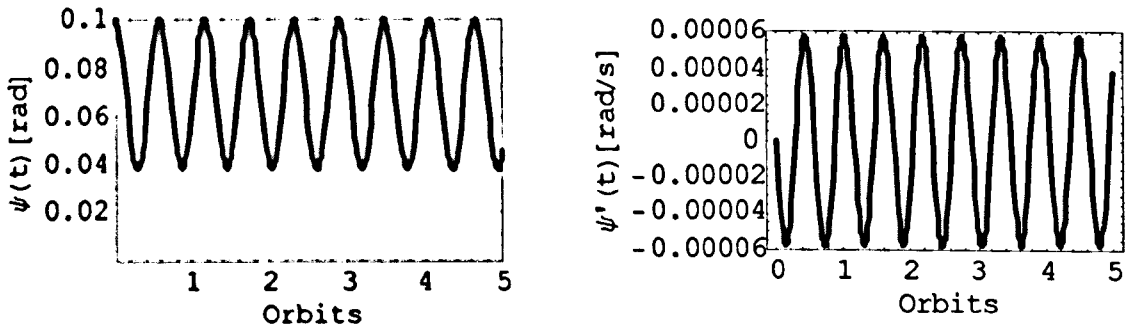


Figure 7.10 Response of angular displacement and velocity of a planar motorised tether on a circular orbit over 5 orbits with $\tau = 100$ kNm, $M_p = 500$ kg, $L = 20$ km, $\psi(0) = 0.1$ rad.

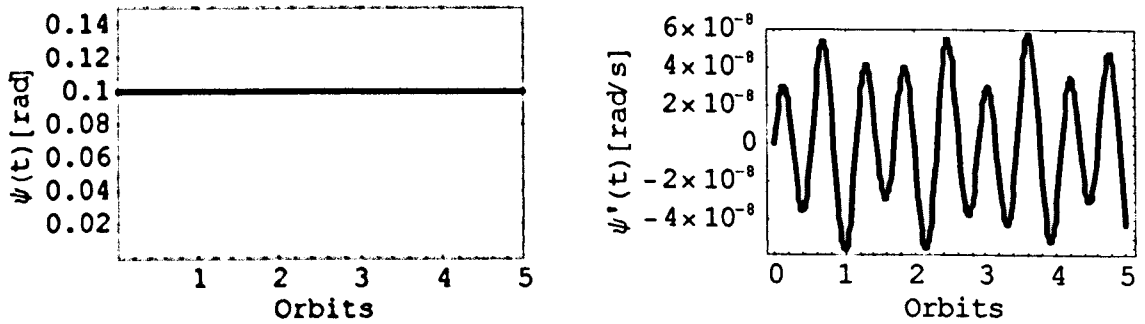


Figure 7.11 Response of angular displacement and velocity of a planar motorised tether on a circular orbit over 5 orbits with $\tau = 144.25$ kNm, $M_p = 500$ kg, $L = 20$ km, $\psi(0) = 0.1$ rad.

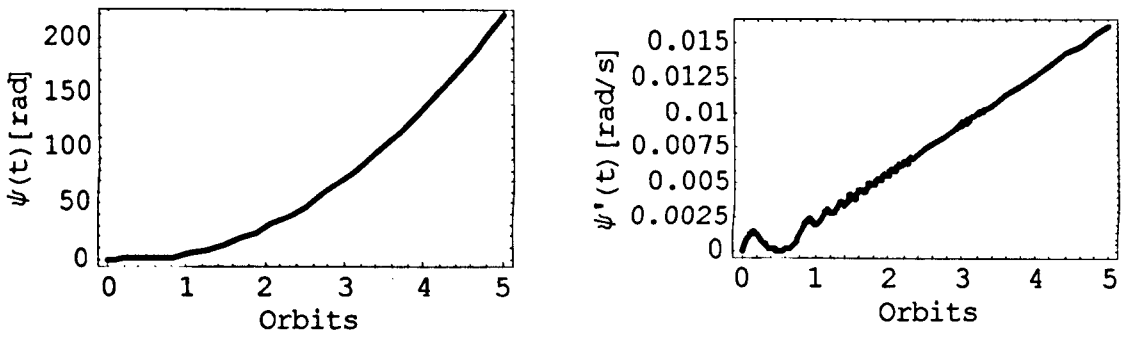


Figure 7.12 Response of angular displacement and velocity of a planar motorised tether on a circular orbit over 5 orbits with $\tau = 250$ kNm, $M_p = 500$ kg, $L = 20$ km, $\psi(0) = -0.575$ rad.

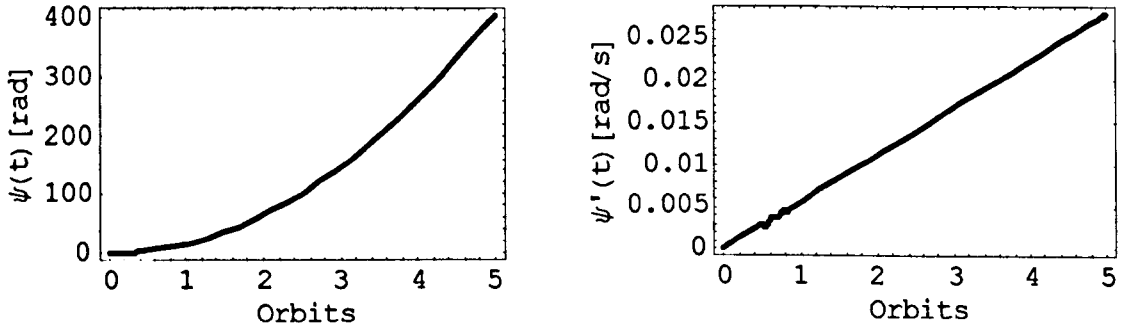


Figure 7.13 Response of angular displacement and velocity of a planar motorised tether on a circular orbit over 5 orbits with $\tau = 400$ kNm, $M_p = 500$ kg, $L = 20$ km, $\psi(0) = -0.575$ rad.

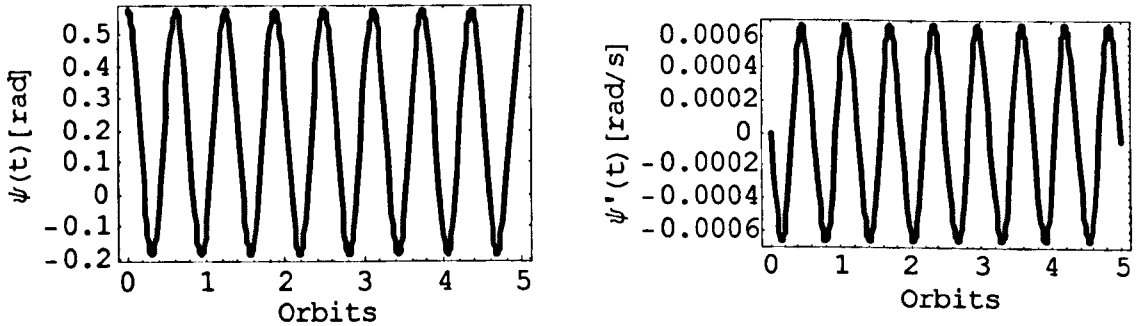


Figure 7.14 Response of angular displacement and velocity of a planar motorised tether on a circular orbit over 5 orbits with $\tau = 250$ kNm, $M_p = 500$ kg, $L = 20$ km, $\psi(0) = 0.575$ rad.

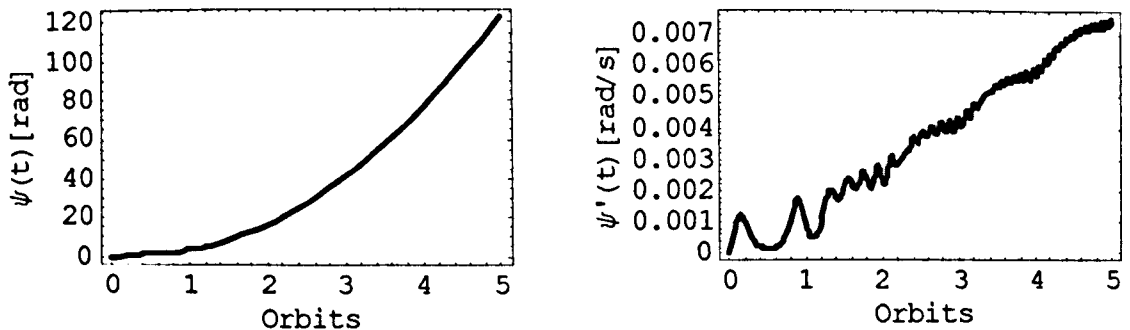


Figure 7.15 Response of angular displacement and velocity of a planar motorised tether over 5 orbits with $e = 0.1$, $\tau = 100$ kNm, $M_p = 500$ kg, $L = 20$ km, $\psi(0) = -0.575$ rad.

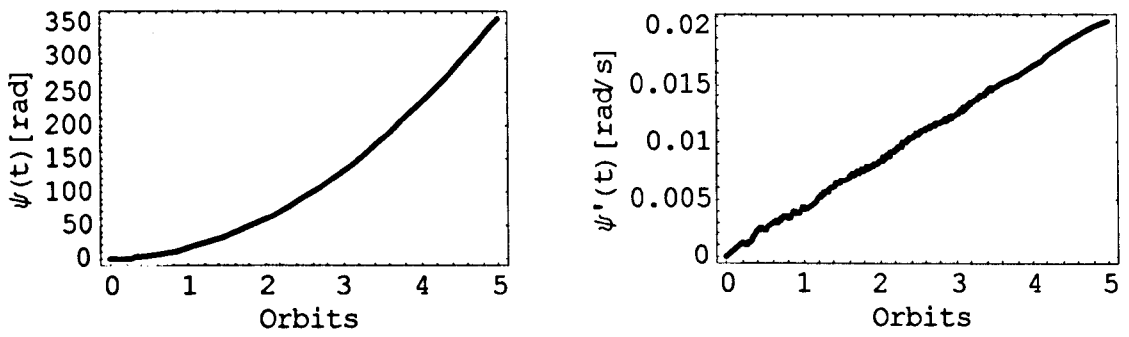


Figure 7.16 Response of angular displacement and velocity of a planar motorised tether over 5 orbits with $e = 0.1$, $\tau = 250$ kNm, $M_p = 500$ kg, $L = 20$ km, $\psi(0) = -0.575$ rad.

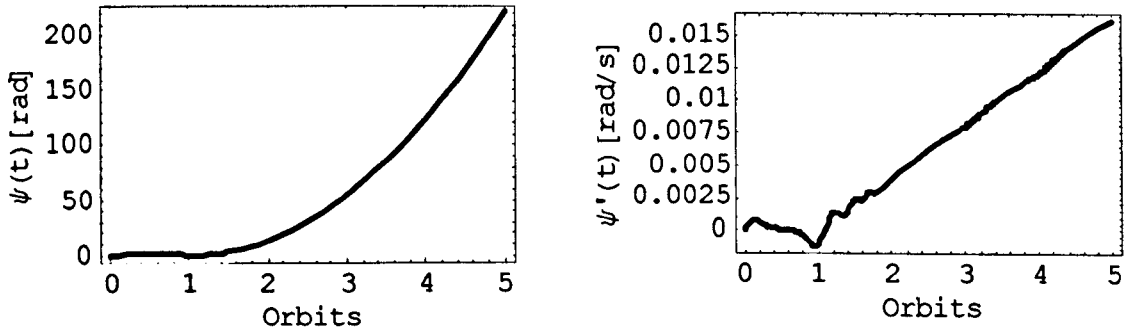


Figure 7.17 Response of angular displacement and velocity of a planar motorised tether over 5 orbits with $e = 0.1$, $\tau = 250$ kNm, $M_p = 500$ kg, $L = 20$ km, $\psi(0) = -0.2$ rad.

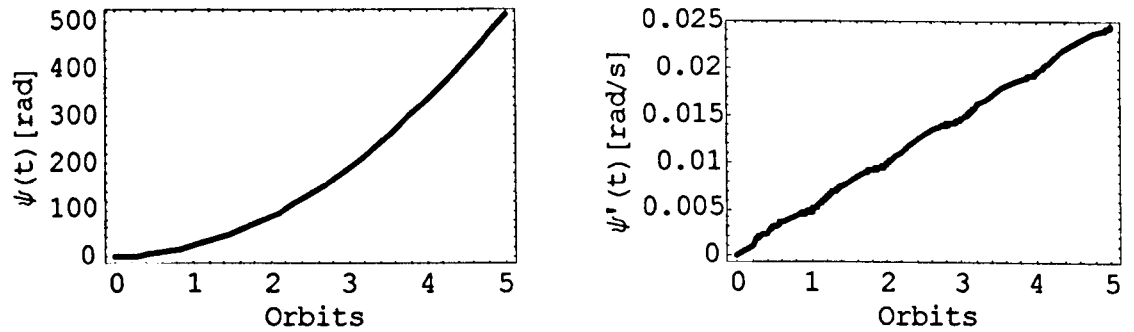


Figure 7.18 Response of angular displacement and velocity of a planar motorised tether over 5 orbits with $e = 0.2$, $\tau = 250$ kNm, $M_p = 500$ kg, $L = 20$ km, $\psi(0) = 1.4$ rad.

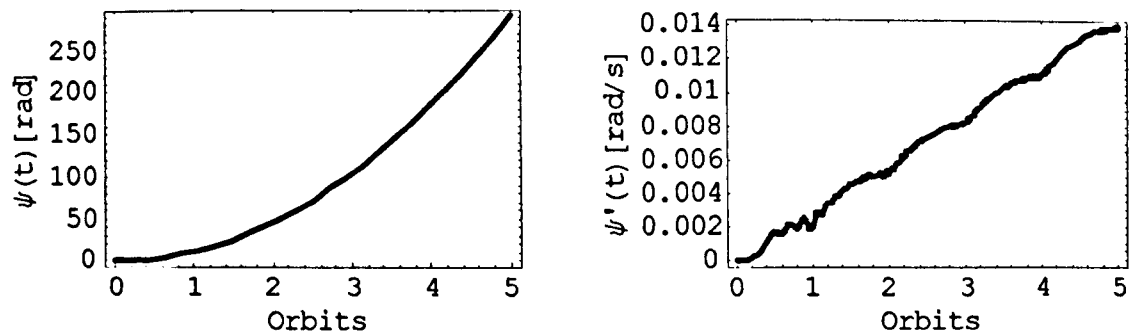


Figure 7.19 Response of angular displacement and velocity of a planar motorised tether over 5 orbits with $e = 0.2$, $\tau = 150$ kNm, $M_p = 500$ kg, $L = 20$ km, $\psi(0) = 1.4$ rad.

The motorised tether remains planar on a circular orbit if the tether has no initial out-of-plane angular displacement and with the motor axis aligned perpendicular to the orbital plane, as seen in Figure 7.20. The graphs in Figure 7.20-Figure 7.27 were obtained by numerically integrating (2.78)-(2.81) using $M_p = 500$ kg, $L = 10$ km, $\tau = 170$ kNm and the same data as before with the planar case. The initial angular velocities are both assumed to be zero. However, with an initial out-of-plane displacement the motorised tether does not return to the orbital plane. Figure 7.21 shows the motorised tether moves during its first two completed orbits through large amplitude oscillations in the out-of-plane whilst beginning to rotate in the pitch direction. The large amplitude oscillations quickly settle, though, into a regime where the motorised tether is precessing in a prograde direction. With time the largest out-of-plane amplitude during precession tapers off. For example, between the motorised tether's eighth and tenth completed orbit, shown in Figure 7.22, a narrow band is established within which the tether precesses. For an initially planar tether on a circular orbit, but with the motor axis no longer perpendicular to the orbital plane, as in Figure 7.23, the response again settles into a precessional motion after initial large out-of-plane oscillations. Since less motor torque is directed into the ψ -angle the rate of tether revolutions must consequently be slower, as is evident by the fewer completed rotations in Figure 7.23 than in Figure 7.21. The combination of both a non-zero γ and $\alpha(0)$ generates at first some large oscillations in Figure 7.24 but as the pitch angular velocity increases the motorised tether returns to its characteristic precession. Figure 7.25 demonstrates that a motorised tether on an elliptical orbit with an initial non-zero zero $\alpha(0)$ but $\gamma = 0$ is qualitatively very similar to the circular orbit case but with the tether completing more revolutions for the same number of completed orbits. The initially planar tether, seen in Figure 7.26, with a non-zero γ enters the zone of precession much faster than the circular case, which suggests the tether is revolving at a higher rate of rotation. Apart from a slightly faster rate of rotation there is little qualitative difference between the motorised tether on an elliptical orbit with a non-zero γ and $\alpha(0)$ in Figure 7.27 and its motion on a circular orbit. Figure 7.20-Figure 7.27 suggest that the motorised tether's motion is regular both on a circular and elliptical orbit. This is an important observation to make for the viability of the motorised tether concept, especially since the planar and 3D tether rotation in Chapters 4 and 5 were found to be chaotic. However, the precession observed in Figure 7.20-Figure 7.27 suggests the possibility of the motorised tether's motion being largely quasi-periodic. If this is proved to be the case then the motorised tether will not be able to deliver the payload reliably along the local vertical at the perigee upon reaching the desired ΔV .

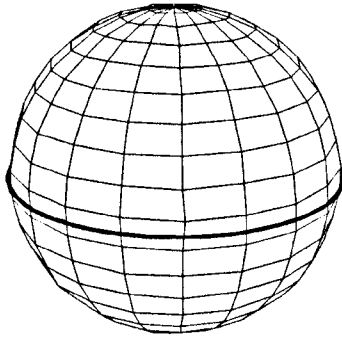


Figure 7.20 Response of a motorised tether plotted on a unit sphere representing the local x_0 - y_0 - z_0 co-ordinate frame over 2 orbits with $\psi(0) = \alpha(0) = \gamma = 0$ and $e = 0$.

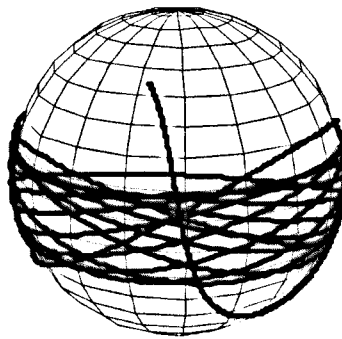


Figure 7.21 Response of a motorised tether plotted on a unit sphere representing the local x_0 - y_0 - z_0 co-ordinate frame over 2 orbits with $\psi(0) = \gamma = 0$, $\alpha(0) = 0.8$ rad and $e = 0$.

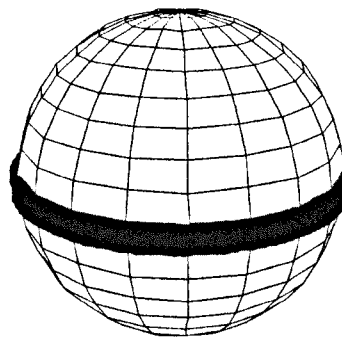


Figure 7.22 Response of a Motorised Tether between the 18th and 20th orbit plotted on a unit sphere representing the local x_0 - y_0 - z_0 co-ordinate frame with $\psi(0) = \gamma = 0$, $\alpha(0) = 0.8$ rad and $e = 0$.

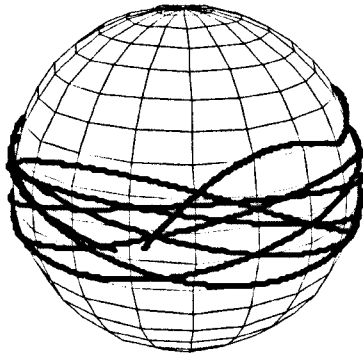


Figure 7.23 Response of a motorised tether plotted on a unit sphere representing the local x_0 - y_0 - z_0 co-ordinate frame over 3 orbits with $\psi(0) = \alpha(0) = 0$, $\gamma = 0.9$ rad and $e = 0$.

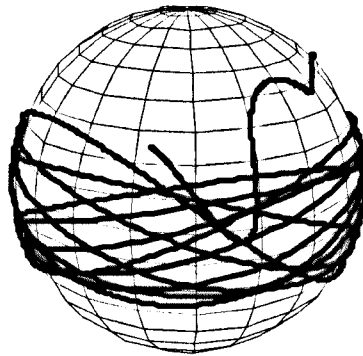


Figure 7.24 Response of a motorised tether plotted on a unit sphere representing the local x_0 - y_0 - z_0 co-ordinate frame over 3 orbits with $\psi(0) = 0$, $\alpha(0) = 0.5$ rad, $\gamma = 0.9$ rad and $e = 0$.

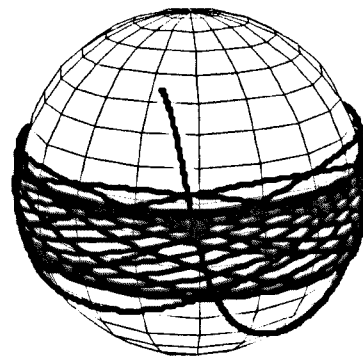


Figure 7.25 Response of a motorised tether plotted on a unit sphere representing the local x_0 - y_0 - z_0 co-ordinate frame over 2 orbits with $\psi(0) = \gamma = 0$ and $\alpha(0) = 0.8$ rad and $e = 0.1$.

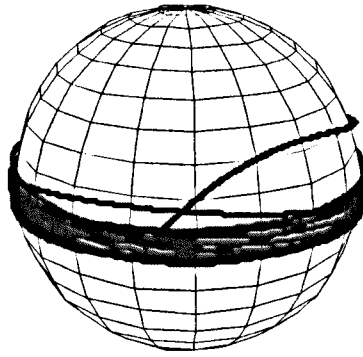


Figure 7.26 Response of a motorised tether plotted on a unit sphere representing the local x_0 - y_0 - z_0 co-ordinate frame over 2 orbits with $\psi(0) = \alpha(0) = 0$, $\gamma = 0.9$ rad and $e = 0.1$.

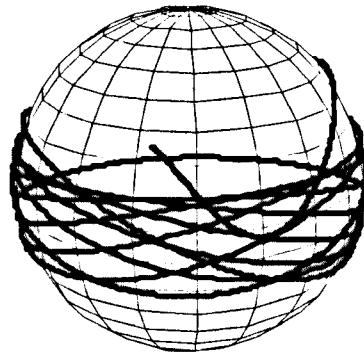


Figure 7.27 Response of a motorised tether plotted on a unit sphere representing the local x_0 - y_0 - z_0 co-ordinate frame over 2 orbits with $\psi(0) = 0$, $\alpha(0) = 0.5$ rad, $\gamma = 0.9$ rad and $e = 0.1$.

Figure 7.28-Figure 7.31 show a view along the z_0 -axis of the relative rotating reference frame centred at the motorised tether's COM in Figure 2.7, which thus represents a view onto the orbital plane. The position of the upper mass about the COM is recorded at every perigee passing and plotted onto a unit circle for $\tau = 230$ kNm, $L = 50$ km, $M_p = 100$ kg and $\alpha(0) = \gamma = 0$. Hence, the x_0 -axis is aligned along the perigee and a collection of points near the x_0 -axis would therefore suggest that the motorised tether is able to reliably release the payload at the perigee. Figure 7.28 shows the tether orientation at the first ten perigee crossing for a motorised tether spinning up within the orbital plane. None of the tether positions are remotely near the local vertical for the given tether. Continuing to plot the tether's orientation over the next 490 perigee crossings as shown in Figure 7.29 leads to the whole unit circle being filled with dots. Note, that the results in Figure 7.29 are wholly

hypothetically as the tether strength is already exceeded in Figure 7.28. Transferring the motorised tether from a circular to an elliptical orbit does not yield any different results. For an eccentricity of 0.1 and 0.2 the given tether in Figure 7.30 and Figure 7.31 does not deliver the upper payload close to the local vertical at the perigee over the first ten orbits. If the tether material could withstand higher stresses then eventually the tether is seen in both these cases to align with the perigee like in Figure 7.29. Consequently, Figure 7.28-Figure 7.31 do not exhibit any periodic motion, which is necessary to reliably release the payload prior to the maximum permissible stress being reached.

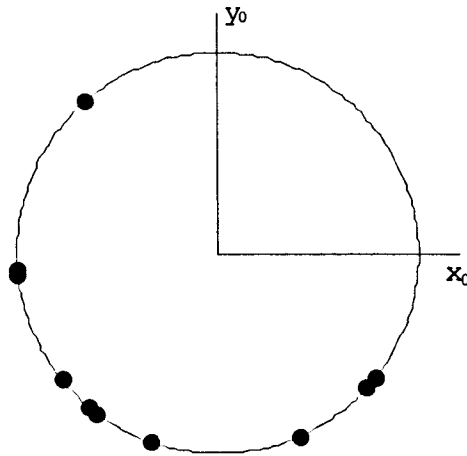


Figure 7.28 Position of the motorised tether’s upper payload at each of the 10 perigee crossing with $e = 0$ and $\psi(0) = -0.9$ rad.

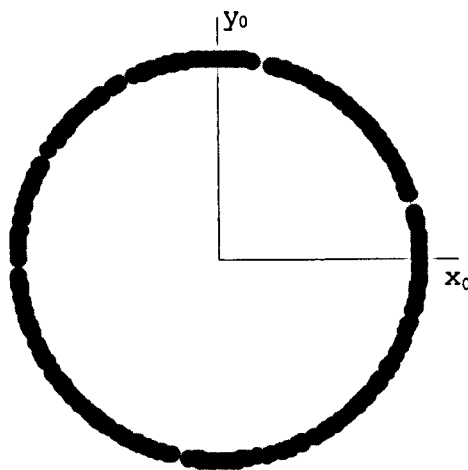


Figure 7.29 Position of the motorised tether’s upper payload at each of the 500 perigee crossing with $e = 0$ and $\psi(0) = -0.9$ rad.

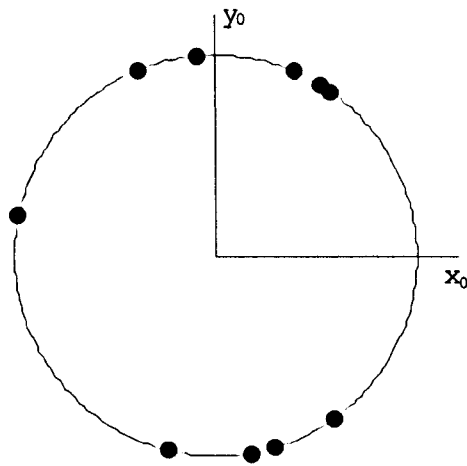


Figure 7.30 Position of the motorised tether's upper payload at each of the 10 perigee crossing with $e = 0.1$ and $\psi(0) = -0.5$ rad.

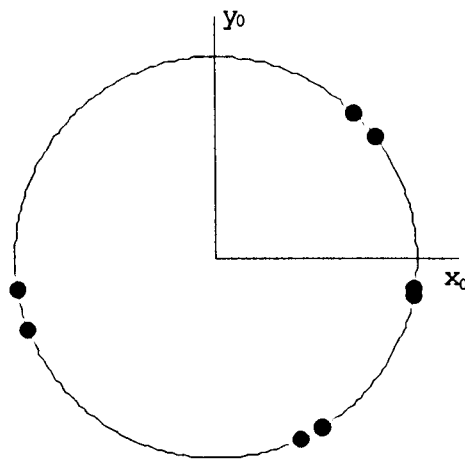


Figure 7.31 Position of the motorised tether's upper payload at each of the 10 perigee crossing with $e = 0.2$ and $\psi(0) = -0.5$ rad.

The bifurcation diagram in Figure 7.32 investigates whether any periodic windows exist for a spinning motorised tether on a circular orbit for the given initial conditions. With the diagram filled with dots and the lack of any periodic windows Figure 7.32 suggests that no periodic motion is present. Placing the motorised tether on elliptical orbits yielded the same result, however, with the angular displacement reaching several hundred thousand radians within the first orbit passing the method of periodically sampling at the perigee in order to generate the bifurcation diagram proved to be prohibitively costly in computational terms. The first Lyapunov exponent in Figure 7.33 demonstrates that the motion in the bifurcation diagram is quasi-periodic and not chaotic. Consequently, the planar or non-planar motorised tether as proposed in this thesis with a constant motor torque is not able to reliably deliver the payload at the point of release along the local vertical due to the presence of the quasi-periodic motion. If the spinning motorised tether is to be of practical use in payload orbital

transfer then in future a method of modulating the motor torque must be investigated. The first goal must be to transform the quasi-periodic motion into a periodic regime followed by shifting one of the periodic windows to coincide with the local vertical at perigee.



Figure 7.32 Bifurcation diagram of the angular displacement with respect to the orbit eccentricity. Initial conditions are $\dot{\psi}(0)=\psi(0)=\alpha(0)=\dot{\alpha}(0)=\gamma=0$, with $M_p = 100$ kg, $L = 20$ km, $\tau = 125$ kNm. The step size in e is 0.01 and each column of results contains 50 points.

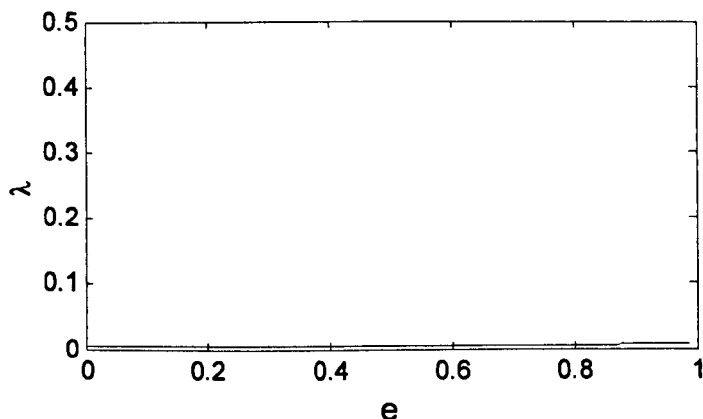


Figure 7.33 First Lyapunov exponent with respect to the orbit eccentricity with $M_p = 100$ kg, $L = 20$ km, $\tau = 125$ kNm and $\dot{\psi}(0)=\psi(0)=\alpha(0)=\dot{\alpha}(0)=\gamma=0$. The step size in e is 0.01 and each exponent is evaluated over 40 orbits.

7.4 Duration of Spin-up

The time required to reach the intended ΔV will depend on many factors. For a 250 kg end mass at the tip of a 50 km long tether with the motor applying a torque of 311 kNm a period of approximately 22 hours is needed to reach the intended release velocity on a circular orbit. Figure 7.34 shows that placing the motorised tether on an elliptical orbit can slightly decrease the time required before the payload must be released. With an orbit eccentricity of

0.3 the motorised tether is found in Figure 7.34 to reach the intended release velocity an hour sooner than the motorised tether on a circular orbit. A relatively large negative initial angular displacement is needed to aid the motor to spin-up, whereas for the shorter tether in Figure 7.35 a smaller torque and initial angular displacement is needed. The 20 km long tether in Figure 7.35 reaches the planned angular velocity in approximately 11 hours, with more favourable initial angular displacements reducing this again by an hour. The point-mass model in (2.78)-(2.81) is employed to generate Figure 7.36 and Figure 7.37. Note how the lack of tether mass and mass moment of inertia in the model reduces the expected spin-up time from 22 hours to 18.5 hours, highlighting the importance of an accurate tether model. When the motorised tether is not initially planar then the spin-up time takes longer the larger the initial out-of-plane angle measures. For the given values in Figure 7.36 the delay is, however, at most 45-60 minutes. Figure 7.37 shows that the initial orientation of the motor torque axis relative to the orbital plane is a critical parameter in the spin-up of the motorised tether. The larger γ is the more time is required to obtain the desired angular velocity. In contrast to the previous cases, though, the delay is not roughly an hour but ranges between 60 minutes and 12 hours for the given values. Consequently, ensuring the motor torque axis is perpendicular to the orbital plane prior to engaging the motor can save a significant amount of spin-up time.

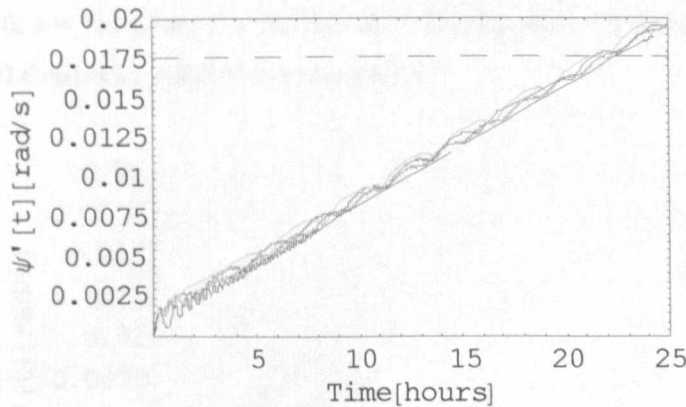


Figure 7.34 Duration of spin-up with a motorised tether to reach payload release velocity (dashed) for $\psi(0) = -1.1$ rad, $\tau = 311$ kNm, $L = 50$ km, $M_p = 250$ kg, $e = 0$ (black), $e = 0.1$ (red), $e = 0.2$ (blue), $e = 0.3$ (green).

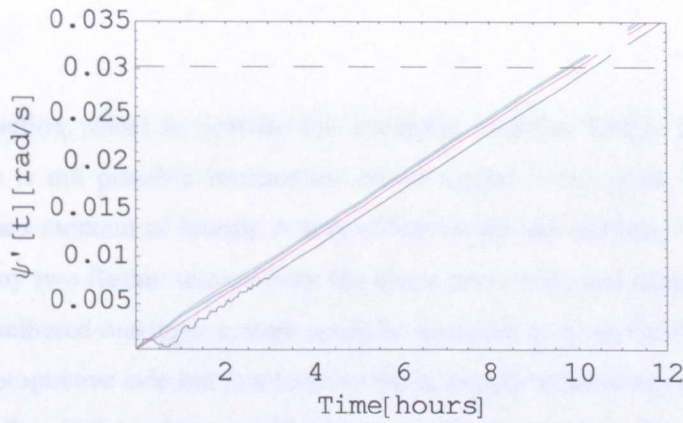


Figure 7.35 Duration of spin-up with a motorised tether to reach payload release velocity (dashed) for $e = 0$, $\tau = 182$ kNm, $L = 20$ km, $M_p = 250$ kg, $\psi(0) = -0.4$ rad (black), $\psi(0) = -0.6$ rad (red), $\psi(0) = -0.8$ rad (blue), $\psi(0) = -1.0$ rad (green).

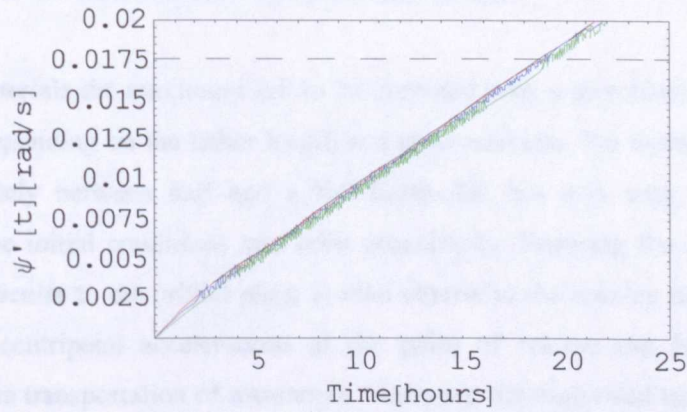


Figure 7.36 Duration of spin-up with a motorised tether to reach payload release velocity (dashed) for $e = 0$, $\tau = 311$ kNm, $L = 50$ km, $M_p = 250$ kg, $\alpha(0) = 0$ rad (black), $\alpha(0) = 0.2$ rad (red), $\alpha(0) = 0.4$ rad (blue), $\alpha(0) = 0.6$ rad (green).

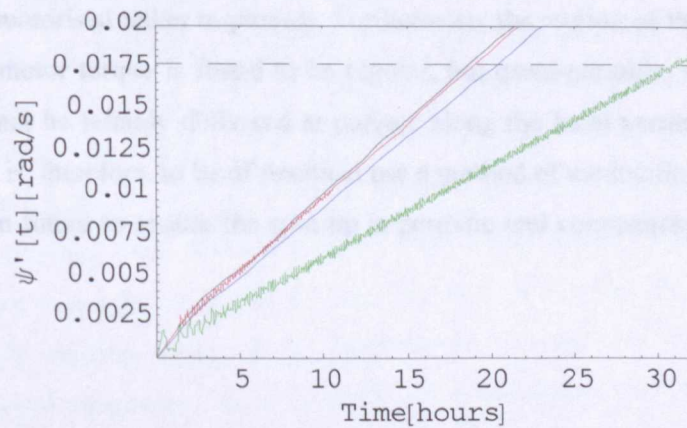


Figure 7.37 Duration of spin-up with a motorised tether to reach payload release velocity (dashed) for $e = 0$, $\tau = 311$ kNm, $L = 50$ km, $M_p = 250$ kg, $\gamma = 0$ rad (black), $\gamma = 0.2$ rad (red), $\gamma = 0.4$ rad (blue), $\gamma = 0.6$ rad (green).

7.5 Conclusions

Employing a reaction wheel to provide the necessary resistive torque for the propulsive tether to spin-up is not possible because the motor torque is too great for the flywheel's relatively low mass moment of inertia. A way of increasing the outrigger's mass moment of inertia is to deploy two further tethers from the stator drum with end masses attached to the tether's tip. The tethered outrigger system could be designed to have the same mass moment of inertia as the propulsive side but this leads to the outrigger tether always being longer than the propulsive tether if the outrigger end masses are to be less than the payloads. A better design is to utilise the gravity gradient and trap the outrigger system with the gravitational potential well. In this manner the outrigger tether length can be significantly reduced and the outrigger end masses can be minimised, thus saving valuable launch mass and cost, as well as exposing less tether surface area to the space environment.

With current materials the maximum ΔV to be expected with a motorised tether is between 600-1400 m/s depending on the tether length and payload mass. The duration of the spin-up lasts approximately between half and a full Earth day but may vary by an hour, say, depending on the initial conditions and orbit eccentricity. Ensuring the motor torque axis remains perpendicular to the orbital plane is vital otherwise the spin-up time will be greatly increased. The centripetal accelerations at the point of release can be designed to be acceptable for the transportation of astronauts. However, the motorised tether is suited more to the transportation of cargo since the tether performs better with lower payload masses. The motorised tether has the ability to shift the datum of a hanging tether, which may have useful applications in Earth monitoring or tethered interferometry. Out-of-plane initial angular displacements or the motor torque axis not remaining perpendicular to the orbital plane cause the motorised tether to precess. Furthermore, the motion of the motorised tether with a constant motor torque is found to be regular, but quasi-periodic, which implies that the payload cannot be reliably delivered at perigee along the local vertical. If the spinning motorised tether is, therefore, to be of practical use a method of modulating the motor torque must be found in future to ensure the spin-up is periodic and commensurate with the local vertical.

Chapter 8

Conclusions and Further Work

8.0 Conclusions

Of the many proposed forms of advanced space propulsion, space tethers have the potential in the near term to reduce the operational costs of the ISS, decrease costs of launching payloads into orbit, deorbit space junk, transfer payloads from low to high orbits and vice versa, and ultimately offer the possibility of a low cost and reusable transportation system for cargo destined from Earth to space stations, asteroids, moons or planets. Space tethers are high strength, low-density cables that connect satellites, probes or space stations to each other in space. The cables are typically very long structures ranging from a few hundred metres to several kilometres and have a relatively small diameter, being only a few millimetres thick. Many applications have been proposed for tethers and much experience and knowledge has been gained through in-orbit flight-testing of conductive and non-conductive tethers. Tethers are also being supported by the major space agencies and companies can already foresee the possibility of commercially exploiting tethers to make a profit. The aim of this thesis was to address some of the issues relating to the performance and dynamics of momentum exchange tethers.

The equations of motion governing a rigid massless tethered dumbbell and a rigid symmetrical motorised tether were derived. Constraining the tether's motion to a Keplerian orbit reduced and considerably simplified the three dimensional equations of motion from four to two ordinary differential equations, thus making them more expedient to integrate numerically. The presented results indicate that the simplified equations appear to be valid approximations as the qualitative behaviour is wholly captured, but small quantitative discrepancies exist, which need to be taken into account when considering payload orbital transfer with tethers, for example. The multiple scales perturbation method successfully generated an approximate closed-form solution to the three dimensional motion of a tethered dumbbell on an elliptical orbit, which is valid for small initial angular displacements close to the gravity vector and orbit eccentricities less than 0.1. Moreover, the derived analytical solution elegantly explains some of the fundamental principles of the tether's motion. However, numerical integration has to be employed if the dynamics of the tether are to be comprehensively studied for values greater than the given initial conditions and those likely to be encountered in space.

The planar attitude dynamics of a tethered dumbbell on an elliptical orbit were numerically explored. The orbit eccentricity and initial angular displacement were found to affect the boundary between long-term libration and tumbling. The largest stable region exists for a tether with no initial angular velocity and initially positioned close to the local vertical. The long-term libration-tumbling boundary is globally symmetrical about the local vertical but was not found in all cases to be a clearly defined and continuous curve since some regions exhibited discontinuities. A further asymmetrical boundary was discovered for the onset of spin during the first completed orbit, which results in a positive initial angular displacement delaying the onset of tumbling, whereas a negative initial condition encourages tether rotation. The two identified boundaries describe a region where tether libration occurs as a transient and a remarkable structure was uncovered within the region that governs the duration of the transient. The onset of chaos was similarly found to be a function of orbit eccentricity and initial angular displacement. The first Lyapunov exponent with respect to the orbit eccentricity and initial condition yielded a region corresponding to the area of long-term libration. The correlation between tumbling and positive increase of the Lyapunov exponent was found to be very striking and unequivocal. The results suggest a planar tether with no initial angular velocity on an elliptical orbit does not indefinitely librate in a chaotic manner and does not tumble in a periodic manner. Finally, the generation of velocity increments upon completion of a single orbit through the spin-orbit coupling on an elliptical orbit was not found to be of particular use. Few initial conditions exist that allow the payload to be reliably released above the facility when the spinning tether is aligned exactly along the gravity vector at perigee. Moreover, the largest positive ΔV of a couple of hundred metres per second at perigee does not necessarily occur when the payload is above the facility with the tether aligned along the gravity vector, thus releasing the payload in a non-optimum configuration in relation to the orbital velocities.

A relatively small out-of-plane initial displacement was not found to significantly affect the region of stable motion observed for the planar tethered dumbbell. The dumbbell deviated from the planar tether's qualitative behaviour only when the initial out-of-plane angular displacement became sufficiently large and the maximum permissible out-of-plane angle for stable motion occurred for a tether initially aligned along the local vertical. A positive initial condition in the orbital plane resisted tumbling within the first orbit but an increase in the orbit eccentricity promoted tether rotation. In general a larger initial condition in the initial out-of-plane angular displacement promoted tether rotation although a narrow band exists for large initial out-of-plane angular displacements where the tether was found to librate during the first completed orbit. The transient dynamics of the tethered dumbbell on a circular orbit were observed to be intricate and complex. A multitude of plateaux exist where the same

number orbits are completed before tumbling ensues. The boundary between two plateaux was not observed to be a discrete jump but rather a peak is formed between two regions where more orbits are completed before spin occurs. A strong link was observed between libration and regular tether motion and between chaos and a tumbling dumbbell, which suggests a dumbbell librating out of the orbital plane is associated with regular motion and a chaotic regime gives rise to tumbling.

Three fundamental tether motions were considered for payload orbital transfer: hanging, prograde libration and prograde motorised spin. The symmetrical double-ended motorised spinning tether performed best and was most efficient, improving by two orders of magnitude on the librating tether which in turn improved on the hanging tether by roughly a factor of two. An upper payload using long tethers with a motorised tether on a circular orbit can be transferred from a low to a geostationary Earth orbit by employing relatively high motor torque and a safety factor on the tether strength close to unity. Multiple tethered stages or tethers on elliptic orbits have to, consequently, be considered for geostationary payload transfer unless expendable tethers are employed. Despite their poor performance, short tethers are worth considering for use in conjunction with the multiple tethered stages because of their efficiency, overall system mass reduction, cost effectiveness, better survivability and greater range of initial conditions for which spin-up is possible. Consequently, the motor should be spun prior to tether deployment rather than deploying the tethers fully before commencing spin-up, as modelled in this thesis. Two common literature results, the constant efficiency index of seven for a hanging tether upper payload release and the maximum efficiency index of fourteen for an upper payload released from a prograde librating tether, were found to be a lower bound and quite readily breached, respectively. Orbit circularisation through tether release was found to be feasible with retrograde librating tethers. Moreover, upon circularising either the upper or lower payload the payload released from the other end of a symmetrical tether travels on a nearly circular orbit. When the point of release does not occur along the local vertical then a non-optimum release of the payload was found to severely reduce the performance of payload transfer with tethers. Consequently, a very precise and accurately timed release is important for the success of payload orbital transfer with tethers since missing the point of release by a single degree with a spinning tether, say, can cause the payload to miss its required target. The large discrepancies in orbit transfer between ideal and non-optimum release scenarios call into question the use of mechanical catch mechanisms and therefore released payloads will most likely have to correct the inaccuracy at release by firing rocket thrusters.

Employing a reaction wheel to provide the necessary resistive torque for the propulsive tether to spin-up was deemed not to be possible because the motor torque is too great for the flywheel's relatively low mass moment of inertia. A way of increasing the outrigger's mass moment of inertia is to deploy two further tethers from the stator drum with end masses attached to the tether's tip. The tethered outrigger system can be designed to have the same mass moment of inertia as the propulsive side but this leads to the outrigger tether always being longer than the propulsive tether if the outrigger end masses are to be less than the payloads. A better design is to utilise the gravity gradient and trap the outrigger system with the gravitational potential well. In this manner the outrigger tether length can be significantly reduced and the outrigger end masses can be minimised, thus saving valuable launch mass and cost, as well as exposing less tether surface area to the space environment.

With current materials the maximum ΔV to be expected with a motorised tether is between 600-1400 m/s depending on the tether length and payload mass. The duration of the spin-up lasts approximately between half and a full Earth day but may vary by an hour, say, depending on the initial conditions and orbit eccentricity. Ensuring the motor torque axis remains perpendicular to the orbital plane was found to be vital otherwise the spin-up time is greatly increased. The centripetal accelerations at the point of release can be designed to be acceptable for the transportation of astronauts. However, the motorised tether is suited more to the transportation of cargo since the tether performs better with lower payload masses. The motorised tether has the ability to shift the datum of a hanging tether, which may have useful applications in Earth monitoring or tethered interferometry. Out-of-plane initial angular displacements or the motor torque axis not remaining perpendicular to the orbital plane caused the motorised tether to precess. Furthermore, the motion of the motorised tether with a constant motor torque was found to be regular, but quasi-periodic, which implies that the payload cannot be reliably delivered at perigee along the local vertical.

8.1 Further Work

In the treatment of the tethered dumbbell this thesis assumed the initial in- and out-of-plane angular velocity to be zero. Karasopoulos and Richardson (1992) carried out a preliminary study for the planar dumbbell with $\dot{\psi}(0) \neq 0$ and the resulting dynamics look intriguing as, for example, a period one window emerges for a librating tether. However, the study is not very deep and thus there is certainly more to be uncovered. Some of the dumbbell's periodic attitude motion was identified in this thesis by inspecting the presented bifurcation diagrams but a map of all possible periodic attractors is still lacking. A full description of the route to chaos and a classification of the bifurcations that occur for the dumbbell have also not appeared so far in the literature. Perhaps software such as Auto97 by Doedel (1981) can aid

in the definition of the possible bifurcations. The Lyapunov exponent should be calculated for the entire parameter space of the three-dimensional tethered dumbbell in order to conclusively prove the link between tumbling and chaos. Moreover, the obtained results could then be compared to the Melnikov function derived by Koch and Bruhn (1989), and Tong and Rimrott (1991), to evaluate how valid the analytical predictions are for the chaotic motion of the dumbbell. During the chaotic regime the rigid-body attitude model of the dumbbell exhibits at times very fast modulations. In practice it is questionable whether a flexible tether can withstand such modulations. A flexible tether model could, therefore, shed light on the validity of the rigid-body model's predictions when chaos is present. The work in this thesis could also be extended by investigating the dynamics of the tethered dumbbell on parabolic and hyperbolic orbits. This has applications for spacecraft on flyby trajectories, as well as the ascent trajectories of rockets from Earth.

The analytical treatment provided by the method of multiple scales in this thesis was not able to provide any valid results for large orbit eccentricities. In particular the modulation equations could not be employed for a stability analysis since these equations each contained only a single term. Semi-analytical techniques used quite regularly in celestial mechanics to analyse celestial dynamics at high orbit eccentricities, as described by Brumberg and Brumberg (1999), can possibly be applied to the tethered dumbbell and thus permit an advance to be made. Furthermore, an analytical or semi-analytical solution may contribute to the physical understanding as to why the transient libration exists and why the instability arises that ultimately causes the tether to tumble.

If the spinning motorised tether is to be of practical use, a method of modulating the motor torque must be found in future to ensure the spin-up is periodic and commensurate with the local vertical. Without this the motorised tether is of no use to payload orbital transfer with tethers. The deployment process as proposed in this thesis should be modelled to investigate whether the gravity gradient torque can in part be overcome by first initiating the motor and then deploying the tethers to full length. A flexible tether model would be desirable to model this deployment process. In addition to this, a flexible tether model could analyse and quantify the potential hazard of the propulsive tethers clashing with the outrigger tethers. A clash is probably highly likely as the distance between the rotor and stator is very small compared to the length of the tethers, where any small out-of-plane angular displacement will lead to a catastrophic failure. This is a fundamental problem that motorised tethers must overcome if the concept is to be proven viable.

If motorised tethers are in future shown to be practically feasible then the concept of employing them in payload orbital transfer becomes interesting. The fundamental issue with payload transfer with tethers is the ability to reliably and accurately catch and release the payload. The release and catch mechanism must be flexible enough to account for the payload's trajectory error, if no onboard fuel is to be expended by the payload, and yet must be highly accurate if no further errors are to be introduced. Some ingenious conceptual design is required here to solve this issue. Only when these issues are resolved can the concept of interplanetary payload exchange with tethers be realistically considered. For this a very realistic model is required to account for all the gravitational perturbations and shifts in the tethers' centre of mass due to the attitude motion. Moreover, the Earth's oblateness needs to be included, for example, to take account of the tether's perigee advance over time, which would have an effect on the tether's pointing accuracy, say. Finally, the equation of motion governing the three-dimensional motion of a massive motorised tether may be desirable for such an analysis. If so then the derivation of these equations is probably best achieved by employing Euler's equations instead of the methodology adopted in this thesis.

References

- ADAMS, W. M. (1970). "Dynamics of Two Slowly Rotating Point-Mass Vehicles Connected by a Massless Tether and in a Circular Orbit", *NASA Technical Note*, NASA TN D-5599, Washington, D.C., USA.
- AHEDO, E., and SANMARTÍN, J. (2000). "Analysis of Electrodynamic Tethers as Deorbiting Systems", *36th AIAA/ASME/SAE/ASEE Joint Propulsion Conference and Exhibit*, AIAA Paper 2000-3763, 17-19 July, Huntsville, Alabama, USA.
- AHEDO, E., and SANMARTÍN, J. R. (2002). "Analysis of Bare-Tether Systems for Deorbiting Low-Earth-Orbit Satellites", *Journal of Spacecraft and Rockets*, Vol. 39, No. 2, pp. 198-205.
- ANAND, D. K., YUHASZ, R. S., and WHISNANT, J. M. (1971). "Attitude Motion in an Eccentric Orbit", *Journal of Spacecraft and Rockets*, Vol. 8, No. 8, pp. 903-905.
- ANSELMO, L., and PARDINI, C. (2000). "On the Survivability of Tethers in Space", *51st International Astronautical Congress*, IAF Paper 00-IAA.6.5.03, 2-6 October, Rio de Janeiro, Brazil.
- ARNOLD, D. A. (1987). "The Behaviour of Long Tethers in Space", *Journal of the Astronautical Sciences*, Vol. 35, No. 1, pp. 3-18.
- BALANCE, J., and JOHNSON, L. (2001). "Propulsive Small Expendable Deployer System (ProSEDS)", *Proceedings of the Space Technology and Applications International Forum*, Editor: M. S. El-Genk, CP552, 11-14 February, Albuquerque, New Mexico, USA, pp. 419-424.
- BANERJEE, A. K. (1990). "Dynamics of Tethered Payloads with Deployment Rate Control", *Journal of Guidance, Control, and Dynamics*, Vol. 13, No. 4, pp. 759-762.
- BEARDSLEY, T. (1999). "The Way to Go in Space", *Scientific American*, Vol. 280, No. 2, pp. 60-77.
- BEKEY, I. (1983). "Tethers Open New Space Options", *Astronautics and Aeronautics*, Vol. 21, No. 4, pp. 32-40.
- BEKEY, I., and PENZO, P. A. (1986). "Tether Propulsion", *Aerospace America*, Vol. 24, No. 7, pp. 40-43.
- BELETSKY, V. V., and LEVIN, E. M. (1993). *Dynamics of Space Tether Systems*, Vol. 83, Advances in the Astronautical Sciences, American Astronautical Society, San Diego, USA.
- BISWELL, B. L., and PUIG-SUARI, J. (2001). "Analysis of Tether Aerobraking Maneuvers Using a Lifting Probe with Parametric Uncertainties", *AAS/AIAA Space Flight*

- BRERETON, R. C., and MODI, V. J. (1966). "On the Stability of Planar Librations of a Dumbbell Satellite in an Elliptic Orbit", *Journal of the Royal Aeronautical Society*, Vol. 70, No. 672, pp. 1098-1102.
- BRUMBERG, V. A., and BRUMBERG, E. V. (1999). *Celestial Dynamics at High Eccentricities*, Advances in Astronomy and Astrophysics, Vol. 3, Gordon and Breach Science Publishers, Amsterdam, The Netherlands.
- CARROLL J. A. (1986). "Tether Applications in Space Transportation", *Acta Astronautica*, Vol. 13, No.4, pp. 165-174.
- CARTMELL, M. P. (1998). "Generating Velocity Increments by Means of a Spinning Motorised Tether", 34th AIAA/ASME/SAE/ASEE Joint Propulsion Conference & Exhibit, AIAA Paper 98-3739, 13-15 July, Cleveland, Ohio, USA.
- CARTMELL, M. P. and ZIEGLER, S. W. (1999). "Symmetrically Laden Motorised Tethers for Continuous Two-way Interplanetary Payload Exchange", 35th AIAA/ASME/SAE/ASEE Joint Propulsion Conference & Exhibit, AIAA Paper 99-2840, 20-24 June, Los Angeles, California, USA.
- CHAPEL, J. D., and FLANDERS, H. (1993). "Tether Dynamics and Control Results for Tethered Satellite System's Initial Flight", *Advances in the Astronautical Sciences*, Guidance and Control, Vol. 81, AAS Paper, 93-042, pp. 327-346.
- CHOBOTOV, V. A. (1996). *Orbital Mechanics*, 2nd edition, AIAA Education Series, Reston, Virginia, USA.
- CHOBOTOV, V. A., and MAINS, D. L. (1999). "Tether Satellite System Collision Study", *Acta Astronautica*, Vol. 44, Nos. 7-12, pp. 543-551.
- CLARKE, A.C. (1981). "The Space Elevator: Thought Experiment or Key to the Universe", *Advances in Earth Oriented Applications of Space Technology*, Vol. 1, pp. 39-48.
- COLOMBO, G., MARTINEZ-SANCHEZ, M., and ARNOLD, D. (1982). *The Use of Tethers for Payload Orbital Transfer*, Smithsonian Astrophysical Observatory, NAS8-33691.
- CORSI, J., and IESS, L. (2000). "Stability and Control of Electrodynamic Tethers for Deorbiting Applications", 51st International Astronautical Congress, IAF Paper 00-S.6.06, 2-6 October, Rio de Janeiro, Brazil.
- COSMO, M. L., and LORENZINI, E. C. (1997). *Tethers in Space Handbook*, 3rd edition, Smithsonian Astrophysical Observatory, Grant NAG8-1160.
- CRELLIN, E. B., and JANSSENS, F. L. (1996). "Some Properties of the In-Plane Motion of a Dumbbell in Elliptic Orbit", *ESTEC Working Paper*, No. 1888, European Space Agency, Noordwijk, Netherlands.
- DANILIN, A. N., GRISHANIA, T.V., SHIKLYARCHIUK, F. N., and BUZLAEV, D. V. (1999).

- “Dynamics of a Space Vehicle with Elastic Deploying Tether”, *Computers and Structures*, Vol. 72, pp. 141-147.
- DECOU, A. B. (1989). “Tether Static Shape for Rotating Multimass, Multitether, Spacecraft for “Triangle” Michelson Interferometer”, *Journal of Guidance, Control, and Dynamics*, Vol. 12, No. 2, pp. 273-275.
- DOBROWOLNY, M. (2002). “Lateral Oscillations of an Electrodynamic Tether”, *Journal of the Astronautical Sciences*, Vol. 50, No. 2, pp. 125-147.
- DOEDEL, E. J. (1981). “AUTO: A program for the automatic bifurcation analysis of autonomous systems”, *Proceedings of the 10th Manitoba Conference on Numerical Mathematics and Computation*, University of Manitoba, Winnipeg, Canada, pp. 265-284.
- EDWARDS, B. C. (2000). “Design and Deployment of a Space Elevator”, *Acta Astronautica*, Vol. 47, No. 10, pp. 735-744.
- ESTES, R. D., LORENZINI, E. C., SANMARTÍN, J., PELÁEZ, J., MARTINEZ-SANCHEZ, M., JOHNSON, C. L., and VAS, I. E. (2000a). “Bare Tethers for Electrodynamic Spacecraft Propulsion”, *Journal of Spacecraft and Rockets*, Vol. 37, No. 2, pp. 205-211.
- ESTES, R. D., SANMARTÍN, J. and MARTINEZ-SANCHEZ, M. (2000b). “Performance of Bare-Tether Systems under Varying Magnetic and Plasma Conditions”, *Journal of Spacecraft and Rockets*, Vol. 37, No. 2, pp. 197-204.
- FORWARD, R. L., and HOYT, R. P. (1995). “Failsafe Multiline Hoytether Lifetimes”, *31st AIAA/ASME/SAE/ASEE Joint Propulsion Conference and Exhibit*, AIAA Paper 95-2890, 10-12 July, San Diego, California, USA.
- FORWARD, R. L., HOYT, R. P., and UPHOFF, C. W. (2000). “Terminator TetherTM: A Spacecraft Deorbit Device”, *Journal of Spacecraft and Rockets*, Vol. 37, No. 2, pp. 187-196.
- FUJII, H. A., and ICHIKI, W. (1997). “Nonlinear Dynamics of the Tethered Subsatellite System in the Station Keeping Phase”, *Journal of Guidance, Control, and Dynamics*, Vol. 20, No. 2, pp. 403-406.
- GALLAGHER, D. L., JOHNSON, L., MOORE, J. and BAGENAL, F. (1998). “Electrodynamic Tether Propulsion and Power Generation at Jupiter”, *NASA Technical Report*, NASA/TP-1998-208475, NASA STI Program Office, Marshall Space Flight Center, USA.
- GATES, S. S., KOSS, S. M., and ZEDD, M. F. (2001). “Advanced Tether Experiment Deployment Failure”, *Journal of Spacecraft and Rockets*, Vol. 38, No. 1, pp. 60-68.
- GAVIRA-IZQUIERDO, J., ROZEMEIJER, H. and MÜNCHBERG, S. (2000). “The Tether System Experiment – Preparing for ESA’s First Tether Mission”, *ESA Bulletin*, Vol. 102, pp. 139-143.
- GILCHRIST, B. E., BILÉN, S. G., PATRICK, T. A., and VAN NOORD, J. L. (2000). “Bare

- Electrodynamic Tether Ground Simulations in a Dense, High-Speed Plasma Flow”, 36th *AIAA/ASME/SAE/ASEE Joint Propulsion Conference and Exhibit*, AIAA Paper 2000-3869, 17-19 July, Huntsville, Alabama, USA.
- GRATUS, J., and TUCKER, R. (2003). “An Improved Method of Gravicraft Propulsion”, *Acta Astronautica*, Vol. 53, No. 3, pp. 161-172.
- HEIDE, E. J. van der, and KRUIJFF, M. (2000). “Tethers and Debris Mitigation”, 51st *International Astronautical Congress*, IAA Paper 00-IAA-6.6.04, 2-6 October, Rio de Janeiro, Brazil.
- HOFFMAN, J. H., MAZZOLENI, A. P., and SANTANGELO, A. (2001). “Design of an Artificial Gravity Generating Tethered Satellite System”, *American Institute of Physics Conference Proceedings 552*, Editor: Mohamed S. El-Genk, Space Technology and Applications International Forum, 11-14 February, Albuquerque, New Mexico, USA, pp. 502-507.
- HOYT, R. P., and FORWARD, R. L. (1997). “Tether Transport from Sub-Earth-Orbit to the Lunar Surface... and Back!”, *International Space Development Conference*, 22-25 May, Orlando, Florida, USA.
- HOYT, R. (2000a). “Design and Simulation of Tether Facilities for the HASTOL Architecture”, 36th *AIAA/ASME/SAE/ASEE Joint Propulsion Conference and Exhibit*, AIAA Paper 2000-3615, 17-19 July, Huntsville, Alabama, USA.
- HOYT, R. (2000b). “Tether Systems for Satellite Deployment and Disposal”, 51st *International Astronautical Congress*, IAF Paper 00-S.6.04, 2-6 October, Rio de Janeiro, Brazil.
- HOYT, R. P., and UPHOFF, C. (2000). “Cislunar Tether Transport System”, *Journal of Spacecraft and Rockets*, Vol. 37, No. 2, pp. 177-186.
- KARASOPOULOS, H., and RICHARDSON, D. L. (1992). “Chaos in the Pitch Equation of Motion for the Gravity-Gradient Satellite”, *Proceedings of the AIAA/AAS Astrodynamics Conference*, AIAA Paper 92-4369-CP, Hilton Head, South Carolina, USA, pp. 53-65.
- KELLY, W. D. (1984). “Delivery and Disposal of a Space-Shuttle External Tank to Low-Earth Orbit”, *Journal of the Astronautical Sciences*, Vol. 32, No. 3, pp. 343-350.
- KESHIMIRI, M., MISRA, A. K., and MODI, V. J. (1996). “General Formulation for *N*-Body Tethered Satellite System Dynamics”, *Journal of Guidance, Control, and Dynamics*, Vol. 19, No. 1, pp. 75-83.
- KHANIN, R., CARTMELL, M. P., and GILBERT, A. (2000). “A Computerised Implementation of the Multiple Scales Perturbation Method using Mathematica”, *Computers and Structures*, Vol. 76, No. 5, pp. 565-575.
- KOCH, B. P., and BRUHN, B. (1989). “Chaotic and Periodic Motions of Satellites in Elliptic Orbits”, *Zeitschrift für Naturforschung Section A*, Vol. 44, No. 12, pp. 1155-1162.

- KRUPA, M., SCHAGERL, M., STEINDL, A. and TROGER, H. (1996). "Relative Equilibria of Tethered Satellite Systems and their Stability", *Zeitschrift für Angewandte Mathematik und Mechanik*, Vol. 76, No. S4, pp. 325-328.
- KUMAR, K., KUMAR, R., and MISRA, A. K. (1992). "Effects of Deployment Rates and Librations on Tethered Payload Raising", *Journal of Guidance, Control and Dynamics*, Vol. 15, No. 5, pp. 1230-1235.
- KYROUDIS, G. A., and CONWAY, B. A. (1988). "Advantages of Tether Release of Satellites from Elliptic Orbits", *Journal of Guidance, Control and Dynamics*, Vol. 11, No. 5, pp. 441-448.
- LANG, D. D., and NOLTING, R. R. (1967). "Operations with Tethered Space Vehicles", *Proceedings of the Gemini Summary Conference*, NASA SP-138, 1-2 February, Houston, Texas, USA, pp. 55-66.
- LEMKE, E. H. (1985). "On a Lunar Space Elevator", *Acta Astronautica*, Vol. 12, No. 6, pp. 385-396.
- LIANGDONG, L. and BAINUM, P. M. (1990). "Dynamics and Control of a Tethered Antenna/Reflector in Orbit", *Journal of the Astronautical Sciences*, Vol. 38, No. 3, pp. 247-268.
- LIAW, D. C., and ABED, E. H. (1990). "Stabilization of Tethered Satellites During Station Keeping", *IEEE Transactions on Automatic Control*, Vol. 35, No. 11, pp. 1186-1196.
- LORENZINI, E. C., and CARROLL, J. A. (1991). "In-Orbit Experimentation with the Small Expendable-Tether Deployment System", *ESA Journal*, Vol. 15, pp. 27-33.
- LORENZINI, E. C., ESTES, R. D., COSMO, M. L., and PELÁEZ, J. (1999). "Dynamical, Electrical and Thermal Coupling in a New Class of Electrodynamical Tethered Satellites", *AAS/AIAA Spaceflight Mechanics Meeting*, AAS Paper 99-192, Breckenridge, CO, USA.
- LORENZINI, E. C., COSMO, M. L., KAISER, M., BANGHAM, M. E., VONDERWELL, D. J., and JOHNSON, L. (2000). "Mission Analysis of Spinning Systems for Transfers from Low Orbits to Geostationary", *Journal of Spacecraft and Rockets*, Vol. 37, No. 2, pp. 165-172.
- MACCONE, C. (1999). "Tethered System to Get Magnified Radio Pictures of the Galactic Center from a Distance of 550 AU", *Acta Astronautica*, Vol. 45, No. 2, pp. 109-114.
- MATNEY, M., KESSLER, D., and JOHNSON, N. (2000). "Calculation of Collision Probabilities for Space Tethers", *51st International Astronautical Congress*, IAA Paper 00-IAA-6.5.02, 2-6 October, Rio de Janeiro, Brazil.
- MAZZOLENI, A. P. (2000). "Dynamics of a Tethered Satellite Technology Demonstrator During Spin-Up", *51st International Astronautical Congress*, IAF Paper 00-I.2.09, 2-6 October, Rio de Janeiro, Brazil.

- MAZZOLENI, A. P., and HOFFMAN, J. H. (2001). "Nonplanar Spin-Up Dynamics of the ASTOR Tethered Satellite System", *AAS/AIAA Space Flight Mechanics Meeting*, AAS Paper 01-193, 11-15 February, Santa Barbara, CA, USA.
- MELVIN, P. J. (1988). "The Figure-of-8 Librations of the Gravity Gradient Pendulum and Modes of an Orbiting Tether", *Quarterly of Applied Mathematics*, Vol. XLVI, No. 4, pp. 637-663.
- MCBRIDE, N., and TAYLOR, E. A. (1997). "The Risk to Satellite Tethers from Meteoroid and Debris Impacts", *ESA Special Publications*, SP-393, Noordwijk, Netherlands, pp. 375-380.
- MIN, B. N., MISRA, A. K., and MODI, V. J. (1999). "Nonlinear Free Vibration of a Spinning Tether", *Journal of the Astronautical Sciences*, Vol. 47, No. 1 and 2, pp. 1-23.
- MISRA, A. K., and MODI, V. J. (1982). "Deployment and Retrieval of Shuttle Supported Tethered Satellites", *Journal of Guidance, Control, and Dynamics*, Vol. 5, No. 3, pp. 278-285.
- MISRA, A. K., and MODI, V. J. (1989). "Dynamics and Control of Tethered Satellite Systems", *American Society of Mechanical Engineers*, Design Engineering Division Publication, Vol. 18, No. 2, pp. 333-345.
- MISRA, A. K., NIXON, M. S., and MODI, V. J. (2001). "Nonlinear Dynamics of Two-Body Tethered Satellite Systems: Constant Length Case", *Journal of the Astronautical Sciences*, Vol. 49, No. 2, pp. 219-236.
- MOCCIA, A., D'ERRICO, M., and VETRELLA, S. (1996). "Space Station Based Tethered Interferometer for Natural Disaster Monitoring", *Journal of Spacecraft and Rockets*, Vol. 33, No. 5, pp. 700-706.
- MODI, V. J., and BRERETON, R. C. (1966). "Libration Analysis of a Dumbbell Satellite Using the WKBJ Method", *Journal of Applied Mechanics*, Vol. 33, No. 3, pp. 676-678.
- MODI, V. J., and BRERETON, R. C. (1968). "Planar Librational Stability of a Flexible Satellite", *AIAA Journal*, Vol. 6, No. 3, pp. 511-517.
- MODI, V. J., and BRERETON, R. C. (1969). "Periodic Solutions Associated with the Gravity-Gradient-Orientated System: Part I. Analytical and Numerical Determination", *AIAA Journal*, Vol. 7, No. 7, pp. 1217-1225.
- MOON, F. C. (1992). *Chaotic and Fractal Dynamics – An Introduction for Applied Scientists and Engineers*, John Wiley & Sons, USA.
- MORAN, J. P. (1961). "Effects of Plane Librations on the Orbital Motion of a Dumbbell Satellite", *ARS Journal*, Vol. 31, pp. 1089-1096.
- MORAVEC, H. (1977). "A Non-Synchronous Orbital Skyhook", *Journal of the Astronautical Sciences*, Vol. 15, No. 4, pp. 307-322.

- MORRIS, D., GILCHRIST, B., GALLIMORE, A., and JENSEN, K. (2000). "Developing Field Array Cathode Systems for Electrodynamic Tether Propulsion", 36th AIAA/ASME/SAE/ASEE Joint Propulsion Conference and Exhibit, AIAA Paper 2000-3867, 16-19 July, Huntsville, Alabama, USA.
- MURRAY, C. D., and DERMOTT, S. F. (1999). *Solar System Dynamics*, Cambridge University Press, Cambridge, UK.
- NAYFEH, A. H. (2000). *Perturbation Methods*, Wiley-Interscience, USA.
- NETZER, E., and KANE, T. R. (1993). "Deployment and Retrieval Optimisation of a Tethered Satellite System", *Journal of Guidance, Control, and Dynamics*, Vol. 16, No. 6, pp. 1085-1091.
- NETZER, E., and KANE, T. R. (1995). "Estimation and Control of Tethered Satellite Systems", *Journal of Guidance, Control, and Dynamics*, Vol. 18, No. 4, pp. 851-857.
- NIXON, M. S., and MISRA, A. K. (1993). "Nonlinear Dynamics and Chaos of Two-Body Tethered Satellite Systems", *AAS/AIAA Astrodynamics Specialist Conference*, AAS Paper 93-731, Victoria, British Columbia, Canada.
- NORDLEY, G. D., and FORWARD, R. L. (2001). "Mars-Earth Rapid Interplanetary Tether Transport System: I. Initial Feasibility Analysis", *Journal of Propulsion and Power*, Vol. 17, No. 3, pp. 499-507.
- PATERA, R. P. (2002). "Method for Calculating Collision Probability Between a Satellite and a Space Tether", *Journal of Guidance, Control, and Dynamics*, Vol. 25, No. 5, pp. 940-945.
- PEARSON, J. (1975). "The Orbital Tower: a Spacecraft Launcher Using the Earth's Rotational Energy", *Acta Astronautica*, Vol. 2, pp. 785-799.
- PELÁEZ, J., LÓPEZ-REBOLLAL, O., RUIZ, M., LORENZINI, E. C., ESTES, R. D., and COSMO, M. L. (1999). "On the Radial Oscillation of an Electrodynamic Tether", *AAS/AIAA Spaceflight Mechanics Meeting*, AAS Paper 99-194, Breckenridge, Colorado, USA.
- PELÁEZ, J., LORENZINI, E. C., LÓPEZ-REBOLLAL, O., and RUIZ, M. (2000). "A New Kind of Dynamic Instability in Electrodynamic Tethers", 10th AIAA/AAS Spaceflight Mechanics Meeting, AAS Paper 00-190, Clearwater, Florida, USA.
- PELÁEZ, J., LÓPEZ-REBOLLAL, O., RUIZ, M., and LORENZINI, E. C. (2001). "Damping in Rigid Electrodynamic Tethers on Inclined Orbits", 11th AS/AIAA Spaceflight Mechanics Meeting, AAS Paper 01-190, 11-15 February, Santa Barbara, California, USA.
- PELÁEZ, J., RUIZ, M., LÓPEZ-REBOLLAL, O., LORENZINI, E. C., and COSMO, M. L. (2002). "Two-Bar Model for the Dynamics and Stability of Electrodynamic Tethers", *Journal of Guidance, Control, and Dynamics*, Vol. 25, No. 6, pp. 1125-1135.
- PELÁEZ, J., and LARA, M. (2003). "Periodic Solutions in Electrodynamic Tethers on

- Inclined Orbits”, *Journal of Guidance, Control, and Dynamics*, Vol. 26, No. 3, pp. 395-406.
- POLTER, J. H. (1967). *Handbook of the Engineering Sciences*, Vol. 2, D. Van Nostrand Company Inc., pp. 989-991.
- PRESS, W. H., TEUKOLSKY, S. A., VETTERLING, W. T., and FLANNERY, B. P. (1995). *Numerical Recipes in C – The Art of Scientific Computing*, 2nd edition, Cambridge University Press, UK.
- PUIG-SUARI, J., LONGUSKI, J. M., and TRAGESSESSER, S. G. (1993). “A Three Dimensional Hinged-Rod Model for Flexible Aerobraking Tethers”, *Advances in the Astronautical Sciences*, Astrodynamics, AAS Paper 93-730, Vol. 85, pp. 755-774.
- PUIG-SUARI, J., LONGUSKI, J. M., and TRAGESSESSER, S. G. (1995a). “Aerocapture with a Flexible Tether”, *Journal of Guidance, Control, and Dynamics*, Vol. 18, No. 6, pp. 1305-1312.
- PUIG-SUARI, J., LONGUSKI, J. M., and TRAGESSESSER, S. G. (1995b). “A Tether Sling for Lunar and Interplanetary Exploration”, *Acta Astronautica*, Vol. 36, No. 6, pp. 291-295.
- QUADRELLI, M. B. (2001). “Modeling and Dynamics Analysis of Tethered Formations for Space Interferometry”, *11th AS/AIAA Spaceflight Mechanics Meeting*, AAS Paper 01-231, 11-15 February, Santa Barbara, California, USA.
- RUIZ, M., LÓPEZ-REBOLLAL, O., LORENZINI, E. C., and PELÁEZ, J. (2001). “Modal Analysis of the Stability of Periodic Solutions in Electrodynamic Tethers”, *AAS/AIAA Astrodynamics Specialist Conference*, AAS Paper 01-405, 30 July – 2 August, Quebec City, Canada.
- SANDRI, M. (1996). “Numerical Calculation of Lyapunov Exponents”, *The Mathematica Journal*, Vol. 6, No. 3, pp. 78-84.
- SCHIECHTER, H. B. (1964). “Dumbbell Librations in Elliptic Orbits”, *AIAA Journal*, Vol. 2, No. 6, pp. 1000-1003.
- SEISL, M., and STEINDL, A. (1989). “Chaotische Schwingungen von Satelliten”, *Zeitschrift für Angewandte Mathematik und Mechanik*, Vol. 69, No. 5, pp. T352-T354, in German.
- SIDI, M. J. (1997). *Spacecraft Dynamics and Control, A Practical Engineering Approach*, Cambridge University Press, Cambridge, UK.
- STEINER, W., STEINDL, A., and TROGER, H. (1995). “Dynamics of a Space Tethered Satellite System with Two Rigid Endbodies”, *Proceedings of the 4th International Conference on Tethers in Space*, Smithsonian Institute, 10-14 April, Washington, D.C., USA, pp. 1367-1379.
- STEINER, W., SCHAGERL, M. and TROGER, H. (1996). “Nonlinear Large Amplitude Oscillation of a Tethered Satellite System with Variable Tether Length”, *EUROMECH –*

- 2nd *European Nonlinear Oscillations Conference*, 9-13 September, Prague, Czech Republic, pp. 239-244.
- TEOFILLATO, P., and GRAZIANI, F. (1996). "On Librational Motion of Spacecraft", *Chaos, Solitons and Fractals*, Vol. 7, No. 10, pp. 1721-1744.
- THOMSEN, J. J. (1997). *Vibrations and Stability - Order and Chaos*, McGraw-Hill Publishing Company, London, UK.
- TONG, X., and RIMROTT, F. P. J. (1991). "Numerical Studies on Chaotic Planar Motion of Satellites in an Elliptic Orbit", *Chaos, Solitons and Fractals*, Vol. 1, No. 2, pp. 179-186.
- TSIOLKOVSKY, K. E. (1961). *A Way to the Stars*, Moscow, Izdatelstvo AN SSSR, in Russian.
- VAUGHN, J. A., FINCKENOR, M. M., KAMENETZKY, R. R., SCHNEIDER, T., and SCHULER, T. (2000). "Polymeric Coatings for Electrodynamic Tethers", 36th *AIAA/ASME/SAE/ASEE Joint Propulsion Conference and Exhibit*, AIAA Paper 2000-3614, 16-19 July, Huntsville, Alabama, USA.
- VAS, I. E. (2000). "Editorial: Tethers in Space", *Journal of Spacecraft and Rockets*, Vol. 37, No. 2, p. 153.
- VAS, I. E., KELLY, T. J., and SCARL, E. A. (2000). "Space Station Reboost with Electrodynamic Tethers", *Journal of Spacecraft and Rockets*, Vol. 37, No. 2, pp. 154-164.
- WELLS, D. A. (1967). *Theory and Problems of Lagrangian Dynamics*, Schaum's Outlines, McGraw-Hill, USA.
- WIEDERMANN, G., STEINDL, A., and TROGER, H. (2000). "Deployment of a Tethered Satellite under the action of a Braking Force", *Zeitschrift für Angewandte Mathematik und Mechanik*, Vol. 80, No. S3, Section 8-23, pp. S853-S854.
- WOLF, A., SWIFT, J. B., SWINNEY, H. L., and VASTANO, J. A. (1985). "Determining Lyapunov Exponents from a Time Series," *Physica D*, Vol. 16, pp. 285-317.
- ZEDD, M. F. (1997). "Experiments in Tether Dynamics Planned for ATEX's Flight", *Advances in the Astronautical Sciences*, Vol. 97, Part 1, American Astronautical Society, San Diego, CA, USA, pp. 25-44.

